INTRA-INVERSION FILTERING FOR USE OF MAGNETIC FIELDS TO LOCATE AND CHARACTERIZE MAGNETIC DIPOLES FOR UNEXPLODED ORDNANCE (UXO) CLEANUP

SEED PROJECT NUMBER: MM-1452

FINAL REPORT

February 26, 2007

Prepared for:

Strategic Environmental Research and Development Program
Arlington, VA 22203

Prepared by:

René Geophysics
2717 Brig's Bend
Bloomington, IN 47401

Lead Principal Investigator: Dr. R. M. René

Co-Performer (Co-Principal Investigator): Dr. K. Y. Kim
(Kangwon National University)

Approved for public release; distribution is unlimited

This report was prepared under contract to the Department of Defense Strategic Environmental Research and Development Program (SERDP). The publication of this report does not indicate endorsement by the Department of Defense, nor should the contents be construed as reflecting the official policy or position of the Department of Defense. Reference herein to any specific commercial product, process, or service by trade name, trademark, manufacturer, or otherwise, does not necessarily constitute or imply its endorsement, recommendation, or favoring by the Department of Defense.

Table of Contents

Table of contents i
List of Acronyms iii
List of Figures iv
List of Tables ix
List of Mathematical Symbols xi
Acknowledgments xiii
1. Executive Summary 1
2. Objective 4
    2.1 Statement of Need 4
    2.2 Identified Problems 4
    2.3 Planned accomplishments 8
3. Background 9
    3.1 Magnetic and EMI methods for UXO surveys 9
    3.2 Need for full and accurate point-dipole magnetic field inversion 9
    3.3 Other filters applied to UXO magnetic fields 11
    3.4 Research and development preliminary to the SEED project 13
4. Methods 14
    4.1 Introduction 14
    4.2 Acquisition of APG and YPG magnetic data 15
    4.3 Development and refinement of UXOPAC 17
    4.4 Least-squares inversion 20
    4.5 Interpolation and the "flag-node" option 23
    4.6 Intra-inversion filtering (IIF) 24
    4.7 Edge-adaptive and gapped gradient-nulling filters 26
5. Results and Accomplishments 28
    5.1 Introduction 28
    5.2 Applications to APG BTA magnetic anomalies 29
    5.3 Results for anomaly A04 (20 mm projectile) 30
    5.4 Results for anomaly I04 (BDU submunition) 33
    5.5 Results for anomaly M08 (105 mm projectile) 36
    5.6 Results for anomaly C09 (40 mm projectile) 39
    5.7 Results for anomaly K09 (155 mm projectile) 43
    5.8 Results for anomaly B01 (rocket warhead) 47
    5.9 Results for anomaly H12 (mortar round) 49
    5.10 Results for anomaly H03 (40 mm projectile) 52
    5.11 Results for anomaly A07 (57 mm projectile) 54
    5.12 Results for anomaly B10 (BDU submunition) 57
    5.13 Results for anomaly A02 (mortar round) 60
    5.14 Applications to Chongcho Lake and Yeosu surveys 63
    5.14 Results with respect to enumerated technical objectives 63
6. Conclusions and recommendations 67
    6.1 Practical uses of this project's results 67
    6.2 Why high-pass IIF works for UXO 69
    6.3 Transitioning status 70

6.4 Transitioning plans 70
7. References 71
Appendix A: Application of GGN filter to a magnetic survey of Lake Chongcho, Korea 74
Appendix B: Dipole inversion applied to archaeological marine magnetic survey 92
Appendix C: Subroutines to compute and apply EAGGN filter 97
Appendix D: Parallelization and profiling of UXOPAC by KISTI 100
Appendix E: Target A04 (20 mm Projectile) 109
Appendix F: Target I04 (BDU submunition) 123
Appendix G: Target M08 (105 mm projectile) 136
Appendix H: Target C09 (40 mm projectile) 148
Appendix I: Target K09 (155 mm projectile) 158
Appendix J: Target B01 (Rocket Warhead) 176
Appendix K: Target H12 (60 mm mortar round) 187
Appendix L: Target H03 (40 mm projectile) 197
Appendix M: Target A07 (57 mm Projectile) 214
Appendix N: Target B10 (BDU submunition) 225
Appendix O: Target A02 (60 mm M49 mortar round) 233
Appendix P: The 40 x 40-m APG BTA MTADS Magnetic Field Data 243
Appendix Q: Anomaly Stack of Yuma Proving Ground Magnetic Anomalies 247
Appendix R: Publications 249

List of Acronyms

AEC	US Army Environmental Center; http://aec.army.mil/usaec
APG	Aberdeen Proving Ground (Maryland); www.apg.army.mil
BTA	Blind Test Area
DGPS	Digital Global Positioning System
EAGGN	Edge-Adaptive Gapped Gradient-Nulling (filter)
EAGN	Edge-Adaptive Gradient-Nulling (filter)
ESTCP	Environmental Security Technology Certification Program; www.estcp.org
GGN	Gapped Gradient-Nulling (filter)
IGRF	International Geomagnetic Reference Field
IIBE	Intra-Inversion (dc) Bias Estimation
IIF	Intra-Inversion Filtering (or filter)
IIGE	Intra-Inversion Gradient Estimation
JPG	Jefferson Proving Ground (Indiana); www.jpgbrac.com
MTADS	Multi-sensor Towed Array Detection System
NRL	Naval Research Laboratory; www.nrl.navy.mil
SEED	SERDP Exploratory Development
SERDP	Strategic Environmental Research and Development Program; www.serdp.org
STS	Standardized Test Site
SUTDSPC	Standardized UXO Technology Demonstration Site Program Committee
USACE	US Army Corps of Engineers; www.usace.army.mil
UXO	Unexploded Ordnance
UXOPAC	UXO Processing and Analysis Package
YPG	Yuma Proving Ground (Arizona); www.yuma.army.mil

List of Figures

1. Effects of de-median filters in the presence of a constant-gradient background ……..……. 5
2. MTADS magnetic field intensity map of the Aberdeen Proving Ground …….…….. 16
3. Method of UXOPAC dipole inversion using a 3-d model space ……. 17
4. Comparison of the UXOPAC inversion with some alternative approaches …… 30
5. Anomaly I04: engulfed by anomaly J04; EAGGN filtering (BDU submunition) …… 33
6. Anomaly M08: regional setting and anomaly in a 3 x 3-m window (105 mm projectile) ….. 36
7. Anomaly M08: with and without EAGGN filtering ……...……..… 38
8. Anomaly C09: EAGGN and x-then-y high-pass filtering (40 mm projectile)……. 39
9. Anomaly K09: regional setting and anomaly in a 3 x 3-m window (155 mm projectile) ….. 43
10. Anomaly K09: anomaly stack and synthetic neighbors ……. 44
11. Anomaly B01: real and hybrid data with and without EAGGN filter (rocket warhead) …... 47
12. Anomaly H12: single- and multi-swath EAGGN filtering (mortar) …….. 49
13. Anomaly H03: with and without EAGGN filtering (40 mm projectile) ……..... 52
14. Anomaly A07: with and without EAGGN filtering (57 mm projectile) ……..... 54
15. Anomaly B10: including GGN and EAGGN filtering (BDU submunition) ……. 57
16. Anomaly A02: including single-swath data with and without filtering (mortar) …….. 60
A1. Map of depths in Chongcho Lake near Sokcho, Kangwon-do, Republic of Korea ……..... 77
A2. Magnetic field in Chongcho Lake with contours at zero and ± 5 • (2n) nT. ……. 78
A3. Magnetic field in Chongcho Lake including Anomaly "A".....……... 79
A4. Filtered magnetic field in Chongcho Lake (using 100 x 100-m EAGGN filter ……... 80
A5. EAGGN filtered magnetic field in Chongcho Lake including Anomaly "A" ……..... 81
A6. Magnetic field with interpolations using kriging and minimum-curvature methods …...…. 83
A7. Modeled fields and residual fields for inversions of anomaly "A" .....……..... 84
A8. Bull's eye stereographic plots of the projections of magnetic dipole orientations ..….. 86
A9. Magnetic field and analytic signal (total gradient) for the Chongcho Lake survey ……. 90
A10. Model space for UXOPAC inversions ……...…. 90
A11. Example of "profile-adaptive" intra-inversion filtering applied to an anomaly ……. 91
B1. Model of an iron-clad late 16th century Korean turtle ship ……..……. 92
B2. Magnetic field in a 130 x 100-m portion of the Yeosu survey ……. 93
B3. Sum of three inverse modeled dipole fields (Yeosu survey) ……...……. 94
B4. Sum of four inverse modeled dipole fields (Yeosu survey) …….……. 95
B5. Residual field: observed field minus three inverse modeled dipole fields …… 96
D1. Flow chart of the subroutines to compute and apply GGN filters …… 100
D2. Original profile of UXOPAC inversion program ……. 101
D3. Profile of tuned code for Program UXOPAC …….. 102
D4. OpenMP profile of UXOPAC program ……. 103
D5. Original code to design and apply GGN filter ……... 104
D6. OpenMP code to design and apply GGN filter …….. 105
D7. Tuned code to design and apply GGN filter – Part 1 ……. 106
D8. Tuned code to design and apply GGN filter – Part 2 ……. 107
D9. Portion of code for parallel processing to compute magnetic field of a dipole …….. 108
E1. Target A04: 20-mm projectile …….…… 110
E2. Regional setting of A04 anomaly …… 111
E3. A04 anomaly in 1.5-m window ……...…… 111

E4. A04 anomaly and 289 flagged nodes in two swaths ……112
E5. A04 anomaly and 199 flagged nodes in one swath ……112
E6. EAGGN filtered A04 anomaly (L_F = 0.5 m, L_D = 1.5 m) ……113
E7. Single-swath EAGGN filtered A04 anomaly (L_F = 0.5 m) ……113
E8. EAGGN filtered A04 anomaly (L_F = 0.75 m, L_D = 1.5 m) ……114
E9. Single-swath EAGGN filtered A04 anomaly (LF = 0.75 m) ……114
E10. EAGGN filtered A04 anomaly (L_F = 1 m, L_D = 1.5 m) ……115
E11. Single-swath EAGGN filtered A04 anomaly (L_F = 1 m) ……115
E12. EAGGN filtered A04 anomaly (L_F = 1.25 m, L_D = 1.5 m) ……116
E13. Single-swath EAGGN filtered A04 anomaly (L_F = 1.25 m) ……116
E14. A04 anomaly and 127 flagged nodes in a 1-m data window ……117
E15. A04 anomaly and 99 flagged nodes in one swath (L_D = 1 m) ……117
E16. Two-swath EAGGN filtered A04 anomaly (L_F = 1 m, L_D = 1 m) ……118
E17. One-swath EAGGN filtered A04 anomaly (L_F = 1 m, L_D = 1 m) ……118
E18. Two-swath EAGGN filtered field of A04 inverse model (L_F = 1 m, L_D = 1 m) ……119
E19. One-swath EAGGN filtered field of A04 inverse model (L_F = 1 m, L_D = 1 m) ……119
E20. Residual field for EAGGN filtered A04 anomaly (L_F = 1 m, L_D = 1 m) ……120
E21. Residual field for 1-swath EAGGN filtered A04 anomaly (L_F = 1 m, L_D = 1 m) …… 120
F1. Target I04: BDU submunition …… 124
F2. Regional setting of I04 anomaly …… 125
F3. I04 anomaly, as manifest by a closed low engulfed by the much larger J04 anomaly …… 125
F4. I04 anomaly in a 1-m data window …… 126
F5. Inverse-modeled I04 dipole's field plus IIBE field …… 126
F6. Residual field: observed anomaly minus sum of I04 dipole's field and IIBE field …… 127
F7. Inverse-modeled I04 dipole's field plus IIGE field …… 127
F8. Residual field: observed anomaly minus sum of I04 dipole's field and IIGE field …… 128
F9. I04 anomaly in a 0.6-m data window …… 128
F10. Inverse-modeled I04 dipole's field plus IIBE field (job 2) …… 129
F11. Inverse-modeled I04 dipole's field plus IIGE field (job 3) …… 129
F12. Residual field: observed anomaly minus sum of dipole's field and IIBE field (job 2) … 130
F13. Residual field: observed anomaly minus sum of dipole's field and IIGE field (job 3) … 130
F14. EAGGN filtered I04 anomaly (L_{FX} = 0.75 m, L_{FY} = 0.3 m) …… 131
F15. EAGGN filtered I04 anomaly (L_{FX} = 0.75 m, L_{FY} = 0.6 m) …… 131
F16. GGN filtered I04 anomaly (L_{FX} = 0.75 m, L_{FY} = 0.6 m) …… 132
F17. GGN filtered I04 anomaly (L_{FX} = 0.75 m, L_{FY} = 0.2 m) …… 132
G1. Target M08: 105-mm projectile …… 137
G2. Regional setting of M08 anomaly …… 138
G3. M08 anomaly in 3-m window …… 138
G4. EAGGN filtered M08 anomaly (L_F = 0.5 m) …… 139
G5. EAGGN filtered M08 anomaly (L_F = 0.75 m) …… 139
G6. EAGGN filtered M08 anomaly (L_F = 1 m) …… 140
G7. EAGGN filtered M08 anomaly (L_F = 1.5 m) …… 140
G8. M08 anomaly (L_D = 2 m) and flagged nodes …… 141
G9. M08 anomaly and flagged nodes for peak-only inversions …… 141
G10. M08 anomaly and flagged nodes for peak-only, single-swath inversions …… 142
G11. Anomaly of the inverse-modeled M08 dipole plus IIBE field …… 142

G12. Residual field (observed field minus sum of M08 dipole's field and IIBE field) …. 143
G13. Residual field (observed field minus sum of M08 dipole's field and IIGE field) …. 143
G14. EAGGN filtered M08 anomaly (L_F = 0.75 m; L_D = 2 m) …… 144
G15. EAGGN filtered M08 anomaly (L_F = 1 m; L_D = 2 m) …… 144
H1. Target C09: 40-mm MKII 230 projectile …… 149
H2. Regional setting of C09 anomaly …… 150
H3. C09 anomaly in 2-m window …… 150
H4. EAGGN filtered C09 anomaly (L_F = 0.5 m, L_D = 2 m) …… 151
H5. EAGGN filtered C09 anomaly (L_F = 1 m, L_D = 2 m) …… 151
H6. EAGGN filtered C09 anomaly (L_F = 1.5 m, L_D = 2 m) …… 152
H7. EAGGN filtered C09 anomaly (L_F = 0.75 m, L_D = 1 m) …… 152
H8. C09 anomaly (L_D = 1 m) and flagged nodes …… 153
H9. C09 anomaly and flagged nodes for peak-only inversions …… 153
H10. X-then-Y highpass filtered C09 anomaly (L_F = 1.5 m) …… 154
H11. X-then-Y highpass filtered C09 anomaly (L_F = 1 m) …… 154
I1. Target K09: 155 mm howitzer projectile …… 159
I2. Regional setting of K09 anomaly …… 160
I3. K09 anomaly in 3-m window …… 160
I4. Inverse-modeled K09 dipole field plus IIGE field (job 18) …… 161
I5. Residual Field – observed minus K09 dipole and IIGE field …… 161
I6. EAGGN filtered K09 anomaly (L_F = 0.5 m, job 19) …… 162
I7. EAGGN filtered K09 anomaly (L_F = 1 m; job 21) …… 162
I8. EAGGN filtered K09 anomaly (L_F = 1.5 m; job 22) …… 163
I9. EAGGN filtered K09 anomaly (L_F = 2 m; job 23) …… 163
I10. Magnetic anomalies in a 6-m data window (used in anomaly stack) …… 164
I11. Stack of the K09 anomaly with other anomalies moved 14 north …… 164
I12. Stack of the K09 anomaly with other anomalies (2-m window) …… 165
I13. Stack of the K09 anomaly with other anomalies scaled by a factor of 3 …… 165
I14. Stack of the K09 anomaly with other anomalies scaled by a factor of 4 …… 166
I15. Stack of the K09 anomaly with other anomalies scaled by a factor of 5 …… 166
I16. The K09 anomaly in a 1.5 m data window used in jobs 37-38 …… 167
I17. Stack of the K09 anomaly with other anomalies (scale factor = 5; jobs 64-70) …… 167
I18. EAGGN filtered stack (L_F = 0.5 m, L_D = 1.5 m) …… 168
I19. EAGGN filtered stack (L_F = 0.75 m, L_D = 1.5 m) …… 168
I20. EAGGN filtered stack (L_F = 1 m, L_D = 1.5 m) …… 169
I21. EAGGN filtered stack (L_F = 1.25 m, L_D = 1.5 m) …… 169
I22. EAGGN filtered stack (L_F = 1.5 m, L_D = 1.5 m) …… 170
J1. Target B01: 2.75-in rocket warhead …… 177
J2. Regional setting of B01 anomaly …… 178
J3. B01 anomaly in 2-m window …… 178
J4. B01 anomaly in 1-m window …… 179
J5. EAGGN filtered B01 anomaly (L_F = 0.5 m) …… 179
J6. EAGGN filtered B01 anomaly (L_F = 0.75 m) …… 180
J7. EAGGN filtered B01 anomaly (L_F = 1 m) …… 180
J8. Synthetic background field used in B01 hybrid data …… 181
J9. Hybrid data equal to B01 anomaly plus synthetic background …… 181

J10. EAGGN filtered synthetic background field …….. 182
J11. EAGGN filtered hybrid data (L_F = 0.75 m) …… 182
K1. Target H12: 60 mm M49 mortar round …… 188
K2. Regional setting of H12 anomaly …… 189
K3. H12 anomaly in 2-m data window with flagged nodes …… 189
K4. H12 anomaly (L_D = 1.5 m) and 328 flagged nodes …… 190
K5. H12 anomaly and flagged nodes for peak-only inversions ……. 190
K6. EAGGN filtered H12 anomaly (L_F = 0.75 m, L_D = 2 m) …….. 191
K7. EAGGN filtered H12 anomaly (L_F = 1 m, L_D = 2 m) …… 191
K8. EAGGN filtered H12 anomaly (L_F = 1.5 m, L_D = 2 m) …….. 192
K9. EAGGN filtered H12 anomaly (L_F = 2 m, L_D = 2 m) …… 192
K10. Single-swath EAGGN filtered H12 anomaly (L_F = 0.5 m, L_D = 1.5 m) …… 193
K11. Single-swath EAGGN filtered H12 anomaly (L_F = 1.25 m, L_D = 1.5 m) …… 193
L1. Target H03: 40-mm projectile …… 198
L2. Regional setting of the H03 anomaly …….. 199
L3. H03 anomaly in 2-m window ……. 199
L4. Inverse-modeled H03 dipole plus IIGE field ……. 200
L5. Inverse-modeled H03 dipole plus IIBE field ……. 200
L6. IIBE inverse-modeled H03 dipole field ……. 201
L7. Difference field: job 26's dipole plus IIGE field, minus job 24's dipole plus IIBE field ... 201
L8. Residual field: observed field minus sum of H03 dipole and IIGE field ……... 202
L9. Residual field: observed field minus sum of H03 dipole and IIBE field ……... 202
L10. Sum of the H03 inverse-modeled dipole and IIGE fields (trough-only inversion) …… 203
L11. Sum of the H03 inverse-modeled dipole and IIBE fields (trough-only inversion) …… 203
L12. The H03 anomaly (L_D = 1 m) and flagged nodes …… 204
L13. Residual field (observed field minus sum of M08 dipole's field and IIGE field) …….. 204
L14. EAGGN filtered H03 anomaly (L_F = 0.5 m; L_D = 1 m) …… 205
L15. EAGGN filtered H03 anomaly (L_F = 0.5 m; L_D = 1.5 m) ……... 205
L16. EAGGN filtered H03 anomaly (L_F = 0.75 m; L_D = 1 m) …… 206
L17. EAGGN filtered H03 anomaly (L_F = 0.75 m; L_D = 1.5 m) …….. 206
L18. EAGGN filtered H03 anomaly (L_F = 1 m; L_D = 1 m) ……... 207
L19. EAGGN filtered H03 anomaly (L_F = 1 m; L_D = 1.5 m) …… 207
L20. EAGGN filtered field of inverse modeled H03 dipole plus IIGE field (L_F = 0.75 m) …. 208
L21. Residual field: filtered anomaly minus filtered dipole and IIGE fields (L_F = 0.75 m) …. 208
L22. EAGGN filtered field of inverse modeled H03 dipole plus IIGE field (L_F = 1 m) …… 209
L23. Residual field: filtered anomaly minus filtered dipole and IIGE fields (L_F = 1 m) …….. 209
L24. The H03 anomaly (L_D = 1.1 m) and flagged nodes in a single-swath window ……. 210
L25. EAGGN filtered H03 anomaly (L_F = 1 m, job 35) …….. 210
M1. Target A07: 57mm M86 projectile ……. 215
M2. Regional setting of A07 anomaly …….. 216
M3. A07 anomaly in 1.5-m window with flagged nodes …… 216
M4. A07 anomaly in 1-m window with flagged nodes …….. 217
M5. A07 anomaly and flagged nodes for trough-only inversion ……. 217
M6. A07 anomaly in 1-m window with 350 flagged nodes …… 218
M7. EAGGN filtered A07 anomaly (L_F = 0.75 m, L_D = 2 m) …….. 218
M8. EAGGN filtered A07 anomaly (L_F = 1.5 m, L_D = 2 m) …….. 219

M9. EAGGN filtered A07 anomaly (L_F = 2 m, L_D = 2 m) ……..…….. 219
M10. EAGGN filtered A07 anomaly (L_F = 0.5 m, L_D = 1.5 m) …… 220
M11. EAGGN filtered A07 anomaly (L_F = 1 m, L_D = 1.5 m) …… 220
M12. EAGGN filtered A07 anomaly (L_F = 0.5 m, L_D = 1 m) ……...…… 221
M13. EAGGN filtered A07 anomaly (L_F = 1 m, L_D = 1 m) …….…… 221
N1. Target B10: BDU submunition ……...…… 226
N2. Regional setting of B10 anomaly …….……...…… 227
N3. B10 anomaly of a BDU submunition (L_D = 1.5 m) and flagged nodes …….. 227
N4. B10 anomaly of a BDU submunition (L_D = 1.0 m) …….…….. 228
N5. EAGGN filtered B10 anomaly (L_F = 0.5 m, L_D = 1.5 m) ……...…… 228
N6. EAGGN filtered B10 anomaly (L_F = 0.5 m, L_D = 1 m) ……..…… 229
N7. EAGGN filtered B10 anomaly (L_F = 0.75 m, L_D = 1 m) ……...…… 229
N8. EAGGN filtered B10 anomaly (L_F = 1 m, L_D = 1 m) ……...…….. 230
N9. EAGGN filtered B10 anomaly (L_F = 1.5 m, L_D = 1.5 m) ……...…… 230
O1. Target A02: 60-mm M49 mortar round …….…… 234
O2. Regional setting of A02 anomaly …….……...…… 235
O3. A02 anomaly and 612 flagged nodes in 2.5-m window …… 235
O4. A02 inverse-model dipole's field plus IIBE field (job 19) ……...…….. 236
O5. Residual field: observed field minus sum of the A02 dipole's field plus IIBE field …….. 236
O6. A02 anomaly in a 2.5 x 2-m data window and 481 nodes ……..…… 237
O7. A02 anomaly and 309 nodes used on single-swath inversions ……..…. 237
O8. EAGGN filtered single-swath A02 anomaly (L_F = 0.75 m) …….……. 238
O9. EAGGN filtered single-swath A02 anomaly (L_F = 1.25 m) …….……. 238
O10. EAGGN filtered single-swath A02 anomaly (L_F = 1.75 m) ……. 239
O11. A02 anomaly and nodes used in single- and multi-swath inversions peak-only jobs …... 239
P1. APG BTA magnetic field intensity map ……..…… 244
P2. APG BTA total gradient (analytic signal) map ……...…… 245
P3. EAGGN filtered APG BTA magnetic field intensity (L_F = 2 m) …… 246
Q1. YPG Calibrations Area total gradient (analytic signal) map …….. 247
Q2. YPG Calibrations Area anomaly stack……..……..…… 248

List of Tables

1. Response of magnetic and EMI methods to physical properties of UXO and clutter …….. 9
2. Comparisons between UXO and clutter that are relevant to magnetic UXO surveys ……... 10
3. Field parameters for the APG magnetic survey ……..…….. 15
4. Comparison of the UXOPAC inversion with some alternative approaches …….. 18
5. UXOPAC inversion options ……..…….. 19
6. Section number, appendix, grid location, target, anomaly descriptions and comments …... 29
7. Dipole and projectile-end offsets from the A04 target's center …….…….. 31
8. A04 job and dipole parameters …….. 32
9. Dipole offsets from the I04 target's center ……..…….…….. 34
10. I04 job and dipole parameters ……..…….…….. 35
11. Dipole and projectile-end offsets from the M08 target's center ……...….. 36
12. M08 job and dipole parameters ……..…….. 37
13. Dipole and projectile-end offsets from the C09 target's center …….. 41
14. Displacements of C09 dipoles from the target's center ……...……..…….. 42
15. Comparison of non-IIF and IIF jobs for the K09 anomaly ……...…….…….. 43
16. Dipole and projectile-end offsets from the K09 target's center …….. 44
17. K09 job and dipole parameters ..…….. 45
18. Deviation angles, θ, for the K09 anomaly and anomaly stack data…….. 45
19. Dipole parameters for constrained and unconstrained K09 inversion …….…….. 46
20. B01 job and dipole parameters ……...……...….. 48
21. Dipole and mortar-end offsets from H12 target's center ……...…….. 50
22. H12 job and dipole parameters ……...……...….. 51
23. Dipole and projectile-end offsets from the H03 target's center …….. 53
24. Dipole and projectile-end offsets from the A07 target's center …….. 55
25. A07 job and dipole parameters ……...…….….. 56
26. B10 dipole, nose, and tail offsets from the target's center ……..…….. 58
27. B10 job and dipole parameters ……...…….….. 59
28. A02 Dipole and mortar-end offsets from the target's center ……... 61
29. A02 job and dipole parameters ……...……...….. 62
A1. Anomaly "A" dipole models (Lake Chongcho, Sokcho, Korea) .....…….. 82
D1. Relative performance for original code, tuned code, and parallel processing ……..…. 108
E1. Ground truth for target A04 ……..……109
E2. Dipole positions for anomaly A04 inversions …….…….……121
E3. Dipole parameters for anomaly A04 inversions ……...……122
E4. A04 data window parameters ……...……122
F1. Ground truth for target I04 …… 124
F2. Dipole positions for anomaly I04 inversions …… 133
F3. Dipole parameters for anomaly I04 inversions …… 134
F4. I04 data window parameters …… 135
G1. Ground truth for target M08 ……..…….. 137
G2. Dipole positions for anomaly M08 inversions ……...……. 145
G3. Dipole parameters for anomaly M08 inversions …….…… 146
G4. M08 data window parameters ……...…….. 147

H1. Ground truth for target C09 149
H2. Dipole positions for anomaly C09 inversions 155
H3. Dipole parameters for anomaly C09 inversions 156
H4. C09 data window parameters 157
I1. Ground truth for target K09 159
I2. Dipole positions for anomaly K09 inversions 171
I3. Dipole parameters for anomaly K09 inversions 173
I4. K09 data window parameters 175
J1. Ground truth for target B01 177
J2. Dipole positions for anomaly B01 inversions 183
J3. Dipole parameters for anomaly B01 inversions 185
J4. B01 data window parameters 187
K1. Ground truth for target H12 188
K2. Dipole positions for anomaly H12 inversions 194
K3. Dipole parameters for anomaly H12 inversions 195
K4. H12 data window parameters 196
L1. Ground truth for target H03 197
L2. Dipole positions for anomaly H03 inversions 211
L3. Dipole parameters for anomaly H03 inversions 212
L4. H03 data window parameters 213
M1. Ground truth for target A07 215
M2. Dipole positions for anomaly A07 inversions 222
M3. Dipole parameters for anomaly A07 inversions 223
M4. A07 data window parameters 224
N1. Ground truth for target B10 226
N2. Dipole positions for anomaly B10 inversions 231
N3. Dipole parameters for anomaly B10 inversions 232
N4. B10 data window parameters 232
O1. Ground truth for target A02 134
O2. Dipole positions for anomaly A02 inversions 240
O3. Dipole parameters for anomaly A02 inversions 241
O4. A02 data window parameters 242

List of Mathematical Symbols

a	The gradient component (x-direction) of a constant-gradient field, Γ
b	The gradient component (y-direction) of a constant-gradient field, Γ
B	Intra-inversion d-c bias estimate; IIBE
c	Constant (d-c) component of a constant-gradient field, Γ
C	Scale factor applied to off-center filter coefficients in transforming F to F*
C*	Scale factor applied to filter coefficients in transforming F to F*
$D^{/}$	Filtered field of a test dipole
D_{ijlmn}	Field at coordinate indices i, j due to a test dipole at coordinate indices l,m,n.
D_T	Target's diameter
E_{ijmn}	Factor equal to 1.0 at flagged node; otherwise equal to 0.0
E_Z	Relative vertical displacement of best-fit dipole from target's center; $E_Z = (Z-Z_C)/(Z_C+H_M)$
F	Intra-inversion filter, or an initial filter transformed into F*
$F_{CP\text{-}BOXCAR}$	Center-point minus boxcar (high-pass) filter
$F_{CP\text{-}PYRAMID}$	Center-point minus pyramid (high-pass) filter
F*	GGN, EAGN, or EAGGN filter (derived from filter F)
G_X, G_Y	Intra-inversion gradient estimate (IIGE) x- and y-components
H_{ij}	"Observed" magnetic field intensity at coordinate indices i, j (input to inversion)
$H^{/}$	Filtered magnetic field intensity (filtered by filter F)
H*	Filtered magnetic field intensity (filtered by filter F*)
H_M	Height of magnetometer above ground
k_{xij}, k_{yij}	Constants used to transform F to F* at filter output location i,j.
K_{lmn}	Intra-inversion dc bias estimate for a test dipole with coordinate indices l,m,n
L_D	Maximum dimension of an inversion input data window (approximate) $L_D = \max(L_{DX}, L_{DY})$
L_{DX}, L_{DY}	Approximate dimensions of inversion data window; actual dimensions are $N_X \bullet \Delta x$, $N_Y \bullet \Delta y$.
L_F	Maximum nominal dimension of a filter; $L_F = \max(L_{FX}, L_{FY})$
L_{FD}	Maximum dimension of a filter input data window (approximate)
L_{FX}	Nominal filter size in the x-direction
L_{FY}	Nominal filter size in the y-direction
L_H	Horizontal projection of the target's length; $L_H = L_T \cos \Psi_T$
L_T	Target's length
L_V	Vertical projection of the target's length; $L_V = L_T \sin \Psi_T$
M	Total magnetic dipole moment (inversion-derived)
M, N	Half-lengths of filters in the x- and y-directions, respectively
M_{klmn}	Test dipole moment at coordinate indices l, m, n. (x-, y-, or z-component for k = 1, 2, or 3, respectively
N_D	Number of dipoles in a multi-dipole inversion
N_F	Number of flagged nodes used for flag-node inversion

N_X	Actual number of grid nodes in the x-direction of the input data window; $L_{DX} \approx Nx \bullet \Delta x$
N_Y	Actual number of grid nodes in the x-direction of the input data window; $L_{DY} \approx N_Y \bullet \Delta y$
R	Correlation coefficient between observed field and inverse-modeled dipole field plus IIBE or IIGE field.
R_{DL}	Ratio of target's center depth below magnetometer to target's length; $R_{DL} = (Z_C+H_M)/L_T$
R_F	Ratio of flagged to total nodes in a specified data window; $R_F = N_F/(N_X \bullet N_Y)$
R_L	Ratio of data window size to target's center depth below magnetometer; $R_L = L_D /(Z_C+H_M)$.
$U^{/}$	Filtered field of a unit dipole
U_{ijklmn}	Field at coordinate indices i, j of unit dipole at coordinate indices l,m,n oriented in x-, y-, or z-direction (k = 1, 2, or 3).
x, y, z	Left-hand coordinate system with z positive downward
X, Y, Z	In tables: Universal Transverse Mercator coordinates of the modeled dipole. In figure axes: Local coordinates along grid east and north directions.
X_C, Y_C, Z_C	UTM coordinates of the target's center
X_i, Y_j	Local coordinates in an inversion data window
X_l, Y_m, Z_n	Local x-, y-, z- coordinates of a test dipole
X_L, Y_M, Z_N	Local x-, y-, z- coordinates of a solution dipole (best fit)
Xn, Yn, Zn	UTM coordinates of target's nose (tip)
X_O, Y_O	Local coordinates of inversion data window center
X_R, Y_R	UTM coordinates of reference point southeast of the APG BTA
X_W, Y_W	UTM coordinates of inversion data window's midpoint
Z_C	Target's center depth
Γ	Constant-gradient regional field
δ	Magnetic declination of a magnetic dipole (inversion-derived)
Δ_C	Horizontal offset of magnetic dipole (inversion derived) from target's center
Δx, Δy	Grid intervals in x- and y-directions
Δz	Depth interval of inversion model space
θ	Angle between magnetic dipole and earth's magnetic field (deviation angle)
λ, μ, ν	Coordinate indices for second dipole in 2-dipole inversion
Σ	Summation over range of indices
$\Sigma^{/}$	Summation over range of indices excluding zero indices
Φ_{lmn}	Objective function (value) for test dipole with coordinate indices l,m,n
Φ_{LMN}	Minimum value of objective function (for best-fit dipole with coordinate indices L, M, N).
Φ_T	Grid azimuth measured clockwise positive (looking down) from reference grid axis. For APG BTA, reference grid axis is approximately magnetic north
Ψ	Magnetic dipole inclination measured positive downward (inversion-derived)
Ψ_T	Tail-to-nose target inclination (measured positive downward)

Acknowledgments

We gratefully acknowledge the contributions of analysis, support, data, and information provided by numerous individuals. These include: Dr. Chan Hong Park, Mr. Changhwan Kim and others at the Korea Ocean Research Development Institute (KORDI); Prof. Hoonyol Lee, Ms. So Young Lee, Mr. Changmin Lee, Mr. Myungho Hong, and others at Kangwon National University (KNU); Dr. Anne Andrews, Program Manager for Munitions Management, Mr. Jeffrey Fairbanks, Mr. Anthony Buschur, Ms. Katherine Kaye, and others at Strategic Environmental Research and Development Program (SERDP); Dr. Herbert Nelson at the Naval Research Laboratory, Dr. Nagi Khadr at AETC, Incorporated; and Mr. Sang-Kyung Lee, Mr. Seungwoo Lee, and others at the Korea Institute of Science and Technology Information (KISTI). We are also very appreciative for the supplementary funding by Kangwon National University and the principal funding of this SERDP Exploratory Development (SEED) Munitions Management Project MM1452 by the U. S. Army Corps of Engineers (USACE) through SERDP under contract W912HQ-05-P-0028.

1. Executive Summary

This SEED project was successful in developing high-pass intra-inversion filtering (IIF) as a new method to improve inversion of magnetic anomalies in unexploded ordnance (UXO) magnetic field surveys. IIF allows accurate inversion of UXO magnetic anomalies in the presence of low-frequency background fields and overlapping anomalies of neighboring UXO and clutter. The need for this has been well recognized by SERDP and the UXO community (ESTCP-ITRC-SERDP, 2006). As part of this project, an unexpected invention of the edge-adaptive gapped gradient-nulling (EAGGN) filter was made. This new filter automatically accommodates data gaps, survey edges and corners, flag-node data, in which only the nodes of a grid that are nearest to magnetometer stations are used, single-swaths of towed-array data, and restrictions of the filter input to any desired data window. Other related high-pass IIF were developed and applied to all-node inversions using data interpolated to all nodes of a regular grid.

High-pass IIF will become an important new tool for magnetic field inversion. The purpose of full point-dipole magnetic field inversion is to extract the location, depth, magnitude and orientation of magnetic dipoles associated with UXO or clutter. Accurate estimates of horizontal location and depth facilitate subsequent excavation, if required. Accurate estimates of depth, magnetic dipole strength, and magnetic orientation are essential to the following processes of geophysical interpretation that seek to discriminate between UXO and clutter and to characterize the likely type of any UXO.

Magnetic and electromagnetic induction (EMI) are the two principal means of UXO geophysical surveys. These two methods complement each other and together are especially successful when used together. The purpose of UXO geophysical surveys is to detect UXO, to discriminate between UXO and clutter, and to characterize the likely type of UXO prior to excavation for remediation of UXO-contaminated lands. Achieving the goals of these surveys will save money by successful detection of UXO for excavation and by identification of clutter that can be left in the ground. The clutter is generally so numerous in UXO-contaminated lands that excavating all of it would be of prohibitive cost and thus the land might be lost to future uses. On the other hand, if UXO are undetected, then dangers of possible explosions and chemical contamination of soils and groundwater may remain. The costs of remediation for UXO contaminated areas will be tens of billions of dollars (Selstrum, 2005).

A major impediment to the success of modern digital UXO magnetic field surveys is the interference of target magnetic anomalies by background fields including overlapping fields of neighboring shallow-sourced anomalies. The standard procedure is to apply a pre-inversion filter that attenuates some components of the background field but leaves the target anomalies without appreciable distortion so that they can be input to full point-dipole inversion. Pre-inversion filtering, especially the de-median filter, is a very valuable tool but unfortunately, without distortion of the target anomalies, significant background fields and overlapping anomalies inevitably remain to hamper inversion or even detection of target anomalies due to UXO or clutter.

To remedy the limitations of pre-inversion filtering, another standard procedure is to compute the total gradient (or analytic signal), which resolves individual anomalies for purposes of detection

and allows a partial inversion to estimate dipole location, depth, and strength of the dipole due to UXO or clutter (Gamey, 2006). The analytic signal is another valuable tool in interpretation of UXO magnetic fields but it has not been used to derive magnetic dipole orientation. That information is needed for discrimination between UXO and clutter. For example, a deviation angle greater than 60 deg between the magnetic dipole and the earth's field will generally indicate a large remanence. UXO projectiles, rockets, and bombs are shock demagnetized on impact so large remanence generally indicates that these types of UXO are not the source of the target anomaly.

The dilemma facing the geophysical interpreter has been to overcome the problems of background fields and overlapping anomalies while at the same time allowing full point-dipole inversion that would accurately recover all of the dipole parameters of the magnetic source. One solution has been to choose small inversion data windows that would exclude some of the worse effects of overlapping neighboring anomalies. Without IIF, this is often a very reasonable approach to the problem of overlapping fields. The analysis may be time consuming as one seeks to properly carve out the portion of the data that is most suitable to inversion. Moreover, use of a small window may only mask the problem by providing a high correlation coefficient yet inaccurate inversion results.

IIF, as developed for this SEED project, offers a solution. It takes the approach that a target anomaly can be severely distorted yet the filtered magnetic field data can be input to full point-dipole inversion with accurate recovery of all of the point dipole parameters that are so valuable to the analysis that follows. It accomplishes this task by high-pass filtering with a digital filter and then applying that exact same filter to the test models' fields used internal to the inversion algorithm. In the case of the least-squares inversion scheme used in this project, the IIF is applied to the fields of three coincident unit-dipoles at each possible depth for all-node inversions or at each possible dipole location for flag-node inversions.

To demonstrate the effectiveness of this method, IIF was applied to anomalies in the Aberdeen Proving Ground (APG) Blind Test Area (BTA) of a UXO Standardized Test Site (STS) wherein clutter and UXO (actually inert ordnance) were emplaced at various depths and inclinations by the United States Army Environmental Center (AEC). The results demonstrate that IIF significantly improves the accuracy of inversions. IIF generally allows use of large data windows so the burden to the interpreter of "carving out" anomalies should be reduced even as more accurate inversion results are obtained. It is demonstrated that IIF allows direct and accurate full-point dipole inversion to target anomalies that are "engulfed" by neighbors and to target anomalies that are "buried" by other anomalies; that is, by small anomalies that do not even produce closed contours but merely disturb the contours closed about a much larger anomaly. In the latter case, conventional non-IIF single-dipole inversion would not even be attempted. Single-swath IIF inversion was also tested on the STS data. This may be useful where swath-overlap noise is observed and multi-swath inversion may reduce inversion accuracy.

To make UXO STS magnetic field data even more valuable for testing algorithms, such as IIF, a method of anomaly stack was applied. This makes use of the principle of superposition for anomalies that are much weaker than the total earth's magnetic field. According to this principle data from one portion of the UXO STS can be stacked, or summed, with data from another

portion of that same site. The result is to add the background fields from two locations and to effectively move targets (buried UXO and clutter) from one location to another location where they become "synthetic neighbors" to target anomalies under investigation. Such hybrid data were used to demonstrate the effectiveness of IIF on an otherwise well-isolated anomaly of UXO. Other hybrid data were generated by addition of synthetic background fields to a well-isolated UXO anomaly. These data also demonstrated the effectiveness of high-pass IIF.

Intra-inversion gradient estimation (IIGE) was also developed as part of this SEED project. IIGE serves as a tool to improve non-IIF inversions in cases where the background field, in an inversion data window, is closely approximated by a constant-gradient field. It also can be used as a diagnostic tool to indicate possible need for IIF. In this application, IIGE inversion results are compared with those of standard non-IIF inversion using intra-inversion dc-bias estimation (IIBE; Billings et al. 2002a, 2002b, 2003; Pasion et al., 2003). Once the problem of interference by background fields and overlapping anomalies is overcome then discrimination between UXO and clutter and identification of types of UXO will be enhanced. Furthermore, any residual field will then be available to possible analysis of quadrupolar-like fields that may further aid the interpretation of the target anomalies.

One-dimensional "profile-adaptive" IIF was developed precursory to this project in applications to relatively sparse marine magnetic survey profiles for magnetic dipole inversions. That method may have application to some UXO surveys. Developments of 3D IIF are also presently being considered to allow application to data not acquired on a level datum relative to a given target magnetic source including data acquired by vertical gradiometry. Further development and testing of IIF on UXO STS and other data is recommended. Although EAGGN and similar filters would be easily specified using a few parameters, it is also recommended that guidelines be developed for choice of such parameters and to choose filter application windows, which may optionally extend beyond the bounds of the inversion data windows.

In summary, IIF will provide a valuable tool for UXO magnetic field interpretations. High-pass IIF can supplement the standard pre-inversion de-median filtering and total gradient methods by providing full and accurate inversions of target anomalies. It will assure the interpreter greater accuracy in many inversions, it will allow inversion of some anomalies otherwise not amenable to non-IIF single-dipole inversion, and it will ease the interpreter's task of "carving out" data windows that do not generally assure accurate inversions. It is shown that IIF generally allows use of larger data windows than non-IIF inversions and with greater accuracy of results, thus small-window non-IIF inversions will often be unnecessary.

To transition the results of this project to the UXO community and others, four Proceedings papers and a published abstract have presented the results of this SEED project as they developed and numerous presentations have been given at symposia and colloquia. It is intended that additional presentations and publications will soon follow including a technical journal paper that has been accepted. To develop IIF, a test platform was needed. Accordingly, a non-commercial package of processes for development and testing of UXO algorithms (UXOPAC) has steadily grown during this project. It is intended that algorithms for IIF, perhaps integrated with the inversion scheme used here, will be transitioned to a commercial UXO software suite that will be maintained by others and generally available to the UXO community.

2. Objective

2.1 Statement of Need. This SEED project was undertaken in response to Broad Agency Announcement BAA-04-002 wherein the Statement of Need sought development of algorithms to exploit data from current state-of-the-art geophysical sensors and advanced sensors that are now becoming available for UXO detection and discrimination from non-hazardous items.

2.2 Identified Problems. For full point-dipole magnetic field inversion, one derives the x-y-z position of the dipole, the strength of the dipole, or dipole moment, and the orientation of the dipole. The accuracy of these parameters is critical to further analysis to classify the target as being UXO or clutter or to specifying the possible type of UXO encountered prior to any excavation (McDonald and Grimm,1998; Beran et al., 2005).

Where target signatures are disturbed by background fields of geologic origin or by overlapping fields of other UXO or clutter, the point-dipole parameters may be inaccurate using current state-of-the-art analysis of magnetic fields for UXO surveys. In some instances, the target signature may be so buried by the background field that full point-dipole inversion may not even be attempted and the target anomaly may fall beneath a threshold for analysis. In some cases, one might settle for the determination of the targets depth and strength using the analytic signal and forego determination of the dipole's orientation.

One response to the problem of overlapping fields is to use small-window inversions. These inversions input only the central portion of an anomaly, which may be less disturbed by neighboring anomalies. Small-window inversions may require difficult decisions for the interpreter. Moreover, large correlation coefficients may be obtained yet not be indicative of a reliable solution. There is a need to determine whether such inversions have provided accurate dipole parameters.

Other responses to the problem of overlapping fields are multi-dipole inversion and dipole stripping. Multi-dipole inversion will work best if all of the interfering anomalies are dipolar and limited in number. For dipole stripping, a dipole solution for one anomaly is required so that its field can be removed from the presence of another anomaly. The removed anomaly should be well approximated by a point-dipole field. Moreover, one must obtain that approximation in the presence of overlapping fields of another anomaly or anomalies and any other background fields. Under favorable conditions, both multi-dipole inversion and dipole stripping may solve the problem of overlapping fields. However, neither of these methods is designed to overcome geologic background fields that are not approximated by point-dipole fields. Even under favorable conditions, a simpler and more powerful method would be desirable. Ideally, that method could replace, supplement, and/or work with the methods of multi-dipole inversion and dipole stripping.

More than one swath of a magnetometer array may pass over a given anomaly. In that event "swath overlap-noise" may occur. This is loosely defined here as the high frequency noise that occurs where the tracks of magnetometers from separate data swaths overlap or approach each other. This phenomenon includes the "herringbone" artifact that results from positional errors, which are familiar to specialists in aeromagnetic surveys. In some surveys, swath overlap noise

may result from varying tilt of the cart carrying the magnetometers. Swath overlap noise may also occur as pre-filtering artifacts. A possible, although generally minor, source of swath overlap-noise is an artifact of de-median filtering (Figure 1).

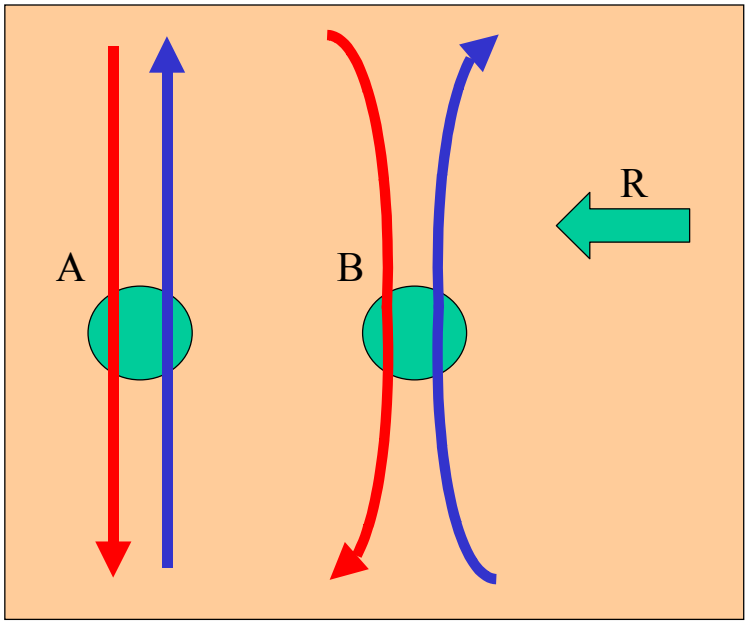

Figure 1. Effects of de-median filters in the presence of a constant-gradient background field. On the left, magnetometer tracks from separate data swaths (red and blue arrows) are separated by 0.25 m where they cross anomaly "A". For a regional field "R" (green arrow) with a constant-gradient of 10 nT/m to the right, and ignoring effects of anomaly "A" tails, the red track median exceeds the blue track median by 2.5 nT. A de-median filter will therefore null the regional field. On the right, two curvilinear tracks cross anomaly "B" where they are separated by 0.25 m. The red track median now exceeds the blue track median by more than 2.5 nT. A de-median filter will distort the anomaly by abruptly decreasing the field values on the red track relative to those on the blue track. This effect of the de-median filter is one possible contribution to "swath-overlap noise".

Even a constant-gradient regional field can result in de-median artifacts if lines are appreciably curvilinear over the length of the filter (Figure 1). If, for example, the regional field has only a constant gradient in the cross-line direction of 10 nT per meter, then the median will differ by 2.5 nT along one straight-line profile relative to an adjacent straight-line profile 0.25 m distant. The de-median filter would exactly cancel the constant gradient field. If on the other hand two adjacent lines are curvilinear in the fashion shown in Figure 1, then a constant-gradient background field with a gradient in the cross-line direction will result in a greater difference than 2.5 nT where the profiles are 0.25 m apart. The gradient will be removed within a given swath. There will be an abrupt offset in the filtered output between adjacent swaths, however. The filtered data in the swath on the up-gradient swath are abruptly decreased relative to the filtered data on the down-gradient swath. If adjacent tracks of two different swaths curved towards each other, then the opposite effect would occur.

To lessen de-median filter artifacts turns of the magnetometer array are positioned well beyond the bounds of the survey area so that the profile lines remain as straight as possible within the survey area and for some distance beyond the bounds of the survey. Some curvature of profiles may be beyond the control of the surveyors, however.

The IGRF magnetic field may be removed and a base-station magnetometer field subtracted from the observed data. Pre-inversion filtering with a de-median filter is also standard procedure. Since the magnetometer array moves forward through the survey area, the de-median filter is both a high-pass temporal and a high-pass spatial filter. It thus attenuates some components of the geomagnetic field variations as well as low spatial frequency components of the background field. In the case of the MTADS APG BTA data used in this project, the length of the de-median filter is 300 points, or 6 s long during which approximately 12 m of profile were obtained.

The median is a robust statistical measure by comparison to the mean. It is less influenced by spikes or anomalies of UXO and clutter anomalies. Nevertheless, it is apparent that a dense distribution of anomalies can affect the median. Relatively sparse anomalies may also affect the median through their tails. For example, induced fields of spheres in northern mid-latitudes yield positive peaks and small lows. Negative tails cover most of the region between sparse anomalies. The sums of those negative tails will result in a background field that mimics a field of geologic origin. Background fields, whether of geologic or cultural origin, may produce some swath-overlap noise as an artifact of de-median filtering. Moreover, de-median filtering will not remove all effects of the magnetic background field because its length is specifically designed to avoid distortion of the target's anomaly.

For residual background fields that remain after de-median filtering, a standard procedure is to obtain an intra-inversion dc-bias estimation (IIBE). The dc-bias will often inadequately represent the residual background field (Nelson et al.,1997). Even for relatively small data windows, the tails of neighboring anomalies will often result in a field that varies significantly within the data window. In such case, the residual distortion of the target's field will likely cause estimates of the vector dipole moment and position to be inaccurate. Nevertheless, higher order pre-inversion or intra-inversion estimates of background field in a small data window may be influenced more by the target's anomaly and measurement errors than by the residual background field within the data window. For small-window inversions, the IIBE may be influenced unduly by slight errors in measurement or slight deviations of the target's anomaly from that of a point dipole.

For purposes of some inversions, or to prepare the data for calculation of the analytic signal or other transforms, the original data in profiles are first interpolated to a regular grid. For anomalies of very near-surface sources, and for anomalies interrupted by supra-nominal data gaps, the interpolation may be inadequate to represent the true form of the target anomaly. For the MTADS APG BTA data used here, the nominal magnetometer elevation and cross-line magnetometer spacing is 25 cm. The shallowest targets yield anomalies that are slightly under-sampled with the result that inversions using interpolated data at all grid nodes may compromise some accuracy in the results. For accurate full point-dipole inversion, it may be better to input data at the measurement station or to limit the distance over which the input data are interpolated. Finally, one must consider the edges of the survey where edge effects of filters may impede analysis of anomalies.

The Standardized Test Sites (STS) provide an extraordinary opportunity to test the accuracy of inversion techniques by providing ground truth for the buried anomalies. The costs of these sites are considerable but they are an extremely valuable resource for development, testing, and evaluation of new technologies. The value of these sites can be enhanced, moreover, by taking advantage of the principle of superposition. By the methods of interpolation and anomaly stacking, one can effectively emplace targets in new juxtapositions and simulate measurements of the magnetic fields. The opportunity to test inversion methods is thus enhanced.

Having identified problems of target fields with overlapping background fields of geologic origin and neighboring UXO and clutter, as well as other problems of data interpolation and under-sampling, swath-overlap noise, data gaps, and survey edges, this SEED project sought to develop and test methods to achieve greater accuracy in full point-dipole inversions. The project was aimed specifically at total magnetic intensity (TMI) surveys. Nevertheless, the project took account that the methods to be developed might also apply to vertical magnetic gradiometry, aeromagnetic and marine surveys and 3D magnetometry (Gamey, 2006). Similarly, the project emphasized land UXO data but consideration was given to, and the project grew out of, applications to marine data in which the coverage was relatively sparse. In meeting the objectives of this project, it was desired to take into account the strengths and limitations of small-window inversions, multi-dipole inversions, dipole stripping, pre-inversion filtering, and IIBE.

2.3 Planned accomplishments. In response to the identified problems and Statement of Need, the principal objective of this SEED project was to develop and prove the innovative concept that intra-inversion filtering (IIF) can improve the accuracy of full point-dipole inversion. Improved accuracy of inversion will support subsequent discrimination between targets that are likely to be UXO or clutter and characterization of the likely type of UXO prior to excavation. That objective has been attained through initial development and testing in the "proof-of-concept" stage of development.

In preparation for this SEED project, "profile-adaptive" IIF was developed for application to a marine magnetic survey of Chongcho Lake in Korea. This was followed by demonstration that 2D IIF could be applied to gridded synthetic UXO data. In the latter case, an unusual x-then-y cascaded high-pass filter was applied to data without gaps. One purpose of that particular filter was to demonstrate the power of intra-inversion filtering even with extreme distortion of the target fields. To achieve the principal objective of the SEED project, it was necessary to develop new methods of IIF filtering and to provide a suitable environment for testing and development of these methods on both real and hybrid real and synthetic data. To that end, specific technical objectives were proposed in undertaking this SEED project. Section 5.15 documents the technical progress of this SEED project by reference to these objectives:

1. Develop and use IIF, and compare various filters for IIF, to more accurately locate and determine the dipole strength and magnetic orientation of UXO and similar magnetic sources for a variety of conditions of noise, residual regional fields, and overlapping fields of nearby magnetic sources in gridded and profile data using both real and synthetic data.

2. Stack and modify magnetic fields in test areas with seeded targets to better model overlapping fields and difficult background fields, and economically provide new test data for comparisons of inversion algorithms.

3. Use IIF to eliminate the need for or enhance effectiveness of the processing steps of subtracting base-station diurnal variations, heading corrections, and estimating and subtracting regional fields.

4. Design IIF filters to accommodate variable target source depths, survey edges, and data gaps.

5. Use estimates of background fields to guide or facilitate applications of IIF, successive inversions to strip away the effects of overlapping dipole fields, and simultaneous multi-dipole inversion.

6. Automatically pick dipole search windows for single- and multiple-dipole inversions.

7. Use parallel processing for efficient inversion.

3. Background

3.1 Magnetic and EMI methods for UXO surveys. The two principal methods for UXO surveys are magnetic and electromagnetic induction (EMI) surveys, which may be used together (Barrow et al.,1996; Pasion et al., 2003) and sometimes are measured together (Stanley et al., 2005). These methods respond to different but overlapping physical properties of the targets, which are either UXO or clutter. They also have different responses to geologic, cultural, and other noise. These differences justify use of both methods in some surveys. EMI methods for UXO respond principally to electrical conductivity and magnetic permeability. Magnetic methods respond to magnetic permeability and remanent magnetization, but not to electrical conductivity (Table 1).

Table 1. Response of magnetic and EMI methods to physical properties of UXO and clutter. †

Physical Property:	Magnetic methods	Electromagnetic Induction (EMI)
Remanent Magnetism	X	O
Magnetic Permeability	X	X
Electrical Conductivity	O	X
Electrical Permitivity	O	X*

† an X indicates response; an O indicates no response.
* important for frequencies higher than are generally used in UXO surveys

EMI and magnetic methods combined can help to distinguish UXO from clutter. For example, some metallic clutter is not ferromagnetic. It will yield an EMI anomaly but not a significant magnetic field anomaly. Most UXO contain significant amounts of ferromagnetic metals. On the other hand, some clutter such as fragments of bombs and projectiles has remanence that far exceeds the induced magnetization. In that case, the EMI anomaly may be relatively small in comparison to total magnetic intensity (TMI) or gradiometer anomalies. Moreover, magnetic field inversion may indicate that the target's dipole moment deviates greatly from the direction of the earth's field. In that case, a larger remanence may be indicated than would be expected from shock demagnetization of UXO and the target may be identified as clutter. Even within a single UXO the relative distribution of ferromagnetic and non-ferromagnetic metals could potentially be extracted using combined EMI and magnetic methods. Magnetic survey dipole solutions have also been used to constrain interpretations of EMI anomalies.

3.2 The Need for full and accurate point-dipole magnetic field inversion. A principal objective of UXO magnetic surveys is to achieve full point-dipole inversion. That is, such surveys seek to determine the point dipole's x,y,z coordinates, strength, or moment, and orientation. Following full point-dipole inversion the geophysical interpreter can seek to classify the target as UXO or clutter based on these dipole parameters, prior knowledge of UXO expected in a given area, and any available EMI-derived parameters. The deviation angle, θ, between the dipole moment and the earth's field is particularly important in identifying remanence and indicating possible orientations of elongated targets. For induced magnetization only, the deviation angle depends on the shape of the target and the angle that that target makes with the earth's field. It does not otherwise depend on the target's orientation relative to the earth's surface. If one can assume, however, that the target is approximately vertical, as may be the case

of mortars and elongated bombs in some environments, then the target's orientation relative to the earth's magnetic field is approximately known and the induced dipole's orientation would be further constrained. The interpreter might also be able to use additional parameters from an EMI survey, to constrain the target's orientation if these are available. Correlations of dipole strength with deviation angle have been used to classify targets. The depth of the target is also an aid to classification and characterization of the possible type of UXO. Comparisons between UXO and clutter related to magnetic surveying are summarized in Table 2.

Given the costs and potential benefits of UXO magnetic data acquisition, it is important that the interpreter obtain the most accurate inversions that are possible. It is the principle objective of this SEED project to develop methods that improve the accuracy of full point-dipole inversion of UXO magnetic field data and expand the applicability of full point-dipole inversion to anomalies that were previously not amenable to that method.

Table 2. Comparisons between UXO and clutter that are relevant to magnetic UXO surveys.

	UXO	Clutter
Objective	Excavate and dispose	Leave in place
Occurrence*	Uncommon relative to clutter	Dominate occurrence
Remanent Magnetization §	Generally small due to shock demagnetism upon firing and impact	Remanence may result in exceptionally large anomalies relative to those that might be expected based on EMI anomalies.
Deviation angle, θ, between the dipole and earth's field §	$0 \leq \theta \leq 60$ deg; The direction and strength of the induced dipole depends on the shape and orientation of the target relative to earth's field.	$0 \leq \theta \leq 180$ deg: Large angles may result from remanence.
Fit to dipole field	Generally, good if the target is isolated from effects of nearby targets. A point dipole model is usually adequate.	Often poor fits because the source is shallow and irregular in shape.
Conductive, non-ferromagnetic targets	Not common; however, tails of some UXO and noses of others are non-ferromagnetic.	Common is some areas; e.g. Cu and Al wire.
Target depth †	Generally deeper penetration for clay (vs. sand) and for larger UXO	Often very shallow
Target orientation	Often nearly vertical for mortars and elongated bombs; variable for other UXO	Variable
Target shape	Generally axially symmetric and commonly elongated.	Often asymmetric, highly irregular and plate-like.
Target size	Detectable targets vary from small bomblets and 20-mm projectiles to 150 mm projectiles and very large bombs.	Variable, but often very small

3.3 Other filters applied to UXO magnetic fields. It is the intent of this SEED project to improve full point-dipole inversions by the method of intra-inversion filtering (IIF). This is defined as the application of a digital filter to the input magnetic field and application of the same digital filter to the test field internal to the inversion. In the method to be developed here, IIF will be applied to the input data and to the fields of three orthogonal unit-strength point dipoles used to construct the inverse model. The purpose of the IIF is to enhance inversion of target anomalies in the presence of background fields of geologic or cultural noise including the anomalies of other nearby UXO and clutter.

Butler (2003) outlined six possibilities for filtering that might assist UXO interpretation of magnetic field data for detection and inversion of UXO signatures in the presence of background fields including geological sources and clutter. These were (1) vertical gradiometry, (2) computed vertical gradient from closely spaced TMI data, (3) upward continuation, (4) bandpass wavenumber filtering, (5) moving-window high-pass median filter, and (6) a moving-window low-pass median filter.

With the exception of vertical gradiometry, these methods are distinct from IIF. Vertical gradiometry is a simple type of IIF. Computation of the vertical gradient from vertically separated magnetometers is equivalent to the application of a two-point filter (1, -1). To apply inversion to these data, one dipole's field is subtracted from the field of that dipole shifted vertically by the amount of separation between the two magnetometers. The same 1-dimensional filter, (1, -1), is thus applied within the inversion. In airborne gradiometry, such an inversion would be complicated by variations of magnetometer array orientation and height above ground.

By contrast, the computed vertical gradient requires two-dimensional filtering of the magnetic field data at the measurement surface. The result will approximate the vertical gradient but be subject to errors in interpolation and use of finite data windows of gridded data. Nevertheless, inversion might then use an analytical expression for the vertical derivative instead of applying a digital IIF. Alternatively, computed vertical and horizontal derivatives can be used in Euler deconvolution to determine x, y, z dipole coordinates. These parameters can then provide a reliable initial guess for subsequent full point-dipole inversion to obtain the dipole position and vector dipole moment (Davis et al, 2005). In extended Euler deconvolution the structural index can also be calculated and dipolar fields can be identified and automatically picked on the basis of the proximity of their structural index to 3 (Davis et al., 2005). The total gradient, or "analytic signal", can also be used to determine position, depth and magnitude of a dipole source; however, this non-linear filter destroys information about the orientation of the vector dipole so full dipole inversion is not then possible.

Upward continuation is a low-pass filter, in contrast to the vertical derivative. The potential intended advantage of upward-continuing the magnetic field would be to attenuate effects of shallow clutter in order to better interpret deeper UXO. If used as a filter prior to inversion, then one could simply use analytic expressions for dipole fields at greater depths than in the case of the unfiltered data. Some of the same limitations would apply as in the case of a computed vertical derivative. As a low-pass filter, the problem of low-frequency interference by neighboring anomalies and geologic noise would be worsened. If one considers the effect of a perfect upward continuation of a dipole field, the effect is quite simple. Both the target and

nearby dipolar anomalies are stretched horizontally by the ratio of the new dipole depth (original depth plus continuation distance) to the original dipole depth. The amplitude is decreased by the cube of the reciprocal of that ratio. For two dipoles near each other, the overlap of the anomalies is inevitably increased, although the anomaly of the shallower dipole will have lesser relative amplitude than that of the deeper dipole. A practical filter to accomplish upward continuation is much larger than the continuation distance. For example, Tsuboi coefficients for (sin x)/x•(sin y)/y upward continuation by one grid interval, may comprise 15 x 15 coefficients (Oldham, 1967). For shallow anomalies, under-sampling may be significant. In any event, the same digital pre-inversion filter would not be applied to the test dipole fields internal to the inversion algorithm. Thus, upward continuation can be distinguished from IIF. By the nature of dipole fields and single-dipole inversion, it will be shown that high-pass filtering provides a separation of dipolar fields that reduces effects of neighboring dipoles on the inversion results. Unfortunately, downward continuation, which is a high-pass filter, is notoriously unstable in the presence of high-frequency noise and shallow sources. Downward continuation would probably not be appropriate for UXO surveys.

Bandpass wavenumber filtering as suggested by Butler (2003) may use a filter with a sufficiently broad band-pass that distortion of the dipole signature might be ignored for purposes of subsequent inversion. Alternatively, the filtered signature might be used more generally for purposes of locating dipolar signatures buried in low-frequency geologic noise. Wenner filtering has been applied experimentally by Sinex and Li (2004) to attenuate geologic noise in non-IIF inversions.

Matched filters have been applied to UXO magnetic data in a procedure to identify and characterize target signatures (Bell, et al., 2001; AETC, Incorporated, 2002). In a plot of matched filter output, the peaks indicate the horizontal position of a matching signal and the strength of that match. If the matched filter equals target dipole field then the output equals the autocorrelation of the target's dipole field plus the cross-correlation of that field with the background noise. Picking peaks from the outputs of many matched filters simulates an inversion program's selection of the maximum correlation between test dipole fields and the observed field.

The inversion process to be described here, automatically considers all possible orientations of the dipole (similar to using an infinite number of matched filters) for each given depth and horizontal location in a dipole search window. Since the interest is primarily in the selected fit only, correlation coefficients for positions that were not selected as best are generally not displayed. Nevertheless, plots of the inverse-modeled dipole's field may be compared to plots of the input anomaly and plots of the difference between those fields (residual background field) may be displayed.

3.4 Research and development preliminary to the SEED project. René (1997, 1999, 2000) developed the "growing model" shape-of-anomaly potential field inversion (SOAPFI) program for separate or simultaneous inversion of gravity and magnetic data on level surfaces. In this program, models were automatically obtained as the sums of many rectangular parallelepipeds. In an application to gravity mapping of an abandoned underground limestone mine, René (1997, 2000) applied a low-pass (smoothing) filter to the gravity data and applied a similar smoothing filter to the fields of the parallelepipeds used to construct the inverse model.

When the SOAPFI program was adapted to a marine magnetic survey of Chongcho Lake in Korea, the inverse models were instead single point dipoles. "Profile-adaptive" intra-inversion filtering (IIF) was developed and applied to the magnetic field data in curvilinear profiles that often crossed each other (Park, et al., 2002). The applied high-pass filter eliminated the need for a base station magnetometer, although one was used for most of the profiles, and for the simple heading corrections that were applied as a constant shift according to whether the profile was from north to south or in the opposite direction. The high-pass filter also attenuated background fields due to nearby anomalies and magnetic rocks beneath the lake. The fields of individual test dipoles used in the inversion were evaluated at the measurement stations and filtered with the exact same weights as were applied to the input data along the profiles. The distortion of the target anomalies by this unusual filter was therefore not harmful to the inversion. The profile-adaptive filter length was automatically changed to accommodate segments of profiles because of missing data or anomalous headings in turns. Implementation of the filter was quite complicated. At the earliest stages of development, the dipoles were restricted to having orientations along the direction of the earth's field, but eventually arbitrary polarization was allowed.

It was then realized that the IIF method could be particularly useful to UXO magnetic surveys. Tests using synthetic dipole data in regular grids were therefore run with an unusual x-then-y cascaded high-pass filter (René et al., 2004). In this case, high-pass filters were applied as 1D filters along the x-direction and then similar 1D filters were applied along the y-direction. The filters could have been combined as a single 2D filter but it was more convenient to apply the filters as a cascade. These filters were applied to the synthetic data that consisted of single, or multiple dipole fields with or without synthetic low-spatial frequency background fields. IIF was quite successful with these tests despite the extreme distortions of the dipolar fields by the x-then-y filter. At the onset of the SEED project, it was realized that other IIF filters might be more useful to UXO data. Program SOAPFI eventually evolved to handle more aspects of UXO magnetic fields. Its successor is now referred to as UXOPAC. Some details of that program will be discussed in the next section.

4. **Methods**

4.1 Introduction. The approach to meeting the objective of demonstrating new techniques for improved inversion of UXO magnetic field data was:

(1) to obtain real magnetic field data acquired by others for the purpose of developing, testing, and demonstrating both new and old methods of processing and analysis;

(2) to prepare those data for input to the inversion algorithm by coordinate transformations, gridding, sorting, etc.;

(3) to develop an inversion platform (UXOPAC) for experimentation with various types of UXO data including hybrid real and synthetic data;

(3) to further develop and test IIF.

Section 4.2 presents the acquisition parameters for the MTADS APG magnetic data. Acquisition parameters for the Chongcho Lake magnetic survey are provided in Appendix A, which is a reformatted copy of a SAGEEP 2006 Proceedings paper. The Yeosu marine magnetic survey, also in Korea, is described in Appendix B. Section 4.3 provides an overview of the UXOPAC Program and section 4.4 gives details of the basic inversion scheme. Section 4.5 discusses interpolation and operation of the "flag-node" option by which only some grid nodes are input to inversion. Section 4.6 provides some details of IIF and Section 4.7 describes the generation and use of EAGGN IIF. Appendices C-D present Fortran algorithms to generate and apply the EAGGN filters for serial or parallel processing.

4.2 Acquisition of APG and YPG magnetic data. UXO STS magnetic data were obtained from AETC, Incorporated with the assistance of the Naval Research Laboratory (NRL). The magnetic field was measured by NRL and AETC, Incorporated using the MTADS system (Table 3). This system used a cart with an array of eight Cs-vapor magnetometers pulled by an all-terrain vehicle. The magnetometers were mounted 0.25 m above ground and spaced at 0.25-m intervals in the cross-line direction. Measurements were at 20-ms intervals corresponding to an approximate spacing of 0.04 m along the direction of profile.

Positions were obtained with DGPS. The data used in this study were pre-processed through application of a 300-point de-median filter with median values interpolated at intervals along the magnetometer tracks or profiles. The APG BTA data set used here had been windowed by a 40-m square area (Figure 2), which truncates anomalies of buried metallic spheres on the north edge of the BTA and target anomalies along the other edges. The emplaced targets, excluding the buried metallic spheres, are labeled according to a 2-m grid system in which rows A and T are nearest to the north and south edges. Columns 1 and 20 are nearest to the east and west edges, respectively. AEC provided ground truth on their web site (USAEC, 2005), including the coordinates of the target's center, UXO orientation, target dimensions and weight, etc. Projectiles were demagnetized prior to burial according to procedures of the SUTDSPC (2002). Ground truth for Yuma Proving Ground (YPG) data (Appendix Q) became available later in the project so initial work with those data (René and Kim, 2005) was put aside in order to concentrate effort on APG data.

Table 3. Field parameters for the APG magnetic survey

Magnetometers	Cs-vapor
Magnetometer array	8 magnetometers
Towing vehicle	all-terrain vehicle
Magnetometer height above ground	0.25 m
Magnetometer cross-line spacing	0.25 m
Magnetometer measurement interval	20 ms
Approximate in-line measurement interval	0.04 m
Positioning	DGPS
Date of field acquisition of data	June 2004

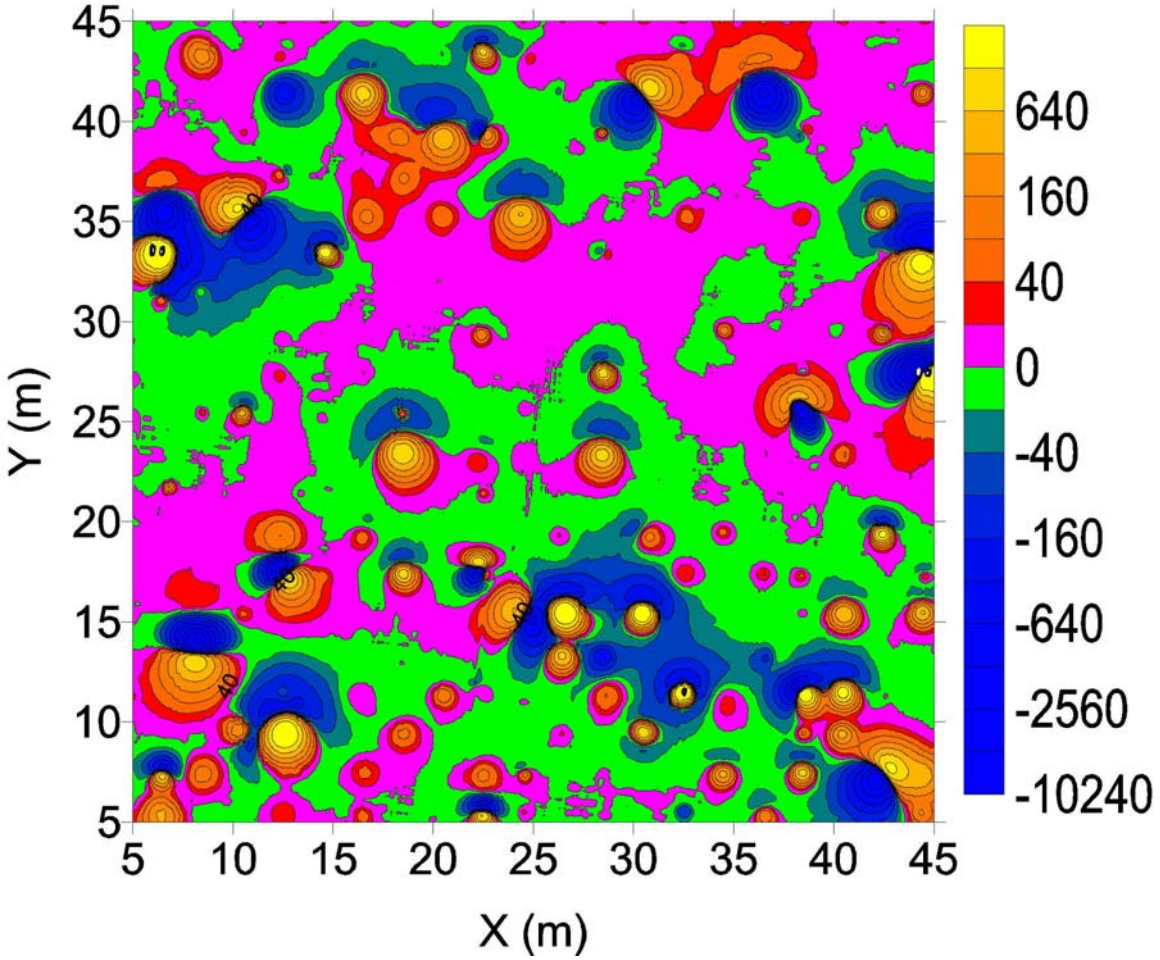

Figure 2. The MTADS magnetic field intensity map of the Aberdeen Proving Ground, UXO Standardized Test Site, Blind Test Area (40 x 40-m window). The contours are at zero and ± 2n • 20 nT, where n is a non-negative integer.

4.3 Development and refinement of UXOPAC. To develop IIF and meet other secondary objectives it was necessary to develop and improve upon a unique inversion package, UXOPAC. This Fortran program was derived, in part through the present SEED project, from an earlier program for growing-model inversion of gravity and magnetic data, SOAPFI (Shape-Of-Anomaly Potential Field Inversion). The basic equations for least-squares inversion are presented in the next section; however, Figure 3 provides an overview of UXOPAC's mode of operation.

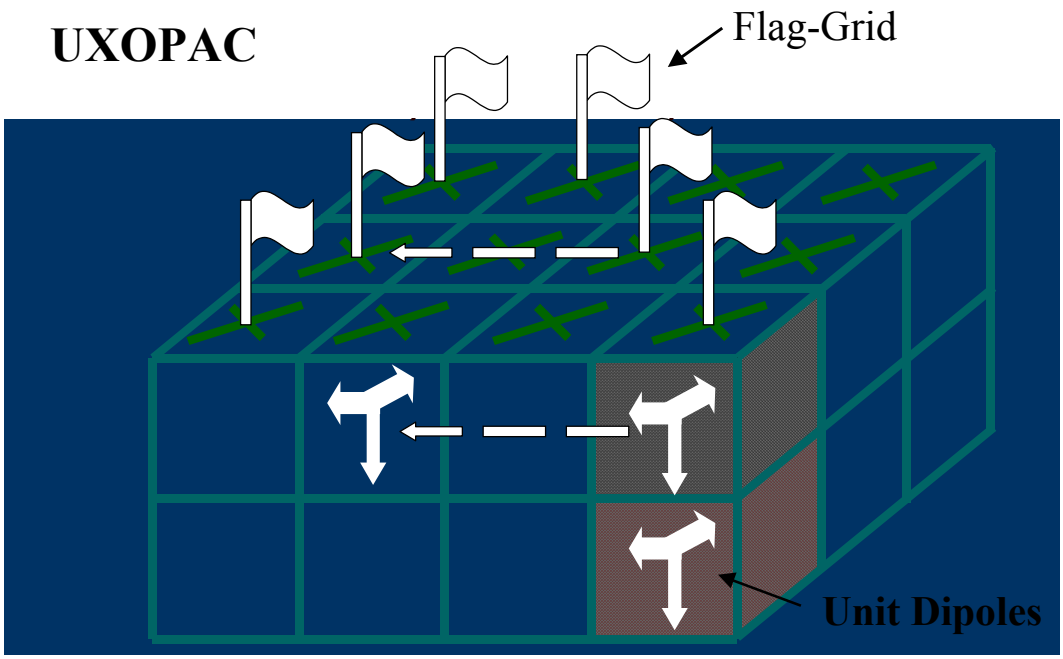

Figure 3. The method of UXOPAC dipole inversion using a 3D model space with dimensions $N_X\Delta x$, $N_Y\Delta y$, and $N_Z\Delta z$, where Δx, Δy, and Δz are the grid intervals in the two-horizontal and the vertical directions, respectively. For each depth of interest, three unit-magnitude dipoles (thick white arrows) are positioned in one corner of the model space (crosshatched). The corresponding unit-dipole fields are computed on the surface at $(2N_X-1)\bullet(2N_Y-1)$ grid nodes (green crosses) for each depth in the dipole search window. To obtain the unit-dipole fields for other dipole positions, these previously computed fields are simply shifted horizontally as shown here for a lateral shift of two grid intervals (broken arrows). For a given test dipole position, the best dipole magnitude and orientation is obtained according to a least-squares criterion that determines the component dipole moments M_X, M_Y, and M_Z as weights applied to the unit-dipole fields. Simultaneously the dc-bias and, optionally, a constant-gradient background field are computed for each dipole test positions. Among all of these positions in a 3D user-specified dipole search window, the position that minimizes the least-squares objective function is selected as the best solution. In the flag-node option, only data at nodes nearest to measurement stations (flags) are used in the inversion. For intra-inversion filtering, the input data on the measurement surface are filtered and the unit dipole fields are filtered with exactly the same filter.

The UXOPAC inversion algorithm differs from some alternative approaches as summarized in Table 4. Using fine grid-intervals there is no practical difference from a method that may allow continuous variation of dipole position. Similarly, using the flag-node option and a fine grid spacing yield the essentially the same result as might be obtained from continuously varying coordinates of measurement stations. Perhaps the most significant difference from a gradient-approach to inversion is the use of an initial 3D dipole search window in lieu of specification of an initial dipole solution. UXOPAC options indicated by asterisks in Table 5 will yield, however, results that closely approximate results of standard procedures applied by other workers.

UXOPAC's restriction of dipoles to positions beneath the grid nodes allows computation of dipole fields once for each allowed vertical position in the model space (Figure 3). For IIF with the all-node inversion, the filter is applied to data at all nodes on the surface of the model space encompassed by the filter. The same filter is applied once only to the three unit dipole fields at each of the allowed vertical levels. The filtered unit dipole fields are stored, retrieved as needed a simply shifted laterally as the test dipoles are moved laterally through the dipole search window in exactly the same way as for inversion without IIF. For IIF with the flag-node option the implementation of filtering the input data and the test fields with exactly the same filter is complicated. The algorithm for this has not been fully optimized at present. The potential relative efficiencies of all-node IIF, which fits the dipole solution to more data points, and the flag-node IIF is therefore not presently established.

The central thrust of this SEED project is to establish the utility of IIF. Other workers have noted difficulties of inversion in the presence of greater than nominal data gaps and survey edges. Flag-node IIF is automatically adapted to these conditions. Other options now available in UXOPAC are indicated in Table 5. In the future UXOPAC may be modified to accommodate data at non-constant elevation above a given target.

Table 4. Comparison of the UXOPAC inversion with some alternative approaches.

UXOPAC	Alternative Solutions	Comments
Field points at regular grid nodes	No interpolation; field points at original measurement stations	Small grid intervals and the flag-node option, which limits interpolation distances to one-half of grid intervals in UXOPAC, make this difference unimportant.
Dipole solutions at nodes of a regular 3D grid in a dipole-search window	Dipole solutions at continuously varying positions	Small grid intervals (and optional multi-pass inversion) in UXOPAC makes this difference unimportant.
Solves a linear system of equations for strengths of three coincident orthogonal dipoles at each test-location in the dipole-search window.	Systematic variation of test dipole orientations Use of Jacobian to iteratively determine dipole parameters. (gradient based)	UXOPAC does not use an initial-solution. It tests all possible dipole solutions in the dipole search window(s).

Table 5. UXOPAC inversion options. #

Option:	Description:	Symbol †
All-node	Uses interpolated data at all nodes of a regular grid	A
Flag-node	Uses data at nodes nearest to measurement stations	
Single-dipole*	Fits a single dipole per inversion	
Multi-dipole	Fits multiple dipoles in a single inversion	M
Dipole stripping	Removes an inverse-modeled dipole field prior to inversion of overlapping anomalies	P
Single-pass	Uses a single dipole search window	
Multi-pass	Uses successive dipole search windows centered on the best positions obtained in the previous search.	
Single-swath	Uses data from a single swath	§
Multi-swath*	Uses multiple swaths occurring in a specified data window	
Polygonal windows*	Applies polygonal bounds to IIF input and/or inversion data input windows.	
Peak (trough) only	Uses data greater than (or less than) a specified value	▲ (▼)
Intra-inversion dc-bias estimation (IIBE)*	Simultaneously determines the best dc-bias and dipole parameters that minimize the objective function.	**B**
Intra-inversion gradient estimation (IIGE)	Simultaneously determines the best constant-gradient background field and dipole parameters that minimize the objective function.	
Pre-inversion filtering*	Applies a filter (e.g., demedian) before input to inversion but not to the test fields used in inversion	
Intra-inversion filtering	Applies the same filter to the inversion input data and to the test fields used in inversion.	E, G, X, etc.
Anomaly-stack	Uses hybrid data obtained by spatially shifting, and optionally scaling, real data before superimposing those data upon other real data from the same survey area	$\mathbf{S_i}$ (i = scale factor)
Synthetic-backround	Uses hybrid data obtained by adding a synthetic background field to real data	$\mathbf{S_B}$
Synthetic-dipole	Uses synthetic data or hybrid data obtained by adding the field of a synthetic dipole to real data	$\mathbf{S_D}$
Fixed-center	Fixes the dipole's position and then determines the dipole's strength and orientation by inversion	T
Fixed horizontal position	Fixes the dipole's horizontal position and then determines the dipole's depth, strength, and orientation by inversion	H
Fixed-depth	Fixes the dipole's depth and then determines the dipole's horizontal position, orientation, and strength by inversion	D

# In tables of inversion results elsewhere, colored entries will indicate the following:
blue = IIF; red = without IIF, violet = hybrid model, and green = constrained inversion.
† symbol used for footnotes and entries in tables of results and job descriptions.
* options that approximate standard procedures.

4.4 Least-Squares Inversion. In UXOPAC least-squares inversion, the input magnetic field, H_{ij}, is specified at grid locations (X_i, Y_j) at constant intervals of Δx and Δy on the measurement surface (Z = 0). In the "flag-node" option, only data at nodes flagged for use in the inversion are included in the equations that follow. The simple least-squares method minimizes the objective function, Φ, which depends on the dipole's field, D, observed field, H, estimated dc-bias, K, and optionally, the regional or background magnetic field gradients, G_x and G_y:

$$\Phi_{lmn} = \Sigma_{ij} [D_{ijlmn} + K_{lmn} + G_{xlmn}(X_i-X_o) + G_{ylmn}(Y_j-Y_o) - H_{ij}]^2; \quad (1)$$

where the magnetic anomaly of a test magnetic dipole at the location (X_l, Y_m, Z_n) is

$$D_{ijlmn} = \Sigma_k (U_{ijklmn} M_{klmn}), \quad (2)$$

and U_{ijklmn} is the magnetic field anomaly of a unit-strength dipole at the test magnetic dipole location within a user specified three-dimensional window of possible dipole locations. Directions of magnetization for the unit dipoles are indicated by indices k (k=1,2,3). Formulae for the evaluation of the unit dipole anomalies are provided by Rao et al. (1977).

For each possible location (l,m,n) the magnetic moments, M_{klmn}, K_{lmn}, G_{xlmn}, and G_{ylmn} that minimize the objective function are solutions to a system of six linear equations:

$$\Sigma_{ij} \{[\Sigma_k (U_{ijklmn} M_{klmn}) + K_{lmn} + G_{xlmn}(X_i-X_o) + G_{ylmn}(Y_j-Y_o) - H_{ij}] U_{ijplmn}\} = 0; \; p = 1, 2, 3; \quad (3)$$

$$\Sigma_{ij} [\Sigma_k(U_{ijklmn} M_{klmn}) + K_{lmn} + G_{xlmn}(X_i-X_o) + G_{ylmn}(Y_j-Y_o) - H_{ij}] = 0. \quad (4)$$

$$\Sigma_{ij} \{[\Sigma_k(U_{ijklmn} M_{klmn}) + K_{lmn} + G_{xlmn}(X_i-X_o) + G_{ylmn}(Y_j-Y_o) - H_{ij}] (X_i-X_o)\} = 0. \quad (5)$$

$$\Sigma_{ij} \{[\Sigma_k(U_{ijklmn} M_{klmn}) + K_{lmn} + G_{xlmn}(X_i-X_o) + G_{ylmn}(Y_j-Y_o) - H_{ij}] (Y_j-Y_o)\} = 0. \quad (6)$$

M_{klmn}, K_{lmn}, G_{xlmn}, and G_{ylmn} are evaluated for all locations in a dipole search window. The least squares solution is then obtained for that dipole location, x_L, y_M, and z_N, which minimizes Φ (Equation 1). The corresponding estimates of dipole moments are M_{kLMN}. The dipole search window must be large enough to avoid the problem of local minima of Φ. Where G_{xlmn} and G_{ylmn} are used, the intra-inversion gradient estimate (IIGE) has been obtained. Often, however, one will wish to set G_{xlmn} and G_{ylmn} equal to zero, in which case only the intra-inversion dc-bias estimate (IIBE) is obtained. For the IIBE option, only 4 linear equations are solved:

$$\Sigma_{ij} \{[\Sigma_k (U_{ijklmn} M_{klmn}) + K_{lmn} - H_{ij}] U_{ijplmn}\} = 0; \; p = 1, 2, 3; \quad (7)$$

$$\Sigma_{ij} [\Sigma_k (U_{ijklmn} M_{klmn}) + K_{lmn} - H_{ij}] = 0. \quad (8)$$

For computational efficiency, the unit dipole fields, U_{ijk00n}, are calculated once for each orientation and depth at the corner locations l = m = 0. The unit dipole fields are than shifted laterally in the x- and y-directions to obtain the fields needed at each dipole test location, U_{ijklmn}. In a previous version of this method (René et al., 2004), a single dipole was used in each corner location and the program iterated through possible declinations and inclinations as in the case of possible dipole locations. In this sense, the algorithm was perhaps similar to one described by Ware and Ware (1996). In the present method, however, three coincident dipoles are positioned in the corner for each possible vertical position. The weights, M_{klmn}, for those horizontally shifted dipoles are then obtained directly as solutions to a linear system of equations for each possible dipole location. Without the need to iterate through possible dipole orientations using a small increments in declination and inclination, the inversion is much more efficient. For a given dipole location the best dipole moments are obtained precisely. The three unit dipoles need not be orthogonal, however, it may be more convenient for subsequent calculation of results, to orient them in vertical and orthogonal horizontal directions.

For each possible dipole location in a user-specified search window, the magnetic moments, M_{klmn}, dc bias, K_{lmn}, and, optionally, the gradients, G_{xlmn} and G_{ylmn} that minimize the objective function are obtained as solutions to equations (x-x) or (y-y), as appropriate. For convenience in interpreting the bias and to lessen roundoff errors, the reference point X_o,Y_o for the gradients is chosen to be at the center of the data window. The standard procedure in magnetic dipole inversions is to use the IIBE option. The generalization to the IIGE option is useful to determine whether a non-constant bias if present and it may be effective in improving an inversion if the background field has a constant non-zero gradient. The IIGE option is not recommended, however, for use with data windows that are small relative to the size of the target window. IIGE and IIBE both differ from pre-inversion estimates of dc-bias, or of constant-gradients of regional fields, hence the term "intra-inversion" is used to distinguish the estimates of B, G_x and G_y obtained here. For IIGE and IIBE, the fields are estimated within the data windows for inversion and are directly determined along with the magnetic parameters of the target source.

M_{klmn}, K_{lmn}, and optionally G_{xlmn} and G_{ylmn} are evaluated for all test locations corresponding to the indices l, m, and n within a dipole search window. The least-squares solution is then obtained for that dipole location, X_L, Y_M, and Z_N, that minimizes the objective function Φ. That is, $\Phi_{LMN} = MIN(\Phi_{lmn})$, where the function MIN indicates a minimum for Φ among all possible locations (l,m,n) within the dipole search window.

The extension to simultaneous inversion of fields to obtain N_D dipoles requires the solution of larger systems of equations. For two dipoles, a system of 9 linear equations would be required if the gradients are included. For three dipoles, a system of 12 linear equations would be needed, etc. Multi-dipole inversions with intra-inversion filtering of synthetic data have shown the potential of these methods for successful inversion where the target fields overlap (René, et al., 2004). If the overlapping fields are from sources more complicated than a point dipole, then multi-dipole inversion will be of lesser use. Even for multiple dipolar sources, implementation can be more complicated than single-dipole inversion since multiple windows in which to search for the dipoles must be specified and accommodated by the algorithm. In the case of the IIBE option for two dipoles at test locations (l,m,n) and (λ,μ,ν), one solves a linear system of 7 linear equations at each possible combination of the test dipole location indices:

$$\Sigma_{ij} \{[\Sigma_k [(U_{ijklmn} M_{klmn}) + (U_{ijk\lambda\mu\nu} M_{k\lambda\mu\nu})] + K_{lmn\lambda\mu\nu} - H_{ij}] U_{ijplmn}\} = 0; \; p = 1, 2, 3; \qquad (9)$$

$$\Sigma_{ij} \{[\Sigma_k [(U_{ijklmn} M_{klmn}) + (U_{ijk\lambda\mu\nu} M_{k\lambda\mu\nu})] + K_{lmn\lambda\mu\nu} - H_{ij}] U_{ijp\lambda\mu\nu}\} = 0; \; p = 1, 2, 3; \qquad (10)$$

$$\Sigma_{ij} \; [\Sigma_k [(U_{ijklmn} M_{klmn}) + (U_{ijklmn} M_{k\lambda\mu\nu})] + K_{lmn\lambda\mu\nu} - H_{ij}] = 0. \qquad (11)$$

The best-fit dipoles are obtained at those dipole locations that minimize the objective function:

$$\Phi_{lmn\lambda\mu\nu} = \Sigma_{ij} [D_{ijlmn} + D_{ij\lambda\mu\nu} + K_{lmn\lambda\mu\nu} - H_{ij}]^2; \qquad (12)$$

where,

$$D_{ijlmn} = \Sigma_k (U_{ijklmn} M_{klmn}); \qquad (13)$$

$$D_{ij\lambda\mu\nu} = \Sigma_k (U_{ijk\lambda\mu\nu} M_{k\lambda\mu\nu}). \qquad (14)$$

The chief impediment to two-dipole inversion by this scheme is the need to evaluate the objective function for all possible combinations of l, m, n, λ, μ, and ν. To speed inversion, either small dipole search windows may be used for one or both dipole, or it may be necessary to limit the search by a gradient method.

As an additional generalization of the method, an iterative technique, or "multi-pass" inversion, can often improve computational efficiency. For example, if the grid spacing is sufficiently fine, then potential dipole locations can be tested within a search window at fewer than all the nodes in that window using dipole search increments greater than the grid intervals, Δx, Δy and Δz. In second or third passes through the procedure, the dipole search window size is then reduced, the new search window is centered on the best-fit location from the previous pass, and the search increments in at least one of the directions is reduced. The initial dipole search window must be large enough and the search increments must be small enough to preclude the problem of local minima for the objective function. The second and any subsequent dipole search windows may be smaller in the directions x, y and z than the corresponding intervals in the previous pass. The final search window will generally use search intervals that are equal to the grid intervals. One can use multi-pass inversion to simulate gradient methods of locating the best dipole solution.

4.5 Interpolation and the "flag-node" option. An inversion scheme may utilize data at their measurement locations directly, at locations interpolated to all nodes of a regular grid, or at only those grid nodes that are nearest to the measurement stations. UXOPAC inputs data interpolated to a regular grid. In the course of this SEED project, however, a flag-node option was developed to efficiently flag those nodes that are nearest to the magnetometer measurement stations. The program separately reads the gridded data and the original data that includes x and y coordinates of the measurement stations. It then creates a flag array, which flags only those nodes nearest to stations for input to filtering and inversion. In the case of APG BTA data used in this SEED project, the cross-line spacing between magnetometers is 25 cm. Excluding the case of MTADS swath overlap, a node half-way between two magnetometer tracks would obtain its interpolated values from stations at distances of 12 cm or more from that node. Given that the magnetometer height above ground level is only 25 cm, it would seem that the anomalies are slightly under-sampled in the cross-line direction for superficial sources. For such sources, inversion results using interpolated data at all nodes (the all-node option) may differ slightly from those obtained from inversion using only those nodes nearest to measurement stations (the flag-node option). For the flag-node option and even wider spaced data one need pay little attention to the choice of interpolation method, for example, minimum curvature or kriging, since the nearest measurement station in a flagged node is closer than one grid. For APG BTA data, minimum-curvature interpolation was generally used for grid intervals of 1 cm and kriging was used for grid intervals of 5 cm. For best accuracy, the 1-cm grid was used with a depth increment also of 1 cm.

4.6 Intra-inversion Filtering. Pre-inversion filtering is a standard procedure for UXO inversion. Commonly a de-median filter is applied to remove geomagnetic variations without the necessity of base station measurements. This filter also removes dc-bias and some very low spatial frequency components of a regional field. The de-median filter has sufficient length that it will not distort the dipole signatures. In the case of overlapping fields of nearby UXO and high spatial frequency geologic noise, however, two-dimensional high-pass IIF that greatly distorts the target field can be used to improve the accuracy of inversion results (René, et al., 2004).

In this method the observed, or interpolated, magnetic field, H, is filtered and the fields of the unit dipoles, U, as used in the inversion process, are filtered with the same filter (Park et al., 2002; René, et al., 2004). The objective function is then:

$$\Phi_{lmn} = \Sigma_{ij} [D'_{ijlmn} + K_{lmn} + G_{xlmn}(X_i - X_o) + G_{ylmn}(Y_j - Y_o) - H'_{ij}]^2; \quad (15)$$

where the magnetic anomaly of a test magnetic dipole at the location (X_l, Y_m, Z_n) is

$$D'_{ijlmn} = \Sigma_k (U'_{ijklmn} M_{klmn}) \quad (16)$$

The primes explicitly indicate filtering of the input fields and the three unit-dipole fields. When the filtering approximately or totally nulls a constant-gradient field, then IIF inversions with or without IIGE will generally yield nearly identical results for the dipole moment components and the best-fit dipole locations. That is, K_{lmn}, G_{xlmn}, or G_{ylmn}, will generally be of little significance when IIF is applied. Furthermore, where there is negligible contamination by noise or overlapping fields of signals, then the results with or without IIF will also be nearly identical.

Use of the terminology "intra-inversion" filtering (IIF) serves to distinguish this method from that of filtering only the input data with a pre-inversion-only filter that is considered mild enough so as not to significantly distort the target field. A very simple example of IIF that has been previously applied to UXO surveys occurs in the case of magnetic gradiometry. A two-point filter is applied before inversion to compute the numerical gradient in the approximately vertical or horizontal directions from the simultaneous measurements of magnetic fields by too closely spaced magnetometers. The inversion process then uses the finite-difference magnetic field gradient using, in effect, the same two-point filter to obtain the inverse-modeled dipole.

Where data are available at all grid nodes through a process of interpolation, then the method of intra-inversion filtering using equations (15-16) can be computationally efficient because for each depth Z_n it is only necessary to filter the unit-dipole field once at the corner location (l = m = 0). In this all-node option, the filtered unit dipole field, U'_{ijk00n}, is than shifted laterally in the x- and y-directions to obtain the field needed at each dipole test location, U'_{ijklmn}. Where one cannot reasonably interpolate and use the data at all locations of a regular grid then the flag-node option is required and intra-inversion filtering requires considerable modification in its design and application.

For many UXO surveys the data are recorded with fine spatial sampling both along the direction of profile and in the cross-profile direction using an array of magnetometers as in the Multi-sensor Towed Array Detection System (MTADS). In most instances, such data may be

interpolated to all grid nodes for input in an inversion data window. Nevertheless, for particularly shallow sources some differences in results may occur between all-node and flag-node inversions with or without IIF. Even with MTADS or similar magnetic data, there are conditions where such filters cannot be applied without modification to allow for missing data. For example, data gaps may occur where rough terrain or vegetation does not allow access by the MTADS cart. Moreover, near the edges of surveys without data gaps intra-inversion filters must be modified to obtain output closer than half a filter width in the direction perpendicular to the edge.

In MTADS surveys, the separation of magnetometers in the cross-line direction may be 0.25 m although an interpolation to grid nodes at 0.05-m intervals, or less, may be desirable for interpretation of the shallow magnetic sources of interest. Under such circumstance it may be desired to input data to inversion at only those grid nodes nearest to the measurement stations. Interpolation distances along the x- and y- directions are then less than or equal to half the corresponding intervals between grid nodes. A suitable modification to filters is developed in the next section (4.7) that will allow applications across data gaps, along survey edges, in survey corners, and to data that are more sparsely interpolated than at every grid node.

4.7 Edge-adaptive and Gapped Gradient-Nulling Filters.

Zero-dc, 2-dimensional filters are gradient-nulling if they are symmetric about the output location. For a symmetric filter with coefficients F_{mn}, the filtered magnetic field, $H^{/}$, at the center of an M x N filter is

$$H^{/}_{i,j} = \Sigma_{mn} F_{mn} \; H_{i+m,j+n} \; ; \; m= -M, M; \; j = -N, N \tag{17}$$

Applying this filter to a constant gradient field, Γ, where

$$\Gamma_{ij} = a X_i + b Y_j + c \tag{18}$$

yields a nulled filtered field, $\Gamma^{/} = 0$, provided that the filter is zero-dc ($\Sigma F_{m,n} = 0$) and symmetric ($F_{-m,n} = F_{m,n}$; $F_{m,-n} = F_{m,n}$). Such a filter is appropriately called gradient-nulling (GN). The GN filter may have rectangular geometry, elliptic geometry, or other symmetric geometry.

Where data are not appropriately interpolated at every point in a grid, then one may derive a modified GN filter, F*, that varies from point-to-point. The filter coefficients will only be defined where they would apply to locations at which the input data are defined or flagged for use in inversion. The filtered magnetic field, H*, is obtained only at grid nodes flagged for input:

$$H^{*}_{i,j} = \Sigma_{m,n} F^{*}_{i,j,m,n} \; H_{i+m,j+n} \; E_{i,j,m,n}; \; m= -M, M; \; j = -N, N; \tag{19}$$

E_{ijmn} is unity if $H_{i+m,j+n}$ is defined and used in the summation of the equation, and zero otherwise. Subscripts i and j for the filter coefficients $F^{*}_{i,j,m,n}$ indicate that the filter varies from point-to-point. The "flag-node" option may be used to select only those nodes nearest to measurement stations for use in inversion. In addition, a non-rectangular filter window can be specified by simply flagging those values beyond an elliptic or circular region, for example, to be excluded from the filter.

These modified filter coefficients, $F^{*}_{m,n,i,j}$, will be related to the original coefficients as follows:

$$F^{*}_{m,n,i,j} = F_{m,n} (1+ k_{xij} X_{i+m} + k_{yij} Y_{j+n}) C^{*}_{ijmn} E_{ijmn} \tag{20}$$

where C^{*}_{ijmn} is unity at the filter origin ($C^{*}_{ij00} = 1$) and is otherwise equal to a constant, C_{ij} over the range of the filter coefficients.

The requirement that F* be gradient-nulling will determine the coefficients k_{xij}, k_{yij}, and C_{ij}. That is, for any coefficients a, b, and c, the filtered constant-gradient field, $\Gamma^{/}$ will be nulled:

$$\Gamma^{/}_{ij} = a (\Sigma_{m,n} F^{*}_{i,j,m,n} X_{i+m}) + b (\Sigma_{m,n} F^{*}_{i,j,m,m} Y_{j+n}) + c (\Sigma_{m,n} F^{*}_{i,j,m,n}) = 0. \tag{21}$$

Each factor multiplying the coefficients a, b, and c is therefore zero. By combining equations (20) and (21) and noting that the filter will only be applied with an origin at a point where the input data are defined ($E_{i,j,0,0} = 1$), one obtains the following three equations:

$$k_{xij} (\Sigma_{m,n} F_{m,n} E_{ijmn} X^2_{i+m}) + k_{yij} (\Sigma_{m,n} F_{m,n} E_{ijmn} X_{i+m} Y_{j+n})$$

$$= - \Sigma_{m,n} F_{m,n} E_{ijmn} X_{i+m} ; \qquad (22)$$

$$k_{xij} (\Sigma_{m,n} F_{m,n} E_{ijmn} X_{i+m} Y_{j+n}) + k_{yij} (\Sigma_{m,n} F_{m,n} E_{ijmn} Y^2_{j+n})$$

$$= - \Sigma_{m,n} F_{m,n} E_{ijmn} Y_{j+n} ; \qquad (23)$$

$$C_{ij} [\Sigma'_{m,n} F_{m,n} E_{ijmn} (1 + k_{xij} X_{i+m} + k_{yij} Y_{j+n})] = - F_{0,0} ; \qquad (24)$$

where the primed summation in equation (23) excludes the origin (m = n = 0).

Equations (22-23) are solved first for k_{xij} and k_{yij} and then equation (24) is solved for C_{ij}. This system of equations will be well conditioned as long as there are a significant number of data points scattered about the data window. The modified filter, F*, will be identical to the original filter, F, wherever all of the input data points are available. Only when it is detected that not all data nodes are filled will the automatic procedure for evaluation of k_{xij} and k_{yij} and C_{ij} be implemented.

If all points are not available because of sparse data interpolation or other data gaps, then F* is a "gapped" gradient-nulling (GGN) filter. If some data points are not available because the filter is being applied near an edge or corner of a survey area then F* is an "edge-adaptive" gradient-nulling (EAGN) filter. When applied at edges or corners and with gaps, F* is referred to as an edge-adaptive, gapped gradient-nulling (EAGGN) filter. The output of the filter is always at the center of the original filter window regardless of missing data points or extension of that filter beyond the bounds of the available data. One may specify in fact that limits of the inversion data window be treated as if they were edges of the survey area. That is, one can force the inversion to use EAGGN filters in preference to non-edge-adaptive GGN filters even when the edges of the survey area are not encountered.

The Fortran subroutine that converts a zero-dc, symmetric filter into a GGN, EAGN, or EAGGN filter is shown in Appendix C, as is a subroutine that applies this IIF to the input data and unit-dipoles' fields used in the inversion. Tests on optimizing these subroutines and others using a supercomputer at the Korea Institute of Science and Technology Information (KISTI) are presented in Appendix D.

5. **Results and Accomplishments**

5.1 Introduction. Applications of UXOPAC inversions, and particularly IIF, to APG BTA magnetic field data will be presented in sections 5.2-5.13 and the appendices to which they refer. Applications of inversions to marine magnetic surveys in Korea will then be presented in section 5.14 and the appendices to which it refers. Finally, a summary of accomplishments will be presented in section 5.15.

In applications to APG BTA magnetic data, EAGGN, EAGN, and GGN IIF were derived from a zero-dc symmetric filter, F, as described in section 4.7. These anomalies (sections 5.2-5.13) are identified by a letter-number grid system. For anomalies A04, B01, and H03, F was a center-point minus two-dimensional boxcar filter, $F_{CP\text{-}BOXCAR}$. For anomalies A02, A07, B10, C09, I04, K09, and M08, F was a center-point minus rectangular pyramid filter, $F_{CP\text{-}PYRAMID}$, which is equivalent to the result of applying linear tapers to all off-center-point $F_{CP\text{-}BOXCAR}$ filter coefficients in two orthogonal directions. In all cases, the center point value is unity ($F_{00} = 1$). For the H12 anomaly, GGN IIF were derived from $F_{CP\text{-}PYRAMID}$ while EAGGN IIF were derived from $F_{CP\text{-}BOXCAR}$. Finally, for C09 x-then-y cascaded high-pass all-node IIF (René et al., 2004), the 1-d filters in the x and y directions were center-point minus triangle filters. The frequency spectra of triangular low-pass filters have smaller side lobes than boxcar filters (Blackman and Tukey, 1958). The frequency spectra of center-point minus triangle filters thus have less variation in the high-frequency pass region than do center-point minus boxcar filters.

In most cases F were defined in a square region with dimensions $L_F = L_{FX} = L_{FY}$. In some cases however rectangular F were applied with the dimension in the y-direction (magnetic north) being less than that in the orthogonal direction ($L_{FY} < L_{FX}$). Although the UXOPAC algorithm allows rectangular and elliptically shaped filters, the latter are not presented for this SEED project. UXOPAC also allows use of cosine tapers such as hamming or hanning, but these are not used here. In the following sections, some tentative conclusions will be made concerning the best filter dimensions for particular anomalies. The best filter dimensions may depend upon the relative scales (frequency content) of the target anomaly and noise, the dimensions of the filter data windows, the amount of separation between the peaks of overlapping anomalies, and other factors. Fortunately, improved inversions using IIF are generally robust with respect to considerable variation in the IIF parameters. The extensive tables of results for various IIF parameters in the Appendices E-O, archive the effects of varying these parameters as guidance for some future developments of the IIF method.

Unless otherwise stated explicitly, the input data window for EAGGN filters will be the same as the input data window for inversion; that is, L_{FD} will be equal to L_D. For GGN filters without use of the edge-adaptive feature, L_{FD} exceeds L_D. For all of the APG BTA inversions the grid interval in the vertical direction, Δz, is 1 cm. The grid intervals Δx and Δy are also generally equal to 1 cm unless otherwise indicated to be 5 cm. Especially for shallow targets, the finer horizontal grid interval is preferred. For the results of tests on 11 APG BTA anomalies, as presented in tables in sections 5.3-5.13 and Appendices E-O, UXOPAC inversion options are generally indicated by symbols that were given in Table 5 of section 4.3.

5.2 Applications to APG BTA magnetic anomalies. The results of tests on 11 APG BTA anomalies are presented in sections 5.3-5.13 and in Appendices E-O, which provide additional figures, target ground truth, and extensive tables of inversion results. Table 6 describes these anomalies and provides some general comments about the results. The result of applying an EAGGN filter to the entire 40 x 40 m data set is shown in appendix P.

Table 6. Section number, appendix, grid location, target, anomaly descriptions and comments.

§	#	Anomaly	Target	Anomaly description and comments
5.3	E	A04	20 mm projectile	Without closed contours; IIF allows accurate full point-dipole single-dipole inversion.
5.4	F	I04	BDU submunition	A small anomaly "engulfed" by a larger neighboring anomaly. IIF improves inversion.
5.5	G	M08	105 mm projectile	A large anomaly but severely disturbed by the tails of larger anomalies. IIF significantly improves the accuracy of inversions.
5.6	H	C09	40 mm projectile	A small anomaly that is nearly "engulfed" by a neighboring anomaly. IIF significantly improves the inversion.
5.7	I	K09	155 mm projectile	A well-isolated and strong anomaly for which IIF and non-IIF results are nearly identical. By the method of anomaly stack, it is provided with synthetic neighbors from 14 m to the south. The resultant hybrid data allow thorough testing of IIF to demonstrate its ability to overcome effects of overlapping anomalies.
5.8	J	B01	Rocket warhead	A large well-isolated anomaly that is truncated by the bounds of a 40 x 40-m data window. A synthetic background field is added to test IIF in the presence of "geologic" noise and a data edge. IIF is successful.
5.9	K	H12	Mortar	A well isolated anomaly. IIF and non-IIF inversions yield very similar results
5.10	L	H03	40 mm projectile	A small anomaly that is severely distorted by the tails of its neighboring anomalies. IIF significantly improves the inversions.
5.11	M	A07	57 mm projectile	The peak of this anomaly merges with the peak of another larger anomaly. IIF significantly improves the inversion
5.12	N	B10	BDU submunition	For this small but fairly well isolated anomaly, there is little difference between non-IIF and IIF inversions.
5.13	O	A02	Mortar	A moderately distorted anomaly for which IIF significantly improves inversion

Appendix number

5.3 Results for anomaly A04. Target A04 is a 20 mm, 0.09-kg projectile, which the AEC emplaced with a slight inclination (Ψ_T = 16 deg,) at a depth to center of 20 cm (Figure E1, Table E1). The A04 anomaly (Figure 4) was input to 16 jobs (Tables 7-8 and E2-E4).

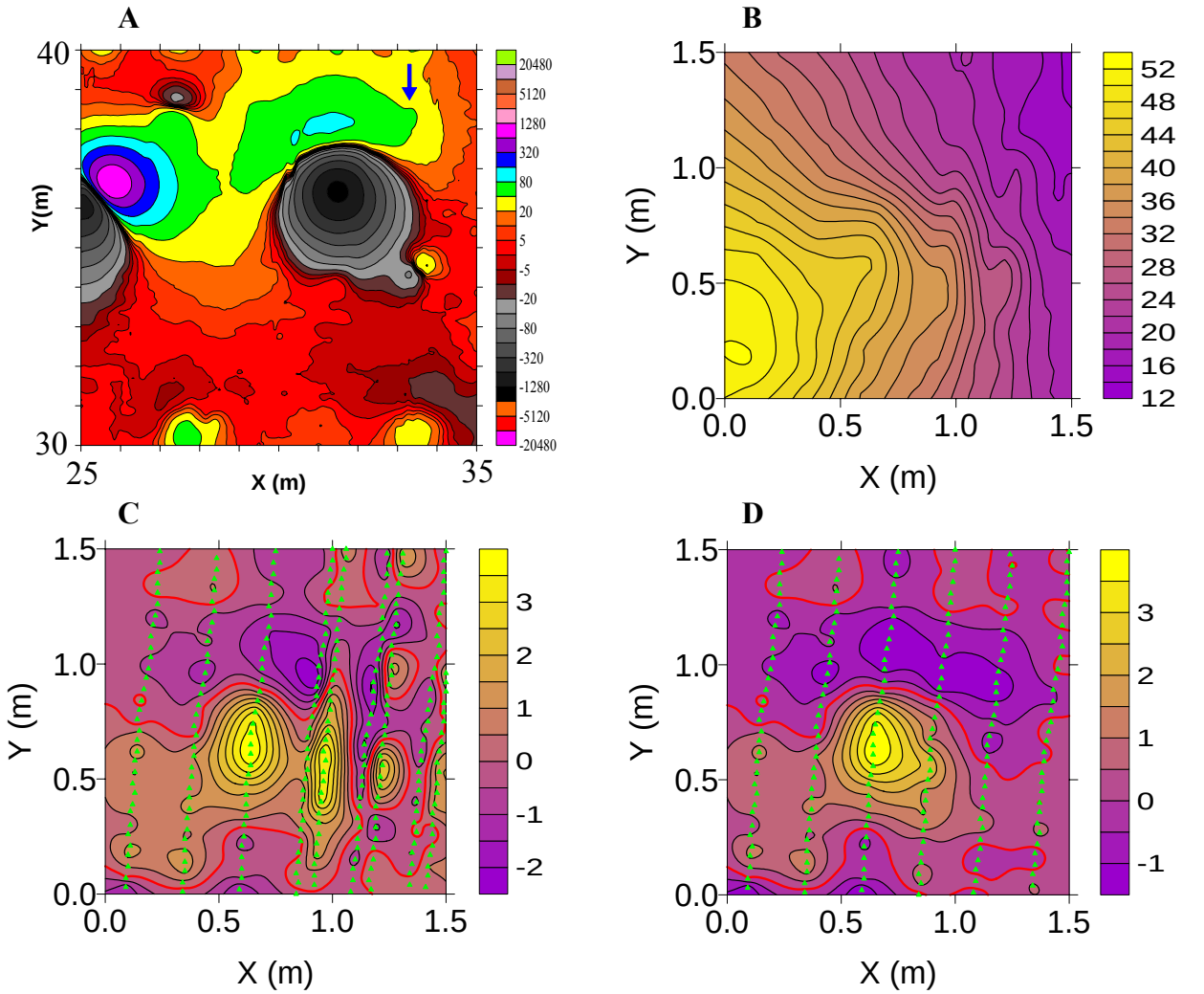

Figure 4. A. The regional setting of anomaly A04 (blue arrow), which occurs within anomaly B05. The contours are at zero and $\pm 2^n \cdot 5$ nT, where n is a non-negative integer. **B**. The A04 anomaly manifest as a minor disturbance to contours of the B05 anomaly's peak; the contour interval is 2 nT. **C**. multi-swath EAGGN filtered A04 anomaly clearly showing swath-overlap noise (L_F = 1 m, L_D = 1.5 m, job 9). The green triangles indicated flagged nodes. The contour interval is 0.5 nT. **D**. single-swath EAGGN filtered A04 anomaly (L_F = 1 m, L_D = 1.5 m, job 14); the contour interval is 0.5 nT.

The A04 anomaly is manifest only by disturbance in the contours of the much larger B05 anomaly (Figures 4A-4B). No attempt could be made therefore to apply non-IIF inversion. IIF inversions were successful, however (Tables 7-8). I04 jobs derived flag-node IIF from symmetric, square ($L_{FY} = L_{FX}$), $F_{CP\text{-}PYRAMID}$ filters. The Single-swath, flag-node, EAGGN IIF inversions with $L_F \geq 0.75$ m were very successful in obtaining dipole solutions for this anomaly. For those inversions, $5 \leq \Delta_C \leq 6$ cm, $2 \leq (Z\text{-}Z_C) \leq 9$ cm, $21.8 \leq \theta \leq 28.4$ deg, and $39.1 \leq \Psi \leq 45.9$ deg. Inversions with L_F equal to 0.5 m were less accurate as the filters were apparently too small in the x-direction, which is approximately in the cross-profile direction. Among the single-swath inversions, IIF with L_F equal to 0.75 or 1 m gave the best results (jobs 5-6 and 13-14). The reason for less accuracy in the case of multi-swath inversion is apparent in figure 4C, which shows the effect of swath-overlap noise in the EAGGN filtered data. The result of single-swath EAGGN filtering is much "cleaner". For the multi-swath inversions with $L_F \geq 0.75$ m, $3 \leq \Delta_C \leq 9$ cm, $11 \leq (Z\text{-}Z_C) \leq 16$ cm, $33.6 \leq \theta \leq 44.7$ deg, and $24.2 \leq \Psi \leq 48.1$ deg. The single-swath IIF inversion for L_D equal to 1.5 m, used data only at those 199 nodes within the data window (Figure 4D) both as inputs to the filter and as inputs of filtered data into the inversion!

For additional figures and tables of results, see Appendix E.

Table 7. Dipole and projectile-end offsets from the A04 target's center at X_C, Y_C, Z_C (UTM coordinates); L_F and L_D are the filter and data window sizes, respectively. Δ_C is the dipole's horizontal displacement from the target center. †

job	description	L_F	L_D	Δ_C (cm)	$X\text{-}X_C$ (cm)	$Y\text{-}Y_C$ (cm)	$Z\text{-}Z_C$ (cm)
	base of projectile				1	3	-1
5	Single-swath EAGGN	0.75	1	6	-6	-1	7
6	Single-swath EAGGN	1	1	5	-5	-1	5
13	Single-swath EAGGN	0.75	1.5	5	-5	0	2
14	Single-swath EAGGN	1	1.5	5	-5	0	5
15	Single-swath EAGGN	1.25	1.5	5	-5	-1	7
16	Single-swath EAGGN	1.5	1.5	5	-5	-1	9
	nose of projectile				-1	-3	1
4	Single-swath EAGGN	0.5	1	7	-7	3	16
12	Single-swath EAGGN	0.5	1.5	8	-7	5	8
1	Multi-swath EAGGN	0.5	1	35	32	-14	2
2	Multi-swath EAGGN	0.75	1	9	-8	4	15
3	Multi-swath EAGGN	1	1	6	-5	3	16
7	Multi-swath EAGGN	0.5	1.5	6	4	-5	22
8	Multi-swath EAGGN	0.75	1.5	5	-5	2	11
9	Multi-swath EAGGN	1	1.5	3	-2	1	14
10	Multi-swath EAGGN	1.25	1.5	3	-2	1	15
11	Multi-swath EAGGN	1.5	1.5	3	-2	1	16

Table 8. A04 job and dipole parameters: job number and type, data window size, L_D, filter size, L_F, relative horizontal and absolute vertical displacements of the dipole from the target center, Δ_C and $(Z\text{-}Z_C)$, deviation angle, θ, and the dipole's declination, δ, and inclination, Ψ.†

job	description	L_F (m)	L_D (m)	Δ_C (cm)	$(Z\text{-}Z_C)$ (cm)	θ (deg)	δ (deg)	Ψ (deg)
5	Single-swath EAGGN	0.75	1	6	7	21.8	-19.9	45.9
6	Single-swath EAGGN	1	1	5	5	22.6	-21.2	45.2
13	Single-swath EAGGN	0.75	1.5	5	2	26.5	-17.9	41.0
14	Single-swath EAGGN	1	1.5	5	5	28.4	-17.9	39.1
15	Single-swath EAGGN	1.25	1.5	5	7	26.7	-19.1	40.9
16	Single-swath EAGGN	1.5	1.5	5	9	27.4	-19.5	40.2
4	Single-swath EAGGN	0.5	1	7	16	41.1	-14.7	26.2
12	Single-swath EAGGN	0.5	1.5	8	8	50.9	-13.2	16.4
1	Multi-swath EAGGN	0.5	1	35	2	83.6	-105.1	8.4
2	Multi-swath EAGGN	0.75	1	9	15	44.7	-30.9	24.2
3	Multi-swath EAGGN	1	1	6	16	37.4	-18.3	30.1
7	Multi-swath EAGGN	0.5	1.5	6	22	22.2	10.4	48.1
8	Multi-swath EAGGN	0.75	1.5	5	11	36.4	-18.2	31.1
9	Multi-swath EAGGN	1	1.5	3	14	33.8	-15.4	33.5
10	Multi-swath EAGGN	1.25	1.5	3	15	34.0	-16.3	33.3
11	Multi-swath EAGGN	1.5	1.5	3	16	33.6	-16.2	33.7

5.4 Results for anomaly I04. Target I04 is a 0.8-kg BDU submunition, which the AEC emplaced at a depth to center of 11 cm (Figure F1, Table F1). The I04 anomaly (Figure 5) was input to 27 jobs (Tables 9-10 and F2-F4).

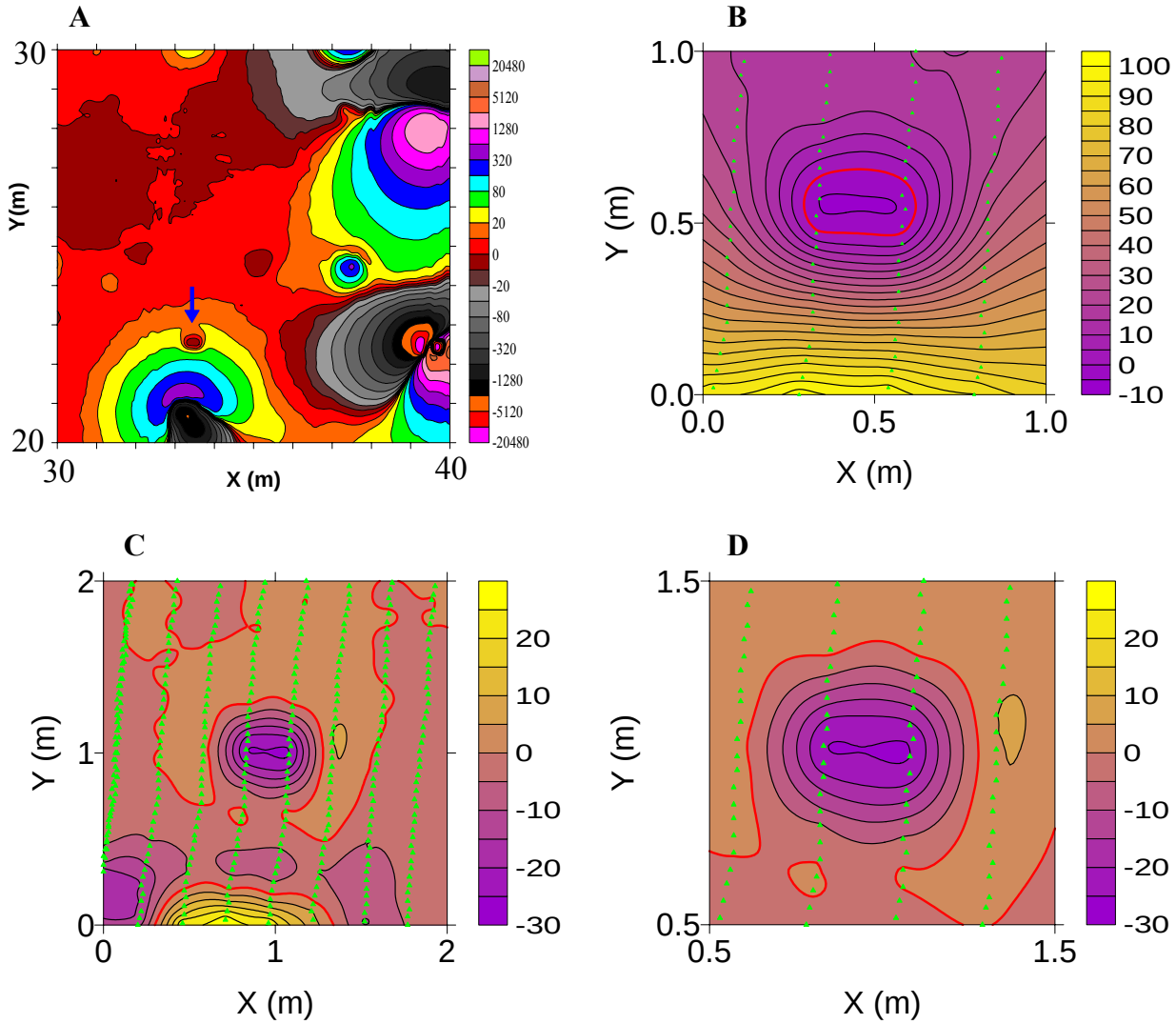

Figure 5. A. Regional setting of the I04 anomaly (blue arrow); contours are at zero and $\pm 2^n \cdot 10$ nT, where n is a non-negative integer. **B.** The I04 anomaly engulfed by the peak of the much larger J04 anomaly; the contour interval is 20 nT. **C.** EAGGN filtered I04 anomaly (L_{FX} = 0.75 m, L_{FY} = 0.6 m); the contour interval is 5 nT. **D.** Co-centered window of those EAGGN filtered data (L_D = 1 m) used in GGN job 18; the contour interval is 5 nT.

This anomaly is engulfed by the much larger J04 anomaly, which results from two pieces of ferrous clutter. For non-IIF inversions, a very small-window (L_D = 0.6 m) gave the best results. For IIBE job 2, Δ_C is 8 cm and (Z-Z_C) is -5 cm (Table 9). For IIGE job 3, Δ_C is 6 cm and (Z-Z_C) is 1 cm. The IIGE inversion gave a dipole closer to the target's center. Non-IIF inversions with L_D equal to 1 m, gave inaccurate results because too much of anomaly J04 was included (Figure

5B). The apparent improvement afforded by IIGE versus IIBE for the non-IIF inversions with L_D equal to 0.6 m suggests that the background field is not constant. This is apparent also from a plot of the anomaly and its environs (Figure 5). Moreover, for job 3 the IIGE gradients are 3.4 and –28.1 nT/m, for G_X and G_Y, respectively (Table F3). This suggests that IIF can provide a more accurate inversion.

Table 9. Dipole offsets from the I04 target's center (UTM coordinates, X_C, Y_C, Z_C). L_F = filter size, L_D = data window size, Δ_C = horizontal displacement from target center.†

job	description	L_F (m)	L_D (m)	Δ_C (cm)	$X-X_C$ (cm)	$Y-Y_C$ (cm)	$Z-Z_C$ (cm)
1	All-node, IIBE	n/a	0.6	10	9	-4	3
2	IIBE	n/a	0.6	8	-2	-7	-5
3	IIGE	n/a	0.6	6	-3	-6	1
4	All-node, IIBE	n/a	1	22	-1	-22	53
5	IIBE	n/a	1	19	-1	-19	53
6	All-node, IIGE	n/a	1	17	-1	-17	19
7	IIGE	n/a	1	16	-1	-16	18
8	EAGGN (L_{DY} = 0.2 m)	0.75	1	9	-3	-9	6
9	EAGGN (L_{DY} = 0.3 m)	0.75	1	7	-3	-7	5
10	EAGGN (L_{DY} = 0.4 m)	0.75	1	5	-2	-4	3
11	EAGGN (L_{DY} = 0.5 m)	0.75	1	3	-2	-2	3
12	EAGGN (L_{DY} = 0.6 m)	0.75	1	3	-2	-2	4
13	EAGGN (L_{DY} = 0.75 m)	0.75	1	5	0	-5	9
14	GGN (L_{FY} = 0.2 m)	0.75	1	2	-2	-1	3
15	GGN (L_{FY} = 0.3 m)	0.75	1	2	-2	0	3
16	GGN (L_{FY} = 0.4 m)	0.75	1	2	-2	1	3
17	GGN (L_{FY} = 0.5 m)	0.75	1	3	-2	2	3
18	GGN (L_{FY} = 0.6 m)	0.75	1	3	-2	2	2
19	GGN (L_{FY} = 0.75 m)	0.75	1	4	-3	2	2
20	GGN	0.5	1	4	-3	2	3
21	EAGGN	0.5	1	2	-2	1	3
22	EAGGN	1	1	13	0	-13	15
23	EAGGN	1.25	1	15	-7	13	24
24	EAGGN	0.5	2	0	0	0	2
25	EAGGN	0.75	2	5	-2	5	1
26	EAGGN	1	2	10	-4	10	6
27	EAGGN	1.25	2	15	-7	13	24

I04 jobs derived flag-node IIF from symmetric, rectangular ($L_{FY} \leq L_{FX}$), $F_{CP\text{-}BOXCAR}$ filters. For GGN IIF jobs 14-20 (L_D = 1 m), excellent and consistent results were obtained: $2 \leq \Delta_C \leq 4$ cm, $2 \leq (Z-Z_C) \leq 3$ cm, $131.7 \leq \theta \leq 146.0$ deg, and $63.8 \leq \Psi \leq 76.7$ deg. For even a very small GGN IIF with L_{FY} = 0.2 m and L_{FX} equal to 0.75 m, Δ_C is 2 cm and $(Z-Z_C)$ is 3 cm. The depth of the target's center beneath the magnetometers is only 36 cm. The fine spatial sampling in the along-profile direction is adequate to define the GGN filtered anomaly and yield an accurate inversion.

EAGGN IIF jobs also gave fairly good results, although not as good as for the GGN inversions. It seems that the truncation of the IIF filter input so close to the target anomaly had some deleterious effect. Even for IIF a window can be too large, particularly if the filter is not short enough to prevent some residual effects of correlation between the selected dipole's field and neighboring anomalies (for example, jobs 26-27). Comparing Figure 5D with Figure 5B, shows how the GGN filter virtually eliminated the effect of the "engulfing" anomaly J04 on the inversion of the target anomaly I04. For additional figures and tables of results, see Appendix F.

Table 10. I04 job and dipole parameters: job number and type, data window size, filter size, horizontal and vertical displacements of the dipole from the target center, deviation angle, and the dipole's declination, inclination, and strength.#

Job	Type	L_D (m)	LF (m)	ΔC (cm)	$Z-Z_C$ (cm)	θ (deg)	δ (deg)	Ψ (deg)	M ($mA \cdot m^2$)
1	AB	0.6	n/a	10	3	81.5	10.9	-12.6	18.8
2	B	0.6	n/a	8	-5	78.2	-17.2	-10.8	10.6
3		0.6	n/a	6	1	99.7	-25.1	-31.9	18.7
4	AB	1	n/a	22	53	67.4	-14.8	-0.1	508
5	B	1	n/a	19	53	72.9	-14.3	-5.6	517
6	A	1	n/a	17	19	80.0	-12.9	-12.8	81.1
7		1	n/a	16	18	84.2	-17.0	-16.8	78.2
8	E_2	1	0.75	9	6	97.6	-24.5	-29.9	29.1
9	E_3	1	0.75	7	5	105.1	-27.6	-37.1	25.0
10	E_4	1	0.75	5	3	115.4	-26.4	-47.6	19.8
11	E_5	1	0.75	3	3	126.9	-22.8	-59.4	18.9
12	E_6	1	0.75	3	4	128.3	-23.1	-60.8	20.8
13	E	1	0.75	5	9	117.5	-12.5	-50.2	33.2
14	G_2	1	0.75	2	3	131.7	-29.3	-63.8	19.2
15	G_3	1	0.75	2	3	136.5	-33.4	-68.4	18.8
16	G_4	1	0.75	2	3	141.3	-40.1	-72.8	18.4
17	G_5	1	0.75	3	3	146.0	-50.8	-76.7	18.2
18	G_6	1	0.75	3	2	145.7	-50.4	-76.5	16.7
19	G	1	0.75	4	2	144.0	-64.0	-72.5	16.8
20	G	1	0.5	4	3	143.2	-64.4	-71.6	18.3
21	E	1	0.5	2	3	141.7	-29.3	-74.0	18.1
22	E	1	1	13	15	91.5	-15.3	-24.2	60.1
23	E	1	0.5	15	24	135.1	1.9	-67.5	17.4
24	E	2	0.75	0	2	160.1	-179.3	-87.1	15.0
25	E	2	1	5	1	179.1	169.3	-68.1	21.9
26	E	2	1.25	10	6	164.3	175.7	-51.9	72.5
27	E	2	1.5	15	24	171.5	163.5	-59.1	31.4

Blue and Red entries indicate jobs with and without IIF, respectively

§ = single-swath. B▲$_0$ = IIBE peak-only (H > 0). ▲$_0$ = IIGE (H>0).

* The IIF filter with L_F = 0.5 m is probably too small in the approximate cross-line direction.

5.5 Results for anomaly M08. Target M08 is a 105-mm, 46-cm long M60 projectile (Figure G1, Table G1). It was emplaced sub-horizontally (Ψ_T = - 2 deg) at a depth to center of 57 cm. The M08 anomaly (Figure 6) was input to 34 jobs (Tables 11-12 and G2-G4).

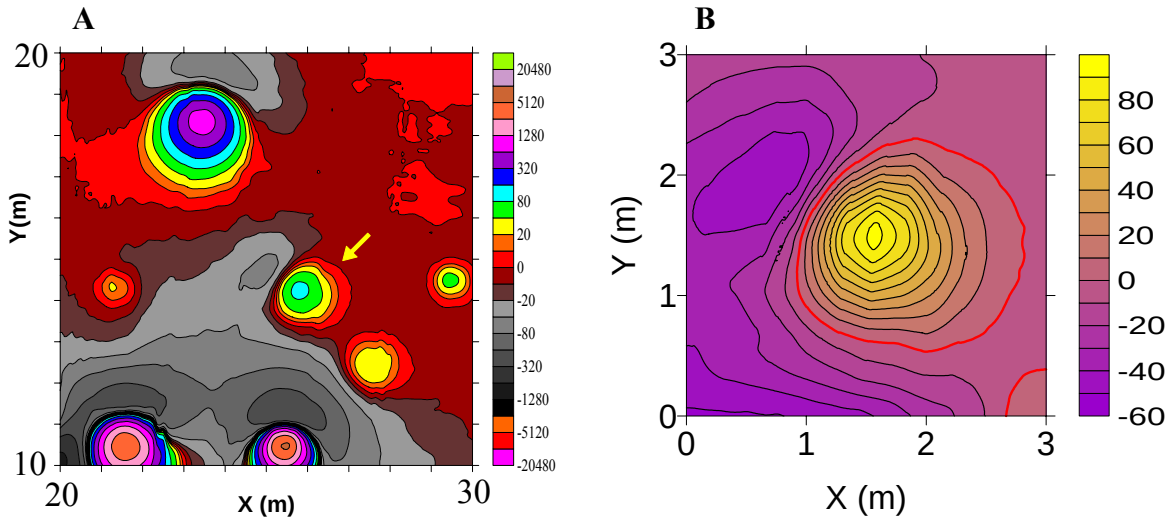

Figure 6. A. The regional setting of anomaly M08 (yellow arrow). The contours are at zero and $\pm 2^n \cdot 10$ nT, where n is a non-negative integer. **B**. The M08 anomaly. The zero contour is red and the contour interval is 20 nT.

IIF inversions gave significantly improved horizontal positions over non-IIF inversions (Table 11). For EAGGN (L_F = 0.75 m) jobs 10, 15 and 32, dipoles are 6 m south of the projectile's axis and 9 cm east of the target's center and towards the nose. For these jobs, $9 \leq \Delta_C \leq 10$ cm. Non-IIF inversions were significantly affected by the tails of neighboring anomalies. For the eight non-IIF jobs in Table 11, dipoles are offset to the south by 10 cm or more and $15 \leq \Delta_C \leq 25$ cm.

Table 11. Dipole and projectile-end offsets from the target's center (UTM coordinates, X_C, Y_C). L_F = filter size, L_D = data window size, Δ_C = horizontal displacement from target center.†

job	description	L_F (m)	L_D (m)	Δ_C (cm)	$X-X_C$ (cm)	$Y-Y_C$ (cm)	$Z-Z_C$ (cm)
	base of projectile				-23	1	1
6	IIBE	n/a	2	22	12	-19	8
8	IIGE	n/a	2	20	15	-13	8
12	single-swath, IIBE	n/a	2	21	12	-18	13
13	single-swath, IIGE	n/a	2	17	14	-10	10
17	peak-only, IIBE	n/a	2	25	22	-12	7
18	peak-only, IIGE	n/a	2	19	5	-18	20
19	single-swath, peak-only IIBE	n/a	2	20	14	-13	15
20	single-swath, peak-only IIGE	n/a	2	15	8	-12	19
10	EAGGN	0.75	2	11	9	-6	10
15	single-swath EAGGN	0.75	2	11	9	-6	10
32	EAGGN	1	3	11	9	-6	9
	nose of projectile				23	-1	-1

In all of these inversions, the calculated dipole depths are greater than the depth to center of the target. This may result from interference by the background field including the O08 anomaly or from deviation of this shallow-sourced field from that of a point dipole.

The differences in dipoles between non-IIF IIBE and IIGE solutions are also indicative of a non-constant background field. Variations in dipoles for different windows using IIGE also may indicate a background field with a non-constant constant gradient. Under such circumstances, it would be anticipated that IIF, with the appropriate parameters, would yield better dipole solutions.

Use of small windows does not necessarily improve the accuracy or overcome the effects of distortion from neighboring anomalies even though the correlation coefficients are very high. For single-swath, peak-only IIBE job 19, Δ_C is 20 cm and $(Z\text{-}Z_C)$ is 15 cm (Table 11) and the correlation coefficient, R is 0.999 (Table G3). For single-swath IIF inversions with L_D equal to 2 m and $0.75 \leq L_F \leq 1$ m (jobs 15-16), Δ_C is 11 cm and $(Z\text{-}Z_C)$ is 12 cm.

IIF generally allows the use of large data windows, relative to the anomaly size. For the multi-swath inversions with L_D equal to 2 m and $0.75 \leq L_F \leq 1$ m (jobs 10-11), $11 \leq \Delta_C \leq 12$ cm and $(Z\text{-}Z_C)$ is 12 cm. Increasing the window size to 3 m (jobs 32-33) yields both Δ_C and $(Z\text{-}Z_C)$ equal to 11 cm. Use of a small EAGGN IIF (L_F = 5 cm) in a larger data window (L_D = 3 m) yielded Δ_C equal to 11 cm and $(Z\text{-}Z_C)$ equal to 12 cm. By contrast, for L_D equal to 2 m, Δ_C is equal to 12 cm and $(Z\text{-}Z_C)$ is equal to 17 cm. This decreased accuracy may be the result of the small filter (L_F = 0.5 m) being truncated against the edges of the smaller data window ($L_{FD} = L_D$). Additional study of such possible effects is planned.

Table 12. The horizontal and vertical displacements of M08 dipoles from the target's center, Δ_C and $(Z\text{-}Z_C)$, the deviation angle, θ, and the dipole's magnetic declination and inclination, δ and Ψ, for selected inversion jobs.†

job	description	Δ_C (cm)	θ (deg)	δ (deg)	Ψ (deg)	$(Z\text{-}Z_C)$ (cm)
6	IIBE (L_D = 2 m)	22	51.6	79.9	42.9	8
8	IIGE (L_D = 2 m)	20	39.4	70.8	53.6	8
12	single-swath, IIBE	21	50.5	80.6	44.5	13
13	single-swath, IIGE	17	39.1	60.8	49.4	10
17	peak-only, IIBE	25	34.8	75.8	61.8	7
18	peak-only, IIGE	19	54.1	84.2	41.8	20
19	single-swath, peak-only IIBE	20	44.0	75.4	49.9	15
20	single-swath, peak-only IIGE	15	44.8	72.6	47.7	19
10	EAGGN (L_F = 0.75 m)	11	42.2	57.3	43.9	10
15	single-swath EAGGN	11	41.8	56.3	44.0	10
32	EAGGN (L_F = 1 m; L_D = 3 m)	11	43.2	56.4	42.3	9

† blue and red entries indicate jobs with and without IIF, respectively.

The background field of anomaly M08 also affects the dipole orientations for non-IIF inversions, which vary significantly according to the choice of data window and whether IIBE or IIGE are

used (Tables 12 and G3). The IIF-derived orientations tend to show less variation as a function of data window choice provided the choice of filter size is reasonable. The IIF-derived θ are consistent with an elongated UXO having little magnetic remanence.

M08 jobs derived the flag-node IIF from symmetric, square ($L_{FY} = L_{FX}$), $F_{CP\text{-}PYRAMID}$ filters. As in the case of other APG BTA anomalies, an EAGGN filter with size L_{FX} equal to 0.5 m is likely too small since this is only twice the separation between magnetometer tracks in a given MTADS swath. For small EAGGN filters, it may be useful for the size of the nominal filter to be greater in the approximate cross-line direction than along the approximate direction of profiling. M08 anomaly and inversion jobs are provided in the figures and tables of Appendix G.

Figure 7 shows a side-by-side comparison of the unfiltered and EAGGN filtered (L_F = 0.75 m) M08 anomaly in a 2-m data window. The filtered anomaly is more compact and the apparent effects of neighboring anomalies are attenuated. IIF generally improves inversion in the case of overlapping dipolar or approximately dipolar fields. Additional observations and details for the

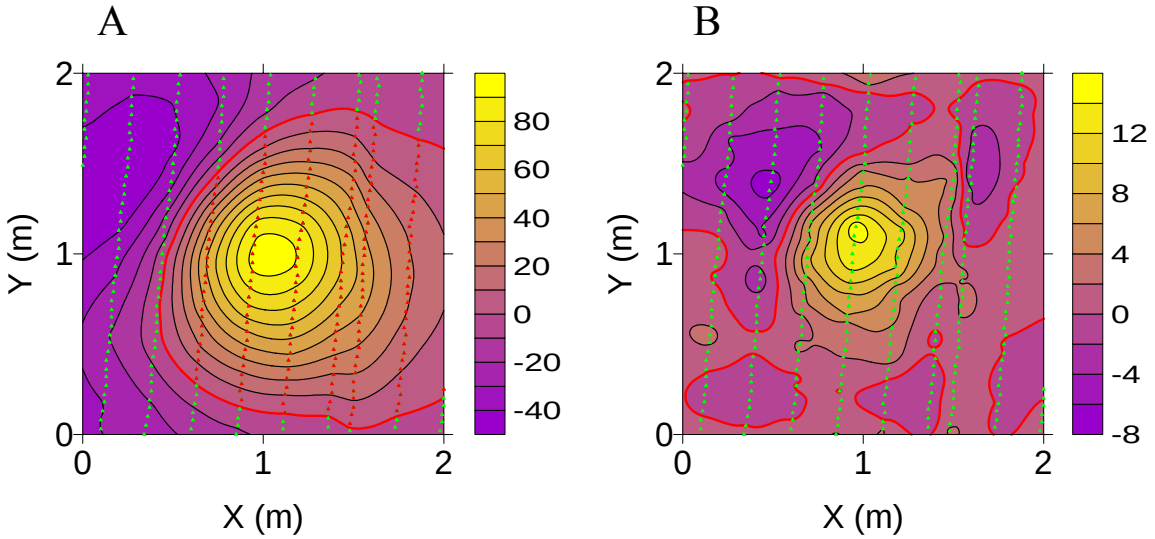

Figure 7. A. The M08 anomaly and flagged nodes (red and green triangles) used in inversions with the flag-node option. For peak-only inversion (H > 0), the red flagged nodes were used. **B**. The EAGGN filtered anomaly (L_F = 0.75 m) used in IIF job 10.

5.6 Results for anomaly C09. Target C09 is a 40 mm 0.6-kg projectile, which the AEC emplaced at an inclination of 19 deg and a depth to center of 14 cm (Figure H1, Table H1). Figures 8 and H2-H11 plot the C09 anomaly and results of inversion jobs. Conclusions are derived from 35 jobs (Tables H2-H4) and selected results are displayed in tables 13 and 14.

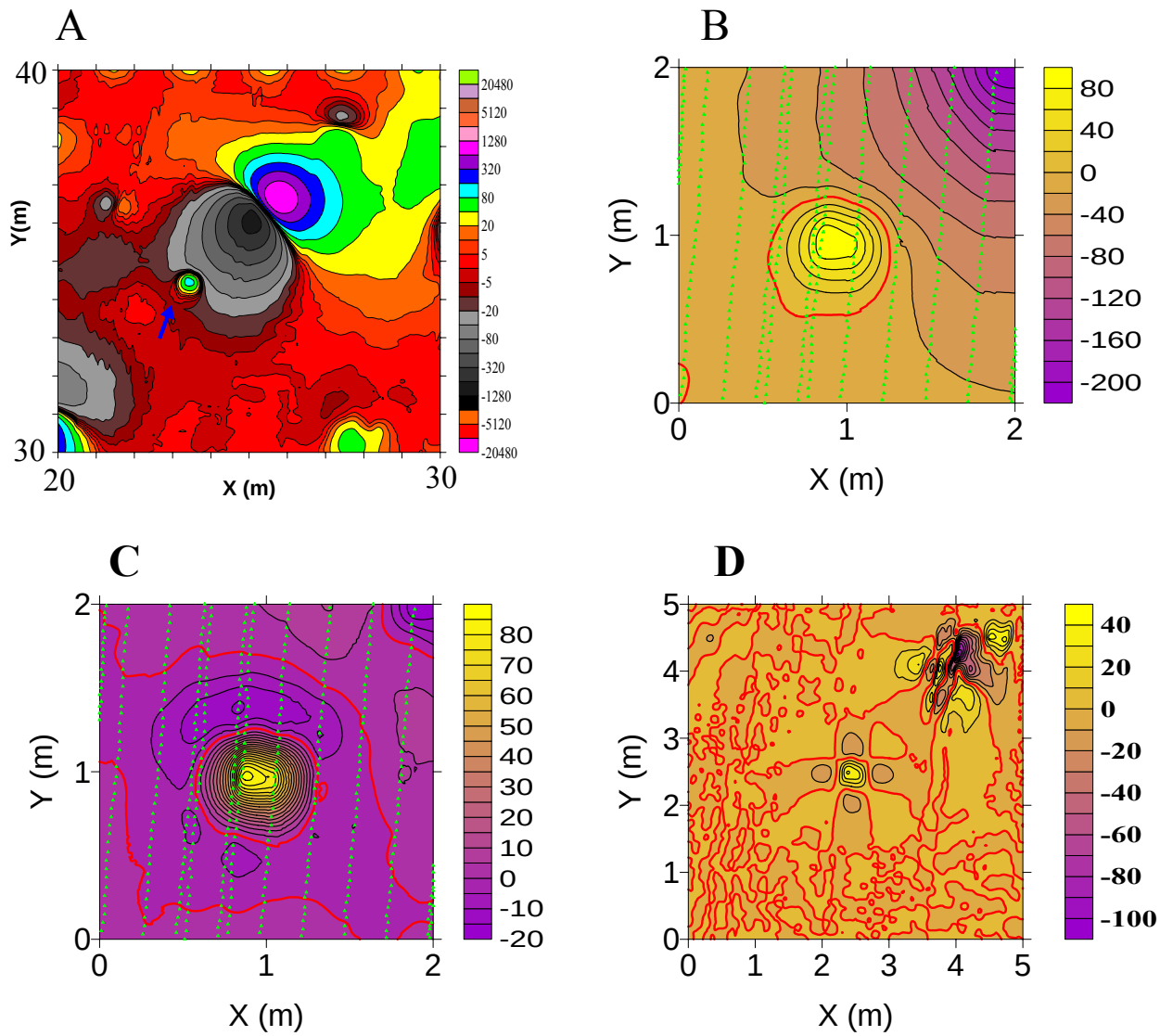

Figure 8. A. Regional setting of the C09 anomaly. **B**. This anomaly in a 2-m data window. **C**. EAGGN filtered anomaly (L_F = 1.5 m, L_D = 2 m). **D**. x-then-y highpass filtered anomaly (L_F = 1 m) showing the collapsed target anomaly (center of the window) and the B08 anomaly (northeast corner).

The C09 anomaly is manifest by closed contours but it is severely disturbed by the large B08 anomaly (Figures 8A-8B). The effect of this disturbance is apparently significant for non-IIF inversions and of little significance to IIF inversions with the appropriate parameters. Clearly, a 2-m window (Figure 8B) would be too large for non-IIF inversion. Tables 13-14 present inverse modeled dipoles for non-IIF 1- and 1.5-m window and peak-only inversions.

C09 jobs derived flag-node IIF from symmetric, square ($L_{FY} = L_{FX}$), $F_{CP\text{-}PYRAMID}$ filters. The EAGGN IIF inversion jobs 5-7 and 14-18 ($0.5 \leq L_F \leq 1.5$ m, $1 \leq L_D \leq 1.5$ m, and $\Delta x = \Delta y = 1$ cm) gave consistent and accurate dipole positions, with Δ_C equal to 4 cm and $1 \leq (Z\text{-}Z_C) \leq 2$ cm (Table 13). The corresponding dipole orientations were $-34.7 \leq \delta \leq -29.0$ deg and $75.2 \leq \Psi \leq 80.1$ deg. The deviation angles ($9.8 \leq \theta \leq 14.0$ deg) are consistent with low remanence and prior demagnetization of the projectile target.

For coarser grid intervals ($\Delta x = \Delta y = 5$ cm, $\Delta z = 1$ cm), all-node, x-then-y and flag-node EAGGN and GGN with L_D equal to 2 m and L_F equal to 1 m, Δ_C were equal to 6, 6, and 3 cm, respectively, and ($Z\text{-}Z_C$) were equal to 3, 1, and 0 cm, respectively. The depth of the target center as measured from the magnetometer datum is only 39 cm. Flag-node IIF may therefore be preferred over all-node x-then-y IIF. Moreover, finer grid intervals would generally be preferred, although these are done at much greater computational expense for all-node inversions.

Of the non-IIF jobs in Table 13, flag-node, IIGE inversions seem to give the best results. This might be expected since the background field due to anomaly B08 is nearly constant-gradient in small data windows containing the C09 anomaly peak (Figure 8B).

The conventional IIBE inversions were apparently less accurate for peak-only and 1-m data windows. For the 1.5-m data window non-IIF, all-node inversions gave particularly poor results. The large differences between all-node and flag-node non-IIF inversions may result from the presence of the high-gradient background field and the greater weight given by flag-node inversions to values in the area of swath overlap (Figure 8B).

IIF inversions, whether using EAGGN (Figure 8C) or x-then-y highpass (Figure 8D) filters, effectively attenuate the background field of the B08 anomaly in the central region of the C09 anomaly. IIF inversions can generally include areas well beyond the central region of the target anomaly because the correlation coefficient is not affected significantly by the correlation of the greatly attenuated tails of the filtered target field with the filtered disturbing anomaly. Nor in the central region of the target anomaly is the correlation coefficient significantly affected by the correlation of the target anomaly's central region with the greatly attenuated tails of the filtered disturbing anomaly. The deviation angles for IIF inversions are consistent with small remanence as would be expected for the demagnetized target. For additional figures and tables of inversion results see Appendix H.

Table 13. Dipole and projectile-end offsets from the C09 target's center (UTM coordinates, X_C, Y_C). L_D = data window size, L_F = filter size, Δ_C = horizontal displacement from target center.†

job	description	L_D (m)	L_F (m)	Δ_C (cm)	$X-X_C$ (cm)	$Y-Y_C$ (cm)	$Z-Z_C$ (cm)
	base of projectile				-6	-2	-2
1	all-node, IIBE	1	n/a	4	-1	4	10
2	IIBE	1	n/a	6	-2	5	5
3	all-node, IIGE	1	n/a	1	0	0	4
4	IIGE	1	n/a	3	-2	2	2
8	Peak-only, IIBE	1	n/a	4	-3	1	-8
9	Peak-only, IIGE	1	n/a	4	-4	2	-3
5	EAGGN	1	0.5	4	-4	2	1
6	EAGGN	1	0.75	4	-4	2	1
7	EAGGN	1	1	4	-4	2	1
	nose of projectile				6	2	2
10	all-node, IIBE	1.5	n/a	12	5	11	29
11	IIBE	1.5	n/a	10	3	9	17
12	all-node, IIGE	1.5	n/a	23	-14	-18	7
13	IIGE	1.5	n/a	1	1	1	3
14	EAGGN	1.5	0.5	4	-4	2	0
15	EAGGN	1.5	0.75	4	-4	2	0
16	EAGGN	1.5	1	4	-4	2	0
17	EAGGN	1.5	1.25	4	-3	1	0
18	EAGGN	1.5	1.5	4	-3	1	1
22	x-then-y highpass*	1	2	6	-4	4	3
23	x-then-y highpass*	1.5	2	6	-4	4	1
25	GGN*	1	2	3[#]	-3[#]	-1[#]	0
26	EAGGN*	1	2	6	-4	4	3
27	GGN*	1.5	2	6	-4	4	0
	base of projectile				-6	-2	-2

† blue and red entries indicate jobs with and without IIF, respectively.
* $\Delta x = \Delta y = 5$ cm.
[#] dipole position shifted one node south relative to dipole position for jobs 22-23 and 26-27

Table 14. The horizontal and vertical displacements of C09 dipoles from the target's center, Δ_C and $(Z-Z_C)$, the deviation angle, θ, and the dipole's magnetic declination and inclination, δ and Ψ, for selected inversion jobs.†

job	description			Δ_C (cm)	θ (deg)	δ (deg)	Ψ (deg)	$(Z-Z_C)$ (cm)
1	all-node, IIBE	n/a	1	4	22.2	-56.1	57.6	10
2	IIBE	n/a	1	6	21.6	-47.4	53.9	5
3	all-node, IIGE	n/a	1	1	23.6	-87.0	75.2	4
4	IIGE	n/a	1	3	15.7	-55.1	70.6	2
8	Peak-only, IIBE	n/a	1	4	12.2	-44.3	72.0	-8
9	Peak-only, IIGE	n/a	1	4	8.8	-34.3	70.7	-3
5	EAGGN	0.5	1	4	10.3	-29.3	76.0	1
6	EAGGN	0.75	1	4	10.2	-31.8	75.2	1
7	EAGGN	1	1	4	10.1	-30.8	75.3	1
10	all-node, IIBE	n/a	1.5	12	41.7	-62.7	36.9	29
11	IIBE	n/a	1.5	10	38.5	-56.6	38.0	17
12	all-node, IIGE	n/a	1.5	23	79.2	122.8	27.5	7
13	IIGE	n/a	1.5	1	25.5	-86.9	70.7	3
14	EAGGN	0.5	1.5	4	10.5	-30.4	76.0	0
15	EAGGN	0.75	1.5	4	9.9	-30.2	75.2	0
16	EAGGN	1	1.5	4	9.8	-29.0	75.4	0
17	EAGGN	1.25	1.5	4	14.0	-34.7	79.9	0
18	EAGGN	1.5	1.5	4	14.0	-32.5	80.1	1
22	x-then-y highpass*	2	1	6	3.6	-20.6	66.7	3
23	x-then-y highpass*	2	1.5	6	3.8	-21.2	68.3	1
25	GGN*	2	1	3[#]	23.0	-101.3	86.7	0
26	EAGGN*	2	1	6	3.1	-19.6	67.7	3
27	GGN*	2	1.5	6	3.1	-18.7	68.8	0

† blue and red entries indicate jobs with and without IIF, respectively.
* $\Delta x = \Delta y = 5$ cm.
[#] dipole position shifted one node south relative to dipole position for jobs 22-23 and 26-27

5.7 Results for anomaly K09. Target K09 is a 155 mm howitzer shell, which the AEC emplaced near vertically (Ψ_T = 81 deg,) at a depth to center of 80 cm (Figure I1, Table I1). The K09 anomaly (Figures 9 and I2-I3), with peak-to-trough amplitude of 936 nT, is well isolated from the effects of its neighbors or other disturbing background fields. Conclusions are based on 69 jobs (Tables 15-19, I2-I4). This anomaly was input to 37 jobs directly. It was also stacked with other anomalies to create hybrid data, which were input to 32 more jobs.

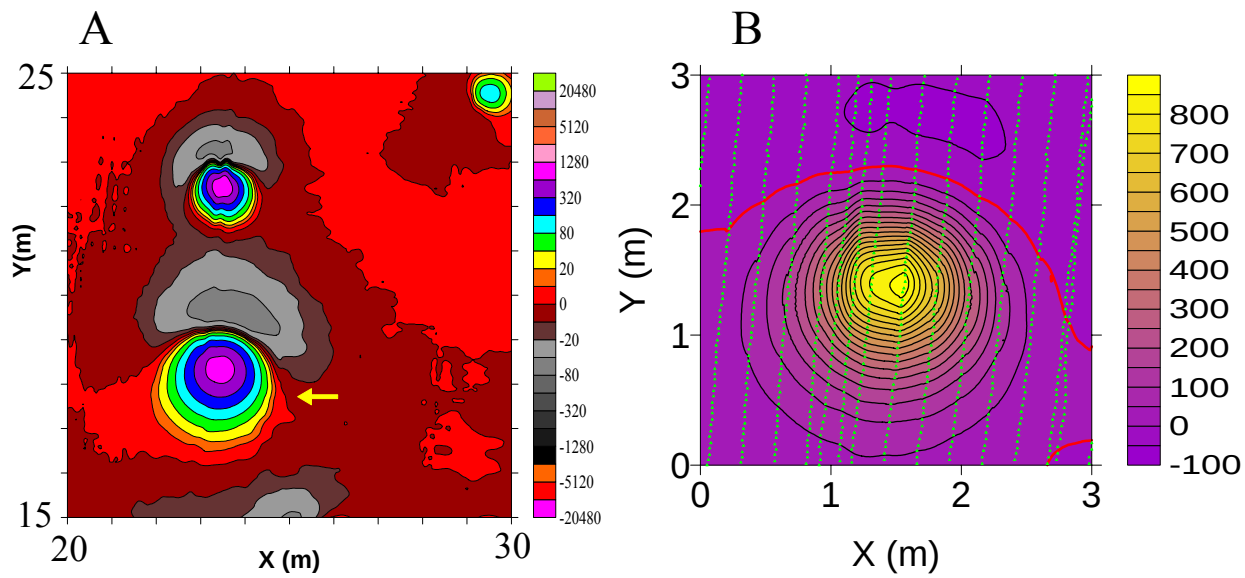

Figure 9. A. Regional setting of the K09 anomaly. Contours are at zero and $\pm 2^n \cdot 10$ nT, where n is a non-negative integer. **B**. The K09 anomaly and the flagged nodes (green) nearest to magnetometer stations. The zero contour is red and the contour interval is 50 nT.

K09 jobs derived flag-node IIF from symmetric, square ($L_{FY} = L_{FX}$), $F_{CP\text{-}PYRAMID}$ filters. Because the effects of the background field are small, IIF inversions (for $L_F \geq 0.75$ m) yield dipoles that approximate those obtained in non-IIF, IIBE and IIGE inversions (table 15). The derived θ are consistent with an elongated UXO having little remanence. EAGGN IIF with L_F equal to 0.5 m gave poor results because the nominal filter size is only twice the cross-line magnetometer spacing. For non-IIF inversions, all-node and flag-node results are nearly identical, as might be expected for a relatively deep source.

Table 15. Comparison of non-IIF and IIF jobs for the K09 anomaly.

non-IIF jobs 15-18	$7 \leq \Delta_C \leq 8$ cm $-13 \leq (Z\text{-}Z_C) \leq -12$ cm	$16.8 \leq \theta \leq 17.3$ deg $82.1 \leq \Psi \leq 83.5$ deg
IIF Jobs 20-23	$7 \leq \Delta_C \leq 8$ cm $(Z\text{-}Z_C) = -13$ cm	$14.6 \leq \theta \leq 17.3$ deg $81.5 \leq \Psi \leq 83.9$ deg

For IIF jobs 20-23, the dipoles lie 30 cm directly below the base of the 155-mm projectile and 13 cm above the projectile's center (Table 16). The dipole depth is approximately equal to the depth to center of the ferromagnetic portion of the projectile, since the ogive is aluminum (Figure I1).

Table 16. Dipole and projectile-end offsets from the K09 target's center (X_C, Y_C, Z_C; UTM coordinates) for jobs 16, 18, and 20-23.

	easting offset (cm)	northing offset (cm)	depth offset (cm)
base of projectile	-6	-4	-43
IIBE dipole (job 16)	-5	-5	-13
IIGE dipole (job 18)	-6	-6	-13
IIF dipole (L_F = 0.75 m)	-5	-5	-13
IIF dipole (L_F = 1 m)	-6	-5	-13
IIF dipole (L_F = 1.5 m)	-6	-6	-13
IIF dipole (L_F = 2 m)	-5	-5	-13
nose of projectile	6	4	43

Since the K09 anomaly is so well isolated, it was chosen as a candidate for the anomaly stack option in which "synthetic neighbors" were introduced from 14 m to the magnetic south (jobs 39-70). Anomalies were shifted 14 m north, scaled by factors of 1, 2, 3, 4, or 5, then stacked with the K09 anomaly. The K09 anomaly and the anomalies of its synthetic neighbors are all much smaller than the earth's field. It follows by principal of superposition of magnetic fields that the anomaly stack option using a scale factor of 1.0, is equivalent to disinterring the targets and re-interring them at the same depth and orientation but in proximity to the K09 target. Thus target Q09, a 0.96-kg piece of metallic clutter at a depth to center of 95 cm, was moved to a position 2 m north of target K09. The applied scale factor is equivalent to scaling the magnetizations of the "synthetic neighbors".

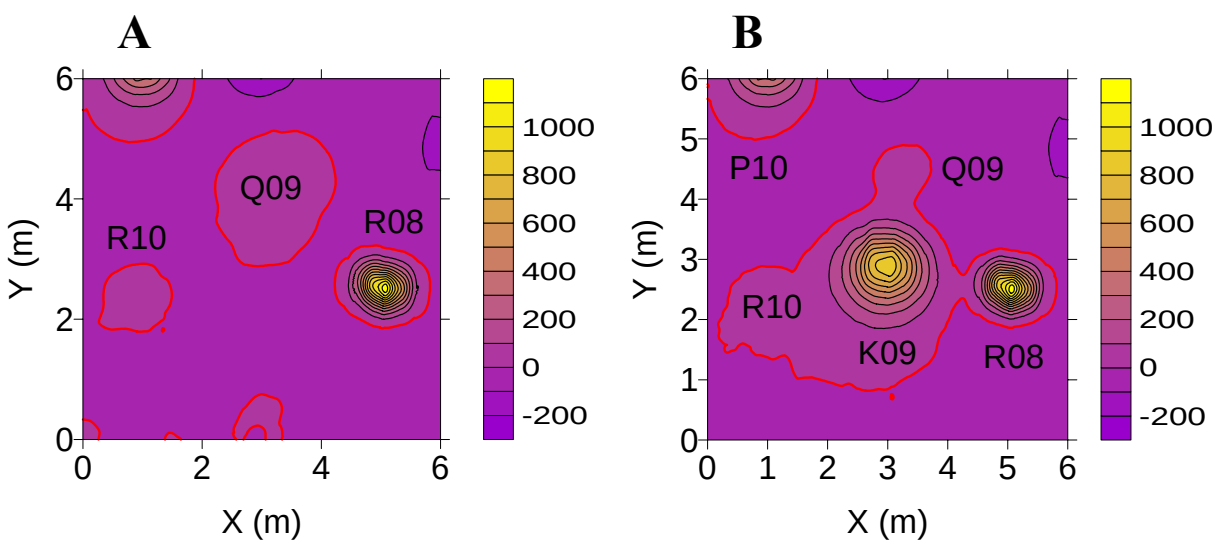

Figure 10. A. The Q09, R08, and R10 anomalies, which are moved north to become "synthetic neighbors" of the K09 anomaly. **B**. The hybrid data obtained by stack of the K09 anomaly and its "synthetic neighbors", with a scale factor equal to 1. The zero contour is red (contour interval = 100 nT).

The "synthetic neighbors" to K09 in the hybrid data posed a challenging environment of interfering fields. Comparisons of stack-anomaly jobs 64-65 (scale factor = 5) with jobs 37-38 (Table 17-18) show that non-IIF inversions, even for relatively small data windows, gave large errors in the dipole parameters. For example, for IIBE hybrid-data job 64, θ is 40.5 deg. For IIGE hybrid-data job 65, θ is 67.6 deg. IIF hybrid-data jobs 68-69, on the other hand, gave results closer to those of non-IIF K09 jobs 37-38. For non-IIF jobs, θ increased greatly as the interference was increased. For IIF jobs, the increase was much less (Table 18).

Table 17. K09 job and dipole parameters: job number and type, data window size, filter size, horizontal and vertical displacements of the dipole from the target center, deviation angle, and the dipole's declination, inclination, and strength.[#]

Job	Type[†]	L_D (m)	LF (m)	ΔC (cm)	$Z-Z_C$ (cm)	θ (deg)	δ (deg)	Ψ (deg)	M ($A \cdot m^2$)
16	IIBE	3	n/a	7	-13	17.2	-49.1	82.1	3.706
18	IIGE	3	n/a	8	-13	16.9	-34.5	83.5	3.693
20	IIF	3	1.0	8	-13	14.6	-24.2	81.5	3.707
21	IIF	3	1.5	8	-13	17.0	-29.7	83.8	3.694
22	IIF	3	2.0	7	-13	17.3	-44.9	82.9	3.703
37	IIBE	1.5	n/a	8	-13	17.0	-35.9	83.4	3.704
38	IIGE	1.5	n/a	8	-13	14.8	-27.4	81.6	3.714
64	IIBE S_5	1.5	n/a	16	-18	40.5	148.6	71.6	2.957
65	IIGE S_5	1.5	n/a	37	-13	67.6	105.5	34.7	4.536
68	IIF S_5	1.5	1	10	-13	20.2	-37.0	87.2	3.429
69	IIF S_5	1.5	1.25	10	-13	20.4	-15.7	87.6	3.613

S_5 = anomaly stack (5 = scale factor, Figure I15)

Table 18. Deviation angles, θ, for the K09 anomaly (scale factor 0) and the anomaly-stack hybrid data (scale factors 1, 2, 3, 4, and 5).

Anomaly stack scale factor:	0	1	2	3	4	5
Inversion jobs:	θ (deg)	θ (deg)	θ (deg)	θ (deg)	θ (deg)	θ (deg)
IIBE (L_D = 1.5 m)	17.0	n/a	n/a	n/a	n/a	40.5
IIBE (L_D = 2 m)	n/a	23.9	n/a	n/a	n/a	n/a
IIBE (L_D = 3 m)	17.2	27.0	n/a	n/a	n/a	n/a
IIBE (L_D = 4 m)	17.2	n/a	n/a	n/a	n/a	n/a
IIGE (L_D = 1.5 m)	14.8	n/a	n/a	n/a	n/a	67.6
IIGE (L_D = 2 m)	n/a	21.5	24.3	29.5	59.4	60.9
IIGE (L_D = 3 m)	16.9	23.3	n/a	n/a	n/a	n/a
IIGE (L_D = 4 m)	16.9	n/a	n/a	n/a	n/a	n/a
EAGGN IIF (L_D = 1.5m, L_F = 1 m)	n/a	n/a	n/a	n/a	n/a	20.2
EAGGN IIF (L_D = 2m, L_F = 1 m)	n/a	16.7	19.2	21.5	21.7	24.1
EAGGN IIF (L_D = 3m, L_F = 1 m)	14.6	23.3	n/a	n/a	n/a	n/a
EAGGN IIF (L_D = 4m, L_F = 1 m)	16.9	n/a	n/a	n/a	n/a	n/a

The anomaly-stack adds synthetic neighbors. The reverse of this process is to strip those neighbors away. In dipole stripping the anomalies to be removed must first be approximated as the fields of inverse-modeled dipoles. Unfortunately, just as the neighbor interferes with the target's field the target interferes with the neighbor's field. One may thus first fit a dipole to the neighbor by multi-dipole inversion or by IIF inversion as developed here. One may also apply multi-dipole, IIF inversion. It follows that dipole stripping may become more complex than simply applying IIF separately to the target and the neighbor anomaly. One may imagine further that one could apply IIF inversions both before and after dipole stripping but an examination of such a process is beyond the scope of the present SEED project.

For IIF to be successful there is no necessity that the neighboring anomalies be smaller than the target anomaly as in the present case. Examples of the target anomaly embedded in or engulfed by much larger anomalies are presented in other sections of this report. It is likely that IIF would often be a more powerful tool than dipole stripping; although additional efforts should be made to refine this tool including analysis that will guide the selection of the filter parameters. For example, using other anomalies the effects of non-square filters have been examined.

Some additional observations can be made, however, based on the results of jobs 1-38 applied to the non-hybrid data (Tables I2-I3). One may note, for example, that results for all-node and flag-node non-IIF jobs are nearly the same. This may be expected since the anomaly is of a relatively deep target (Z_C = 80 cm) and there is little apparent effect of high-frequency background fields.

Jobs 1-14 used kriging, with $\Delta x = \Delta y = 5$ cm, as opposed to minimum-curvature interpolation with $\Delta x = \Delta y = 1$ cm. Each of these jobs gave the same horizontal dipole position: $(X-X_C) = -6$ cm, and $(Y-Y_C) = -7$ cm. The solutions were "stabilized" at a node in the 5-cm grid, which happened to be very close to nodes in the 1-cm grid where the dipoles were located. If this had not occurred then the dipole in jobs 1-14 would probably have moved to adjoining grid nodes as the job parameters varied. The sensitivity of depth and dipole orientation to horizontal position is generally less for a deeper target such as K09; however even for this target, the sensitivity is significant.

To demonstrate that sensitivity, Table 19 compares results for a non-IIF, IIGE unconstrained inversion with an inversion that fixes the dipole at a node nearest to the target's center (job 18). The job parameters are otherwise the same, and $\Delta x = \Delta y = 1$ cm. Although the constraint moved the dipole by only 8 cm, the inclination, Ψ, changed by 11 deg. To obtain the best estimates of dipole orientation and position, it is desirable to use the smaller grid interval ($\Delta x = 1$ cm).

Table 19. Dipole parameters for a constrained and unconstrained inversion of the K09 anomaly.

	Δ_C cm	$(Z-Z_C)$ cm	θ deg	Δ deg	Ψ deg
Job 18 (unconstrained)	8	-13	16.9	-34.5	83.5
Job 32 ($X=X_C$, $Y=Y_C$)	1	-12	15.4	-54.9	72.1

Additional figures and tables of results for the K09 anomaly are provided in Appendix I.

5.8 Results for anomaly B01. Target B01 is a 2.75-in XM230 rocket warhead, which the AEC emplaced at a depth to center of 23 cm (Figure J1, Table J1). The B01 anomaly (Figure 11) was input to 19 jobs directly. In 20 other inversion jobs, a synthetic background field was added to create hybrid real and synthetic data. Details of these results are presented in Appendix J (Figures J1-J11 and Tables J1-J4).

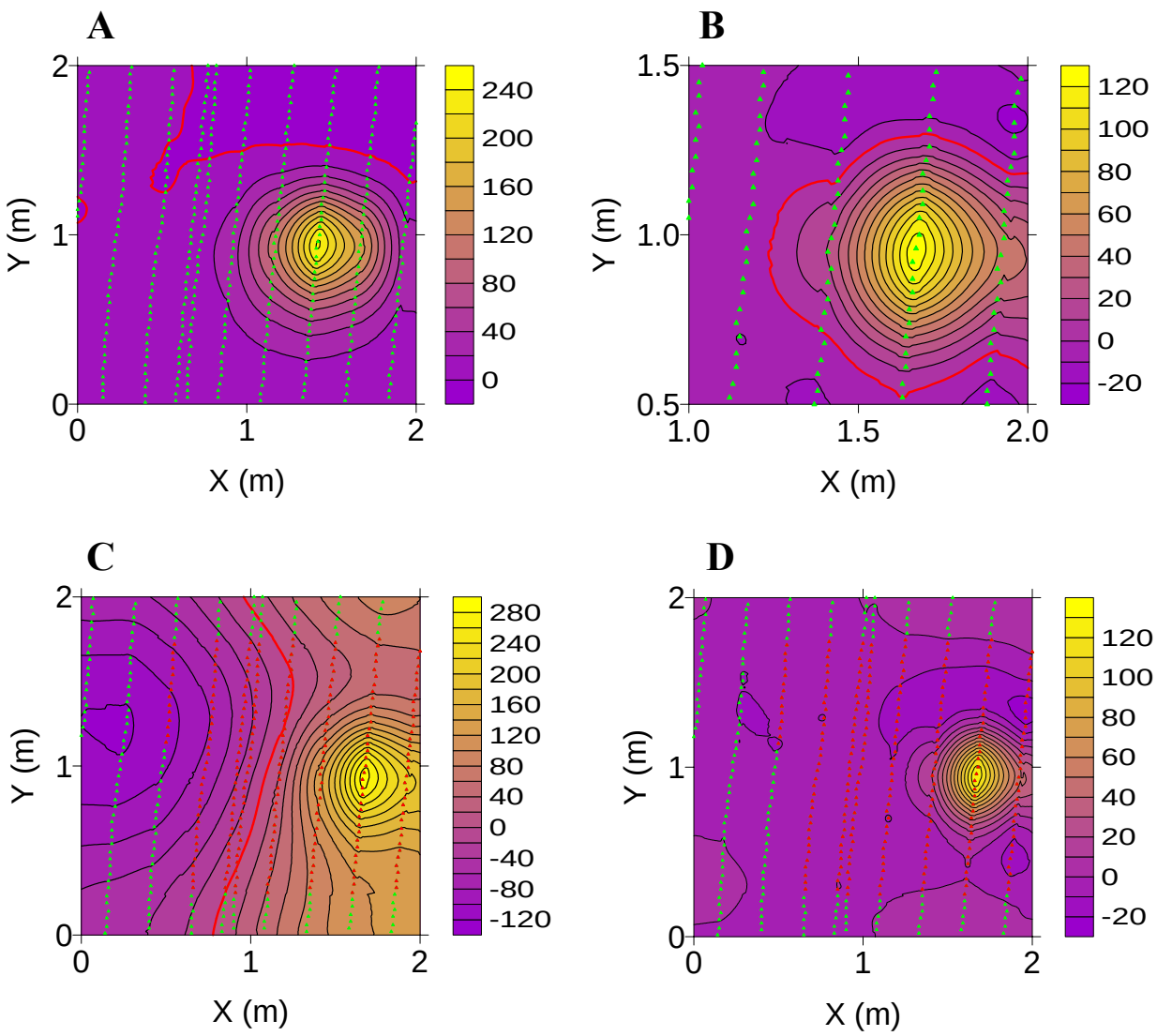

Figure 11. A. the B01 anomaly; **B**. EAGGN filtered B01 anomaly (L_F = 0.75 m); **C**. hybrid data equal to the B01 anomaly plus synthetic background field; **D**. EAGGN filtered hybrid data (L_F = 0.75 m). Contour intervals are 20 and 10 nT for unfiltered and filtered data, respectively.

The B01 anomaly (Figure 11A) is apparently well isolated from effects of its neighbors or other disturbing background fields. This SEED project used a data set for the APG BTA that truncated the eastern part of the B01 anomaly peak. Another data set that provided data for the survey of the entire BTA and adjacent areas was available but was not used. The truncated data set tests

and demonstrates the edge-adaptive feature of the EAGGN IIF. The peak value of the anomaly is 229 nT. Within the data window used here, the minimum value in the associated low is – 7 nT.

Non-IIF, IIGE and IIF inversions gave consistent results for the dipole position and orientation. These results show only minor differences with the standard method of non-IIF, IIBE inversion. For IIBE job 18, IIGE job 19, and IIF jobs 6 and 7, Δ_C is 4 cm, $4 \leq (Z\text{-}Z_C) \leq 5$ cm, $21.4 \leq \theta \leq 26.5$ deg, and $81.6 \leq \Psi \leq 88.4$ deg (Table 20). The deviation angles, θ, are consistent with UXO having little remanence.

B01 jobs derived flag-node IIF from symmetric, rectangular ($L_{FY} \leq L_{FX}$), $F_{CP\text{-}BOXCAR}$ filters. IIF allows successful inversion in the case of strong local anomalies simulating geologic noise. Adding a synthetic background field yields the hybrid data of Figure 11C. The synthetic background field is of sufficiently high spatial frequency that its effect would not be eliminated by a conventional pre-inversion filter such as the de-median filter applied to the real data. Such pre-inversion filters are designed to avoid significant distortion of the target field.

Non-IIF inversions of the hybrid data gave inconsistent results with some large positional errors and significant deviations of dipole orientations from those of the original data without the synthetic background (Table 20). For EAGGN IIF jobs applied to the hybrid data, the dipole solutions closely approximate the results obtained without the synthetic background. For hybrid data EAGGN IIF jobs 27-28 ($L_D = 1$ m, $0.75 \leq L_F \leq 1$ m), $4 \leq \Delta_C \leq 5$ cm, $5 \leq (Z\text{-}Z_C) \leq 6$ cm, and $25.5 \leq \theta \leq 25.8$ deg. For the real-data EAGGN IIF jobs 6-7 ($L_D = 1$ m, $0.75 \leq L_F \leq 1$ m), Δ_C is 4 cm, $4 \leq (Z\text{-}Z_C) \leq 5$ cm, and $26.1 \leq \theta \leq 26.5$ deg.

Hybrid data EAGGN IIF inversions with rectangular filters ($L_{FX} = 0.75$ m, $0.2 \leq L_{FY} \leq 0.6$ m) demonstrate that smaller filter dimensions in the y-direction also yield excellent results since there is adequate sampling in the along-profile direction (jobs 29-33; Tables J2-J3).

Table 20. B01 job and dipole parameters: job number and type, data window size, L_D, filter size, L_F, relative horizontal and absolute vertical displacements of the dipole from the target center, Δ_C and $(Z\text{-}Z_C)$, deviation angle, θ, and the dipole's declination, δ, inclination, Ψ, and strength, M.†

Job	Type	L_D (m)	L_F (m)	Δ_C (cm)	$Z\text{-}Z_C$ (cm)	θ (deg)	δ (deg)	Ψ (deg)	M ($A\bullet m^2$)
18	IIBE	1.5	n/a	4	4	21.6	-56.3	88.4	176
19	IIGE	1.5	n/a	4	5	21.4	-46.3	88.4	185
6	IIF	1	0.75	4	4	26.5	96.0	81.6	176
7	IIF	1	1	4	5	26.1	99.2	82.8	187
21#	IIBE	1.5	n/a	33	49	63.5	84.6	31.5	1555
23#	IIGE	1.5	n/a	7	-2	13.7	-44.9	64.6	120
24#	IIBE	0.75	n/a	5	4	25.5	69.5	73.8	188
25#	IIGE	0.75	n/a	18	4	73.5	104.9	28.1	238
27#	IIF	1	0.75	4	5	25.8	97.0	82.9	162
28#	IIF	1	1	5	6	25.5	97.8	83.7	173

† blue and red entries indicate jobs with and without IIF, respectively
# hybrid model (B01 anomaly plus synthetic background field).

5.9 Results for anomaly H12. Target H12 is a 60-mm, 1.3-kg M49 mortar round, which the AEC emplaced vertically at a depth to center of 22 cm (Figure K1, Table K1). The H12 anomaly (Figure 12) was input to 34 jobs (Tables 21-22 and K2-K4).

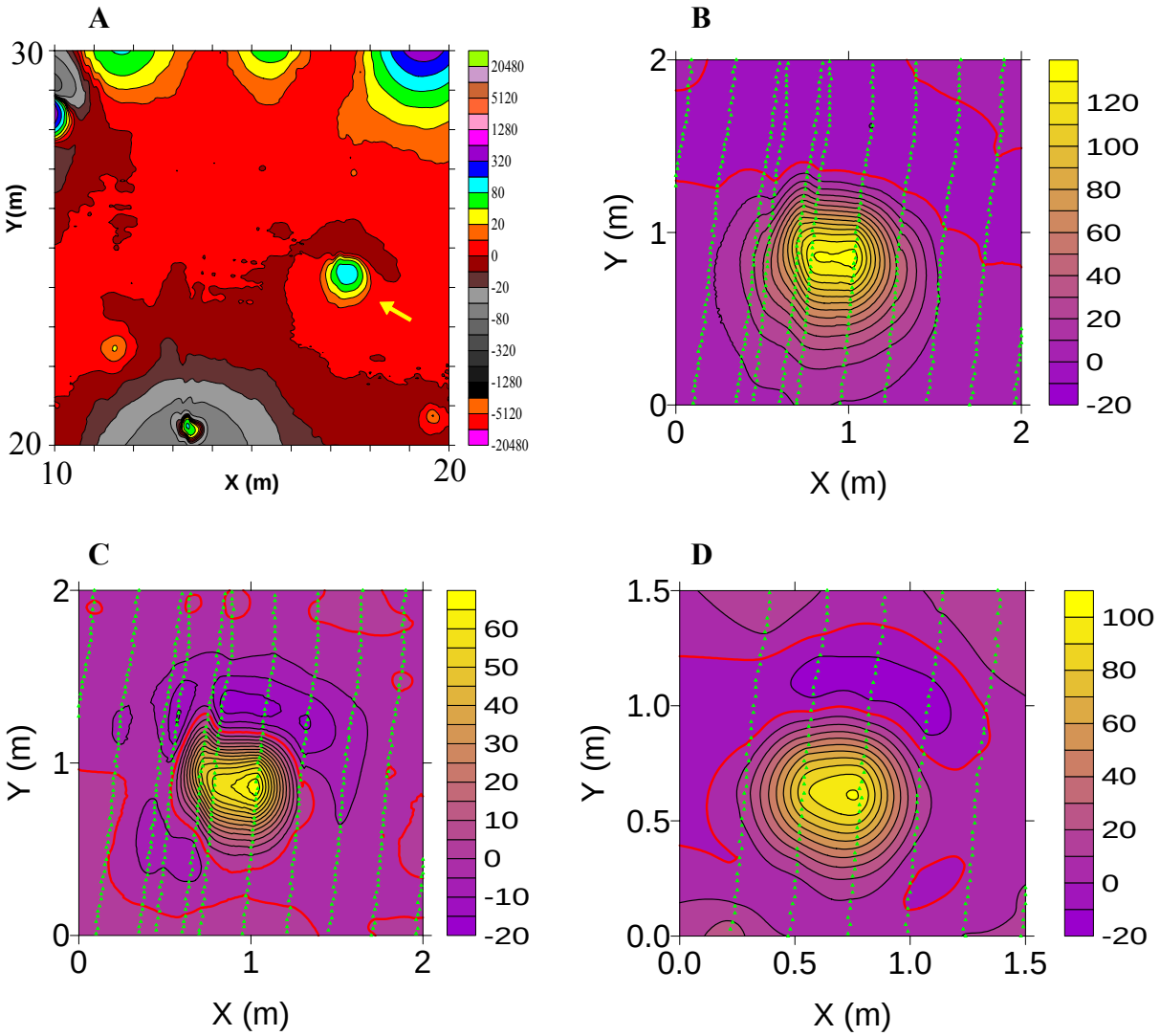

Figure 12. A. Regional setting of the H12 anomaly (yellow arrow); contours at zero and $\pm 2^n \cdot 10$ nT, where n is a non-negative integer. **B.** The H12 anomaly showing swath-overlap noise and flagged nodes (green triangles) nearest to measurement stations; the contour interval is 10 nT. **C.** EAGGN filtered H12 anomaly (L_F = 0.5 m, L_D = 2 m) used in IIF job 25; the contour interval is 5 nT. **D.** single-swath, EAGGN filtered H12 anomaly (L_F = 1.25 m, L_D = 1.5 m) used in IIF job 15; the contour interval is 10 nT.

The H12 anomaly is very well isolated from other anomalies (Figures 12A-12B). Both non-IIF and IIF inversions yield dipoles closer to the nose than the tail of the vertical mortar round (Table K1).

For 12 non-IIF inversions with Δx and Δy equal to 1 cm, $2 \leq \Delta_C \leq 6$ cm, $6 \leq (Z-Z_C) \leq 10$ cm, $5.9 \leq \theta \leq 22.5$ deg, and $69.4 \leq \Psi \leq 76.0$. Excluding the peak-only inversions (jobs 31-32) the ranges for Δ_C and θ are narrower: $2 \leq \Delta_C \leq 5$ cm and $5.9 \leq \theta \leq 11.9$ deg. For the peak-only (H > 20 nT) IIGE job 32, θ is 22.5 deg, which is significantly higher than for the peak-only IIBE inversion. For windows that are small relative to the anomaly, as in the case of this peak-only inversion, IIGE will commonly yield inaccurate results.

H12 GGN jobs 20-21 derived flag-node IIF from symmetric, square ($L_{FY} = L_{FX}$), $F_{CP\text{-}PYRAMID}$ filters. The EAGGN IIF were derived from square $F_{CP\text{-}BOXCAR}$ filters. For all 16 IIF inversions with Δx and Δy equal to 1 cm, $3 \leq \Delta_C \leq 4$ cm, $7 \leq (Z-Z_C) \leq 9$ cm, $3.3 \leq \theta \leq 15.6$ deg, and $69.9 \leq \Psi \leq 73.6$ deg. For the single-swath EAGGN jobs 13-15 ($0.75 \leq L_F \leq 1.25$ m, $L_D = 1.5$ m), $3 \leq \Delta_C \leq 4$ cm, $(Z-Z_C)$ is equal to 7 cm, and $3.3 \leq \theta \leq 6.5$ deg (Table K2). These small deviation angles are consistent with UXO having small remanence. For the corresponding multi-swath EAGGN jobs 6-8, $3 \leq \Delta_C \leq 4$ cm, $7 \leq (Z-Z_C) \leq 8$ cm, and $9.9 \leq \theta \leq 15.6$ deg. The differences between single-and multi-swath inversions may result from swath-overlap noise (Figures 12B-12C).

Additional details concerning target H12 and all 28 inversions are provided in the Appendix K.

Table 21. Dipole and mortar-end offsets from H12 target's center (X_C, Y_C, Z_C; UTM)
L_F = filter size, L_D = data window size, Δ_C = horizontal displacement from target center.†

job	description	L_F (m)	L_D (m)	Δ_C (cm)	$X-X_C$ (cm)	$Y-Y_C$ (cm)	$Z-Z_C$ (cm)
	base of projectile				0	0	-12
1	All-node, IIBE	n/a	1.5	5	1	-5	9
2	Flag-node, IIBE	n/a	1.5	4	1	-4	7
3	All-node, IIGE	n/a	1.5	4	1	-4	10
4	Flag-node, IIGE	n/a	1.5	3	1	-3	7
10	single-swath, IIBE	n/a	1.5	5	0	-5	7
11	single-swath, IIGE	n/a	1.5	4	0	-4	7
31	peak-only, IIBE	n/a	2	5	3	-4	8
32	peak-only, IIGE	n/a	2	6	3	-6	8
6	EAGGN	0.75	1.5	4	2	-4	8
7	EAGGN	1	1.5	3	1	-3	8
8	EAGGN	1.25	1.5	3	1	-3	7
13	single-swath EAGGN	0.75	1.5	3	0	-3	7
14	single-swath EAGGN	1	1.5	4	0	-4	7
15	single-swath EAGGN	1.25	1.5	4	0	-4	7
	nose of projectile				0	0	12

Table 22. H12 job and dipole parameters: job number and type, data window size, L_D, filter size, L_F, relative horizontal and absolute vertical displacements of the dipole from the target center, Δ_C and $(Z\text{-}Z_C)$, deviation angle, θ, and the dipole's declination, δ, inclination, Ψ, and strength, M.[#]

Job	Type †	L_D (m)	L_F (m)	Δ_C (cm)	$Z\text{-}Z_C$ (cm)	θ (deg)	δ (deg)	Ψ (deg)	M ($A\bullet m^2$)
1	AB	1.5	n/a	5	9	11.9	-37.7	76.0	135
2	B	1.5	n/a	4	7	11.0	-36.3	75.0	128
3	A	1.5	n/a	4	10	9.0	-33.3	72.3	145
4		1.5	n/a	3	7	9.1	-34.0	71.9	130
10	B§	1.5	n/a	5	7	9.3	-21.5	76.0	128
11	§	1.5	n/a	4	7	5.9	-17.8	72.8	129
31	B▲$_2$	2	n/a	5	8	15.4	-54.6	71.5	137
32	▲$_2$	2	n/a	6	8	22.5	-81.8	74.7	135
6	E	1.5	0.75	4	8	15.6	-55.3	71.8	138
7	E	1.5	1	3	8	9.9	-36.8	72.0	137
8	E	1.5	1.25	3	7	10.1	-37.2	72.1	130
13	E§	1.5	0.75	3	7	3.3	-16.6	69.9	130
14	E§	1.5	1	4	7	6.6	-17.3	73.6	129
15	E§	1.5	1.25	4	7	6.5	-17.4	73.4	129

blue and red entries indicate jobs with and without IIF, respectively

† flag-node and IIGE unless noted: **A** = all-node; **B** = IIBE. **E** = EAGGN ($L_{FD} = L_D$).

▲$_2$ = peak-only (H > 20). **§** = single-swath.

5.10 Results for the H03 anomaly. Target H03 is a 40-mm projectile (Figure L1, Table L1). It was emplaced sub-horizontally (Ψ_T = 8 deg) at a depth of 40 cm. The M08 anomaly (Figure 13) was input to 35 jobs (Tables 23 and L2-L4).

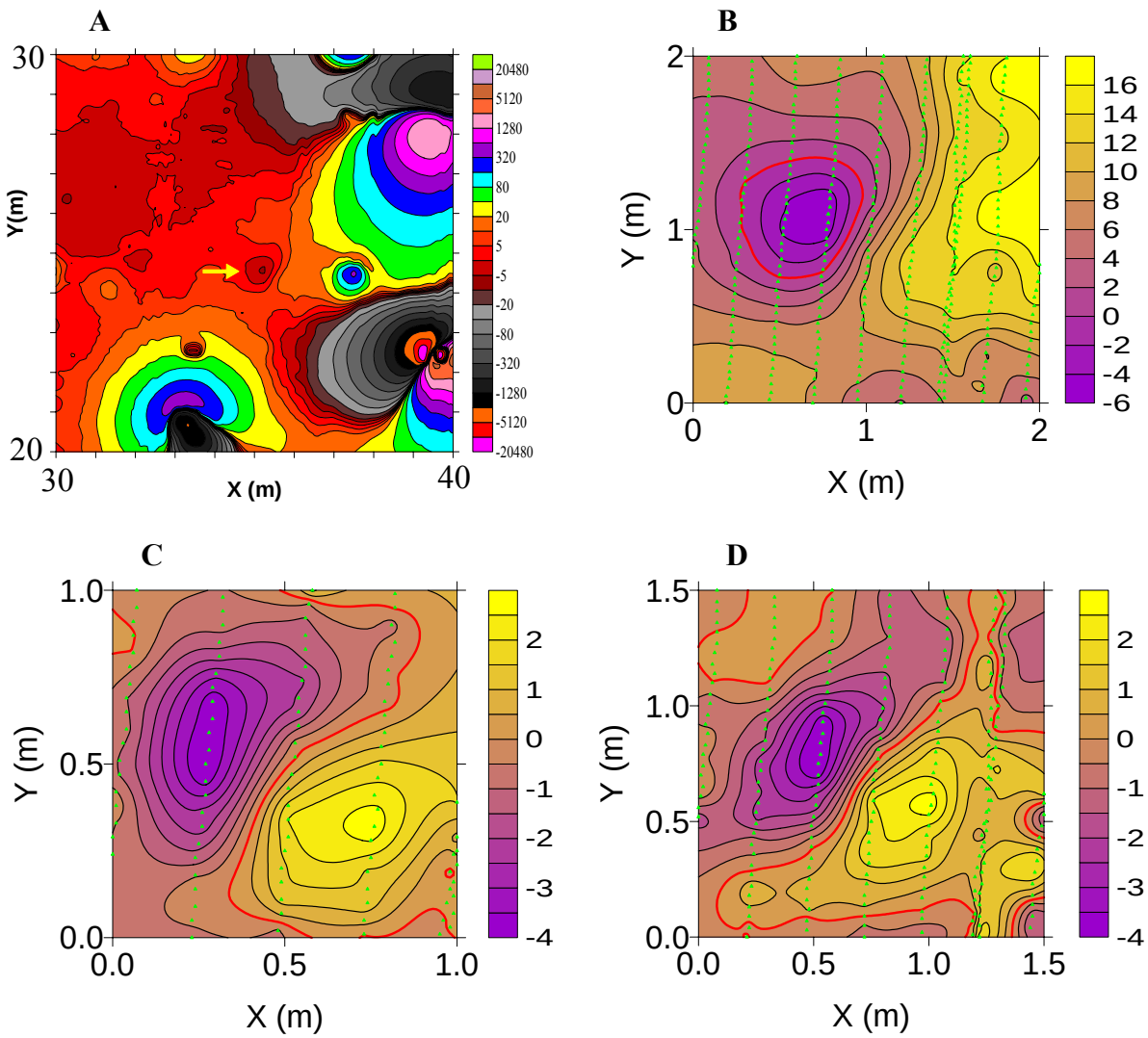

Figure 13. A. Regional setting of the H03 anomaly (yellow arrow), which is strongly disturbed by several nearby anomalies. The magnetic field contours are at zero and $\pm 2^n \cdot 5$ nT, where n is a non-negative integer. **B.** H03 anomaly with a minimum of –5.0 nT any significant associated peak may be merged with the neighboring anomalies. Flagged nodes (399 green triangles) were used in flag-node inversions. **C.** EAGGN filtered H03 anomaly (L_F = 0.5 m, L_D = 1 m) **D.** EAGGN filtered anomaly (L_F = 0.5 m, L_D = 1.5 m).

The H03 anomaly has a weak minimum of only -5.0 nT. The shapes of contours that define this minimum and the shape of any associated peak are strongly disturbed by much larger nearby anomalies (Figures 13A-13B). In a 2 m x 2 m data window, the maximum value of 19.0 nT occurs on the northern edge of that window but it is clearly not the result of a positive peak associated with the target H03 anomaly.

H03 jobs derived flag-node IIF from symmetric, square ($L_{FY} = L_{FX}$), $F_{CP\text{-}BOXCAR}$ filters. EAGGN filtering seems to extract the missing peak from the complicated regional field that results from overlap by the tails of multiple neighboring anomalies (Figures 13C-13D). The IIF inversions gave more consistent dipole positions closer to the target's center (Tables 23 and L2). The also gave somewhat smaller deviation angles; however, even the IIF-derived deviation angles exceeded 60 deg. Given the difficult environment of the background field the dipole positions are fairly good however the large deviation angles seem to indicate strong remanence, which is inconsistent with the demagnetization of the projectile before emplacement. For additional Figures, including residual fields, and more extensive tables of results see Appendix L.

Table 23. Dipole and projectile-end offsets from the target's center (UTM coordinates, X_C, Y_C). L_F = filter size, L_D = data window size, Δ_C = horizontal displacement from target center.†

Job	description	L_F (m)	L_D (m)	Δ_C (cm)	$X\text{-}X_C$ (cm)	$Y\text{-}Y_C$ (cm)	$Z\text{-}Z_C$ (cm)
	base of projectile				9	-4	-1
1	All-node IIBE	n/a	1	8	3	-7	8
2	Flag-node IIBE	n/a	1	11	4	-10	7
3	All-node IIGE	n/a	1	9	6	-6	30
4	Flag-node IIGE	n/a	1	12	7	-10	26
27	trough-only, IIBE $\blacktriangledown_2$	n/a	2	19	4	-18	19
28	trough-only, IIGE $\blacktriangledown_2$	n/a	2	12	-5	-11	9
29	trough-only, IIBE $\blacktriangledown_0$	n/a	2	19	5	-18	8
30	trough-only, IIGE $\blacktriangledown_0$	n/a	2	17	-15	-9	0
5	EAGGN	0.5	1	5	2	-5	-10
6	EAGGN	0.75	1	7	0	-7	-5
7	EAGGN	1	1	5	0	-5	0
15	EAGGN	0.5	1.5	7	-1	-7	0
16	EAGGN	0.75	1.5	11	1	-11	5
17	EAGGN	1	1.5	9	6	-7	9
34	Single-swath, EAGGN	0.75	2	12	-1	-12	2
35	Single-swath, EAGGN	1	2	13	-5	-12	0
	nose of projectile				-9	4	1

† blue and red entries indicate jobs with and without IIF, respectively

$\blacktriangledown_0$ = trough-only (H < 0). $\blacktriangledown_2$ = trough only (H < 2)

5.11 Results for anomaly A07. Figures 14 and M2-M13 plot the A07 anomaly and results of inversion jobs. Target A07 is a 57 mm M86 projectile (Figure M1), which the AEC emplaced at a depth to center, Z_C, of 26 cm (Table M1). Conclusions are derived from the results of 23 inversion jobs (Tables 24-25 and M2-M4).

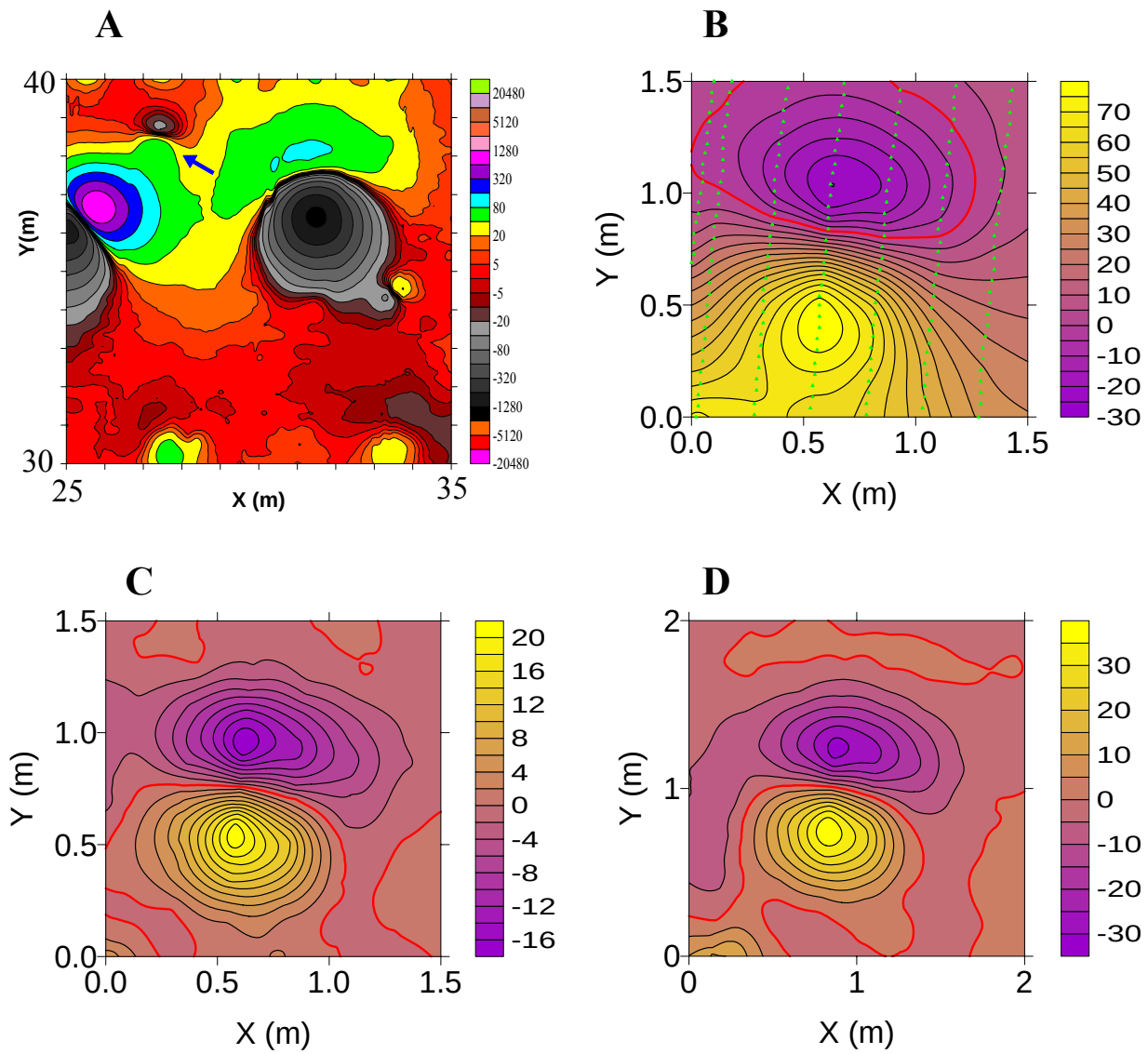

Figure 14. A. Regional setting of the A07 anomaly (blue arrow); the contours are at 0 and $\pm 2^n \cdot 10$ nT, where n is a non-negative integer. **B.** The A07 anomaly; the contours of its peak merge with those of a larger anomaly to the southwest; the contour interval is 5 nT. **C.** EAGGN filtered A07 anomaly (L_F = 1 m, L_D = 1.5 m); the contour interval is 2 nT. **D.** EAGGN filtered A07 anomaly (L_F = 2 m, L_D = 2 m); the contour interval is 5 nT.

The peak of the A07 anomaly merges with the much larger B08 anomaly to the southwest (Figures 14A and 14B). As a result, non-IIF inversions yield inaccurate depths for this horizontal projectile (Table 24).

A07 jobs derived flag-node IIF from symmetric, square ($L_{FY} = L_{FX}$), $F_{CP\text{-}PYRAMID}$ filters. EAGGN IIF inversions gave improved depth estimates and therefore better estimates of the dipole moment, which are used to estimate the size of the target (Table 25). The EAGGN filtered anomalies (Figures 14C and 14D) show better separation of the A07 anomaly from its neighboring anomaly to the southwest.

Without IIF, a geophysical interpreter might try to use a small-window inversion by drawing a polygonal window about the trough and perhaps a portion of the peak of the A07 anomaly. With IIF, the choice of the data window is less critical and thus the burden on the interpreter may be lessened even as more-accurate inversions are obtained. EAGGN IIF inversions with $0.75 \leq L_F \leq 1.25$ and L_D equal to 2 m, yield $51.7 \leq \theta \leq 52.0$ deg and identical dipole locations as the corresponding jobs with L_D equal to 1.5 m for which $52.2 \leq \theta \leq 52.3$ deg. For these jobs, Δ_C is 4 cm, ($Z\text{-}Z_C$) is 6 cm, and the correlation coefficient, R, decreases with decreasing filter size and increasing inversion data window size. For L_D equal to 1.5 m, $0.988 \leq R \leq 0.993$; while for L_D equal to 2 m, $0.961 \leq R \leq 0.976$. The effects of noise, especially anomaly B08, significantly decrease R with increasing L_D. Nevertheless, the consistency of IIF dipole solutions indicates that these effects are not inimical to the extraction of accurate target parameters based on the least-squares IIF inversion. For a given L_D and L_F, the B08 anomaly has little effect on variations of least-squares error as a function of test dipole positions in the vicinity of the target's dipole.

Table 24. Dipole and projectile-end offsets from the A07 target's center (UTM coordinates, X_C, Y_C). L_F = filter size, L_D = data window size, Δ_C = horizontal displacement from target center

job	description	L_F (m)	L_D (m)	Δ_C (cm)	$X\text{-}X_C$ (cm)	$Y\text{-}Y_C$ (cm)	$Z\text{-}Z_C$ (cm)
	base of projectile				1	8	0
1	All-node, IIBE	n/a	1	5	-5	-1	15
2	Flag-node, IIBE	n/a	1	5	-5	-1	14
9	Flag-node, IIBE	n/a	1.5	9	-9	-2	25
3	All-node, IIGE	n/a	1	6	-6	0	14
4	Flag-node, IIGE	n/a	1	6	-6	0	12
11	Flag-node, IIGE	n/a	1.5	9	-9	-1	13
5	EAGGN	0.5	1	6	-5	4	7
6	EAGGN	0.75	1	6	-5	3	6
7	EAGGN	1	1	5	-4	3	5
12	EAGGN	0.5	1.5	5	-5	2	6
13	EAGGN	0.75	1.5	4	-4	2	6
14	EAGGN	1	1.5	4	-4	2	6
15	EAGGN	1.25	1.5	4	-4	2	6
16	EAGGN	1.5	1.5	4	-4	2	6
	nose of projectile				-1	-8	0

Table 25. A07 job and dipole parameters: job number and type, data window size, L_D, filter size, L_F, relative horizontal and absolute vertical displacements of the dipole from the target center, Δ_C and (Z-Z_C), deviation angle, θ, and the dipole's declination, δ, inclination, Ψ, and strength, M.†

Job	Type	L_D (m)	L_F (m)	Δ_C (cm)	Z-Z_C (cm)	θ (deg)	δ (deg)	Ψ (deg)	M (mA•m^2)
1	IIBE	1	n/a	5	15	49.9	-20.8	17.7	176
2	IIBE	1	n/a	5	14	49.8	-20.9	17.8	171
9	IIBE	1.5	n/a	9	25	51.0	-19.3	16.5	268
3	IIGE	1	n/a	6	14	51.7	-19.8	15.8	166.5
4	IIGE	1	n/a	6	12	51.7	-19.0	15.8	154
11	IIGE	1.5	n/a	9	13	52.1	-16.0	15.2	149
5	IIF	1	0.5	6	7	59.1	-23.0	8.7	110
6	IIF	1	0.75	6	6	54.6	-19.3	12.9	101
7	IIF	1	1	5	5	55.1	-19.4	12.4	95
12	IIF	1.5	0.5	5	6	52.3	-25.5	15.7	102
13	IIF	1.5	0.75	4	6	52.3	-22.2	15.5	101
14	IIF	1.5	1	4	6	52.3	-22.1	15.4	102
15	IIF	1.5	1..25	4	6	52.2	-22.2	15.5	102
16	IIF	1.5	1.5	4	6	52.3	-22.2	15.4	102

† blue and red entries indicate jobs with and without IIF, respectively

5.12 Results for anomaly B10. Target B10 is a 0.8-kg BDU submunition, which the AEC emplaced at a depth to center of 13 cm (Figure N1, Table N1). The B10 anomaly (Figure 15) was input to 17 jobs (Tables 26-27 and N2-N4).

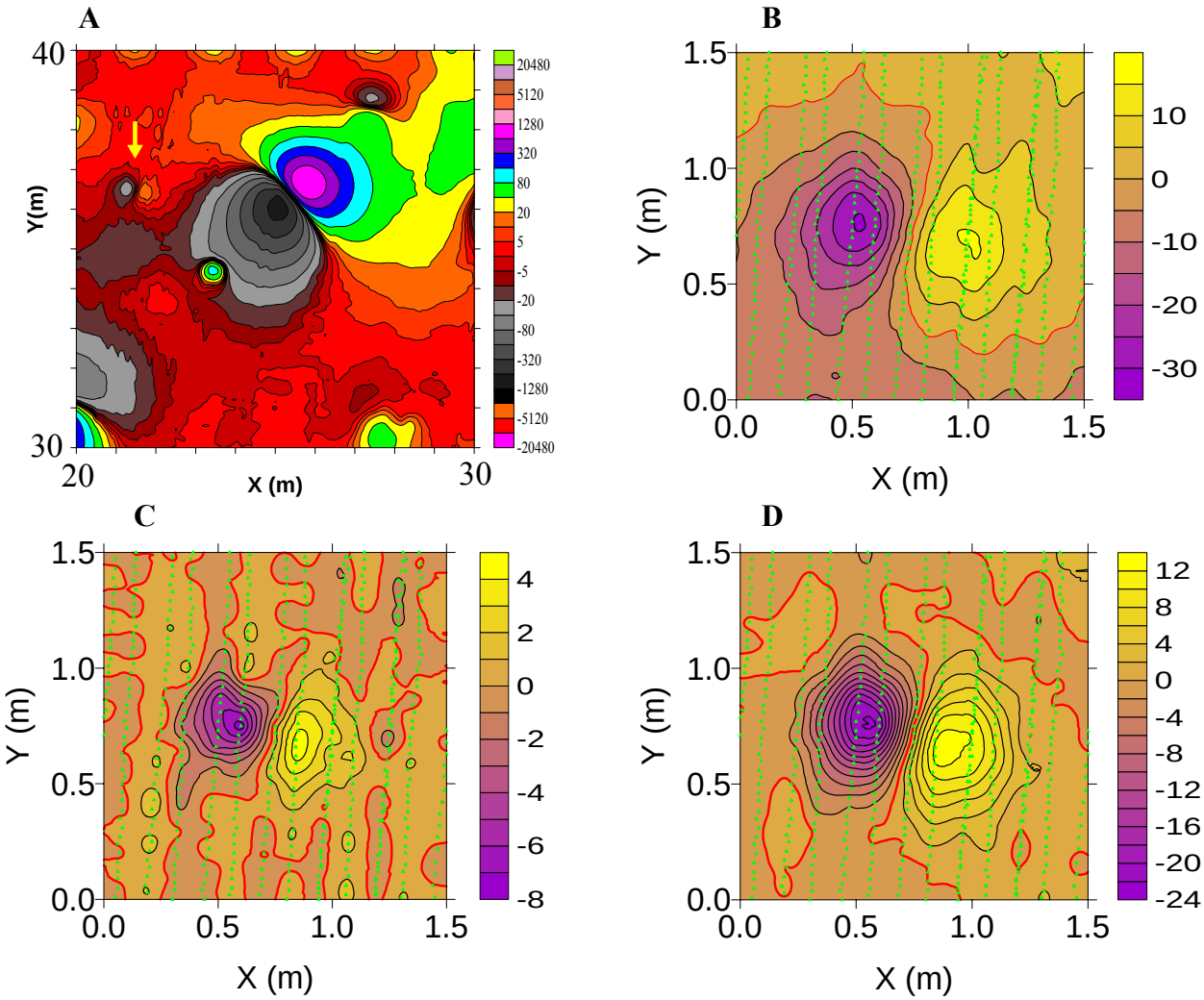

Figure 15. A. Regional setting of the B10 anomaly (yellow arrow); contours at zero and $\pm 2^n \cdot 5$ nT, where n is a non-negative integer. **B.** The B10 anomaly showing swath-overlap noise and flagged nodes (green triangles); contour interval is 5 nT. **C.** EAGGN filtered B10 anomaly (L_F = 0.5 m, L_D = 1.5 m) the central 1 x 1-m area was used in the GGN IIF inversion job 5; the contour interval is 2 nT. **D.** EAGGN filtered B10 anomaly (L_F = 1.5 m, L_D = 1.5 m) used in job 17; the contour interval is 2 nT.

The B10 anomaly has an interpolated minimum value of –30 nT and an associated peak value 15 nT about 50 cm to the east of the minimum value (Figure 15B). The anomaly is fairly well isolated from the effects of neighboring anomalies; however, The IIGE background field in a 1-m x 1-m data window (job 4) is described by a dc-bias of –2.6 nT and a gradient of 7.3 nT/m. The background field may affect the accuracy of θ slightly; however there is not much difference

between the positions of non-IIF and IIF dipoles for this target (Table 26). For non-IIF IIGE job 4, θ is 82.8 deg; and for IIBE job 2, θ is 90.6 deg (Table 27). The GGN and EAGGN IIF jobs 5-8 (L_D = 1 m) yield θ that are intermediate between those two values; that is, $84.3 \leq \theta \leq 86.8$ deg. For a larger data window (L_D = 1.5 m), most of the IIF dipoles (jobs 13-17) are a little closer to the target's center than the non-IIF dipoles (jobs 9-12) but the difference may not be significant.

B10 jobs derived flag-node IIF from symmetric, square ($L_{FY} = L_{FX}$), $F_{CP\text{-}PYRAMID}$ filters with Δx and Δy equal to 1 cm. For GGN IIF with L_F equal to 0.5 m, θ is 84.8 deg versus 86.8 deg for EAGGN IIF with the same nominal filter size. For such a small filter and small data window, GGN IIF would generally be preferred. The actual sizes of EAGGN filters would be only 0.25 m x 0.25 m in the corners of the data window. Since the cross-line magnetometer spacing is 0.25 m, filters of that size in the cross-line direction may not sample the magnetic field adequately. In the present example, however, MTADS swaths are overlapped more than usual and the cross-line separation of the magnetometer stations is less than 0.25 m across most of the data window. Accordingly, the denser cross-line sampling accommodates smaller filters.

For this small but fairly well isolated anomaly, there is little difference between non-IIF and IIF inversions. Additional details of the B10 target, figures and more extensive tables of inversion results are available in Appendix N.

Table 26. B10 dipole, nose, and tail offsets from the target's center (UTM coordinates, X_C, Y_C). L_F = filter size, L_D = data window size, Δ_C = horizontal displacement from target center.

job	description	L_F (m)	L_D (m)	Δ_C (cm)	$X-X_C$ (cm)	$Y-Y_C$ (cm)	$Z-Z_C$ (cm)
	tail of submunition				2	4	-2
1	All-node, IIBE	n/a	1	6	4	-4	3
2	IIBE	n/a	1	6	4	-4	2
3	All-node, IIGE	n/a	1	6	5	-4	5
4	IIGE	n/a	1	8	6	-5	4
5	GGN	0.5	1	3	3	-1	4
6	EAGGN	0.5	1	2	2	-1	4
7	EAGGN	0.75	1	3	3	-1	4
8	EAGGN	1	1	4	4	-1	3
9	All-node, IIBE	n/a	1.5	7	4	-5	5
10	IIBE	n/a	1.5	7	4	-5	3
11	All-node, IIGE	n/a	1.5	8	6	-5	3
12	IIGE	n/a	1.5	8	6	-5	2
13	EAGGN	0.5	1.5	3	3	-1	3
14	EAGGN	0.75	1.5	3	3	-1	3
15	EAGGN	1	1.5	4	4	-2	2
16	EAGGN	1.25	1.5	4	4	-2	2
17	EAGGN	1.5	1.5	6	5	-3	2
	nose of submunition				-2	-4	2

Table 27. B10 job and dipole parameters: job number and type, data window size, L_D, filter size, L_F, relative horizontal and absolute vertical displacements of the dipole from the target center, Δ_C and (Z-Z_C), deviation angle, θ, and the dipole's declination, δ, inclination, Ψ, and strength, M.†

Job	Type	L_D (m)	L_F (m)	Δ_C (cm)	Z-Z_C (cm)	θ (deg)	δ (deg)	Ψ (deg)	M ($A \bullet m^2$)
1	AB	1	n/a	6	3	90.7	68.5	-4.6	19.0
2	B	1	n/a	6	2	90.6	68.5	-4.8	17.9
3	A	1	n/a	6	5	83.9	63.6	0.4	22.4
4		1	n/a	8	4	82.8	64.3	1.9	21.1
5	G	1	0.5	3	4	84.8	60.5	-1.8	21.7
6	E	1	0.5	2	4	86.8	59.4	-4.4	21.3
7	E	1	0.75	3	4	85.5	59.9	-2.8	21.6
8	E	1	1	4	3	84.3	60.9	-1.1	19.9
9	AB	1.5	n/a	7	5	94.9	75.7	-6.6	20.8
10	B	1.5	n/a	7	3	94.5	74.7	-6.4	18.7
11	A	1.5	n/a	8	3	83.5	64.7	1.3	18.9
12		1.5	n/a	8	2	83.3	64.2	1.3	18.0
13	E	1.5	0.5	3	3	85.3	61.1	-2.1	19.6
14	E	1.5	0.75	3	3	86.1	60.6	-3.1	19.7
15	E	1.5	1	4	2	84.5	61.6	-1.0	18.2
16	E	1.5	1.25	4	2	84.8	61.6	-1.3	18.3
17	E	1.5	1.5	6	2	83.1	62.5	0.8	18.3

† blue and red entries indicate jobs with and without IIF, respectively

† flag-node and IIGE unless noted: **A** = all-node; **B** = IIBE. **E** = EAGGN ($L_{FD} = L_D$). **G** = GGN ($L_{FD} > L_D$).

5.13 Results for anomaly A02. Target A02 is a 60-mm, 1.3-kg M49 mortar round, which the AEC emplaced nose-up at a slight inclination of –9 deg and a depth to center of 61 cm (Figure O1, Table 1). The A02 anomaly (Figure 16) was input to 35 jobs (Tables 28 and Tables O2-O4 in Appendix O).

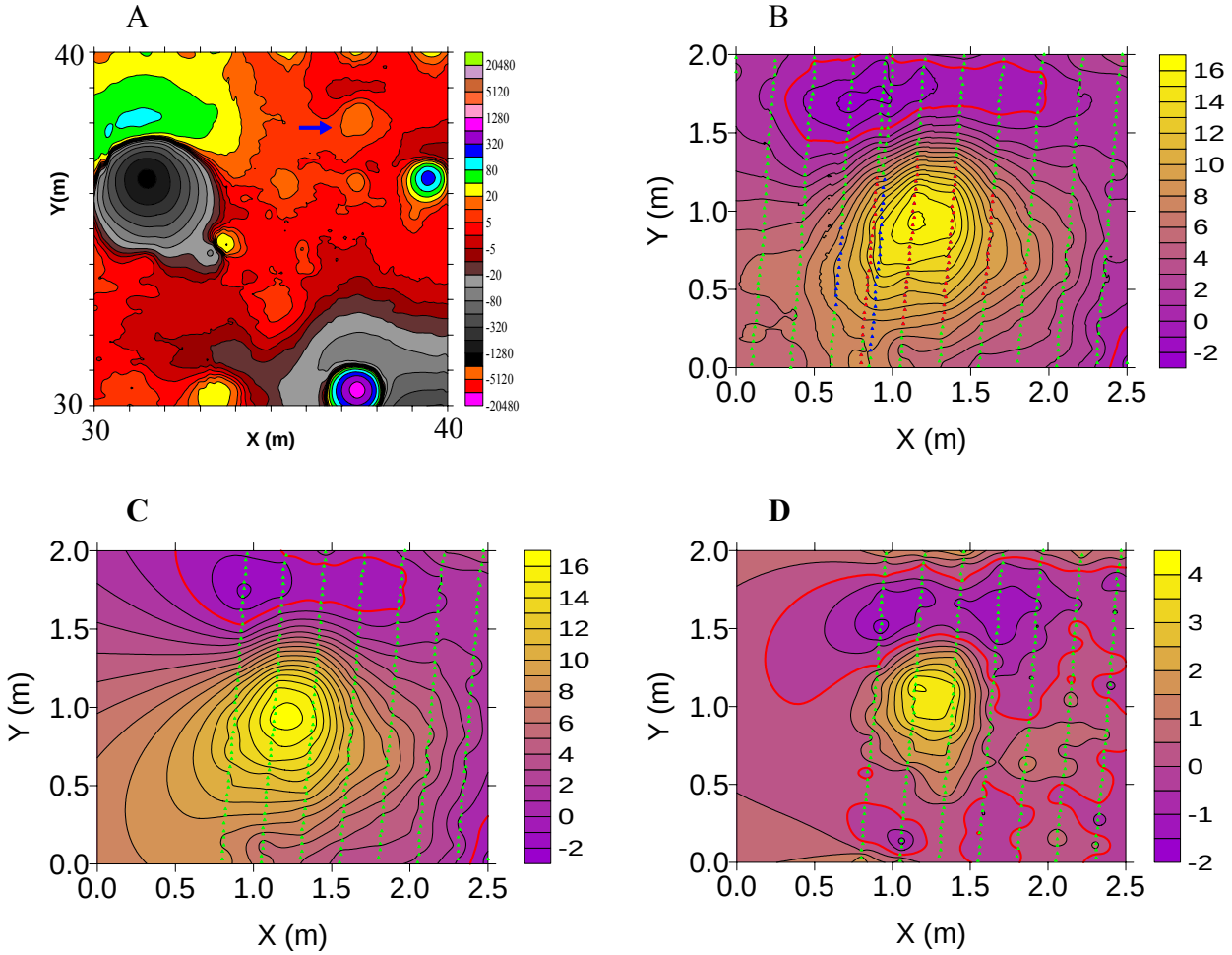

Figure 16. A. Regional setting of anomaly A02 (blue arrow) with contours at 0 and $\pm 2^n \cdot 5$ nT, where n is a non-negative integer. **B**. The A02 anomaly with flagged nodes for single-swath, peak-only inversion (red triangles), for multi-swath, peak-only inversion (red and blue triangles) and for unrestricted flag-node inversion (all triangles); 1-nT contour interval. **C**. The A02 anomaly defined by a single MTADS swath. **D**. Single-swath EAGGN filtered anomaly (L_F = 1.25 m); 0.5-nT contour interval.

Table 28 shows a comparison of dipole positions with positions of the center and ends of the mortar round. The dipole positions are accurate, within a few centimeters, of the target center, except for the non-IIF, single- and multi-swath, peak only inversions (Figure 16B; jobs 24-25 and 28-29). For these peak-only jobs, $7 \leq \Delta_C \leq 16$ cm, and $-14 \leq (Z\text{-}ZC) \leq -4$ cm. By contrast, for single-swath EAGGN IIF inversion with L_F equal to 1.25 m and a 2.5 x 2-m data window (job 32), Δ_C is equal to 4 cm and $(Z\text{-}Z_C)$ is equal to 3 cm. The EAGGN-filtered A02 anomaly (Figure 16D) is very compact and nicely separated from the effects of neighboring anomalies and

regional fields. The single-swath IIF dipole positions and orientations vary slightly for filter sizes in the range $0.75 \leq LF \leq 2$ m (jobs 30-35; tables O2-O3). A02 jobs derived flag-node IIF from symmetric, square ($L_{FY} = L_{FX}$), $F_{CP\text{-}PYRAMID}$ filters.

Some swath-overlap noise is apparent in the A02 anomaly (Figure 16B). This occurrence may be related to the differences observed between results for single- and multi-swath peak-only inversions. For single-swath EAGGN IIF inversions with $1 \leq L_F \leq 2$ m (jobs 31-35), $25.3 \leq \theta \leq 28.8$ deg (Table 29). These deviation angles are consistent with UXO having little remanence. Tables and figures, allowing comparisons of results for the 35 inversions, are presented in Appendix O.

Table 28. A02 Dipole and mortar-end offsets from the target's center (UTM coordinates, X_C, Y_C). L_F = filter size, L_D = data window size, Δ_C = horizontal displacement from target center.†

job	description	L_F (m)	L_D (m)	Δ_C (cm)	$X\text{-}X_C$ (cm)	$Y\text{-}Y_C$ (cm)	$Z\text{-}Z_C$ (cm)
	base of mortar round				-8	8	2
2	Flag-node, IIBE	n/a	2	6	-5	-4	-2
4	flag-node, IIGE	n/a	2	5	-6	-3	-3
24	Peak-only, IIBE	n/a	2.5#	16	-13	-10	-11
25	Peak-only, IIGE	n/a	2.5#	11	-9	-7	-4
28	Peak-only, single-swath, IIBE	n/a	2.5#	10	-7	-7	-14
29	Peak-only, single-swath, IIGE	n/a	2.5#	7	-2	-6	-10
5	EAGGN	0.75	2	5	-4	4	-5
6	EAGGN	1	2	5	-4	3	-3
7	EAGGN	1.25	2	4	-4	2	-2
8	EAGGN	1.5	2	4	-4	2	-1
9	EAGGN	1.75	2	4	-4	2	-1
10	EAGGN	2	2	4	-4	0	0
30	single-swath EAGGN	0.75	2.5#	5	1	4	3
31	single-swath EAGGN	1	2.5#	5	1	4	3
32	single-swath EAGGN	1.25	2.5#	4	0	4	3
33	single-swath EAGGN	1.5	2.5#	4	0	4	3
34	single-swath EAGGN	1.75	2.5#	3	0	3	2
35	single-swath EAGGN	2	2.5#	3	0	3	2
	nose of mortar round				8	-8	-2

† blue and red entries indicate inversions with and without IIF, respectively
# $L_{DY} = 2$ m

Table 29. A02 job and dipole parameters: job number and type, data window size, filter size, horizontal and vertical displacements of the dipole from the target center, deviation angle, and the dipole's declination, inclination, and strength.†

Job	Type†	L_D (m)	LF (m)	ΔC (cm)	$Z-Z_C$ (cm)	θ (deg)	δ (deg)	Ψ (deg)	M ($mA \cdot m^2$)
2	IIBE	2	n/a	6	-2	30.3	0.8	37.7	60.7
4	IIGE	2	n/a	5	-3	33.5	7.1	35.5	59.7
24	IIBE ▲	2.5#	n/a	16	-11	40.2	28.5	34.2	36.2
25	IIGE ▲	2.5#	n/a	11	-4	35.6	28.4	39.3	51.1
28	IIBE ▲§	2.5#	n/a	10	-14	32.1	14.4	38.9	29.3
29	IIGE ▲§	2.5#	n/a	7	-10	25.0	15.1	46.4	34.2
5	EAGGN	2	0.75	5	-5	34.2	10.7	35.5	52.6
6	EAGGN	2	1	5	-3	33.0	9.8	36.5	58.8
7	EAGGN	2	1.25	4	-2	31.3	8.3	38.0	61.8
8	EAGGN	2	1.5	4	-1	31.6	6.5	37.4	65.3
9	EAGGN	2	1.75	4	-1	32.1	4.9	36.6	65.6
10	EAGGN	2	2	4	0	32.0	5.5	36.7	68.5
30	EAGGN §	2.5#	0.75	5	3	23.2	-16.5	44.2	72.1
31	EAGGN §	2.5#	1	5	3	25.2	-16.4	42.2	72.3
32	EAGGN §	2.5#	1.25	4	3	26.3	-14.1	41.0	72.3
33	EAGGN §	2.5#	1.5	4	3	27.6	-13.4	39.6	72.4
34	EAGGN §	2.5#	1.75	3	2	27.4	-11.3	39.9	68.8
35	EAGGN §	2.5#	2	3	2	28.8	-9.7	38.5	69.2

† blue and red entries indicate inversions with and without IIF, respectively
▲ peak-only inversion
§ single-swath inversion
# L_{DY} = 2 m

5.14 Applications to Chongcho Lake and Yeosu surveys. Some results of UXOPAC inversions applied to Chongcho Lake and Yeosu marine survey in Korea are presented in Appendices A and B, respectively. Appendix A is a reformatted copy of a SAGEEP 2006 Proceedings paper (René et al., 2006) it includes an application of the EAGGN filter as a pre-inversion filter only for the sparse data of Chongcho Lake. Figure A11 is appended to show the results of "profile-adaptive" IIF inversion applied to Chongcho Lake (Park et al., 2002), which preceded this SEED project. Appendix B shows some data from the Yeosu archaeological marine magnetic survey near the south coast of Korea (René and Kim, 2005). It includes an example of multi-dipole inversion and dipole stripping.

5.15 Results with respect to enumerated technical objectives. Specific technical objectives (section 2.3) and results are presented in succession:

1. Develop and use IIF, and compare various filters for IIF, to more accurately locate and determine the dipole strength and magnetic orientation of UXO and similar magnetic sources for a variety of conditions of noise, residual regional fields, and overlapping fields of nearby magnetic sources in gridded and profile data using both real and synthetic data;

Results**:** Improved accuracy with IIF inversion applied to data was demonstrated for several APG BTA anomalies using both for all-node for the all-node option (gridded data) and for the flag-node option (profiles defined at grid nodes nearest to measurement stations). Comparison of non-IIF and IIF inversion used the pre-inversion de-median filter applied by others as a standard procedure. Single-swath inversion with and without IIF was developed for applications where swath-overlap noise occurred. Multiple possible causes for such noise were considered but a definitive explanation was beyond the scope of the SEED project. Comparisons of single- and multi-swath inversions suggest that single-swath IIF is a useful tool. Since they are non-linear, short de-median filters and the total gradient, or analytic signal are unsuitable as IIF. On the other hand, a very long filter cannot be used as an IIF either so small IIF filters that significantly distort the target field are used and the GGN filters were invented to accommodate flag-grid data as part of this SEED project. The x-then-y high-pass filter demonstrated that extreme distortion of the target field is properly accommodated by IIF, however, more conventional 2D IIF are preferred. The EAGGN and EAGN filters accommodate even irregular edges and corners of surveys.

2. Stack and modify magnetic fields in test areas with seeded targets to better model overlapping fields and difficult background fields, and economically provide new test data for comparisons of inversion algorithms.

Results: The anomaly stack used with anomaly K09 (section 5.7, Appendix I) demonstrated the accurate recovery of the vector dipole moment and dipole position using IIF after introduction of "synthetic neighbors" by moving anomalies northward by 14 m. The value of the APG BTA data was thus enhanced. The addition of a synthetic background field to anomaly B01 (section 5.8, Appendix J) demonstrated the success of EAGGN IIF in overcoming extreme background noise in a difficult environment of anomaly truncation by an artificial survey edge.

3. Use IIF to eliminate the need for or enhance effectiveness of the processing steps of subtracting base-station diurnal variations, heading corrections, and estimating and subtracting regional fields.

Results: The 2D IIF filters clearly remove background fields more effectively than the de-median filter which must avoid distortion of the target anomalies. Profile-adaptive IIF was previously used in profile marine magnetic data (Park, et al., 2002) to eliminate the need for heading corrections and base-station corrections, which were not available during part of the survey. For land UXO data such as the MTADS APG survey; however, 2D IIF was used to enhance or supplement the effects of the de-median filter and other pre-inversion processing in order to attenuate effects of residual regional fields. In the event that pre-processing or measurement

errors, including positional errors, produced swath-overlap noise, single-swath IIF can often be used. The method of IIGE was developed as a diagnostic tool to help indicate the need for IIF although it can also be used to improve non-IIF inversions where a constant-gradient background field occurs and the data window is not too small.

4. Design IIF filters to accommodate variable target source depths, survey edges, and data gaps.

Results: Originally it was conceived that all-node filters could be modified at data edges by cascading zero-dc, asymmetric 2D filters at edges of data gaps or survey edges. Such filters would be gradient-nulling. Implementation would have been complicated however. Fortunately, the EAGN and EAGGN filters were invented instead, as part of this SEED project. These high-pass gradient-nulling filters adapt automatically to any kind of data gap or edge including irregular edges. The GGN and EAGGN filters also allow use of the flag-node option, which eliminates concerns about data interpolation near data gaps or over very shallow targets. With convenient flag-grid software developed for UXOPAC, one can interpolate or extrapolate data onto a regular grid and then input a file of the original magnetometer stations to automatically flag nodes for use. Editing data can also "turn off" selected elements of the flag-grid array on the basis of spatial position, to produce custom (non-rectangular) data windows, and/or based on values for peak-only or trough-only inversions. As a bonus, it is often convenient to specify an EAGGN filter by simply allowing the filter application window to be equal to the inversion data window.

5. Use inversion-derived background estimates to guide or facilitate applications of (a) IIF, (b) successive inversions to strip away the effects of overlapping dipole fields, and (c) multi-dipole inversion.

Results: During this seed project dipole stripping, multi-dipole inversion, and evaluation of the background estimates were applied to data of the Yeosu marine magnetic survey (Figures 3-5; Appendix B) and to APG BTA data (René and Kim, 2005); however, a coordinate transform "bug" was found in the UXOPAC software subsequent to that early work on APG data. IIF was generalized to include IIGE for both single- and multi-dipole inversions (Section 4.4). Several examples of background estimates in applications of IIF are presented in section 5 and the corresponding Appendices for individual anomalies.

6. Automatically pick dipole search windows for single- and multiple-dipole inversions.

Results: Centers of dipole search windows were positioned relative to anomaly extrema or to the inversion data windows for single-pass inversions or for the first dipole search window in multi-pass inversions. Multi-pass inversion was developed to more efficiently obtain the best dipole by automatically positioning successive search windows relative to the best fit obtained in a previous search. The code was also modified to allow search increments greater than the grid interval, which is particularly useful in the multi-pass option (section 4.4)

7. Use parallel processing for efficient inversion.

Results: With larger data windows, large dipole search windows, larger IIF filters, and smaller grid intervals, computational efficiency becomes a significant concern. Accordingly, program profiles were run on the KISTI supercomputer (Appendix D) and suggestion for changes were generously made by personnel at KISTI that were helpful to APG BTA inversions both at KISTI and on a laptop computer without benefit of parallel processing. Tests at KISTI also revealed some non-standard code that was replaced in order to increase portability. Many inversions run in Korea were helpful to the project. After modifying UXOPAC code for greater efficiency in single-pass inversions, the multi-pass inversion method was developed to facilitate applications without parallel processing. All of the inversion results shown in this report were obtained with a 1.6 GHz laptop computer.

6. Conclusions and Recommendations

6.1 Practical uses of this project's results. After a UXO magnetic survey has been made, the geophysical interpreter must extract useful information from a large number of anomalies. Pre-processing is applied and anomalies are selected for inversion, often with the aid of the total gradient (analytic signal). The interpreter then uses full point-dipole inversion to extract the x-, y-, z- coordinates and the vector dipole moment. Upon the accuracy of inversions, hang the decisions that are subsequently made as to whether the target is likely UXO, which must be excavated, or clutter, which can be left in the ground. The projected cost of UXO surveys and excavation at contaminated sites is tens of billions of dollars. The potential savings by making correct distinctions between UXO and clutter are considerable.

Where, as commonly is the case, geologic noise or overlapping fields of neighboring UXO or clutter are present, the interpreter's task is more difficult. Commonly, to lessen effects of interference by neighboring anomalies the interpreter may select a small data window. In that window, the target's anomaly is relatively large by comparison to the background field. Unfortunately, a small background field that is not constant in that window may result in significant inaccuracies in the inversion results that will later cause the target to be misidentified as a false positive (UXO) or false negative (clutter). For small anomalies, the correlation coefficient may be particularly large despite the greater effects of disturbance by its neighboring anomalies or geologic noise. The de-median filter is generally relied on to remove some low-frequency components of the regional field but it is intentionally designed to have minimal distortion on the target fields input to inversion. The residual background noise cannot be attacked because it has frequency content that overlaps that of the target fields to a significant degree.

High-pass IIF, developed through this SEED project, takes a different approach. The target's anomaly is intentionally distorted then compensated for within the inversion. Using IIF, the interpreter can use larger data windows and generally have assurance that more accurate inversions can be obtained than for small-window non-IIF inversions. The task of the interpreter is thus reduced with respect to selecting a data window and the IIF inversion is often significantly more accurate as shown by the experiments of this SEED project using APG BTA UXO data.

In some cases, small target anomalies may be so buried by larger neighboring anomalies of UXO or clutter, or by background noise of geologic origin, that there are no closed contours clearly defining the target anomaly. Use of the analytic signal facilitates detection of the anomaly and even allows a partial inversion without determination of the magnetic dipole orientation. By contrast, high-pass IIF, developed as part of this SEED project, allows the interpreter to perform full and often accurate point-dipole inversions on such highly disturbed or buried target anomalies and to thereby allow a more confident discrimination of the target as possible UXO or clutter.

The EAGGN, EAGN, and GGN IIF, invented specifically for this SEED project, are particularly easy to use and they automatically adapt to supra-nominal data gaps, corners and edges of survey areas as well as to user-imposed data windows. Development of guidelines to selecting the filter

sizes should further lessen the interpreter's task. Non-IIF IIGE inversions were developed and used here as a diagnostic tool for apparently well-isolated anomalies to indicate the need for IIF by comparison of results with the standard non-IIF IIBE inversion. In the case of well-isolated anomalies, IIF does not alter the inversion results. Results of non-IIF IIGE inversions may be more accurate than the standard inversions in the case of nearly constant-gradient background fields but generally, IIF inversions should be preferred.

Many sources in UXO surveys are very shallow and UXOPAC inversions should then use very fine grid intervals, on the order of 1 cm. Generally, the flag-node option may be preferred over the all-node option since interpolations will not be exact. Accordingly, either EAGGN or GGN IIF options might be used. Whether EAGGN or GGN filtering is preferred may depend on the choice of generating symmetric filters, $F_{CP\text{-}BOXCAR}$, $F_{CP\text{-}PYRAMID}$, or other tapered filters; the choice of filter dimensions, choice of inversion data windows, and computational efficiency. For single-swath IIF, EAGGN filtering is generally applicable. The most critical parameters are likely to be the size of the filters as indicated by dimensions L_{FX} and L_{FY}. If the x-direction is approximately along a cross-line direction that is less densely sampled than in the along-line direction, then it is possible that L_{FX} should exceed L_{FY} in order to maintain sufficient distribution of samples in each direction. L_{FX} and L_{FY} should be small enough to attenuate noise or resolve overlapping anomalies so that IIF is effective. In the case of EAGGN IIF inversion of APG BTA data, with a cross-line sampling interval of 0.25 m, it was often necessary that L_{FX} exceed 0.5 m. In general, filter dimensions can be significantly smaller than the depth of the target.

Because EMI and magnetic UXO surveys are complementary to each other in classification of targets as UXO or clutter, both may be run in a given area. Furthermore, in some cases both surveys may be run simultaneously. Furthermore, helicopter or airborne magnetic and EMI surveys have been used for wide-area assessment of potentially UXO contaminated areas. Marine or lake UXO surveys are also being used. IIF has potential applications to such airborne and marine survey including vertical gradient magnetometry. The UXOPAC inversion is adaptable to inversion of 3D data, and 3D IIF are feasible in UXOPAC. Furthermore, preliminary to this SEED project, "Profile adaptive" adaptive IIF was developed for application to marine magnetic profiles. That capability remains in UXOPAC and is available to further development that may be quite useful to land, airborne, or marine UXO surveys. Somewhat related to "profile-adaptive" IIF, single-swath IIF has been developed as part of this SEED project. It may facilitate application and accuracy of IIF inversions in the common case where swath-overlap noise occurs in land towed array surveys. Furthermore, the yet undeveloped 3D IIF may be used in such surveys where a tiltmeter and other means are used to provide accurate elevations above the target source of individual magnetometers.

In summary, IIF and other methods developed as part of this SEED project can help the interpreter perform more accurate full point-dipole inversions that are critical to the essential goal of UXO surveys to detect UXO and to distinguish between UXO and clutter prior to excavation. Transitioning of IIF, and perhaps other portions of UXOPAC, to an existing UXO software suite is feasible and should provide the geophysical interpreter with some powerful and much needed tools even as the capabilities of field acquisition continue to increase at impressive rates. It is recommended that further development and transitioning of IIF should proceed.

6.2 Why high-pass IIF works for UXO. Inversion selects an inverse model from among test models based on the best fit of a test model's anomaly to the observed target's anomaly plus noise. In UXO magnetic field surveys, the relevant noise is principally low-frequency background noise, often of geologic origin, and the overlapping fields of neighboring UXO and clutter. Either the central regions (cores) or the tails of neighboring anomalies may overlap the core of a target anomaly depending on the spacing and relative depths of the target and neighboring sources. Where the anomaly of much deeper-sourced neighbor overlaps the target's anomaly the effect is similar to that of low frequency background noise of geologic origin.

High-pass IIF is generally effective for UXO surveys because:

- The same filter is applied to the test models' anomalies and the target anomaly plus noise.

- Point-dipole fields have relatively high-frequency components of a spatially varying spectra concentrated in their cores instead of their tails.

- The attenuated low-frequency tails of the best-fit test model's anomaly contribute little to the correlation coefficient where they overlap the attenuated low-frequency background noise low- or the attenuated low-frequency tails or the high-frequency cores of filtered neighboring anomalies.

- The filter "sharpens" or compacts the cores of target, neighbor, and test models' anomalies while suppressing their tails.

- Provided a neighboring source is not both too close (cores overlap) and at similar depth as the target, then contributions to the correlation between the filtered best fit test model's anomaly and the filtered input is mainly the result of correlation between the core of the filtered best-fit test model's anomaly and the core of the filtered target's anomaly. That is, for test dipoles in the vicinity of the target dipole, the lack of correlation between a neighboring filtered anomaly and the tails of the test dipole anomalies decreases the correlation coefficient by a nearly constant amount with respect to test dipole position. This lack of correlation does not significantly influence, therefore, the least-squares selection of the best-fit dipole. Additional discussion of this effect in the case of anomaly A07 and its neighbor anomaly B08 was presented in section 5.11.

In a sense, because it concentrates the effects on the correlation coefficient to the core of the target anomaly, high-pass IIF is analogous to small-window inversion. IIF is so much more effective, however, because it lessens effects of background fields within the core of the target field. Furthermore, the portions of the target anomaly on the periphery of the target's anomaly core are incorporated into the inversion as input to the filtered field; they are not simply trimmed away as may be the case in small-window inversion. Where a target and neighboring source are very close to each other (horizontally) and at approximately the same depth, the cores of the target and neighboring anomalies will overlap and have similar frequency content (spectra). In that case, single-dipole high-pass IIF may not succeed and multi-dipole inversion, including perhaps IIF multi-dipole inversion, would then be required.

6.3 Transitioning status. Concepts and examples of applications developed through this SEED project have been presented in this Final Report, four proceedings papers, a technical journal and in published abstracts (Appendix R).A paper on IIF applications to APG BTA data has also been accepted for publication and presentation at the Symposium on the Application of Geophysics to Engineering and Environmental Problems (SAGEEP 2007). Oral or poster presentations of project results were given at the following symposia and colloquia:

- 2005 Partners in Environmental Technology Technical Symposium and Workshop
- Symposium on the Application of Geophysics to Engineering and Environmental Problems (SAGEEP 2006; two papers);
- Joint Conference of Korean Geological Survey and Korean Society of Exploration Geophysicists (2006),
- Research Institute for Development of Earth Resources (RIDER), Kangwon National University (2006),
- Korea Polar Research Institute (KOPRI) in 2006,
- Korea Ocean Research and Development Institute (KORDI) in 2006
- 2006 Partners in Environmental Technology Technical Symposium and Workshop

6.4 Transitioning plans. Presently IIF and other features developed during this SEED project are part of a non-commercial package, UXOPAC, designed for development and testing. Relevant software in UXOPAC should be integrated with a UXO software suite maintained and supported by others for the general benefit of the UXO community.

In transitioning IIF algorithms, two possibilities would arise (1) adjusting IIF algorithms to fit the commercial inversion process, or (2) incorporating the basic UXOPAC inversion with IIF in a working package in the commercial inversion process. The second option might be the easiest to implement. Use Graphical User Interface of the same or similar control parameters as in the existing commercial inversion would be convenient for users.

Future work (in non-chronological order) would:

- Integrate IIF inversion and other UXOPAC software with existing commercial software
- Partner with others to demonstrate improved inversion accuracy using IIF
- Publish and present results in journals, reports, symposia, and technical meetings
- Develop 3D IIF inversion capabilities by modifying UXOPAC inversion and GGN IIF code
- Develop IIF capabilities for vertical gradiometry and aeromagnetic data
- Investigate possible IIF applications to rotor noise in helicopter surveys
- Develop and test IIF capabilities for dense- or sparse-coverage marine or lake UXO surveys
- Develop and test new IIF concepts and guidelines for applications
- Investigate swath-overlap noise and appropriate remedies
- Modify multi-pass UXOPAC inversion to better simulate the gradient method
- Develop efficient single-swath and/or “profile-adaptive” IIF using track and swath numbers
- Further explore relative merits of all-node and flag-node options for inversion and IIF
- Explore relative merits of “profile-adaptive” and 2D IIF for various survey types

7. REFERENCES

AETC, Incorporated, 2002, Matched filter processor for detection and discrimination of unexploded ordnance: OASIS Montaj integration: VA-3499-009-02-TR

Barrow, B., Khadr, N., DiMarco, R., and Nelson, H. H., 1996, The combined use of magnetic and electromagnetic sensors for detection and characterization of UXO: Proceedings of the Symposium on the Application of Geophysics to Environmental and Engineering Problems (SAGEEP 1996), p. 469-477.

Bell, T., Jones, R., Soukup, J., and Puc, B., 2001, Matched filter processor for detection and discrimination of unexploded ordnance: AETC Final Report VA-095-050-TR-01, November 2001.

Beran, L. S., Oldenburg, D. W., and Billings, S. D., 2005, Statistical classification for discrimination of unexploded ordnance: a tutorial: FastTIMES, Environmnetal and Engineering Geopysical Society, Summer 2005, Vol. 10, No. 2, p. 11, 13, 15, and 17.

Billings, S. D. and Herrmann, F., 2003, Automatic detection of position and depth of potential UXO using continuous wavelet transforms: Proceedings of SPIE, Vol. 5089, pp 1012-1022.

Billings, S. D., Pasion, L. R., and Oldenburg, D. W., 2002a, Discrimination and identification of UXO by geophysical inversion. Phase II: Inversion of total-field magnetics: Technical report, USACE Waterways Experiment Station, April 2002; Geophysical Inversion Facility, Univ. of British Columbia, Canada.

Billings, S. D., Pasion, L. R., and Oldenburg, D. W., 2002b, UXO discrimination and identification using magnetometry: Proceedings of the Symposium on the Application of Geophysics to Environmental and Engineering Problems (SAGEEP 2002).

Billings, S. D., Pasion, L. R., and Oldenburg, D. W., 2003, Discrimination and classification of UXO using magnetometry: Inversion and error analysis using robust statistics: Proceedings of the Symposium on the Application of Geophysics to Environmental and Engineering Problems (SAGEEP 2003).

Blackman, R. B., and Tukey, J. W., 1958, The Measurement of Power Spectra, Dover Publications, New York, 190 pages.

Butler, D. K., 2003, Implications of magnetic backgrounds for unexploded ordnance detection: Journal of Applied Geophysics, Vol. 54, p 111-125.

ESTCP-ITRC-SERDP, 2006, Survey of munitions response technologies: Environmental Security Technology Certification Program (ESTCP), Interstate Technology & Regulatory Council (ITRC), Strategic Environmental Research and Development Program (SERDP), June, 2006, 215 pages.

Gamey, T. J., 2006, Collection and analysis of 3D magnetic data for UXO: Journal of Environmental and Engineering Geophysics, Vol. 11, Issue 3, p. 185-196.

McDonald, J. R., and Grimm, Robert, 1998, Model-based data fusion and discrimination of UXO magnetometry and EM surveys: SERDP Project UX/1092/8, Annual Report – FY 1998.

Nelson, H. H., Altshuler, T. W., Rosen, E. M., McDonald, J. R., Barrow, B., and Khadir, N., 1996, Magnetic modeling of UXO and UXO-like targets and comparison with signatures measured by MTADS: Proceedings 1996 UXO Forum

Nelson, H. H., McDonald, J. R., and Robertson, R., 1997, Multi-sensor ordnance signatures for algorithm development and model training: Proceedings of the Symposium on the Application of Geophysics to Environmental and Engineering Problems (SAGEEP 1997)

Oldham, C. H. G., 1967, The (sin x)/x•(sin y)/y method for continuation of potential fields: Society of Exploration Geophysicist's Mining Geophysics, Volume II, Theory; p. 591-605.

Park, C. H., René, R. M., and Kim, K. Y., 2002, Location of magnetic dipoles in Chongcho Lake, Republic of Korea: an application of the SOAPFI (Shape-of-anomaly potential field inversion) program: Proceedings of the Symposium on the Application of Geophysics to Environmental and Engineering Problems (SAGEEP 1997).

Pasion, L. R., Billings, S. D., Oldenburg, D. W., 2003, Joint and cooperative inversion of magnetic and time domain electromagnetic data for the characterization of UXO: Proceedings of the Symposium on the Application of Geophysics to Environmental and Engineering Problems (SAGEEP 2003).

Rao, B. S. R., Prakasa Rao, T. K. S., and Krisha Murthy, A. S., 1977, A note on magnetization of magnetized spheres: Geophysical Prospecting, Vol. 25, No. 4, p. 746-775.

René, R. M., 1997, Gravity inversion using a "shape-of-anomaly" method: developments in three-dimensional modeling and application to gravity over an abandoned underground limestone mine in southeastern Indiana: Proceedings of the Symposium on the Application of Geophysics to Environmental and Engineering Problems (SAGEEP 1997), p. 549-558.

René, R. M., 1999, Three-dimensional "shape-of-anomaly" inversion of gravity and magnetic fields: Expanded Abstracts of the Technical Program, Society of Exploration Geophysicists 56th Annual International Meeting and Exposition, 4 p.

René, R. M., 2000, Three-dimensional "shape-of-anomaly" gravity inversion with an application to gravity over an abandoned underground limestone mine in Indiana: Journal of Environmental and Engineering Geophysics, Vol. 5, No. 1, p. 17-26.

René, R. M., Park, C. H., and Kim, K. Y., 2004, Intra-inversion filtering for least-squares inversion of magnetic dipole fields in the presence of residual non-dc background magnetic fields and overlapping dipole fields: Proceedings of the Symposium on the Application of Geophysics to Environmental and Engineering Problems (SAGEEP 2004), CD, p. 1315-1331.

René, R. M., and Kim, K. Y., 2005, Intra-inversion filtering for use of magnetic fields to locate and characterize magnetic dipoles for unexploded ordnance (UXO) cleanup: abstract and Munitions Management Poster Number 143, Partners in Environmental Technology Technical Symposium and Workshop, SERDP and ESTCP, Washington, D. C., November 29-December 1, 2005.

René, R. M., and Kim, K.Y., 2006, Edge-adaptive and gapped gradient-nulling intra-inversion filters for application to UXO magnetic field surveys: SAGEEP Proceedings, 1710-1724.

René, R. M., Park, C. H., and Kim, K.Y., 2006, Edge-adaptive gapped gradient-nulling filters and inversion of magnetic fields in a lake survey of possible dredging hazards and UXO: SAGEEP Proceedings, 1697-1709.

René, R. M., Kim, K. Y. and Park, C. H., 2006, Magnetic field inversion and intra-inversion filtering using edge-adaptive, gapped gradient-nulling filters: applications to surveys for unexploded ordnance (UXO); Proceedings of Joint Conference of Korean Geological Survey and Korean Society of Exploration Geophysicists, 6 pages (includes abstract in Korean).

Sinex, D. and Li, Y., 2004, Effects of magnetic soils on magnetometry in uxo discrimination problems: Proceedings of the Symposium on the Application of Geophysics to Environmental and Engineering Problems (SAGEEP 2004), CD,

Selstrum, J., 2005, The Defense Science Board provides DOD a roadmap for the future on unexploded ordnance: FastTIMES, Environmnetal and Engineering Geopysical Society, Summer 2005, Vol. 10, No. 2, p. 19, 21, 23, and 25.

Stanley, J. M., Cattach, M. K., Griffin, S. M., Townsend, J., and Helms, L., 2005, Simultaneous magnetic and electromagnetic mapping using sub-audio magnetics: FastTIMES, Environmnetal and Engineering Geopysical Society, Summer 2005, Vol. 10, No. 2, p. 43-45 and 47.

SUTDSPC (Standardized UXO Technology Demonstration Site Program Committee), 2002, Standardized UXO technology demonstration handbook: U.S. Army Environmental Center Aberdeen Proving Ground, Maryland, DTC Project No. 8-CO-160-UXO-010, Report No. ATC-8539, AEC Report No. SFIM-AEC-PC-TR-2002032, 199 pages.

USAEC (U.S. Army Environmental Center), 2005, Aberdeen Proving Ground (APG) Blind Grid, http://aec.army.mil/usaec/technology/apg-blind.pdf (10 Jan. 2006).

Ware, G. H. and Ware, H. A., 1996, Magnetic interpretation by scanning multiple models for best fit: Proceedings of the Symposium on the Application of Geophysics to Environmental and Engineering Problems (SAGEEP 1996), p. 695-700.

APPENDIX A

EDGE-ADAPTIVE GAPPED GRADIENT-NULLING FILTERS AND INVERSION OF MAGNETIC FIELDS IN A LAKE SURVEY OF POSSIBLE DREDGING HAZARDS AND UXO

René, R. M., Park, C. H., and Kim, K. Y.

The following Paper was presented at the Symposium on the Application of Geophysics to Environmental and Engineering Problems (SAGEEP 2006) and published in the Proceedings of that meeting. This paper has been reformatted. The page margins and mathematical symbols have been changed to conform to those of this Final Report. Selected slides from the oral presentation are included at the end of this Appendix with explanations in their figure captions.

Appendix A Figures

A1. Map of depths in Chongcho Lake near Sokcho, Kangwon-do, Republic of Korea ……..... 76
A2. Magnetic field in Chongcho Lake with contours at zero and ± 5 • (2^n) nT. ……. 77
A3. Magnetic field in Chongcho Lake including Anomaly "A".....……... 78
A4. Filtered magnetic field in Chongcho Lake (using 100 x 100-m EAGGN filter ……... 79
A5. EAGGN filtered magnetic field in Chongcho Lake including Anomaly "A" ……..... 80
A6. Magnetic field with interpolations using kriging and minimum-curvature methods …...… 82
A7. Modeled fields and residual fields for inversions of anomaly "A" .....……..... 83
A8. Bull's eye stereographic plots of the projections of magnetic dipole orientations ..….. 85
A9. Magnetic field and analytic signal (total gradient) for the Chongcho Lake survey ……. 89
A10. Model space for UXOPAC inversions ……...… 90
A11. Example of "profile-adaptive" intra-inversion filtering applied to an anomaly ……. 91

Appendix A Table

A1. Anomaly "A" dipole models .....…….. 78

EDGE-ADAPTIVE GAPPED GRADIENT-NULLING FILTERS AND INVERSION OF MAGNETIC FIELDS IN A LAKE SURVEY OF POSSIBLE DREDGING HAZARDS AND UXO

R. M. René, Indiana Geological Survey, Indiana University, Bloomington, IN
Chan Hong Park, Korea Ocean Research and Development Institute, Seoul, Korea
Ki Young Kim, Kangwon National University, Chunchon, Korea

Abstract

A method of modifying a zero-dc symmetric filter to obtain an edge-adaptive gapped gradient-nulling (EAGGN) filter is developed and tested on sparse magnetic field data. These data were obtained in a magnetic field survey on Chongcho Lake in the Republic of Korea to determine possible dredging hazards or impediments including possible unexploded ordnance (UXO). The data are interpolated to a regular grid but only grid points proximate to the observed field stations are flagged for use in inversion. The least-squares inversion simultaneously estimates a modeled magnetic dipole, dc-bias and, optionally, a constant-gradient background (regional) field. The EAGGN filter is applied as a pre-inversion filter here, but is also useful as an intra-inversion filter for other applications including UXO surveys. Bull's eye plots present a stereographic projection of a dipole's orientation onto a plane perpendicular to the earth's field. These help visualize the deviation of a magnetic dipole's orientation from the direction of the earth's field. Deviations of less than 60 deg are consistent with UXO that have been shock demagnetized by firing or impact.

Introduction

In lake or marine magnetic surveys, data are often sparse relative to a regular grid onto which the data may be interpolated to facilitate processing and analysis including inversion. For such data, it may be desired to flag only those grid nodes nearest to measurement stations for filtering, inversion or other processes. A method will be presented here for the modification of zero-dc symmetric filters to application as gradient-nulling filters for data that are sparsely interpolated or gapped. The same procedure also facilitates filter application along regular or irregular bounds of a survey without introduction of significant edge effects or other artifacts. The resultant edge-adaptive gapped gradient-nulling (EAGGN) filter is useful for many purposes including intra-inversion filtering (René et al., 2006).

Least-squares inversion to model a magnetic dipole source can simultaneously estimate dc-bias and a constant-gradient background. For sparse data such as are available in many marine or lake surveys, the inversion may have greater uncertainty than for the case of finely sampled surveys on land using for example carts containing an array of magnetometers for unexploded ordnance (UXO) surveys. Accordingly, it may be desirable to test a range of inversion parameters on such data to estimate the accuracy of results based on their consistency. An example of this procedure will be presented using data from a magnetic survey that was conducted in 2000 on the 1 km^2 Lake Chongcho in the Republic of Korea. That survey was designed to investigate possible

hazards to planned dredging including perhaps UXO. Particular attention is paid to the orientation of a modeled dipole source. Non-UXO are often distinguished from UXO by their greater angles between the estimated dipoles and the earth's field when significant remanence is present. UXO generally have little remanence because of shock demagnetization from firing and impact.

This paper will present the inversion method with some improvements on the method as previously described by René, et al. (2004). The magnetic survey of Lake Chongcho for dredging hazards is then presented and the application of the EAGGN filter is shown. A particular anomaly is selected for tests of the inversion method with and without gradient estimation and with and without pre-inversion EAGGN filtering. Possible reasons for the residual field after inversion are discussed, as is the consistency of magnetic dipole orientation and depth for the various inversions. The bull's eye plot of stereographic projection of a dipole's orientation onto a plane perpendicular to the earth's field is then presented. Following the conclusions, details for the design of EAGGN filters are given in an Appendix.

Inversion method

Least-squares inversion minimizes the sum of squares of the difference between the modeled and observed field values. In the method used here, the input magnetic field, H_{ij}, is either measured at, or interpolated to, grid locations (X_i, Y_j) with constant intervals of Δx and Δy on the measurement surface (Z = 0). The modeled field is that of a point magnetic dipole plus a constant bias, K, and, optionally, one or both of the constant-gradients Gx and Gy in the x- and y-directions, respectively. The simple least-squares method minimizes the objective function, Φ:

$$\Phi_{lmn} = \Sigma_{ij} [D_{ijlmn} + K_{lmn} + G_{xlmn}(X_i - X_o) + G_{ylmn}(Y_j - Y_o) - H_{ij}]^2; \quad (1)$$

where the indices i and j indicate the field point Xi, Yj and the indices l, m, n indicate the source point or test magnetic dipole at location (X_l, Y_m, Z_n) . The coordinates Xo and Yo are arbitrarily chosen at or near the center of the data window. The field of the test dipole in equation (1) is

$$D_{ijlmn} = \Sigma_k (U_{ijklmn} M_{klmn}), \quad (2)$$

where the index k indicates the direction of a unit dipole. U_{ijklmn} is the magnetic field anomaly of a unit-strength dipole at the test magnetic dipole location within a user specified three-dimensional window of possible dipole locations. Formulae for the evaluation of the point dipole anomalies are provided by Rao, et al. (1977). For each location the magnetic moments, M_{klmn}, dc bias, K_{lmn}, and, optionally, one or more of the gradients, G_{xlmn} and G_{ylmn} are obtained as solutions to a system of four, five, or six linear equations that minimize the objective function for east test location. The least-squares solution is then obtained for that test dipole location, X_L, Y_M, and Z_N, which minimizes the objective function Φ. Dipole locations can be tested at fewer than all the grid nodes of the dipole window on a first pass using increments of dipole positions greater than the grid intervals. To avoid the problem of a local minimum, the initial dipole search window must be sufficiently large. A second pass using a smaller window of possible locations refines the optimum solution for the dipole location.

Magnetic survey of Chongcho Lake

The purpose of the Lake Chongcho magnetic survey in the port city of Sokcho, Kangwon-do in the northeast of the Republic of Korea (ROK), was to evaluate impediments to planned dredging of the lake (Park, et al., 2001). Such impediments might include large metallic objects and unexploded ordnance (UXO). Figure 1 shows the depth of the lake as it existed at the time of the magnetic survey in 26-28 November 2000. The northern part of the lake was generally deeper (about 4-6 m) than the southern part. The lake is open to the Sea of Japan (East Sea) and therefore serves as a shallow port. To conform to previous work in this area, Korean Transverse Mercator (KTM) coordinates are used instead of UTM coordinates. Chongcho Lake is in the eastern KTM zone, which uses the base longitude of 129 deg East and the base latitude of 38 deg North.

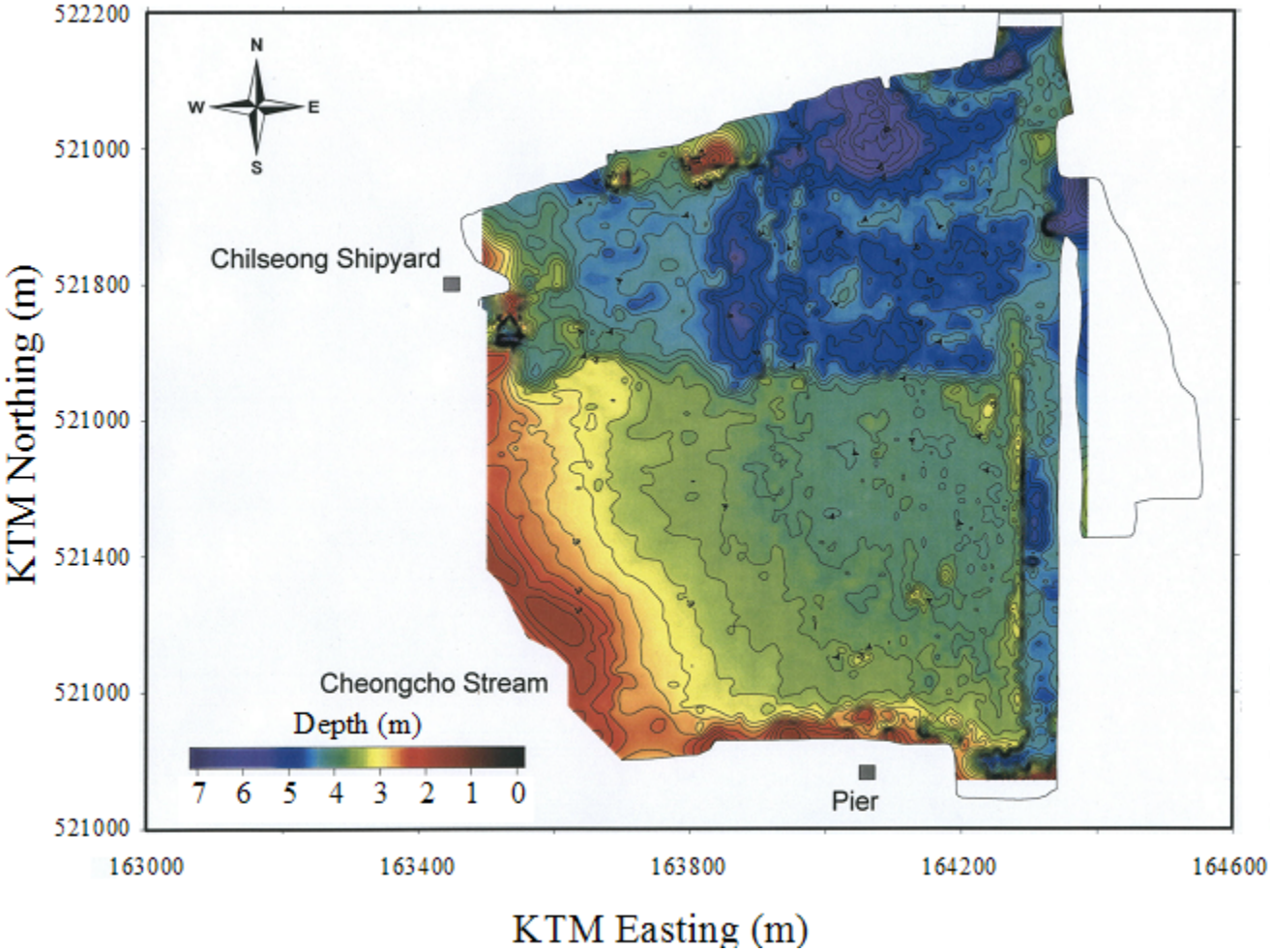

Figure 1. Map of depths in Chongcho Lake near Sokcho, Kangwon-do, Republic of Korea at the time of the magnetic survey. Korean Transverse Mercator (KTM) coordinates are indicated in meters.

Magnetic survey and pre-processing. The magnetic field (Figure 2) was measured along 90 km of profiles with a single magnetometer towed a distance of 10 m behind a 3-ton, 5-m long wooden boat. The magnetometer was towed at a constant depth of 0.5 m maintained with the use of a float. Although latitude and longitude of the GPS receiver were obtained with a precision of about 10^{-6} deg using DGPS, the location of the towed magnetometer was much less precise. The magnetic field was specified with a precision of 0.1 nT. The magnetic field was measured at 1-s intervals using a Marine Magnetics Corporation Sea Spy Overhauser magnetometer. Stations were at approximately 1.6-m intervals along the direction of profile, which was generally approximately north or south, except where the boat was turned at the edges of the lake or in the case of a few east-west tie lines. The profiles were nominally spaced about 10 m apart, but these frequently crossed each other. A stationary G866 Geometrics proton precession magnetometer was used as a base station to measure the magnetic field at 1-s intervals. That base station's field was subtracted from the magnetic survey data.

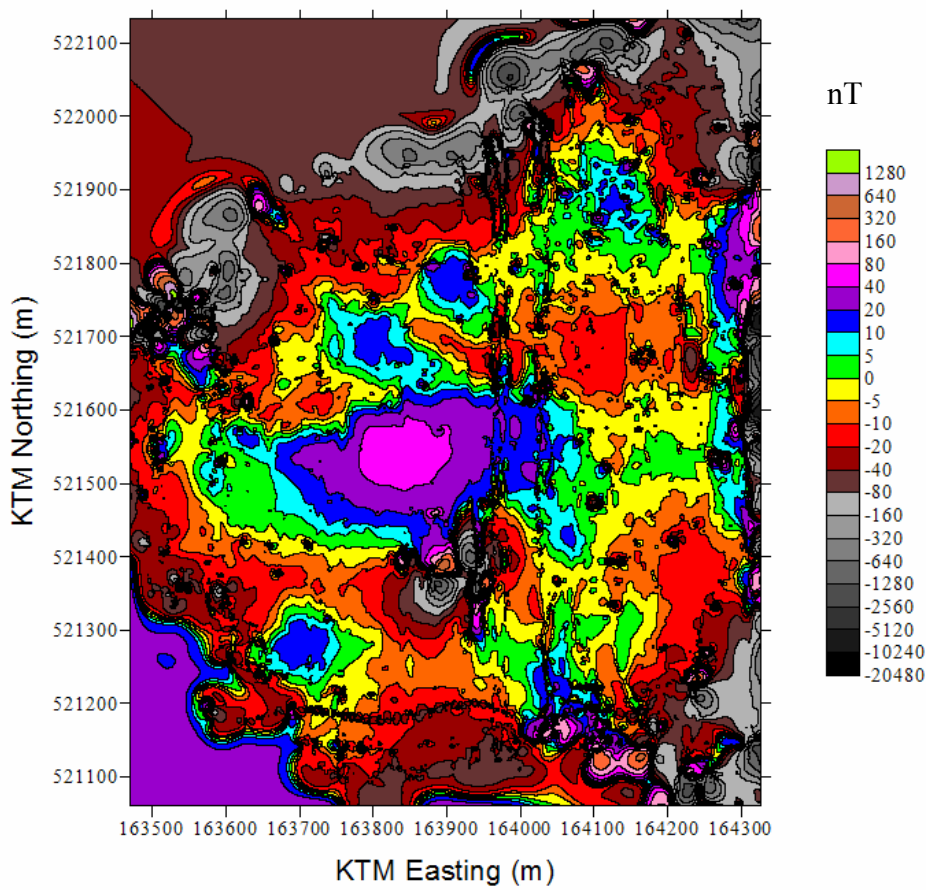

Figure 2. Magnetic field in Chongcho Lake with contours at zero and ± 5 (2^n) nT. The data were interpolated to a 0.5 x 0.5 m grid using the minimum-curvature method. The extrapolated data beyond the edge of the lake are left intact for comparison purposes with the map of filtered data (Figure 4).

Constant corrections for the boat's magnetic field were applied separately to the profiles with southerly and northerly headings. The effect of the boat's field resulted in a difference of about 22 nT between the profiles in opposing directions. The field shown in Figure 2 includes profile segments with headings that are not approximately north or south. One can therefore see the effect of the boat's engine in the string of apparent anomalies along the east-west tie line at an approximate northing of 521180 m in the southern part of the lake (Figure 2). In order to see a range of both small and large anomalies a variable contour interval is used with contours at zero and ± 5 (2^n) nT. The data of Figure 2 were contoured following interpolation to a regular grid with 0.5 m between grid nodes. A 100- x 100-m data window (Figure 3) from those data includes an anomaly identified here as anomaly "A". It appears that this local anomaly is superposed on a regional field with a gradient of roughly 0.4 nT directed to southwest.

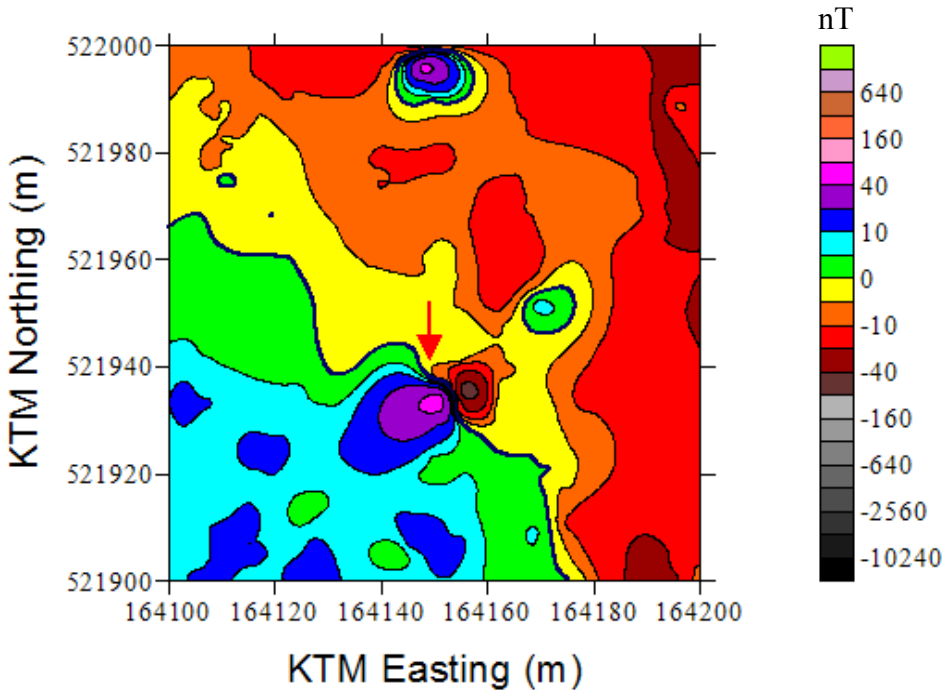

Figure 3. Magnetic field in Chongcho Lake showing a portion of the map of Figure 2. Anomaly "A" (red arrow) is superposed on a regional field with a gradient of approximately 0.4 nT/m to the southwest. Contours are at zero and ± 5 (2^n) nT.

Application of EAGGN Filtering. To attenuate regional fields and enhance the observation and analysis of local anomalies, the data were filtered with a 100 x 100-m edge-adaptive gapped gradient-nulling (EAGGN) filter. The resulting filtered field is shown in Figure 4 where it is apparent that the regional field has been attenuated by this filter. This is also apparent in the corresponding filtered data in the 100- x 100-m window of Figure 5 that includes anomaly "A". The EAGGN filter is defined in Appendix A of this paper and in the text of René and Kim (2006), where it is used for intra-inversion filtering.

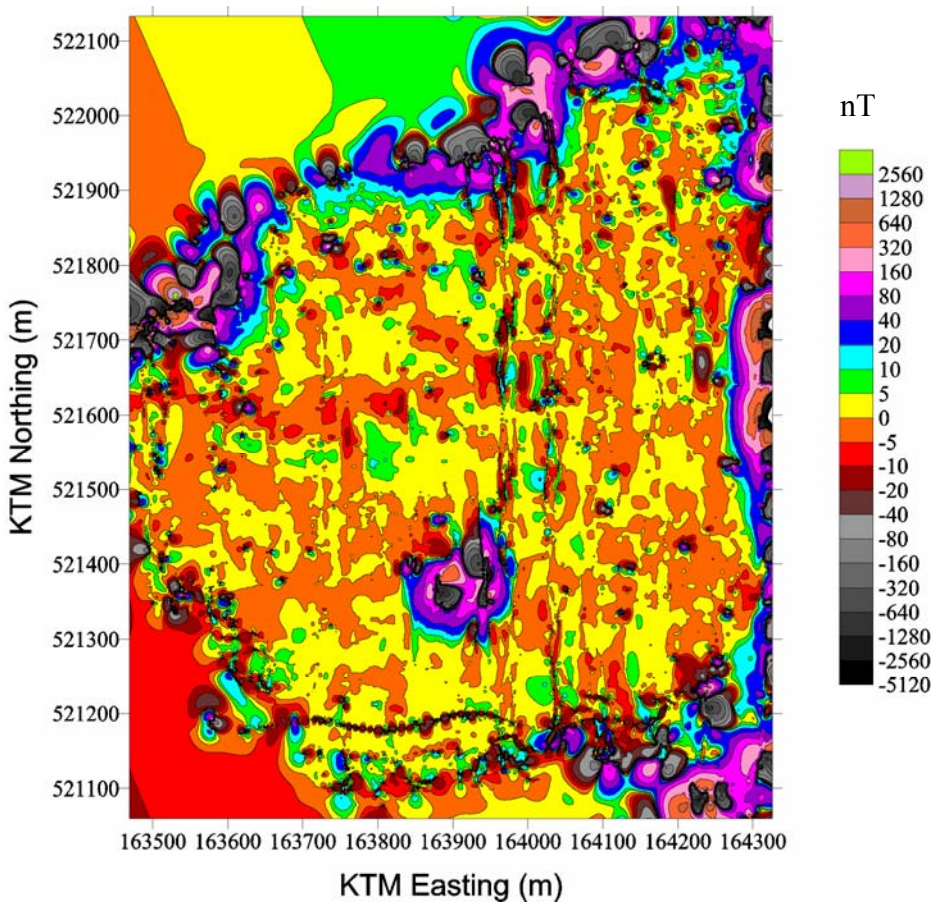

Figure 4. Filtered magnetic field in Chongcho Lake with contours at zero and ± 5 (2^n) nT. A 100 x 100-m edge-adaptive gapped gradient-nulling (EAGGN) filter was applied to data interpolated by minimum-curvature to grid intervals of 0.5 m and flagged for filtering at grid nodes nearest to the measurement stations.

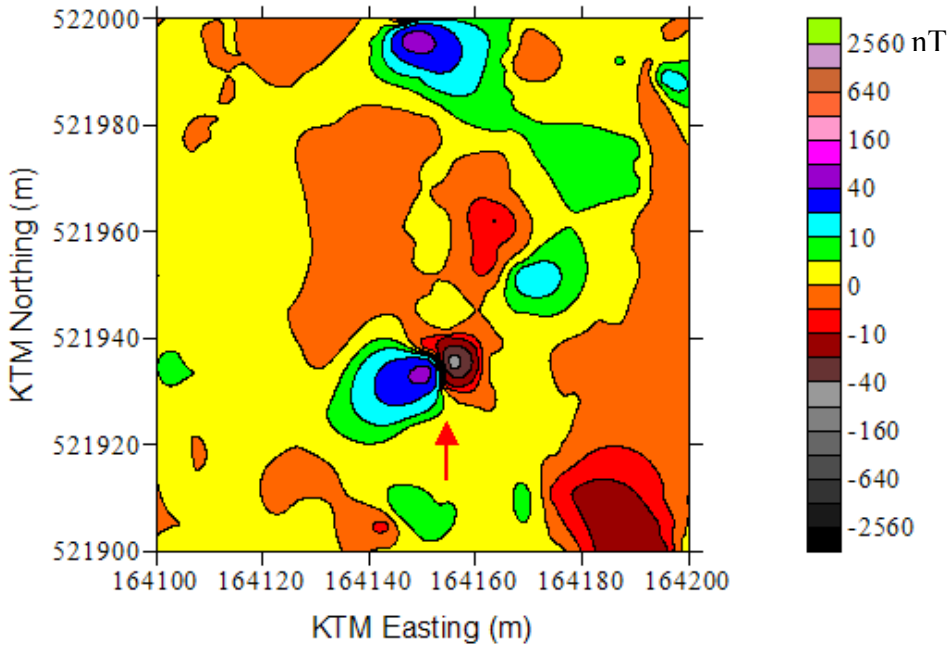

Figure 5. EAGGN filtered magnetic field in Chongcho Lake showing a portion of the map of Figure 4. Inverse models will be obtained for anomaly A (red arrow). Contours are at zero and $\pm 5\ (2^n)$ nT.

In the present application of the EAGGN filter, the profile data at 46,718 stations were first interpolated to a 3,682,105-node grid with intervals of 0.5 m. Interpolated data at 45,625 grid nodes nearest to the measurement stations were flagged for filtering. A 100- x 100-m (201- x 201-point) highpass filter was then designed as a center point minus tapered boxcar filter. The cosine taper was applied in both the x- and y-directions over the entire width of the filter. Since this filter was designed for application to all 40401 points in a regular grid, the original filter is then modified for application to only those points flagged for filtering. The modification is, as described in Appendix A, such that the modified filter is also gradient-nulling. That is, if the input at the flagged grid nodes were a constant-gradient regional field only, then the output would be everywhere zero. The modified filter is applied to data throughout the area including along the irregular edges of the survey where application of conventional filters would likely produce undesirable artifacts or edge effects. The filter design procedure (Appendix A) can transform any zero-dc symmetric filter into a gradient-nulling form that better accommodates edges, corners, gaps and sparse data.

The actual filter coefficients vary from point of application to point of application according to the distribution of points within the input data window associated with a given output location. For application of the EAGGN filter to the data of Figure 2, between 62 and 970 data points were input to obtain an output value at each of the 45,625 nodes selected for filtering. The run time for design and application of the EAGGN filter was 113 s using a 1.6 GHz laptop computer. Where the output location is at or near the survey edge, the distribution of points about the center point is far from symmetric and yet the gradient-nulling attribute is maintained. Thus, the filter is referred to as edge-adaptive. The filter output is only computed at the same locations as were

flagged for input. The filtered data of Figures 4 and 5 were thus interpolated a second time to a regular grid for purposes of contouring.

Inversions of anomaly "A". For purposes of inversion of anomaly "A", data were interpolated to a finer grid interval ($\Delta x = \Delta y = 0.1$ m). The depth interval was $\Delta z = 0.1$ m. The results of magnetic dipole parameters for eight inversions are summarized in Table 1. For seven of these inversions only the data at 19 grid nodes nearest to the measurement stations were flagged for inversion. For model A_K, however, all 40,401 nodes in the 20 x 20-m data window were used. Model A_K yielded a significantly deeper dipole solution than the other models because the data were too sparse within the grid. The separation of about 20 m between the westernmost profile across the central portion of anomaly "A" and the next profile to the west greatly exceeds both the interval Δx and the width of the anomaly.

Table 1. Anomaly "A" models indicating the angle between the estimated dipole's direction and the earth's field, θ, dipole's declination, δ, inclination, Ψ, and depth, z. Declination is measured in the clockwise direction from true north. Models G, Y, and B compute gradient components Gx and Gy, Gy only, and dc bias, B, only, respectively. Models FG and FB input EAGGN filtered data. Model A_K uses interpolated data at all of the 25,921 grid nodes in the 20 x 20-m data window. Other models use only the interpolated data at 19 grid nodes nearest to measurement stations in that data window. Subscripts M and K indicate interpolation by minimum-curvature and kriging methods, respectively.

Model	θ (deg)	δ (deg)	Ψ (deg)	Z (m)	B (nT)	Gx (nT/m)	Gy (nT/m)
G_M	35.1	16.3	24.3	4.8	-1.16	-0.79	-1.53
B_M	43.1	24.1	18.8	5.6	0.31	0.00	0.00
G_K	36.7	17.0	22.8	4.9	-0.58	-0.74	-1.40
Y_K	37.4	14.7	21.1	5.3	-0.50	0.00	-1.26
B_K	43.4	23.8	18.4	5.7	0.76	0.00	0.00
FG_K	38.9	16.6	20.2	5.0	0.72	-0.72	-1.09
FB_K	44.8	22.4	16.1	5.3	2.00	0.00	0.00
A_K	40.4	13.7	17.6	6.4	2.63	-0.29	-0.82

For very sparse data, kriging will often yield better results (Figure 6A) than interpolation using the minimum-curvature method (Figure 6B). For large data sets, however, kriging can be computationally very expensive. Thus, one may question whether kriging is necessary in the case for which the interpolated results are only used at the grid nodes nearest to the measurement station. In the present case in which $\Delta x = \Delta y = 0.1$ m, the greatest interpolation distance in either the x- or y-direction would be only 0.05 m. Subscripts M and K for inverse models indicate data interpolated by minimum-curvature and krigging methods, respectively (Table 1). Models G_M and B_M yield essentially the same results as Models G_K and B_K (Table 1) because the maximum interpolation distance for data used in the inversion was limited to half of the grid spacing. The models G_M and G_K evaluated both components of the gradient (Gx and Gy in equation 1) while models B_M and B_K evaluated neither component of the gradient under the assumption that Gx = Gy = 0.

There is a significant but small difference between the dipole orientations of inverse models G_K and B_K (Table 1) and the estimated depth is 0.8 m greater for model B_K. These differences are also evident in the plots of the modeled fields and the residual fields of observed minus modeled fields (Figure 7). The gradient is only defined by 19 data points within the 20 x 20-m data window so it is not apparent as to which of the solutions G_K or B_K might be more correct. The gradient (Gx = -0.74 nT/m; Gy = -1.40 nT/m) that is estimated in model G_K significantly exceeds the regional gradient of about 0.4 nT/m that is roughly estimated from the contours in the plot of Figure 3. This may not indicate that the model G_K is less accurate than model B_K, however. The residual field for anomaly "A", although small relative to the modeled field for both models (Figure 7), is nevertheless not negligible. The residual may be attributed to one or more of the following: (1) measurement errors especially in the magnetometer positions, (2) the presence of a single magnetic source that differs from a point dipole, equivalent to a uniformly magnetized sphere, (3) the presence of smaller magnetic sources within a few meters of the primary source, or (4) a more complicated regional field resulting from larger and perhaps deeper sources than is readily discerned from the contours of Figure 3.

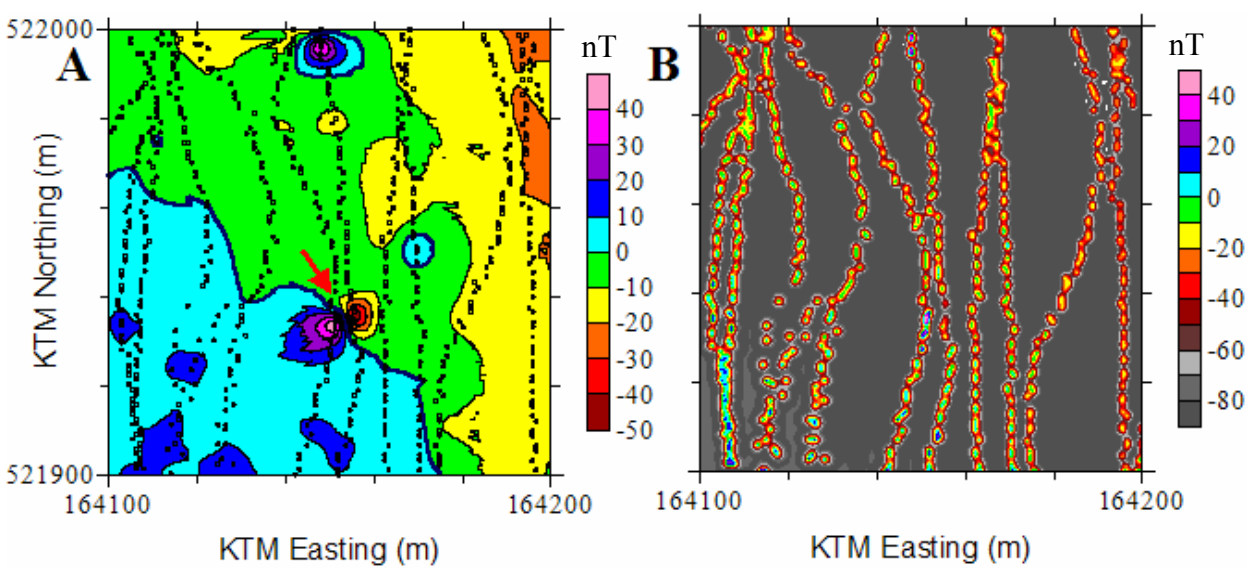

Figure 6. Magnetic field in a portion of Chongcho Lake derived from interpolation at grid intervals of 0.1 m using (**A**) kriging and (**B**) minimum-curvature methods. Raw, measurement station locations are posted. Inverse models will be obtained for anomaly "A" (red arrow). The contour intervals are 10 nT. The data are flagged for inversion at grid nodes nearest to the measurement stations.

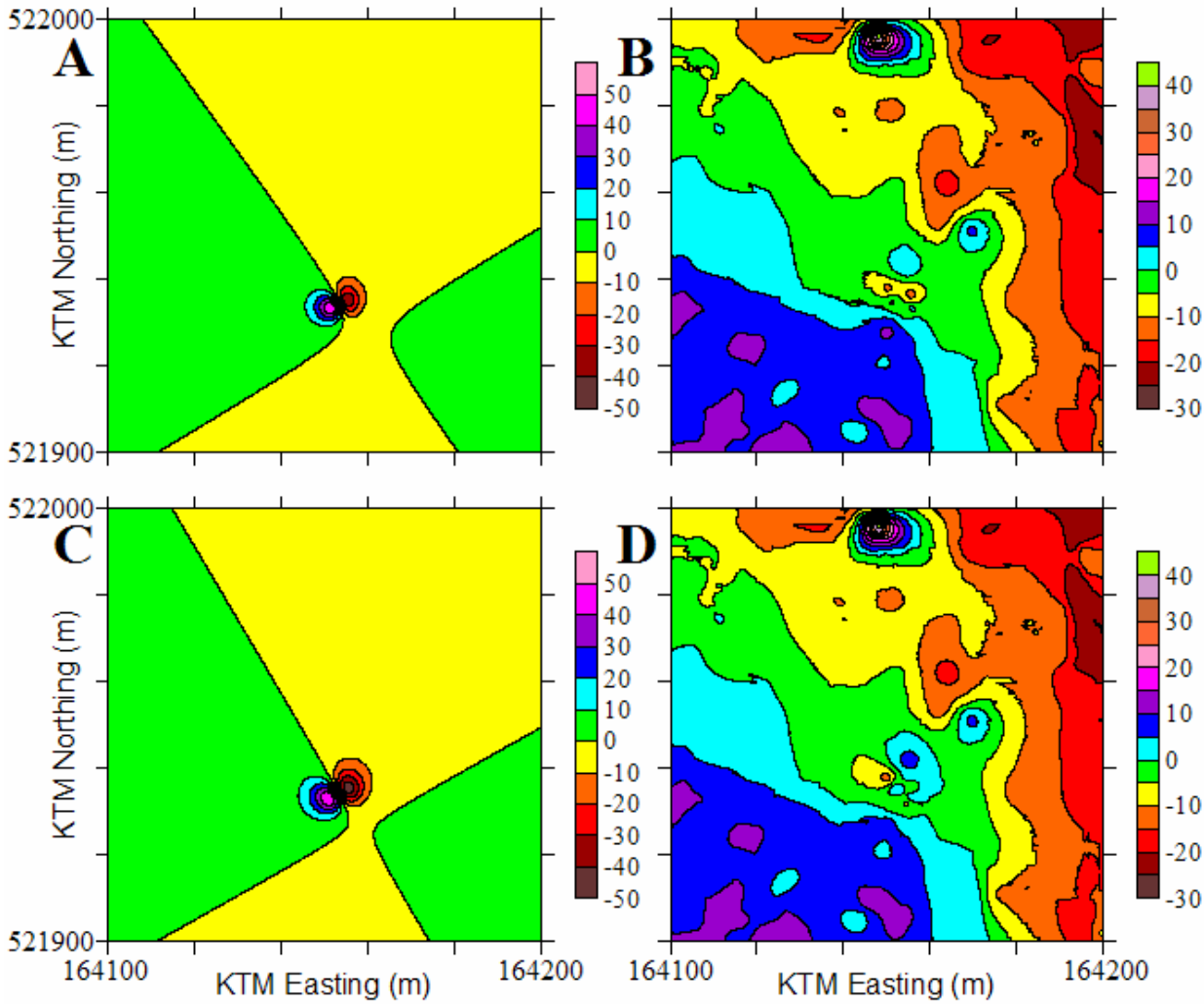

Figure 7. For model G_K: (**A**) the modeled magnetic field of the dipole and (**B**) the residual magnetic field equal to the observed minus the modeled field. For model B_K: (**C**) modeled dipole field and (**D**) residual magnetic field. The contour interval is 10 nT for the modeled fields and 5 nT for the residual fields.

Although one may not be able to resolve the cause of the residual field, given especially the sparsity of the data, the approximate consistency of the magnetic dipole orientation for models G_K and B_K is useful. There is a greater density of stations along the north (y-) direction of profiles. Thus, the gradient component Gy may be better defined within the data window. Model Y_K was obtained under the assumption that Gx is zero in equation 1. The dipole orientation for this model is closer to that of model G_K than B_K, and the depth is intermediate to those of the other two models.

The lake bottom is at a depth of approximately 4.4 m at the modeled dipole locations. For the models with gradient estimation, the estimated dipoles are a few tenths of a meter below the lakebed and for the models without gradient estimation; the modeled dipoles are about 1 m below the lakebed (Table 1). It is not known whether the models are more reasonable with or without gradient estimation particularly as there are only 19 measurement points within the data window and determination of gradients is, in any case, uncertain. The gradients estimated by

inversion are 0.7 to 0.8 nT/m to the west and 1.4 to 1.5 nT to the south. The peak-trough anomaly is 92 nT and the peak-trough separation is 5.5 m. Removing the estimated gradients would decrease the peak-trough amplitude of the anomaly by approximately 9% (8 nT). The effect of estimating gradients is to reduce the angle between the modeled dipole and the earth's field by 7 to 8 deg. Even if it cannot be determined whether the gradients are accurately determined, given the sparsity of the data, it is still useful to note the effect of including the gradient estimation as a means of determining the reliability of the modeled dipole's orientation.

The 100 x 100-m EAGGN filter applied to the data of Figure 4 is of sufficient size that it removed low spatial frequency components of the regional field yet did not significantly distort the anomaly "A". Accordingly, Models FG_K and FB_K (Table 1) were obtained by inversion of data derived by interpolation of the EAGGN filtered data to a 0.1 x 0.1-m grid that were flagged for inversion only at the grid nodes nearest to the measurement stations. The orientations and depths of models FG_K and FB_K are nearly the same as for models G_K and B_K, respectively. The magnitudes of the gradient components Gx and Gy for Model FG_K are both reduced slightly, as would be expected from the coincidence of an estimated southwesterly gradient in the model G_K and in the regional field estimated from the unfiltered data of Figure 3.

The EAGGN filtering applied here was pre-inversion and not intra-inversion as in the case of "profile-adaptive" filtering previously applied to Chongcho Lake magnetic data by Park et al. (2002) or EAGGN filtering applied to Multi-Sensor Towed Array Detection System (MTADS) UXO magnetic data by René et al. (2006). The "profile-adaptive" filtering attenuated gradients along the y-direction of profiling, but did not have significant effect on gradients in the x-direction. As many steps of processing were different from the present case, time did not allow a direct comparison of results for "profile-adaptive" filtering versus estimation of gradients in the present work. Certainly, the evaluation of gradients in equation 1 is much less computationally expensive than "profile-adaptive" intra-inversion filtering as applied by Park et al. (2002). Small intra-inversion EAGGN filters were not applied here because the data are so much sparser than in the case of the MTADS UXO data.

Orientation relative to the earth's field. Relatively small deviations of inverse modeled dipole directions from the earth's magnetic field may indicate that the observed field is largely induced or else results from remanent magnetization that happens to be in the approximate direction of the earth's field. In surveys for unexploded ordnance it is generally assumed that shock demagnetization from firing and impact destroys most of the remanent magnetization of the ordnance (Nelson, et al., 1996). An angle θ in excess of 60 deg is therefore generally taken as an indication that the magnetic source is not UXO although high remanent magnetization of UXO may be acquired because of lightning strikes. Figure 8 plots the inverse modeled magnetic dipole orientations for five of the models obtained for anomaly "A". The plot is a "bull's eye" stereographic projection of the dipole orientations onto a plane perpendicular to the earth's field. Since constant angles of deviation between the dipole orientation and the earth's field are mapped as circles, this plot presents a particularly useful representation of the dipole orientation. In the particular plot of Figure 8, the inner circle (bull's eye), intermediate circle and outer circle map θ = 30, 60, and 90 deg, respectively. If the angle θ exceeded 90 deg then one may either use a distinct symbol (for example, an "x" instead of a filled circle) or a separate plot, as shown in the lower right of Figure 8 for magnetization antiparallel to the earth's field. Since for models of

the anomaly "A", θ is well within the intermediate circle (θ = 60 deg), the source of the anomaly A is a candidate for UXO that experienced shock demagnetization. Given the activity of the Korean War (1950-1953) in this area north of the 38th parallel the possibility of UXO exists. The deviation of the modeled moments from the earth's magnetic field by less than 40 degrees may indicate that the source of anomaly "A" is largely induced or else has remanent magnetization that happens to be in the approximate direction of the earth's field.

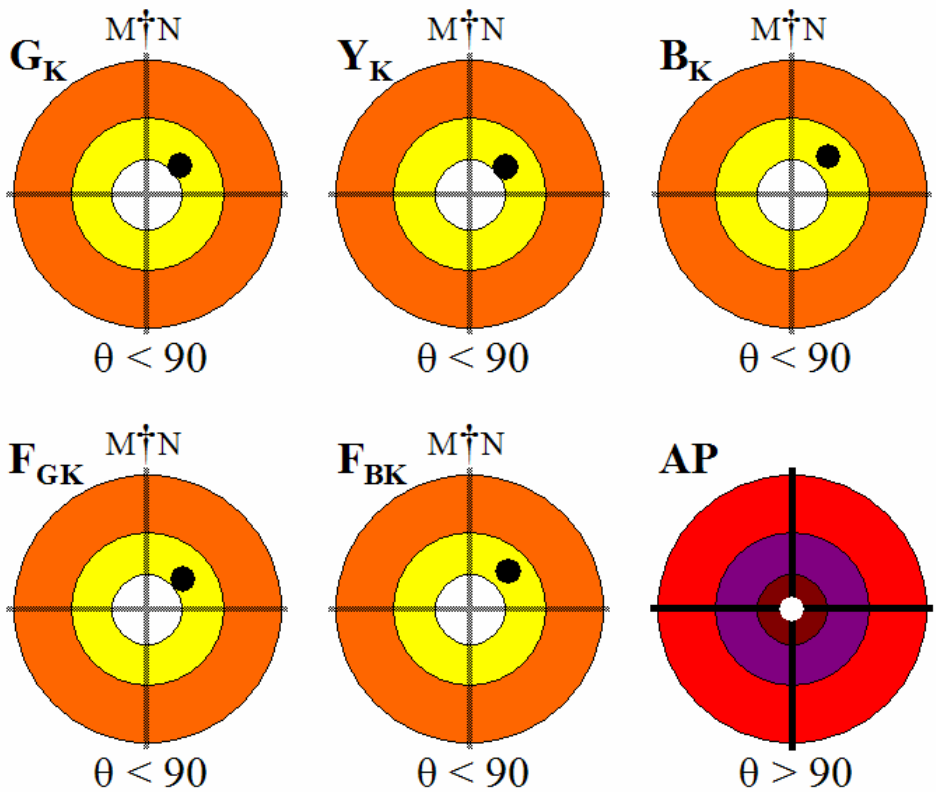

Figure 8. Bull's eye stereographic plots of the projections of magnetic dipole orientations onto a plane perpendicular to the earth's field. Plots are for models G_K, Y_K, B_K, FG_K, and FB_K (Table 1) and an orientation antiparallel to the earth's field (AP).

Conclusions

Highpass EAGGN filtering aids the definition of anomalies in the presence of significant regional fields and it automatically adapts to irregular survey bounds as well as data gaps without significant edge-effect artifacts. The EAGGN filters are derived automatically by evaluation of three parameters at each output location. The methods of pre-inversion or intra-inversion filtering can be repeated for a single anomaly with and without gradient estimation and with and without filtering as a means to test the conditions of noise in the environment and the consistency of results as a possible indication of their reliability. The bull's eye stereographic plot helps to visualize the magnetic dipole's orientation, which is used, for example, to distinguish UXO from non-UXO.

References

Nelson, H. H., Altshuler, T. W., Rosen, E. M., McDonald, J. R., Barrow, B., and Khadir, N., 1996, Magnetic modeling of UXO and UXO-like targets and comparison with signatures measured by MTADS: Proceedings 1996 UXO Forum

Park, C. H., et al., 2001, Geomagnetic survey report in Dredging project at the Cheoncho Onee, 2001, Korea Research and Development Institute, Service Report, Korean Ocean Research and Development Institute.

Park, C. H., René, R. M., and Kim, K. Y., 2002, Location of magnetic dipoles in Chongcho Lake, Republic of Korea: an application of the SOAPFI (Shape-of-anomaly potential field inversion) program: Proceedings of the Symposium on the Application of Geophysics to Environmental and Engineering Problems (SAGEEP 2002), 12 pages.

Rao, B. S. R., Prakasa Rao, T. K. S., and Krisha Murthy, A. S., 1977, A note on magnetization of magnetized spheres: Geophysical Prospecting, Vol. 25, No. 4, p. 746-775.

René, R. M., Park, C. H., and Kim, K. Y., 2004, Intra-inversion filtering for least-squares inversion of magnetic dipole fields in the presence of residual non-dc background magnetic fields and overlapping dipole fields: Proceedings of the Symposium on the Application of Geophysics to Environmental and Engineering Problems (SAGEEP 2004), CD, p. 1315-1331.

René, R. M. and Kim, K. Y., 2006, Edge-adaptive and gapped gradient-nulling intra-inversion filters for application to uxo magnetic field surveys: Proceedings of the Symposium on the Application of Geophysics to Environmental and Engineering Problems (SAGEEP 2006), CD, 14 pages.

Appendix A (Note: within Final Report Appendix A)

Edge-adaptive gapped gradient-nulling filters. Data may be interpolated onto a regular grid to facilitate applications of processing, data analysis, including some inversions, and display. For data that contains high-spatial frequencies that are under-sampled, however, such interpolation can introduce lower spatial frequency content that may degrade the analysis. It may then be best to flag only those grid nodes nearest to measurement stations for use in the steps of analysis or processing that follow. For example, one may apply a digital highpass or bandpass filter to the interpolated data and then by the method of intra-inversion filtering obtain a fit of dipoles to the data (René, et al. 2002; René and Kim, 2006). In the present application, the data are very sparse and the edges of the survey area are irregular. Accordingly a filter will be derived that adapts to these conditions automatically by varying the filter weights with each new output location according to the distribution of input data locations within the specified data window.

Where all points on a regular rectangular grid are available within an M x N-point 2-dimensional filter, a zero-dc symmetric filter will be "gradient-nulling" (GN). That is, if the input is a constant-gradient regional field

$$R = ax + by + c \tag{A1}$$

then the filtered field,

$$R'_{ij} = a \Sigma F_{m,n}\, x_{i+m} + b \Sigma F_{m,n}\, y_{j+n} + c \Sigma F_{m,n} \tag{A2}$$

is nulled ($R' = 0$) provided the sum of the filter coefficients is zero and the filter coefficients are symmetric ($F_{-m,n} = F_{m,n}$, $F_{m,-n} = F_{m,n}$). The GN filter may have rectangular, elliptic, or other symmetric geometry.

Where the filter is to be applied in a window for which only some of the grid nodes are flagged for input to the filter, then a modified filter, F*, is defined here with coefficients

$$F^*_{i,j,m,n} = F_{m,n} (1 + K_{xij} X_{i+m} + K_{yij} Y_{j+n}) C^*_{ijmn} E_{ijmn} \tag{A3}$$

where E_{ijmn} is unity if the grid node at (X_{i+m}, Y_{j+n}) is flagged for inversion. $E_{ijmn} = 0$ if that grid node is not available for input because the magnetic field is not defined at that given location. C^*_{ijmn} in equation A3 is unity at the filter origin ($C^*_{ij00} = 1$), and is otherwise equal to a constant, C_{ij}, over the range of the filter coefficients. Subscripts i and j for the filter coefficients, $F^*_{i,j,m,n}$, indicate that the filter varies from point-to-point. For the filter F* to be gradient-nulling it is required that

$$R'_{ij} = a (\Sigma_{m,n} F^*_{i,j,m,n} X_{i+m}) + b (\Sigma_{m,n} F^*_{i,j,m,m} Y_{j+n}) + c (\Sigma_{m,n} F^*_{i,j,m,n}) = 0, \tag{A4}$$

for any coefficients a, b, and c.

Combining equations (A3) and (A4) and noting that the filter will only be applied with an origin at a point where the input data are defined ($E_{i,j,0,0} = 1$), yields the following three equations:

$$K_{xij} (\Sigma_{m,n} F_{m,n} E_{ijmn} X^2_{i+m}) + K_{yij} (\Sigma_{m,n} F_{m,n} E_{ijmn} X_{i+m} Y_{j+n}) = - \Sigma_{m,n} F_{m,n} E_{ijmn} X_{i+m} ; \quad (A5)$$

$$K_{xij} (\Sigma_{m,n} F_{m,n} E_{ijmn} X_{i+m} Y_{j+n}) + K_{yij} (\Sigma_{m,n} F_{m,n} E_{ijmn} Y^2_{j+n}) = - \Sigma_{m,n} F_{m,n} E_{ijmn} Y_{j+n} ; \quad (A6)$$

and

$$C_{ij} [\Sigma'_{m,n} F_{m,n} E_{ijmn} (1 + K_{xij} X_{i+m} + K_{yij} Y_{j+n})] = - F_{0,0} ; \quad (A7)$$

where the primed summation in equation (A7) excludes the origin (m = n =0).

Solving these equations at each output filter location yields the coefficients K_{xij}, K_{yij}, and C_{ij} that define the modified filter coefficients through equation (A3). The equations are generally well conditioned, although that will not be the case if all available grid nodes for filtering lie on or a straight line. If all grid nodes are available to the filter, then the modified filter, F*, will be identical to the original filter, F. If some grid nodes are unavailable because there exist gaps in the data then F* is a "gapped" GN filter. If on the other hand some grid nodes are not available because the filter is at or near an edge or corner of the survey area, then F* is an "edge-adaptive" GN filter. More generally when both data gaps and edges occur, as in the present application, F* can be referred to as an edge-adaptive, gapped gradient-nulling (EAGGN) filter. The output of the filter is always at the center of the original symmetric filter window regardless of missing data points or extension of that filter beyond the bounds of the available data.

Acknowledgments

We gratefully acknowledge the contributions of analysis, support, data, and information provided by numerous individuals. These include Mr. Changhwan Kim at the Korean Ocean Research Development Institute (KORDI), Prof. Hoonyol Lee, Ms. So Young Lee, Mr. Changmin Lee, and Mr. Myungho Hong at Kangwon National University (KNU), and Messrs. Sang-Kyung Lee and Seungwoo Lee and other staff at the Korea Institute of Science and Technology Information (KISTI). We are most appreciative of the helpful suggestions of an anonymous reviewer. We are also very grateful that this work was partially funded by Kangwon National University and by the U. S. Army Corps of Engineers (USACE) as part of the SERDP Exploratory Development (SEED) Project MM1452 (formerly UX1452) by the U. S. Army Corps of Engineers (USACE) through the Strategic Environmental Research and Development Program under contract W912HQ-05-P-0028.

Selected Slides presented at SAGEEP showing relevant figures not included in the Proceedings paper

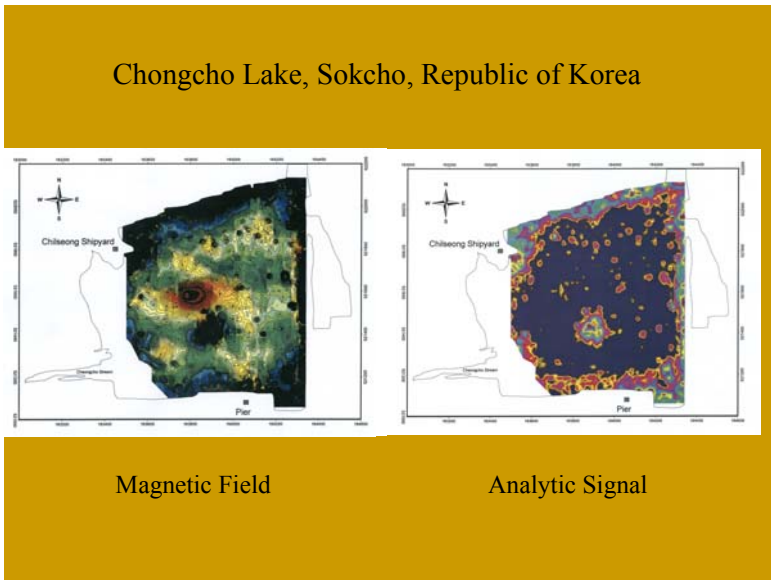

Figure A9. The magnetic field and the analytic signal (total gradient) for the Chongcho Lake survey.

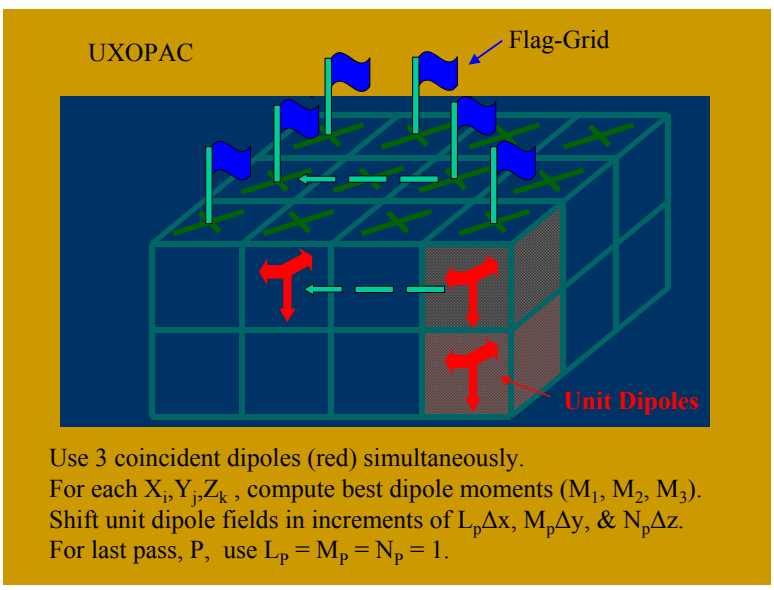

Figure A10. The model space for UXOPAC inversions using fields of three coincident orthogonal unit-dipoles positioned in one corner of the model space for each allowed depth in a dipole search window. The unit-dipole fields are shifted laterally as necessary. Flags indicated flagged nodes nearest to measurement stations.

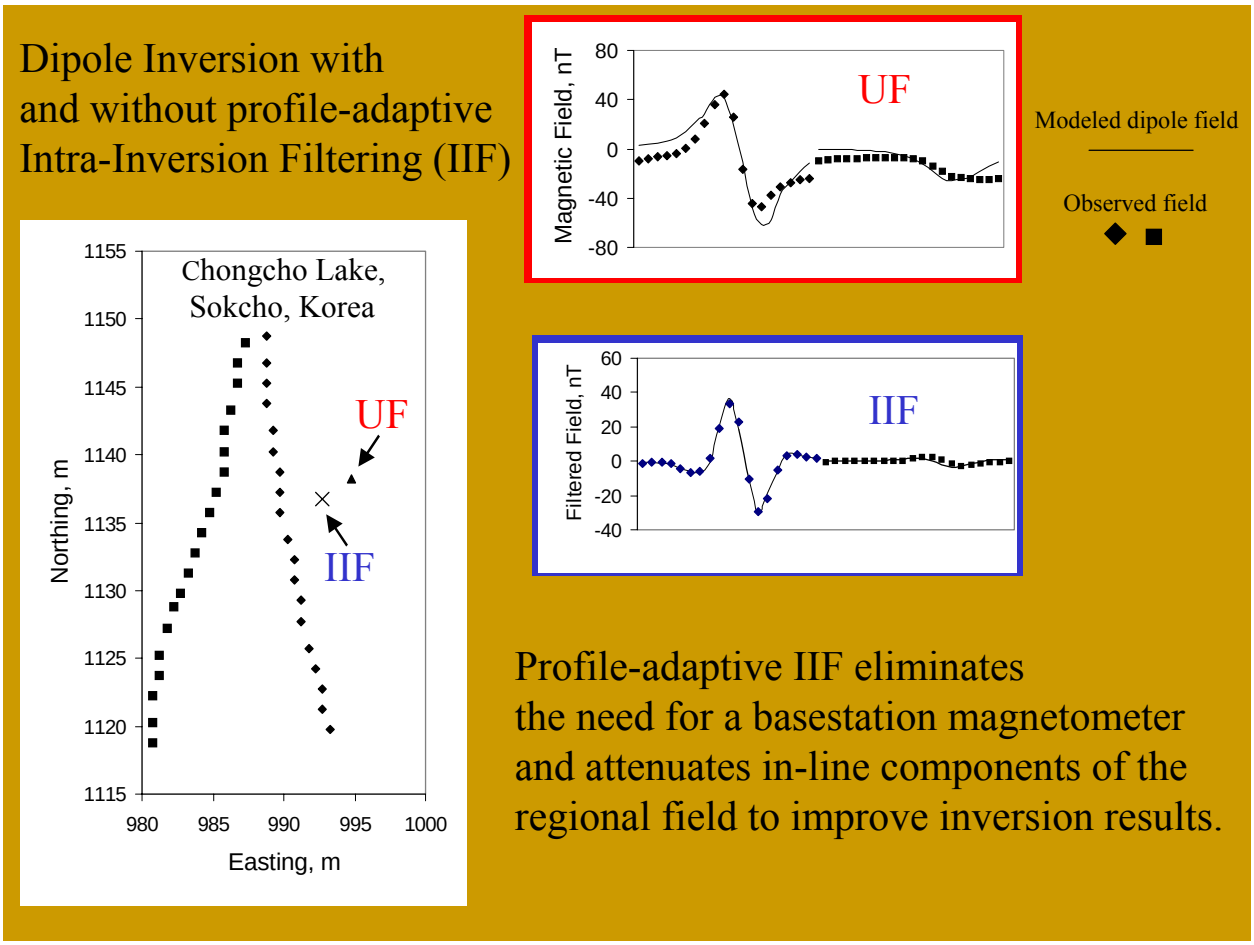

Figure A11. Example of single-dipole "profile-adaptive" intra-inversion filtering of a magnetic anomaly in Chongcho Lake. Observed and modeled profiles are shown unfiltered (UF) and after filtering (IIF) The fit was improved using IIF and the resultant dipole moved significantly closer to the magnetic profiles shown here. The early version of SOAPFI used here was adapted to dipole inversion using only dipoles that were parallel to the earth's field. That program evolved into UXOPAC.

APPENDIX B

Dipole Inversion Applied to Archaeological Marine Magnetic Survey off the South Coast of Korea near Myo-Do

René, R. M., Park, C. H., and Kim, K. Y.

The Yeosu archaeological marine magnetic survey was conducted in the Korea Strait off the southern coast of Korea, southeast of Myo-do (island) and north of the peninsula on which the port city of Yeosu is located. One objective of this survey was to find cannon that were used aboard a Korean turtle ship, an armored vessel of the late 16th century A.D. (Figure B1). Various items were dredged at sites of magnetic anomalies but these were not of much archaeological interest.

As part of the SEED program, marine magnetic data from the Yeosu survey and from a survey of Chongcho Lake in the northeast Republic of Korea were used to help develop and test software including dipole stripping and multi-dipole inversions. Both of these magnetic surveys were conducted by the Korea Ocean Research and Development Institute (KORDI). Originally, work on the Chongcho Lake data led to the development of the "profile-adaptive" intra-inversion filter (IIF). During this SEED project, work with marine and MTADS UXO land magnetic data led to development of the 2-d gapped gradient-nulling (GGN) filter as an alternative to all-node IIF. The sparsity of the marine data was an impetus for that development. When considered relative to the desired positional accuracy of modeled dipoles, MTADS or similar data with cross-line spacing of 25 cm are also sparse enough to warrant consideration of gapped filters. Flag-node inversions use only grid nodes nearest to magnetometer stations. For a regular grid with a 1-cm grid interval, the flagged nodes are only about 1 % of the total nodes in the case of APG BTA data. To emphasize MTADS data and to take advantage of closer profile spacing and previous experience with the Chongcho Lake data, work on Yeosu data was discontinued early in the project. Four of the figures presented here were also presented in a poster at the Partners in Environmental Technology Technical Symposium and Workshop, November 29 – December 1, 2005.

Figure B1. Model of an iron-clad late 16th century Korean turtle ship.

The Yeosu archaeological marine survey yielded sparse data (Figure B2) by comparison with land UXO surveys. Nevertheless, the data were gridded at 10-cm spacing and nodes nearest stations were flagged for inversion. Within the data window of Figure B2 three anomalies where chosen for application of dipole inversion. One of these anomalies in the southeast quadrant of the data window, was chosen for both single- and multi-dipole inversion. The inverse modeled dipole fields are shown in Figure B3, for the case of three single-dipole inversions, and in Figure B4, for the case of two-single dipole inversions and one multi-dipole inversion for the anomaly in the southeast quadrant. Figure B5 shows the result of three-dipole "stripping"; that is, the fields of three dipoles obtained by single-dipole inversions were summed and subtracted from the observed field. The resultant residual field can be useful in evaluating the success of inversions. Denser data near the target anomaly might better distinguish between an extended magnetic source and single- or two-dipole sources.

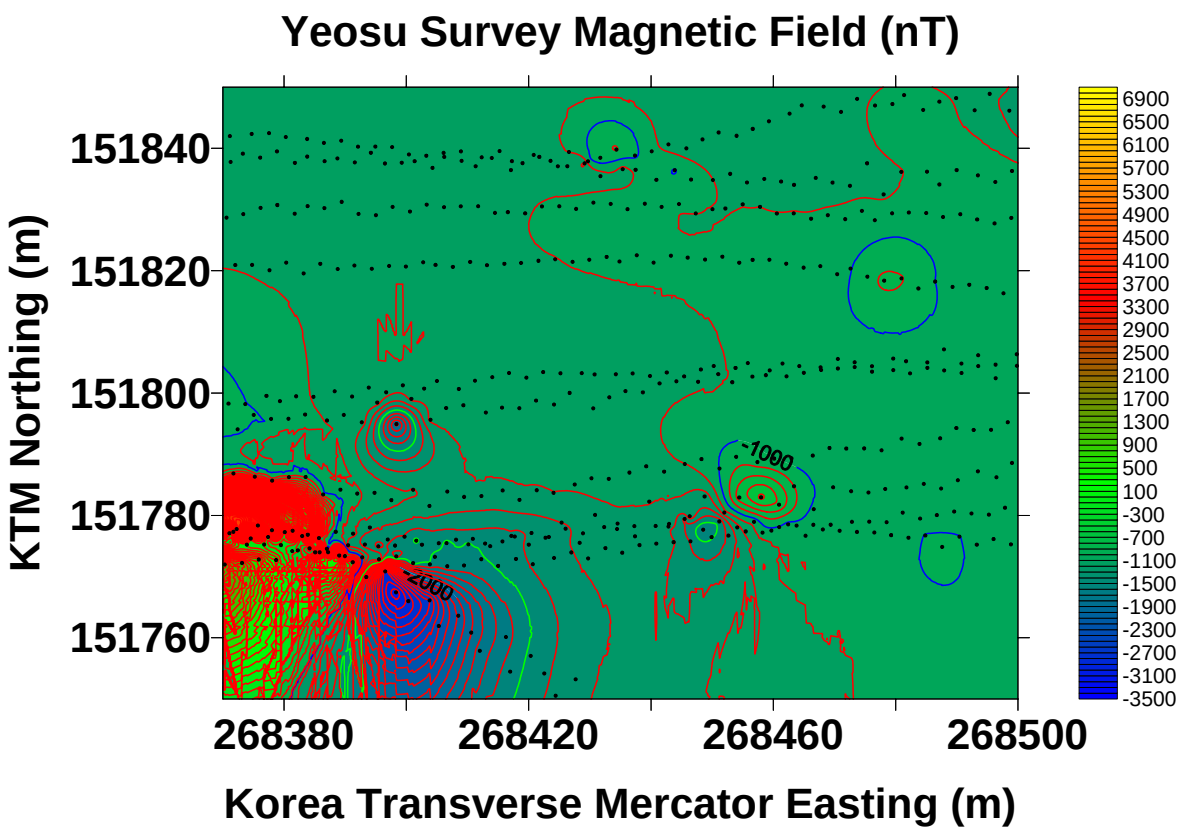

Figure B2. The magnetic field in a portion of the Yeosu survey area. Three anomalies were selected for inversion. The large anomaly in the southeast quadrant was selected for both single- and multi-pole inversions. The zero contour is red and the contour interval is 100 nT.

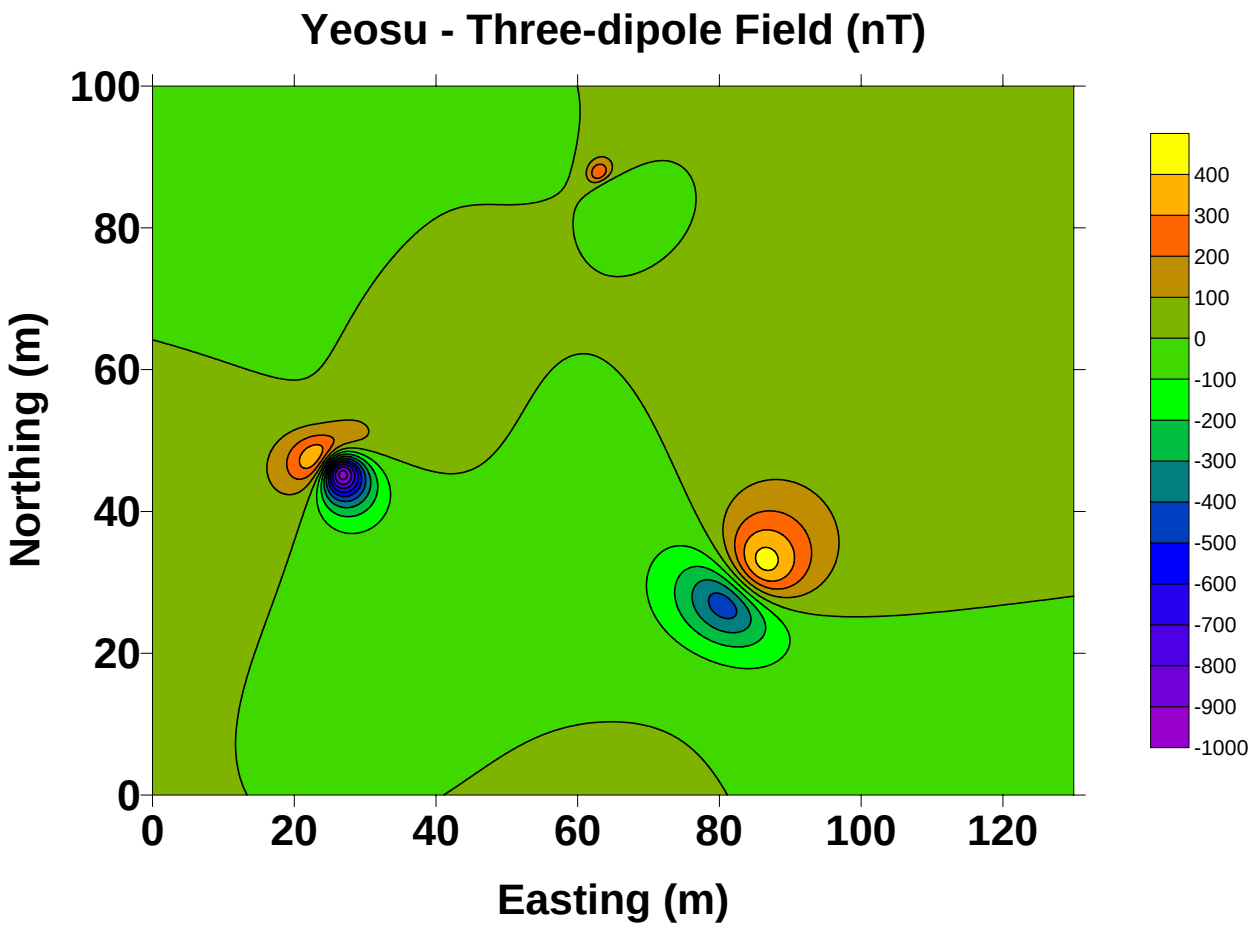

Figure B3. The sum of inverse modeled dipole fields for three dipoles in the 130 x 120-m area of Figure B2. The contour interval is 100 nT.

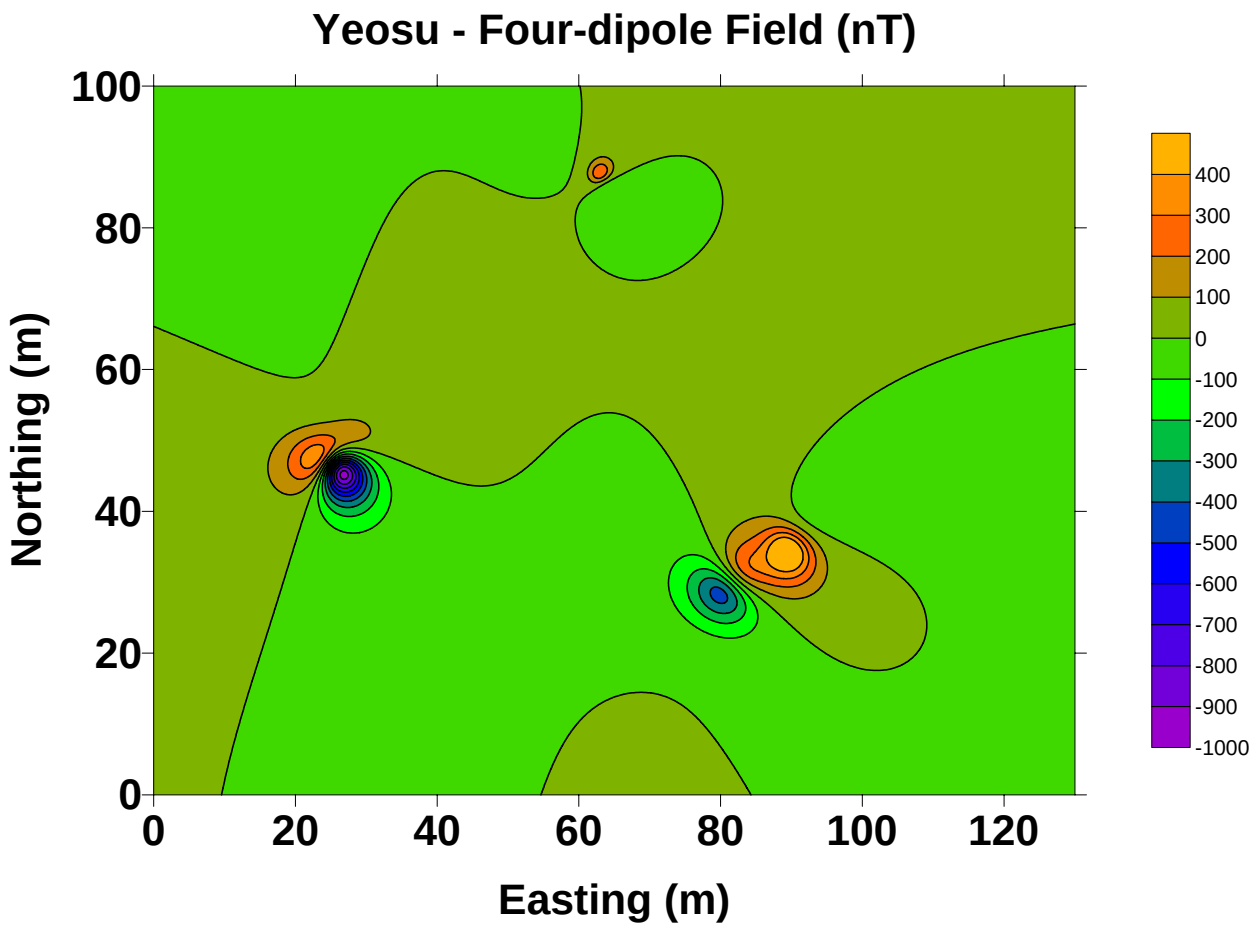

Figure B4. The sum of inverse modeled dipole fields for four dipoles in the 130 x 120-m area of Figure B2. Two of the dipoles were used to model the large anomaly in the southeast quadrant of the area. The contour interval is 100 nT.

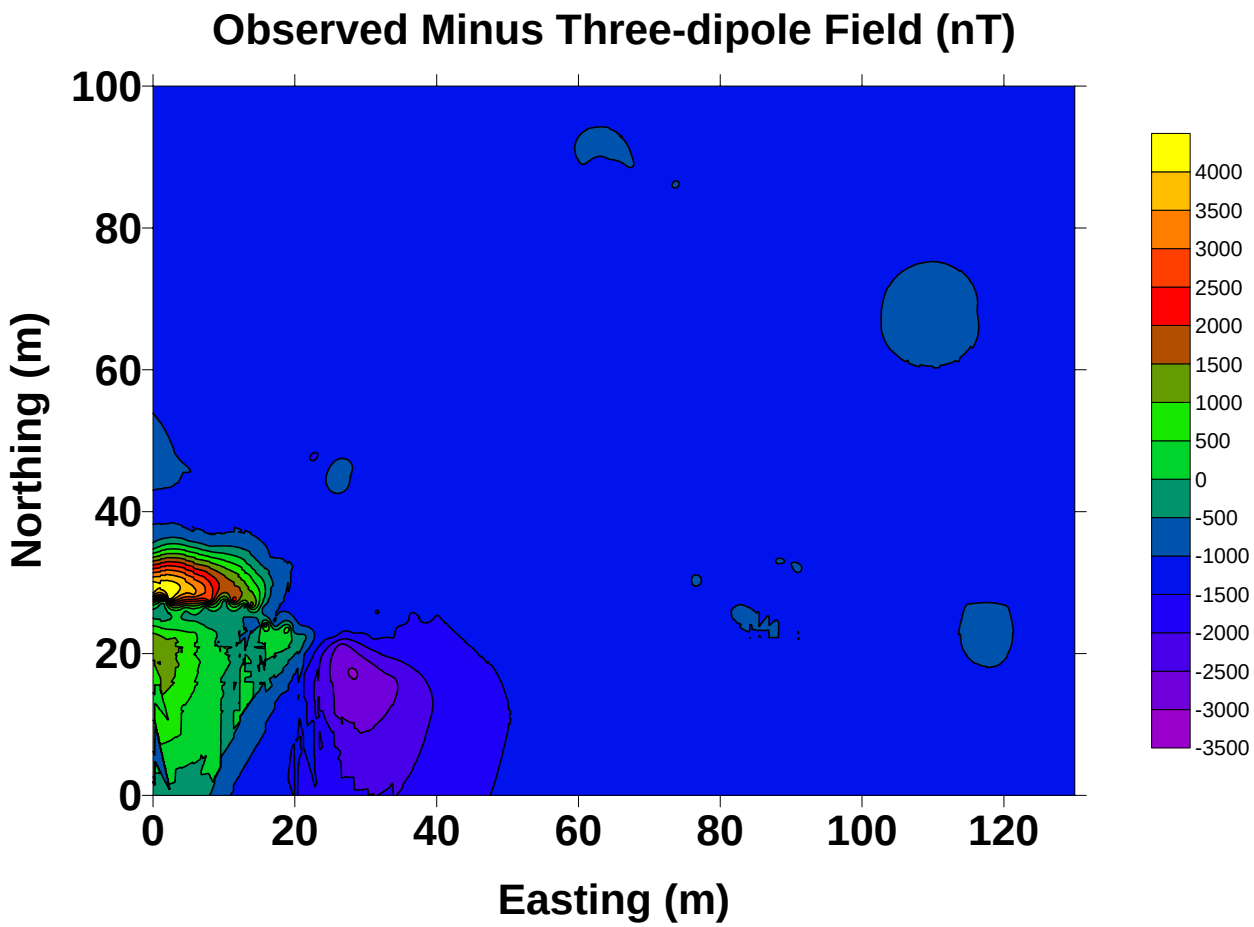

Figure B5. The residual field equal to the observed field minus the sum of inverse modeled dipole fields for three dipoles in the 130 x 120-m area of Figure B2. The contour interval is 100 nT.

APPENDIX C
Subroutines to compute and apply EAGGN Filter

This appendix presents two subroutines. The subroutine COMPUTE_GAPPED_GN_FILTER modifies a symmetric, zero-dc, 2-d filter, FILTER_RANK2, into an EAGGN filter by computing three parameters: SCALE_OFF_CENTER, XK_SUBX, and XK_SUBY. The parameters XK_SUBX and XK_SUBY assure that the filter has a center of gravity at the output node, and the parameter SCALE_OFF_CENTER assures that the filter is zero-dc. In applications of IIF, those three parameters are stored. They are later recalled for repeated use because the spatially varying filter depends only on the distribution of flagged nodes about each output node. Applications of the same filter to the input magnetic anomaly and to the unit-dipole fields used in inversion are accomplished by subroutine APPLY_GAPPED_GN_FILTER.

```
SUBROUTINE COMPUTE_GAPPED_GN_FILTER
        (FILTER_RANK2, LXM1D2, LYM1D2, FLAG_GAPPED_DATA,
        SCALE_OFF_CENTER, XK_SUBX, XK_SUBY,
        IX_START_GAPPED, IX_END_GAPPED, IY_START_GAPPED,
        IY_END_GAPPED)
IMPLICIT NONE
REAL, INTENT(OUT)     :: SCALE_OFF_CENTER, XK_SUBX, XK_SUBY
INTEGER, INTENT(IN)  :: LXM1D2,  LYM1D2,  IX_START_GAPPED,  IX_END_GAPPED,
                IY_START_GAPPED,  IY_END_GAPPED
REAL, INTENT(IN)       :: FILTER_RANK2 (-LXM1D2:LXM1D2, -LYM1D2:LYM1D2)
LOGICAL, INTENT(IN)::FLAG_GAPPED_DATA(-LXM1D2:LXM1D2, LYM1D2:LYM1D2)
REAL    ::  SUM_FXX, SUM_FXY, SUM_FYY, SUM_FX, SUM_FY,
       SUM_F, FILTER, FACTOR, RECIPROCAL_SCALE_OFF_CENTER_MAX,
          SUM_OFF_CENTER, RECIPROCAL_SCALE_OFF_CENTER,
          FILTER_AT_CENTER
INTEGER :: IX, IY
! SCALE_OFF_CENTER_MAX is a global parameter of type real. It allows computations to
! continue with a warning that the transformation cannot be accomplished.
!
RECIPROCAL_SCALE_OFF_CENTER_MAX = 1. / SCALE_OFF_CENTER_MAX
!
SUM_F   = 0.
SUM_FXX = 0.
SUM_FX  = 0.
SUM_FYY = 0.
SUM_FY  = 0.
SUM_FXY = 0.
!
FILTER_AT_CENTER = FILTER_RANK2 (0,0)
```

```
DO  IY = IY_START_GAPPED,IY_END_GAPPED !-LYM1D2, LYM1D2
   DO  IX = IX_START_GAPPED,IX_END_GAPPED !-LXM1D2, LXM1D2
      IF (FLAG_GAPPED_DATA(IX,IY)) THEN
         FILTER = FILTER_RANK2(IX,IY)
         SUM_F   = SUM_F   + FILTER
         SUM_FXX = SUM_FXX + FILTER*FLOAT(IX*IX)
         SUM_FX  =   SUM_FX  + FILTER*FLOAT(IX)
         SUM_FYY = SUM_FYY + FILTER*FLOAT(IY*IY)
         SUM_FY  =   SUM_FY  + FILTER*FLOAT(IY)
         SUM_FXY = SUM_FXY + FILTER*FLOAT(IX*IY)
      END IF
   END DO
END DO
IF (SUM_FX == 0. .AND. SUM_FY == 0.) THEN
   XK_SUBX = 0.
   XK_SUBY = 0.
   SUM_OFF_CENTER = SUM_F - FILTER_AT_CENTER
   SCALE_OFF_CENTER = -FILTER_AT_CENTER/SUM_OFF_CENTER
ELSE IF (SUM_FX == 0.  .AND.  SUM_FXX == 0. .AND. SUM_FXY == 0.) THEN
   XK_SUBX = 0.
   XK_SUBY = - SUM_FY / SUM_FYY
   SUM_OFF_CENTER = SUM_F - FILTER_AT_CENTER
                + XK_SUBY * SUM_FY
   SCALE_OFF_CENTER = -FILTER_AT_CENTER/SUM_OFF_CENTER
ELSE IF (SUM_FY == 0.  .AND.  SUM_FYY == 0.  .AND.  SUM_FXY == 0.) THEN
   XK_SUBY = 0.
   XK_SUBX = - SUM_FX / SUM_FXX
        SUM_OFF_CENTER = SUM_F - FILTER_AT_CENTER    + XK_SUBX * SUM_FX
   SCALE_OFF_CENTER = -FILTER_AT_CENTER/SUM_OFF_CENTER
ELSE
   FACTOR    =  SUM_FXY**2 - SUM_FXX * SUM_FYY
   XK_SUBX = (SUM_FX*SUM_FYY - SUM_FY*SUM_FXY)/FACTOR
   XK_SUBY = (SUM_FY*SUM_FXX - SUM_FX*SUM_FXY)/FACTOR
   SUM_OFF_CENTER = SUM_F - FILTER_AT_CENTER
                + XK_SUBX * SUM_FX + XK_SUBY * SUM_FY
       RECIPROCAL_SCALE_OFF_CENTER
                = -SUM_OFF_CENTER/ FILTER_AT_CENTER
        IF (ABS (RECIPROCAL_SCALE_OFF_CENTER)
      < RECIPROCAL_SCALE_OFF_CENTER_MAX) THEN
                SCALE_OFF_CENTER = SCALE_OFF_CENTER_MAX
        ELSE
      SCALE_OFF_CENTER = 1. / RECIPROCAL_SCALE_OFF_CENTER
        END IF
END IF
RETURN
END SUBROUTINE COMPUTE_GAPPED_GN_FILTER
```

```
SUBROUTINE APPLY_GAPPED_GN_FILTER
        (FILTER_RANK2, GAPPED_DATA, CENTER_POINT_OUT,                    LXM1D2,
LYM1D2,   FLAG_GAPPED_DATA,                          SCALE_OFF_CENTER,
XK_SUBX, XK_SUBY)
!
IMPLICIT NONE
REAL, INTENT(OUT)   :: CENTER_POINT_OUT
REAL, INTENT(IN)         :: SCALE_OFF_CENTER,  XK_SUBX,  XK_SUBY
INTEGER, INTENT(IN) :: LXM1D2, LYM1D2
REAL, INTENT(IN)     :: FILTER_RANK2(-LXM1D2:LXM1D2, -LYM1D2:LYM1D2)
REAL, INTENT(IN)     :: GAPPED_DATA (-LXM1D2:LXM1D2, -LYM1D2:LYM1D2)
LOGICAL,INTENT(IN):: FLAG_GAPPED_DATA(-LXM1D2:LXM1D2,-LYM1D2:LYM1D2)
REAL    :: ONE_KYY, ONE_KXX_KYY
INTEGER :: IX, IY
!
CENTER_POINT_OUT = GAPPED_DATA(0,0)*FILTER_RANK2(0,0)
                 * (1.-SCALE_OFF_CENTER)
DO  IY = -LYM1D2, LYM1D2
   ONE_KYY = 1. + XK_SUBY * FLOAT(IY)
   DO  IX = -LXM1D2, LXM1D2
      ONE_KXX_KYY = ONE_KYY + XK_SUBX * FLOAT(IX)
      IF (FLAG_GAPPED_DATA(IX,IY)) THEN
         CENTER_POINT_OUT = CENTER_POINT_OUT
                        + GAPPED_DATA (IX, IY)
                             * FILTER_RANK2(IX, IY)
                             * SCALE_OFF_CENTER
                             * ONE_KXX_KYY
      END IF
   END DO
END DO
END SUBROUTINE APPLY_GAPPED_GN_FILTER
```

Appendix D

Parallelization and profiling of UXOPAC by KISTI

Lee, S. K. and Lee S. W.

The following figures were provided by Messrs. Sang-Kyung Lee and Seungwoo Lee at the Korea Institute of Science and Technology Information (KISTI).

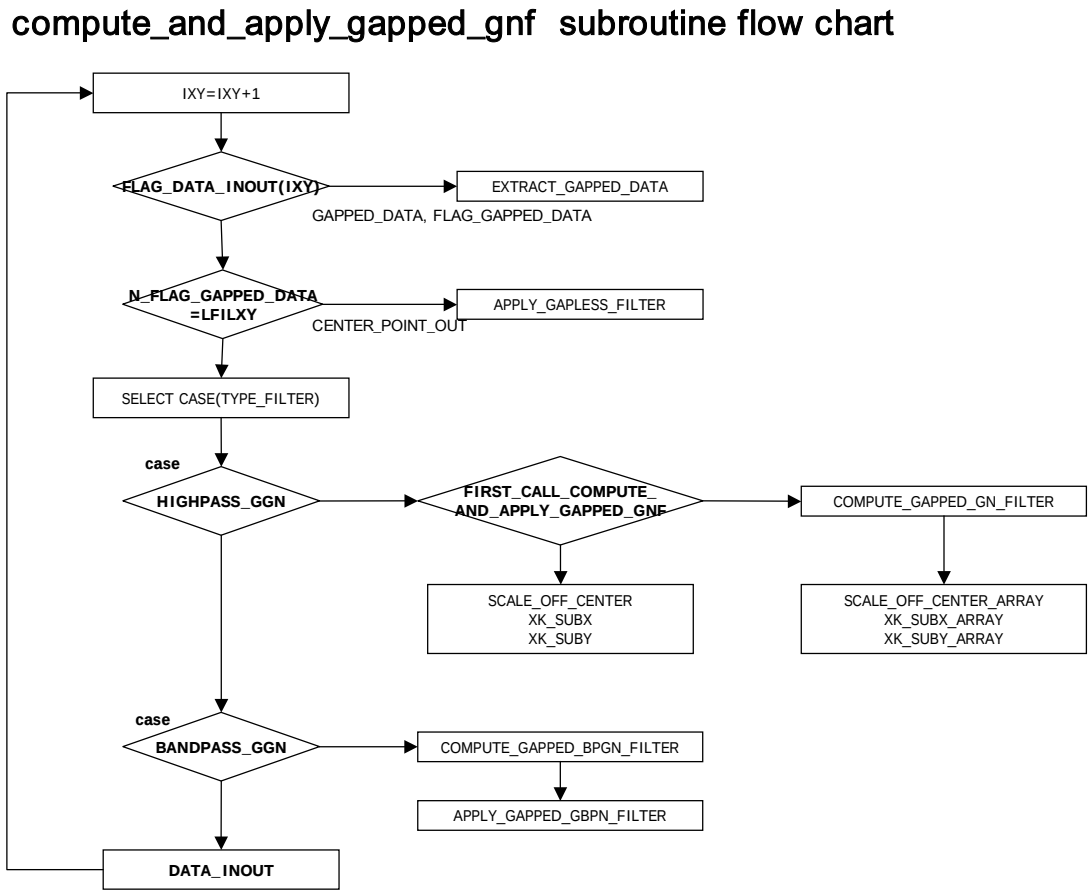

Figure D1. Flow chart of the subroutines to compute and apply GGN filters.

```
ngranularity: Each sample hit covers 4 bytes. Time: 59.49 seconds
  %   cumulative   self              self     total
 time   seconds   seconds    calls  ms/call  ms/call  name
 28.4     16.90    16.90  1526070     0.01     0.01  .__design_and_apply_filters_module_MOD_apply_gapped_gn_filter [10]
 21.6     29.75    12.85  1526070     0.01     0.01  .__design_and_apply_filters_module_MOD_extract_gapped_data [11]
 15.4     38.89     9.14       10   914.00  4317.00  .__design_and_apply_filters_module_MOD_compute_and_apply_gapped_gnf [4]
  7.2     43.17     4.28   305214     0.01     0.01  .__design_and_apply_filters_module_MOD_compute_gapped_gn_filter [17]
  7.1     47.38     4.21       40   105.25   105.25  .dipole_magnetics [18]
  4.4     50.01     2.63       36    73.06    73.06  .retrieve_current_model [20]
  2.4     51.42     1.41       18    78.33    78.33  .get_xmag_from_unit_xmag [24]
  2.3     52.77     1.35        2   675.00   710.00  .__fill_model_per_model_states_module_MOD_input_model [23]
  1.3     53.55     0.78       11    70.91    70.91  .__growing_model_inversion_module_MOD_count_prism_states [27]
  1.2     54.28     0.73        4   182.50  1235.00  .get_mag_3d_dipoles [14]
  0.7     54.72     0.44        3   146.67  1649.25  .filter_mag_field_of_elemental_sources_if_needed [13]
  0.7     55.13     0.41                               ._clc [29]
  0.6     55.51     0.38                               .LDScan [30]
  0.6     55.85     0.34        9    37.78    37.78  .get_cog_vs_z [32]
  0.6     56.18     0.33        1   330.00  4507.74  .__design_and_apply_filters_module_MOD_intra_inversion_filter [15]
  0.6     56.51     0.33        1   330.00   330.00  .get_n_extrema [33]
  0.6     56.84     0.33        1   330.00  1710.50  .start_model [22]
  0.5     57.13     0.29       10    29.00    29.00  .get_model_center [34]
  0.4     57.38     0.25        3    83.33  1730.00  .compute_mag_field_of_elemental_sources_if_needed [12]
  0.4     57.59     0.21        1   210.00  3630.59  .__growing_model_inversion_module_MOD_grow_model [19]
  0.3     57.75     0.16                               .IOGetByte [38]
  0.2     57.89     0.14   305653     0.00     0.00  .cvtloop [41]
  0.2     58.03     0.14                               .__mcount [42]
  0.2     58.14     0.11                               .__mcount [44]
  0.2     58.23     0.09        5    18.00    18.00  .restore_multimodel_model [48]
  0.2     58.32     0.09        1    90.00    90.00  .store_model_prev_seed [49]
  0.1     58.39     0.07   366756     0.00     0.00  .strtod [51]
  0.1     58.46     0.07        3    23.33    23.33  .store_model_number_array [52]
  0.1     58.53     0.07        1    70.00   100.00  .__input_and_apply_flags_module_MOD_input_flags [46]
  0.1     58.59     0.06        9     6.67  4323.67  .get_multimodel_xmagmodt [9]
  0.1     58.65     0.06        2    30.00    30.00  .__shift_dipole_or_seed_module_MOD_dipole_number_array [53]
  0.1     58.71     0.06        1    60.00    60.00  .model_forward_mag [55]
  0.1     58.76     0.05                               .WriteUnit [56]
  0.1     58.80     0.04   305996     0.00     0.00  .__cvt_r [37]
  0.1     58.84     0.04                               ._xlfBeginIO [57]
  0.1     58.88     0.04                               .memmove [58]
  0.1     58.91     0.03   699418     0.00     0.00  .pwr10 [59]
  0.1     58.94     0.03   349709     0.00     0.00  .mf2x1 [60]
  0.1     58.97     0.03        9     3.33     3.33  .get_alpha_l2 [61]
  0.1     59.00     0.03        3    10.00    10.00  .extrema_locations_flagged [62]
  0.1     59.03     0.03                               ._xlfWriteLDInt [66]
```

Figure D2. Original profile of UXOPAC inversion program applied to a test inversion of an APG BTA magnetic anomaly.

```
ngranularity: Each sample hit covers 4 bytes. Time: 57.60 seconds
  %   cumulative   self              self     total
 time   seconds   seconds    calls  ms/call  ms/call  name
 25.0     14.42    14.42  1526070     0.01     0.01  .__design_and_apply_filters_module_MOD_apply_gapped_gn_filter [10]
 20.2     26.08    11.66  1526070     0.01     0.01  .__design_and_apply_filters_module_MOD_extract_gapped_data [11]
 18.5     36.73    10.65       10  1065.00  4127.00  .__design_and_apply_filters_module_MOD_compute_and_apply_gapped_gnf [4]
  7.9     41.27     4.54   305214     0.01     0.01  .__design_and_apply_filters_module_MOD_compute_gapped_gn_filter [13]
  5.2     44.26     2.99       40    74.75    74.75  .dipole_magnetics [19]
  4.3     46.75     2.49       36    69.17    69.17  .retrieve_current_model [20]
  2.5     48.21     1.46       18    81.11    81.11  .get_xmag_from_unit_xmag [23]
  2.4     49.58     1.37        2   685.00   725.00  .__fill_model_per_model_states_module_MOD_input_model [24]
  1.3     50.33     0.75       11    68.18    68.18  .__growing_model_inversion_module_MOD_count_prism_states [27]
  1.2     51.05     0.72        4   180.00   927.50  .get_mag_3d_dipoles [17]
  1.2     51.73     0.68                               vssqrt [29]
  1.0     52.29     0.56                               ._clc [30]
  0.9     52.78     0.49                               .vsrec_ [31]
  0.8     53.23     0.45        3   150.00  1594.62  .filter_mag_field_of_elemental_sources_if_needed [12]
  0.7     53.62     0.39        1   390.00  1770.50  .start_model [22]
  0.6     53.99     0.37                               .LDScan [32]
  0.6     54.33     0.34        1   340.00  4333.87  .__design_and_apply_filters_module_MOD_intra_inversion_filter [14]
  0.6     54.66     0.33        1   330.00   330.00  .get_n_extrema [34]
  0.6     54.98     0.32        9    35.56    35.56  .get_cog_vs_z [35]
  0.5     55.28     0.30       10    30.00    30.00  .get_model_center [36]
  0.4     55.53     0.25        3    83.33  1320.00  .compute_mag_field_of_elemental_sources_if_needed [16]
  0.4     55.74     0.21        1   210.00  3459.32  .__growing_model_inversion_module_MOD_grow_model [18]
  0.3     55.90     0.16                               .IOGetByte [40]
  0.2     56.03     0.13   305643     0.00     0.00  .cvtloop [43]
  0.2     56.15     0.12                               .__mcount [45]
  0.2     56.25     0.10        5    20.00    20.00  .restore_multimodel_model [48]
  0.2     56.34     0.09        1    90.00    90.00  .store_model_prev_seed [50]
  0.1     56.42     0.08   366756     0.00     0.00  .strtod [52]
  0.1     56.50     0.08        3    26.67    26.67  .store_model_number_array [53]
  0.1     56.57     0.07        1    70.00   110.00  .__input_and_apply_flags_module_MOD_input_flags [47]
  0.1     56.64     0.07                               .memcpy [54]
  0.1     56.70     0.06        2    30.00    30.00  .__shift_dipole_or_seed_module_MOD_dipole_number_array [57]
  0.1     56.76     0.06        1    60.00    68.00  .model_forward_mag [56]
  0.1     56.81     0.05                               .IOPutByte [58]
  0.1     56.86     0.05                               .__mcount [59]
  0.1     56.90     0.04   305986     0.00     0.00  .__cvt_r [39]
  0.1     56.94     0.04       15     2.67     2.67  .get_prisms_mag [60]
  0.1     56.98     0.04                               ._xlfWriteLDInt [61]
  0.1     57.01     0.03        9     3.33  4133.00  .get_multimodel_xmagmodt [9]
  0.1     57.04     0.03        3    10.00    10.00  .extrema_locations_flagged [62]
  0.1     57.07     0.03                               .IOSetRecordOffset [66]
  0.1     57.10     0.03                               .PrepareUnit [67]
  0.1     57.13     0.03                               .WriteUnit [68]
```

Figure D3. Profile of tuned code for Program UXOPAC.

```
ngranularity: Each sample hit covers 4 bytes. Time: 56.15 seconds
  %   cumulative   self              self     total
 time   seconds   seconds    calls  ms/call  ms/call  name
 28.7     16.14    16.14  1142399     0.01     0.01  .__design_and_apply_filters_module_MOD_apply_gapped_gn_filter [3]
 20.2     27.46    11.32  1151201     0.01     0.01  .__design_and_apply_filters_module_MOD_extract_gapped_data [6]
  8.1     32.02     4.56   273053     0.02     0.02  .__design_and_apply_filters_module_MOD_compute_gapped_gn_filter [8]
  7.9     36.46     4.44                             .__mcount [9]
  6.0     39.81     3.35       40    83.75    83.75  .dipole_magnetics [13]
  4.9     42.57     2.76       36    76.67    76.67  .retrieve_current_model [14]
  3.5     44.53     1.96       18   108.89   108.89  .get_xmag_from_unit_xmag [17]
  2.4     45.87     1.34        2   670.00   710.00  .__fill_model_per_model_states_module_MOD_input_model [18]
  1.4     46.68     0.81       11    73.64    73.64  .__growing_model_inversion_module_MOD_count_prism_states [25]
  1.4     47.44     0.76        4   190.00  1027.50  .get_mag_3d_dipoles [11]
  1.3     48.18     0.74                               vssqrt [27]
  1.0     48.76     0.58                             .__mcount [29]
  1.0     49.31     0.55        3   183.33   333.87  .filter_mag_field_of_elemental_sources_if_needed [24]
  0.9     49.83     0.52                             .vsrec [30]
  0.8     50.27     0.44        1   440.00   451.61  .__design_and_apply_filters_module_MOD_intra_inversion_filter [31]
  0.7     50.67     0.40                             .LDScan [32]
  0.7     51.06     0.39        1   390.00  2080.00  .start_model [15]
  0.7     51.43     0.37                             ._clc [33]
  0.6     51.76     0.33        1   330.00   330.00  .get_n_extrema [35]
  0.5     52.06     0.30      160     1.88   202.00  .__design_and_apply_filters_module_MOD_compute_and_apply_gapped_gnf@OL@1 [1]
  0.5     52.36     0.30       10    30.00    30.00  .get_model_center [36]
  0.5     52.66     0.30        3   100.00  1470.00  .compute_mag_field_of_elemental_sources_if_needed [10]
  0.5     52.95     0.29        9    32.22    32.22  .get_cog_vs_z [37]
  0.4     53.20     0.25        1   250.00  3760.36  .__growing_model_inversion_module_MOD_grow_model [12]
  0.4     53.40     0.20                             .IOGetByte [41]
  0.3     53.59     0.19                             .qincrement [42]
  0.3     53.76     0.17   305643     0.00     0.00  .cvtloop [43]
  0.3     53.92     0.16                             ._xlsmpSyncRegionItem [44]
  0.3     54.07     0.15                             .__mcount [45]
  0.3     54.22     0.15                             .local_unlock_ppc_mp [46]
  0.2     54.32     0.10   366756     0.00     0.00  .strtod [48]
  0.2     54.42     0.10        1   100.00   100.00  .store_model_prev_seed [52]
  0.2     54.51     0.09        5    18.00    18.00  .restore_multimodel_model [54]
  0.1     54.59     0.08   305986     0.00     0.00  .__cvt_r [39]
  0.1     54.67     0.08        3    26.67    26.67  .store_model_number_array [56]
  0.1     54.75     0.08        2    40.00    40.00  .__shift_dipole_or_seed_module_MOD_dipole_number_array [57]
  0.1     54.82     0.07        1    70.00   100.00  .__input_and_apply_flags_module_MOD_input_flags [51]
  0.1     54.89     0.07                             .local_unlock_lw_ppc_mp [59]
  0.1     54.95     0.06        1    60.00    62.00  .model_forward_mag [62]
  0.1     55.01     0.06                             ._xlfBeginIO [53]
  0.1     55.07     0.06                             .local_lock_ppc_mp [63]
  0.1     55.12     0.05        9     5.56     8.22  .get_multimodel_xmagmodt [58]
  0.1     55.17     0.05                             ._moveeq [64]
```

Figure D4. OpenMP profile of UXOPAC program

design_and_apply_filter_module Original

```
      DO IY_CENTER_POINT = 1, NY
      DO IX_CENTER_POINT = 1, NX
        IXY = IXY + 1
        IF (FLAG_DATA_INOUT(IXY)) THEN
!       COMPUTE GAPPED_DATA AND FLAG_GAPPED_DATA
        CALL EXTRACT_GAPPED_DATA (GAPPED_DATA, FLAG_GAPPED_DATA,
     &                            LXM1D2, LYM1D2, NX, NY,
     &                            IX_CENTER_POINT,
     &                            IY_CENTER_POINT,
     &                            DATA_IN, FLAG_DATA_IN)
!
          N_FLAG_GAPPED_DATA = COUNT(FLAG_GAPPED_DATA)
          IF (N_FLAG_GAPPED_DATA == LFILXY) THEN
!
            CALL APPLY_GAPLESS_FILTER(CENTER_POINT_OUT,
     &                                LXM1D2, LYM1D2,
     &                                GAPPED_DATA, FILTER_RANK2)
          ELSE
!               IF(PROCESS == 'FILTER')
!    &                WRITE(6,*) 'N_FLAG_GAPPED_DATA=',
!    &                           N_FLAG_GAPPED_DATA
!
            SELECT CASE (TYPE_FILTER)
              CASE ('HIGHPASS_GGN')
                IF (FIRST_CALL_COMPUTE_AND_APPLY_GAPPED_GNF) THEN
!               COMPUTE SCALE_OFF_CENTER, XK_SUBX, XK_SUBY
                CALL COMPUTE_GAPPED_GN_FILTER (FILTER_RANK2,
     &                                         LXM1D2, LYM1D2,
     &                                         FLAG_GAPPED_DATA,
     &                                         SCALE_OFF_CENTER,
     &                                         XK_SUBX, XK_SUBY)
                  IF (PROCESS == 'INVERSE_MODEL') THEN
                  SCALE_OFF_CENTER_ARRAY(IXY)
     &                          = SCALE_OFF_CENTER
                  XK_SUBX_ARRAY(IXY) = XK_SUBX
                  XK_SUBY_ARRAY(IXY) = XK_SUBY
                  END IF
                ELSE
                  SCALE_OFF_CENTER = SCALE_OFF_CENTER_ARRAY(IXY)
                  XK_SUBX                = XK_SUBX_ARRAY(IXY)
                  XK_SUBY                = XK_SUBY_ARRAY(IXY)
                END IF
```

```
                CALL APPLY_GAPPED_GN_FILTER (FILTER_RANK2,
     &                                       GAPPED_DATA,
     &                                       CENTER_POINT_OUT,
     &                                       LXM1D2, LYM1D2,
     &                                       FLAG_GAPPED_DATA,
     &                                       SCALE_OFF_CENTER,
     &                                       XK_SUBX, XK_SUBY)
              CASE('BANDPASS_GGN','LOG_GGN')
                CALL COMPUTE_GAPPED_BPGN_FILTER (FILTER_RANK2,
     &                                           LXM1D2, LYM1D2,
     &                                           FLAG_GAPPED_DATA,
     &                                           SCALE_OFF_CENTER,
     &                                           XK_SUBX, XK_SUBY)
                CALL APPLY_GAPPED_BPGN_FILTER (FILTER_RANK2,
     &                                         GAPPED_DATA,
     &                                         CENTER_POINT_OUT,
     &                                         LXM1D2, LYM1D2,
     &                                         FLAG_GAPPED_DATA,
     &                                         XK_SUB_ZERO,
     &                                         XK_SUBX, XK_SUBY)
            END SELECT
          END IF
          DATA_INOUT(IXY) = CENTER_POINT_OUT
        END IF
      END DO
      END DO
```

Figure D5. Original code to design and apply GGN filter.

design_and_apply_filter_module OpenMP

```
!$omp parallel do
!$omp+ private(IXY,N,gapped_data,flag_gapped_data,
!$omp+ center_point_out,scale_off_center,xk_subx,
!$omp+ xk_suby)
    DO IY_CENTER_POINT = 1, NY
    DO IX_CENTER_POINT = 1, NX
c       IXY = IXY + 1
        IXY = IX_CENTER_POINT + (IY_CENTER_POINT-1)*NX
        IF (FLAG_DATA_INOUT(IXY)) THEN
!       COMPUTE GAPPED_DATA AND FLAG_GAPPED_DATA
          CALL EXTRACT_GAPPED_DATA (GAPPED_DATA, FLAG_GAPPED_DATA,
    &                       LXM1D2, LYM1D2, NX, NY,
    &                       IX_CENTER_POINT,
    &                       IY_CENTER_POINT,
    &                       DATA_IN, FLAG_DATA_IN,N)
!
c         N_FLAG_GAPPED_DATA = COUNT(FLAG_GAPPED_DATA)
c         IF (N_FLAG_GAPPED_DATA == LFILXY) THEN
          IF (N == LFILXY) THEN
!
            CALL APPLY_GAPLESS_FILTER(CENTER_POINT_OUT,
    &                       LXM1D2, LYM1D2,
    &                       GAPPED_DATA, FILTER_RANK2)
            ELSE
            SELECT CASE (TYPE_FILTER)
              CASE ('HIGHPASS_GGN')
            IF (FIRST_CALL_COMPUTE_AND_APPLY_GAPPED_GNF) THEN
!             COMPUTE SCALE_OFF_CENTER, XK_SUBX, XK_SUBY
              CALL COMPUTE_GAPPED_GN_FILTER (FILTER_RANK2,
    &                           LXM1D2, LYM1D2,
    &                           FLAG_GAPPED_DATA,
    &                           SCALE_OFF_CENTER,
    &                           XK_SUBX, XK_SUBY)
                IF (PROCESS == 'INVERSE_MODEL') THEN
                SCALE_OFF_CENTER_ARRAY(IXY)
    &                   = SCALE_OFF_CENTER
                XK_SUBX_ARRAY(IXY) = XK_SUBX
                XK_SUBY_ARRAY(IXY) = XK_SUBY
                END IF
```

```
                ELSE
                SCALE_OFF_CENTER =
                                SCALE_OFF_CENTER_ARRAY(IXY)
                XK_SUBX         = XK_SUBX_ARRAY(IXY)
                XK_SUBY         = XK_SUBY_ARRAY(IXY)
                END IF
            CALL APPLY_GAPPED_GN_FILTER (FILTER_RANK2,
    &                       GAPPED_DATA,
    &                       CENTER_POINT_OUT,
    &                       LXM1D2, LYM1D2,
    &                       FLAG_GAPPED_DATA,
    &                       SCALE_OFF_CENTER,
    &                       XK_SUBX, XK_SUBY)
            CASE('BANDPASS_GGN','LOG_GGN')
              CALL COMPUTE_GAPPED_BPGN_FILTER (FILTER_RANK2,
    &                         LXM1D2, LYM1D2,
    &                         FLAG_GAPPED_DATA,
    &                         SCALE_OFF_CENTER,
    &                         XK_SUBX, XK_SUBY)
              CALL APPLY_GAPPED_BPGN_FILTER (FILTER_RANK2,
    &                       GAPPED_DATA,
    &                       CENTER_POINT_OUT,
    &                       LXM1D2, LYM1D2,
    &                       FLAG_GAPPED_DATA,
    &                       XK_SUB_ZERO,
    &                       END SELECT
        END IF
          DATA_INOUT(IXY) = CENTER_POINT_OUT
      END IF
  END DO
  END DO
```

Figure D6. OpenMP code to design and apply GGN filter.

design_and_apply_filter_module tuned 1/2

```
 SELECT CASE (TYPE_FILTER)
      CASE ('HIGHPASS_GGN')
       IF (FIRST_CALL_COMPUTE_AND_APPLY_GAPPED_GNF) THEN
         IF (PROCESS == 'INVERSE_MODEL') THEN
          DO IY_CENTER_POINT = 1, NY
          DO IX_CENTER_POINT = 1, NX
             IXY = IXY + 1
             IF (FLAG_DATA_INOUT(IXY)) THEN
!          COMPUTE GAPPED_DATA AND FLAG_GAPPED_DATA
      CALL EXTRACT_GAPPED_DATA (GAPPED_DATA, FLAG_GAPPED_DATA,
    &                           LXM1D2, LYM1D2, NX, NY,
    &                           IX_CENTER_POINT,
    &                           IY_CENTER_POINT,
    &                           DATA_IN, FLAG_DATA_IN,N)
              IF (N == LFILXY) THEN
               CALL APPLY_GAPLESS_FILTER(CENTER_POINT_OUT,
    &                              LXM1D2, LYM1D2,
    &                              GAPPED_DATA, FILTER_RANK2)
              ELSE
               CALL COMPUTE_GAPPED_GN_FILTER (FILTER_RANK2,
    &                                  LXM1D2, LYM1D2,
    &                                  FLAG_GAPPED_DATA,
    &                                  SCALE_OFF_CENTER,
    &                                  XK_SUBX, XK_SUBY)
               SCALE_OFF_CENTER_ARRAY(IXY) = SCALE_OFF_CENTER
               XK_SUBX_ARRAY(IXY) = XK_SUBX
               XK_SUBY_ARRAY(IXY) = XK_SUBY
               CALL APPLY_GAPPED_GN_FILTER (FILTER_RANK2,
    &                                 GAPPED_DATA,
    &                                 CENTER_POINT_OUT,
    &                                 LXM1D2, LYM1D2,
    &                                 FLAG_GAPPED_DATA,
    &                                 SCALE_OFF_CENTER,
    &                                 XK_SUBX, XK_SUBY)
              END IF
              DATA_INOUT(IXY) = CENTER_POINT_OUT
             END IF
          END DO
          END DO
           FIRST_CALL_COMPUTE_AND_APPLY_GAPPED_GNF = .FALSE.
```

```
        ELSE              !.NOT. INVERSE MODEL
          DO IY_CENTER_POINT = 1, NY
           DO IX_CENTER_POINT = 1, NX
             IXY = IXY + 1
             IF (FLAG_DATA_INOUT(IXY)) THEN
!          COMPUTE GAPPED_DATA AND FLAG_GAPPED_DATA
        CALL EXTRACT_GAPPED_DATA (GAPPED_DATA, FLAG_GAPPED_DATA,
    &                           LXM1D2, LYM1D2, NX, NY,
    &                           IX_CENTER_POINT,
    &                           IY_CENTER_POINT,
    &                           DATA_IN, FLAG_DATA_IN,N)
!
              IF (N == LFILXY) THEN
               CALL APPLY_GAPLESS_FILTER(CENTER_POINT_OUT,
    &                              LXM1D2, LYM1D2,
    &                              GAPPED_DATA, FILTER_RANK2)
              ELSE
               CALL COMPUTE_GAPPED_GN_FILTER (FILTER_RANK2,
    &                                  LXM1D2, LYM1D2,
    &                                  FLAG_GAPPED_DATA,
    &                                  SCALE_OFF_CENTER,
    &                                  XK_SUBX, XK_SUBY)
               CALL APPLY_GAPPED_GN_FILTER (FILTER_RANK2,
    &                                 GAPPED_DATA,
    &                                 CENTER_POINT_OUT,
    &                                 LXM1D2, LYM1D2,
    &                                 FLAG_GAPPED_DATA,
    &                                 SCALE_OFF_CENTER,
    &                                 XK_SUBX, XK_SUBY)
              END IF
              DATA_INOUT(IXY) = CENTER_POINT_OUT
             END IF
           END DO
          END DO
          FIRST_CALL_COMPUTE_AND_APPLY_GAPPED_GNF = .FALSE.
        ENDIF             !IF (PROCESS == 'INVERSE_MODEL')

      ELSE   !FIRST_CALL_COMPUTE_AND_APPLY_GAPPED_GNF
```

Figure D7. Tuned code to design and apply GGN filter – Part 1

design_and_apply_filter_module tuned 2/2

```
== .FALSE.
      DO IY_CENTER_POINT = 1, NY
        DO IX_CENTER_POINT = 1, NX
          IXY = IXY + 1
          IF (FLAG_DATA_INOUT(IXY)) THEN
          CALL EXTRACT_GAPPED_DATA (GAPPED_DATA, FLAG_GAPPED_DATA,
  &                        LXM1D2, LYM1D2, NX, NY,
  &                        IX_CENTER_POINT,
  &                        IY_CENTER_POINT,
  &                        DATA_IN, FLAG_DATA_IN, N)

           IF (N == LFILXY) THEN
             CALL APPLY_GAPLESS_FILTER(CENTER_POINT_OUT,
  &                          LXM1D2, LYM1D2,
  &                          GAPPED_DATA, FILTER_RANK2)

           ELSE
             CALL APPLY_GAPPED_GN_FILTER (FILTER_RANK2,
  &                            GAPPED_DATA,
  &                            CENTER_POINT_OUT,
  &                            LXM1D2, LYM1D2,
  &                            FLAG_GAPPED_DATA,
  &                            SCALE_OFF_CENTER_ARRAY(IXY),
  &                            XK_SUBX_ARRAY(IXY),
  &                            XK_SUBY_ARRAY(IXY))
           END IF
           DATA_INOUT(IXY) = CENTER_POINT_OUT
          END IF
        END DO
       END DO
       FIRST_CALL_COMPUTE_AND_APPLY_GAPPED_GNF = .FALSE.
     ENDIF    !IF (FIRST_CALL_COMPUTE_AND_APPLY_GAPPED_GNF)
         CASE('BANDPASS_GGN','LOG_GGN')
     DO IY_CENTER_POINT = 1, NY
     DO IX_CENTER_POINT = 1, NX
        IXY = IXY + 1
        IF (FLAG_DATA_INOUT(IXY)) THEN
         CALL EXTRACT_GAPPED_DATA (GAPPED_DATA, FLAG_GAPPED_DATA,
  &                        LXM1D2, LYM1D2, NX, NY,
  &                        IX_CENTER_POINT,
  &                        IY_CENTER_POINT,
  &                        DATA_IN, FLAG_DATA_IN,N)
           IF (N == LFILXY) THEN
           CALL APPLY_GAPLESS_FILTER(CENTER_POINT_OUT,
  &                          LXM1D2, LYM1D2,
  &                          GAPPED_DATA, FILTER_RANK2)
```

```
           ELSE
           CALL COMPUTE_GAPPED_BPGN_FILTER (FILTER_RANK2,
  &                            LXM1D2, LYM1D2,
  &                            FLAG_GAPPED_DATA,
  &                            SCALE_OFF_CENTER,
  &                            XK_SUBX, XK_SUBY)
           CALL APPLY_GAPPED_BPGN_FILTER (FILTER_RANK2,
  &                            GAPPED_DATA,
  &                            CENTER_POINT_OUT,
  &                            LXM1D2, LYM1D2,
  &                            FLAG_GAPPED_DATA,
  &                            XK_SUB_ZERO,
  &                            XK_SUBX, XK_SUBY)
          END IF
          DATA_INOUT(IXY) = CENTER_POINT_OUT
         END IF
        END DO
       END DO
       FIRST_CALL_COMPUTE_AND_APPLY_GAPPED_GNF = .FALSE.
     END SELECT
```

Figure D8. Tuned code to design and apply GGN filter – Part 2.

dipole_magnetics

```
      IXY = 1
      LOOP_Y:
     &DO  IY = 1, NY
          YPRIME      = (FLOAT(IY)-CENTER_IY) * DELTAY
          DO  IX = 1, NX
               XPRIME = (FLOAT(IX)-CENTER_IX) * DELTAX
               X = XPRIME * COS_THETA - YPRIME * SIN_THETA
               Y = YPRIME * COS_THETA + XPRIME * SIN_THETA
               XSQ = X**2
               YSQ = Y**2
               R = SQRT(XSQ + YSQ + ZSQ)
               DIPOLE_MOMENT_DIV_R5 = DIPOLE_MOMENT/R**5
               DELTA_V_MAGF = (2.*ZSQ - XSQ - YSQ) * SIN_ALPHA
     &                      - 3. * X * Z * COS_ALPHA_COS_DELTA
     &                      - 3. * Y * Z * COS_ALPHA_SIN_DELTA
               DELTA_H_MAGF = (2.*XSQ - YSQ - ZSQ) * COS_ALPHA_(
     &                      - 3. * X * Z * SIN_ALPHA
     &                      - 3. * X * Y * COS_ALPHA_SIN_DELTA
!
               DELTA_T_MAG = (DELTA_V_MAGF * SIN_EYE
     &                     + DELTA_H_MAGF * COS_EYE)
     &                     * DIPOLE_MOMENT_DIV_R5
!
               XMAGOBS(IXY) = XMAGOBS(IXY) + DELTA_T_MAG
               IXY = IXY + 1
          END DO
      END DO LOOP_Y
```

```
      yprime = (/((float(i)-center_iy)*deltay, i=1,ny)/)
      xprime = (/((float(i)-center_ix)*deltax, i=1,nx)/)

      DO  IY = 1, NY
      DO  IX = 1, NX
          X(IX,IY) = XPRIME(IX) * COS_THETA - YPRIME(IY) * SIN_THETA
          Y(IX,IY) = YPRIME(IY) * COS_THETA + XPRIME(IX) * SIN_THETA
      ENDDO
      ENDDO
      XSQ = X*X
      YSQ = Y*Y
      call vssqrt(R, xsq+ysq+zsq, NX*NY)
      R = R*R*R*R*R                    !R^5
      call vsrec(R, R, NX*NY)
!$omp parallel do
!$omp+ private(
!$omp+ dipole_moment_div_r5, delta_v_magf,
!$omp+ delta_h_magf, delta_t_mag)

      LOOP_Y:
     &DO  IY = 1, NY
          DO  IX = 1, NX
                IXY = IX + (IY-1)*NX
               DIPOLE_MOMENT_DIV_R5 = DIPOLE_MOMENT*R(IX,IY)
               DELTA_V_MAGF = (2.*ZSQ - XSQ(IX,IY) - YSQ(IX,IY)) * SIN_ALPHA
     &                      - 3. * X(IX,IY) * Z * COS_ALPHA_COS_DELTA
     &                      - 3. * Y(IX,IY) * Z * COS_ALPHA_SIN_DELTA
              DELTA_H_MAGF=(2.*XSQ(IX,IY)-YSQ(IX,IY)-ZSQ)*COS_ALPHA_COS_DELTA
     &                      - 3. * X(IX,IY) * Z * SIN_ALPHA
     &                      - 3. * X(IX,IY) * Y(IX,IY) * COS_ALPHA_SIN_DELTA
!
               DELTA_T_MAG = (DELTA_V_MAGF * SIN_EYE
     &                     + DELTA_H_MAGF * COS_EYE)
     &                     * DIPOLE_MOMENT_DIV_R5
!
               XMAGOBS(IXY) = XMAGOBS(IXY) + DELTA_T_MAG
          END DO
      END DO LOOP_Y
```

Figure D9. Portion of code for parallel processing to compute magnetic field of a dipole.

	small	large
Original	35.56	62.01
Tuned	32.56	52.78
2cpu	25.18	35.79
4cpu	20.24	25.76
8cpu	17.75	21.06
16cpu	16.60	18.85

Table D1. Relative performance for small and large jobs using the original code, tuned code, and parallel processing with variable numbers of central processing units.

Appendix E
Target A04 (20 mm Projectile)

Target A04 is a 20 mm, 0.09-kg projectile, which the AEC emplaced with a slight inclination (Ψ_T = 16 deg,) at a depth to center of 20 cm (Figure E1, Table E1). Figures E2-E21 plot the A04 anomaly and results of inversion jobs. The results and parameters of 16 jobs are presented in Tables E2-E4).

Appendix E - Figures

E1. Target A04: 20-mm projectile …… 110
E2. Regional setting of A04 anomaly …… 111
E3. A04 anomaly in 1.5-m window …… 111
E4. A04 anomaly and 289 flagged nodes in two swaths ……112
E5. A04 anomaly and 199 flagged nodes in one swath ……112
E6. EAGGN filtered A04 anomaly (L_F = 0.5 m, L_D = 1.5 m) ……113
E7. Single-swath EAGGN filtered A04 anomaly (L_F = 0.5 m) ……113
E8. EAGGN filtered A04 anomaly (L_F = 0.75 m, L_D = 1.5 m) ……114
E9. Single-swath EAGGN filtered A04 anomaly (L_F = 0.75 m) ……114
E10. EAGGN filtered A04 anomaly (L_F = 1 m, L_D = 1.5 m) ……115
E11. Single-swath EAGGN filtered A04 anomaly (L_F = 1 m) ……115
E12. EAGGN filtered A04 anomaly (L_F = 1.25 m, L_D = 1.5 m) ……116
E13. Single-swath EAGGN filtered A04 anomaly (L_F = 1.25 m) ……116
E14. A04 anomaly and 127 flagged nodes in a 1-m data window ……117
E15. A04 anomaly and 99 flagged nodes in one swath (L_D = 1 m) ……117
E16. Two-swath EAGGN filtered A04 anomaly (L_F = 1 m, L_D = 1 m) ……118
E17. One-swath EAGGN filtered A04 anomaly (L_F = 1 m, L_D = 1 m) ……118
E18. Two-swath EAGGN filtered field of A04 inverse model (L_F = 1 m, L_D = 1 m) ……119
E19. One-swath EAGGN filtered field of A04 inverse model (L_F = 1 m, L_D = 1 m) ……119
E20. Residual field for EAGGN filtered A04 anomaly (L_F = 1 m, L_D = 1 m) ……120
E21. Residual field for 1-swath EAGGN filtered A04 anomaly (L_F = 1 m, L_D = 1 m) ……120

Appendix E - Tables

E1. Ground truth for target A04 ……109
E2. Dipole positions for anomaly A04 inversions ……121
E3. Dipole parameters for anomaly A04 inversions ……122
E4. A04 data window parameters ……122

Figure 21. Target A04; 20 mm projectile.

Table 1. A04 ground truth parameters.

Description	Projectile
Material	Alloy Steel
Length, L_T	75 mm
Diameter, D_T	20 mm
Weight	0.091 kg
Grid azimuth, Φ_T	207 deg
Inclination, Ψ_T	16 deg
Depth, Z_C	20 cm
UTM northing, Yc	4369584.949 m
UTM easting, X_C	402812.334 m
Ratio of depth below magnetometer to target length, R_{DL} †	6.0
Vertical projection of target's length, L_V (= $L_T \sin \Psi_T$)	2 cm
Horizontal projection of target's length, L_H (= $L_T \cos \Psi_T$)	7 cm
Nose-to-center offsets (Xn-Xc, Yn-Yc, Zn-Zc)	(-1, -3, 1) cm

† $R_{DL} = (Z_C+H_M)/L_T$; magnetometer elevation, $H_M = 0.25$ m

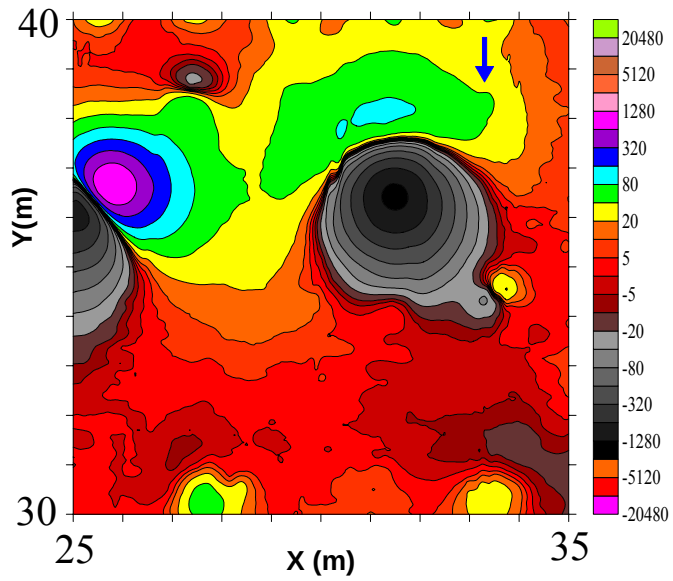

Figure E2. Regional setting of the A04 anomaly (blue arrow), which is a slight disturbance to the peak of the much larger B05 anomaly. The magnetic field contours are at zero and $\pm 2^n \cdot 5$ nT, where n is a non-negative integer.

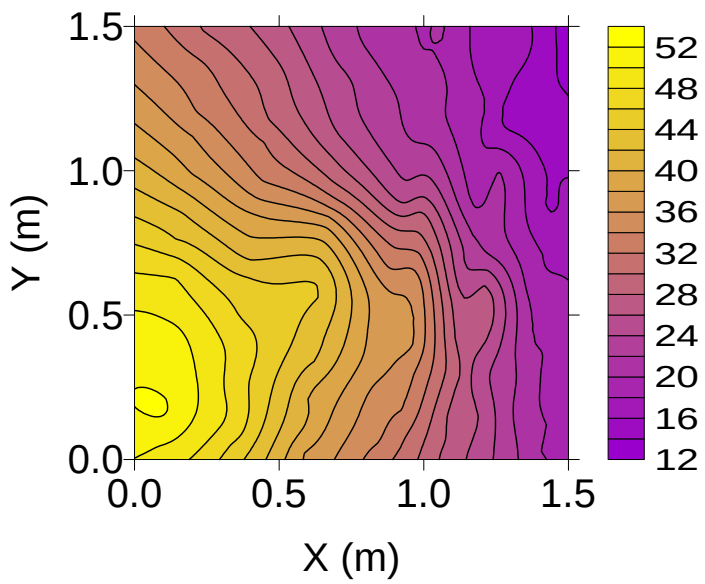

Figure E3. The anomaly of target A04 as evidenced by a slight disturbance to the peak of the much larger B05 anomaly. High frequency noise is associated with the overlap of two swaths of the MTADS cart. Despite the lack of closed contours associated with this anomaly resultant from a 20 mm projectile, EAGGN IIF was used to obtain successful inversions. The contour interval is 2 nT.

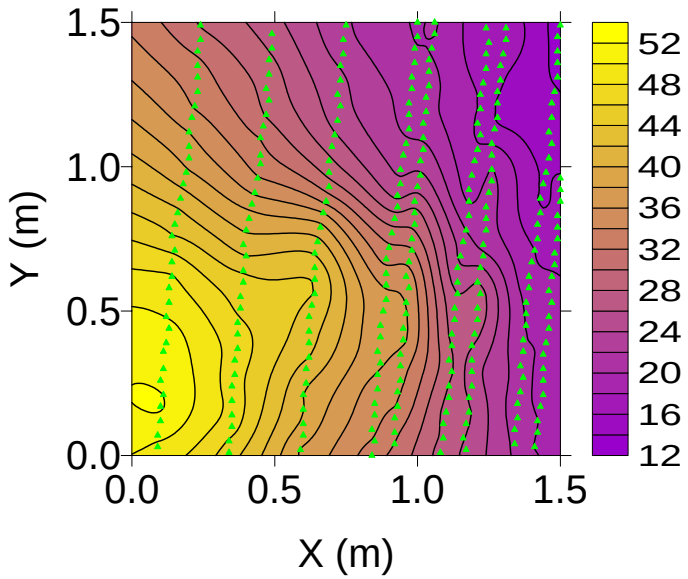

Figure E4. The A04 anomaly and the 289 flagged nodes (green triangles) nearest to stations in two swaths of the MTADS cart. Noise associated with the overlap of these swaths may indicate positional errors or artifacts of the pre-inversion filtering. These data were input to flag-node inversion jobs 7-11, which used EAGGN IIF. For $1 \leq L_F \leq 1.5$ m (jobs 9-11), Δ_C is 3 cm, $14 \leq (Z\text{-}Z_C) \leq 16$ cm, $33.6 \leq \theta \leq 34.0$ deg, and $33.3 \leq \Psi \leq 33.7$ deg. Results may be improved by use of single-swath inversion. The contour interval is 2 nT.

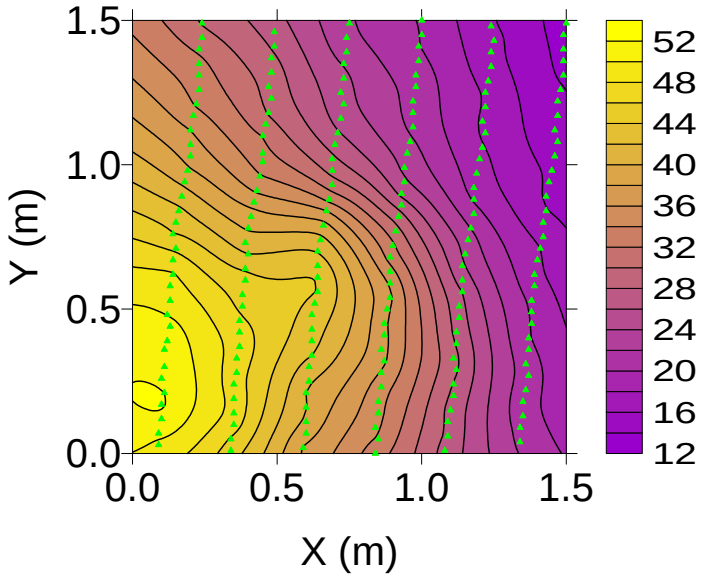

Figure E5. The A04 anomaly as defined by 199 flagged nodes (green triangles) nearest to stations in a single swath of the MTADS cart. These data were input to single-swath inversions using EAGGN IIF (jobs 12-16). For $0.75 \leq L_F \leq 1.25$ m (jobs 13-15), Δ_C is 5 cm, $2 \leq (Z\text{-}Z_C) \leq 7$ cm, $26.5 \leq \theta \leq 28.4$ deg, and $39.1 \leq \Psi \leq 41.0$ deg. The contour interval is 2 nT.

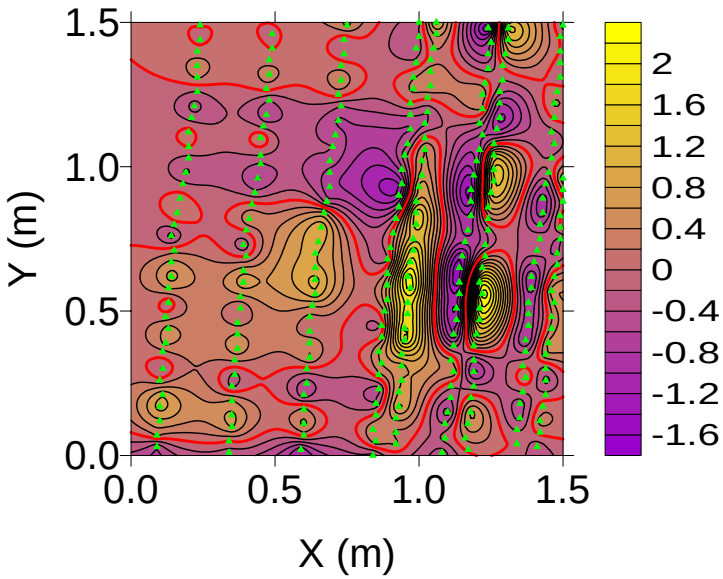

Figure E6. The EAGGN filtered A04 anomaly (L_F = 0.5 m, L_D = 1.5 m) as defined by 289 flagged nodes (green triangles) nearest to stations in two swaths of the MTADS cart. For job 7, using these data, Δ_C is 6 cm, (Z-Z_C) is 22 cm, θ is 22.2 deg, and Ψ is 48.1 deg. Larger filters (L_F > 0.5 m) yielded better results (jobs 8-11). The zero contour is red (contour interval = 0.2 nT).

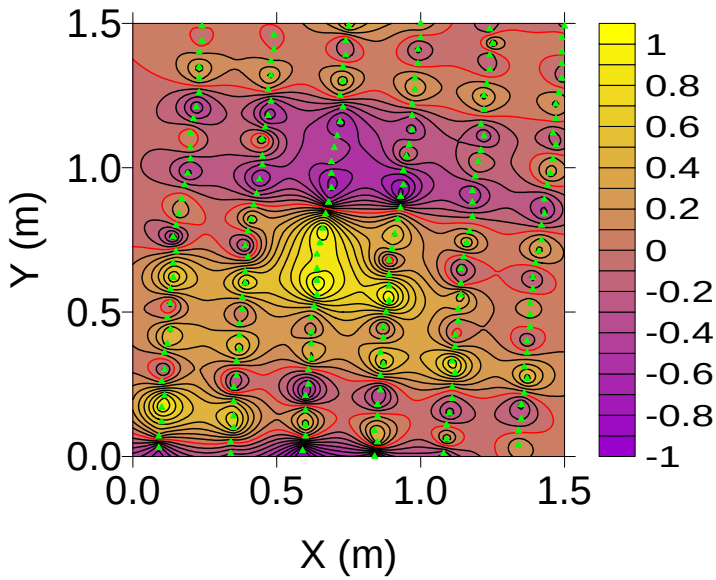

Figure E7. The EAGGN filtered A04 anomaly (L_F = 0.5 m, L_D = 1.5 m) as defined by 199 flagged nodes (green triangles) nearest to stations in one swath of the MTADS cart. For the single-swath inversion using these data (job 12), Δ_C is 8 cm, (Z-Z_C) is 8 cm, θ is 50.9 deg, and Ψ is 16.4 deg. Large filters (L_F > 0.5 m) yielded better results (jobs 13-16). The zero contour is red and the contour interval is 0.1 nT.

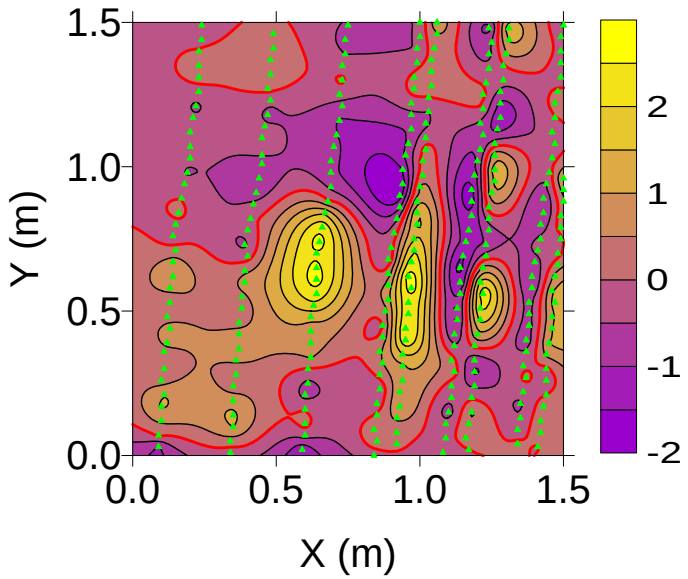

Figure E8. The EAGGN filtered A04 anomaly (L_F = 0.75 m, L_D = 1.5 m) as defined by 289 nodes (green triangles). For job 8, using these data, Δ_C is 5 cm, (Z-Z_C) is 11 cm, θ is 36.4 deg, and Ψ is 31.1 deg. Single-swath inversion yielded a better result. The zero contour is red and the contour interval is 0.5 nT.

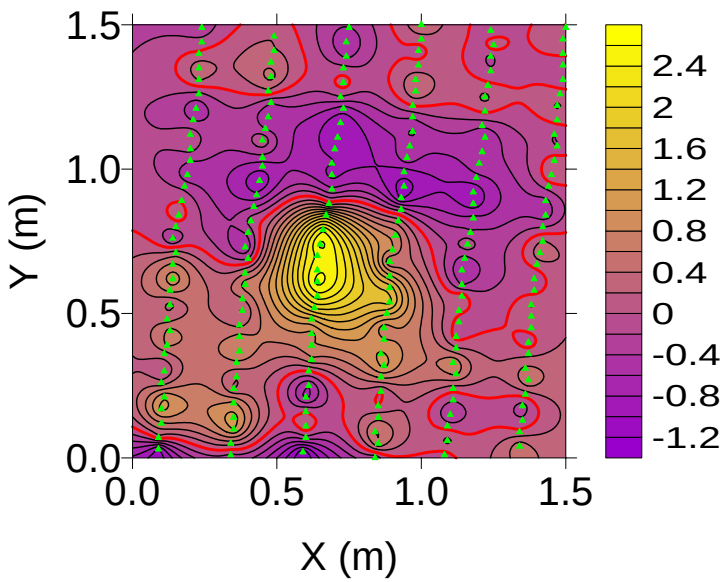

Figure E9. The EAGGN filtered A04 anomaly (L_F = 0.75 m, L_D = 1.5 m) as defined by 199 flagged nodes (green triangles) nearest to stations in a single swath. The central peak is well defined in these filtered data. For single-swath inversion using these data (job 13), Δ_C is 5 cm, (Z-Z_C) is 2 cm, θ is 26.5 deg, and Ψ is 41.0 deg. The anomaly is better defined by single-swath filtering. The zero contour is red and the contour interval is 0.1 nT.

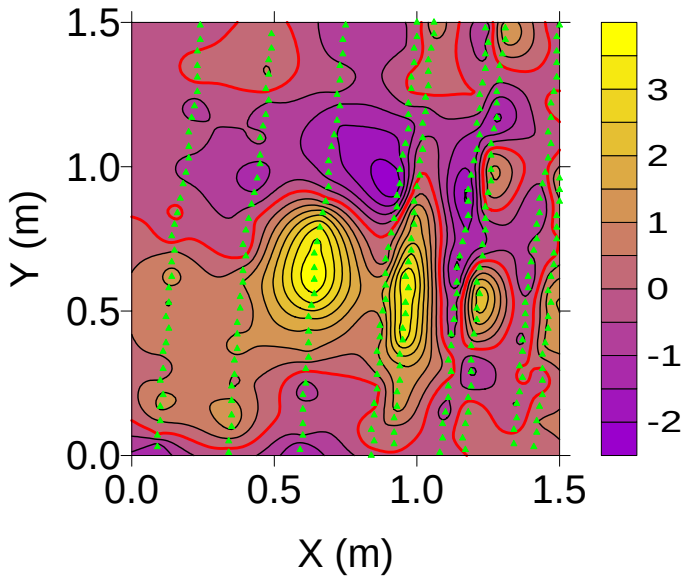

Figure E10. The EAGGN filtered A04 anomaly (L_F = 1 m, L_D = 1.5 m) as defined at 289 nodes (green triangles). For job 9, using these data, Δ_C is 3 cm, (Z-Z_C) is 14 cm, θ is 33.8 deg, and Ψ is 33.5 deg. High-frequency noise in these multi-swath data is apparent. By contrast, for single-swath inversion (job x) (Z-Z_C) is 5 cm. The zero contour is red and the contour interval is 0.5 nT.

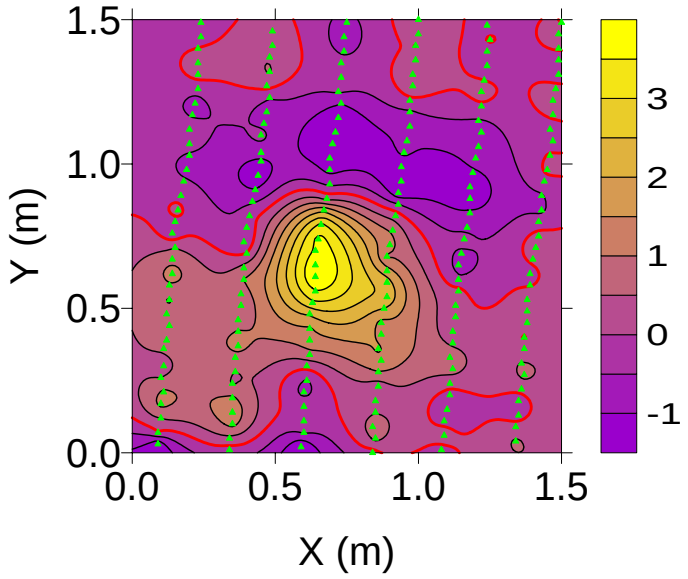

Figure E11. The EAGGN filtered A04 anomaly (L_F = 1 m, L_D = 1.5 m) as defined by 199 nodes (green triangles). The central peak and associated low are apparent. For single-swath inversion of these data (job 14), Δ_C is 5 cm, (Z-Z_C) is 5 cm, θ is 28.4 deg, and Ψ is 39.1 deg. The zero contour is red and the contour interval is 0.5 Nt.

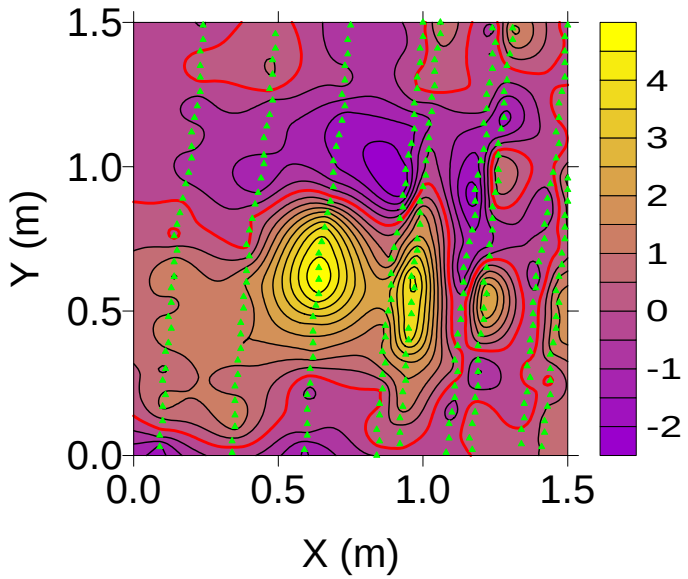

Figure E12. The EAGGN filtered A04 anomaly (L_F = 1.25 m, L_D = 1.5 m) as defined by 289 nodes (green triangles). High frequency noise is associated with swath overlap. For job 10 using these data, ΔC is 5 cm, $(Z\text{-}Z_C)$ is 11 cm, θ is 34.0 deg, and Ψ is 33.3 deg. By contrast, for single-swath inversion θ is 26.7 deg, and Ψ is 40.9 deg. The zero contour is red and the contour interval is 0.5 nT.

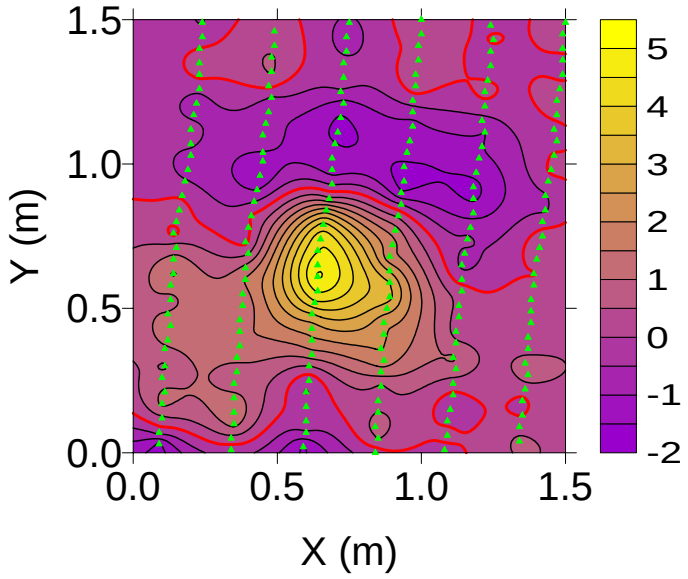

Figure E13. The EAGGN filtered A04 anomaly (L_F = 1.25 m, L_D = 1.5 m) and 199 flagged nodes (green triangles). For job 15 using these data, Δ_C is 5 cm, $(Z\text{-}Z_C)$ is 7 cm, θ is 26.7 deg, and Ψ is 40.9 deg. Similarly, for single-swath IIF with L_F equal to 1.5 m, θ is 27.4 deg, and Ψ is 40.2 deg. The zero contour is red and the contour interval is 0.5 nT.

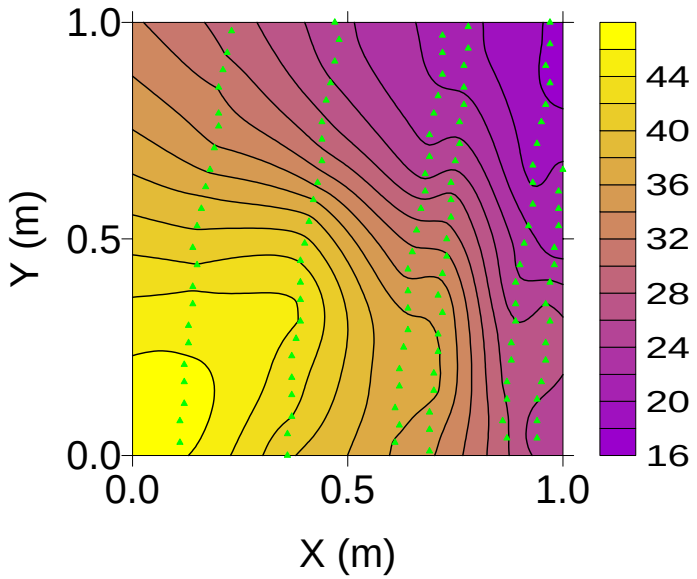

Figure E14. The A04 anomaly as defined by 127 flagged nodes (green triangles) nearest to stations in two swaths of the MTADS cart in a 1-m data window. Noise associated with the overlap of these swaths may indicate positional errors or artifacts of the pre-inversion filtering. These multi-swath data were input to EAGGN IIF inversion jobs 1-3. The contour interval is 2 nT.

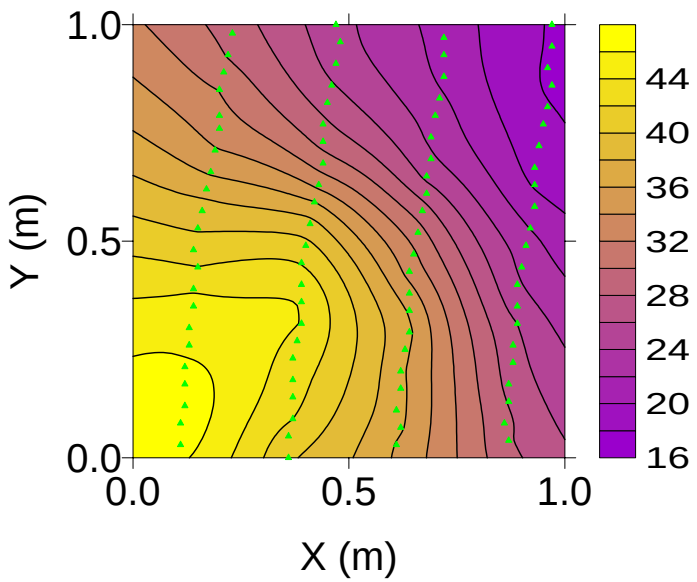

Figure E15. The A04 anomaly and 99 flagged nodes (green triangles) nearest to stations in a single swath. These data were input to single-swath, EAGGN IIF inversions (jobs 4-6). For L_F equal to 0.75 m (job 5), Δ_C is 6 cm, $(Z-Z_C)$ is 7 cm, θ is 21.8 deg, and Ψ is 45.9 deg. Similarly, for L_F equal to 1 m (job 6), Δ_C is 5 cm, $(Z-Z_C)$ is 5 cm, θ is 22.6 deg, and Ψ is 45.2 deg. The contour interval is 2 nT.

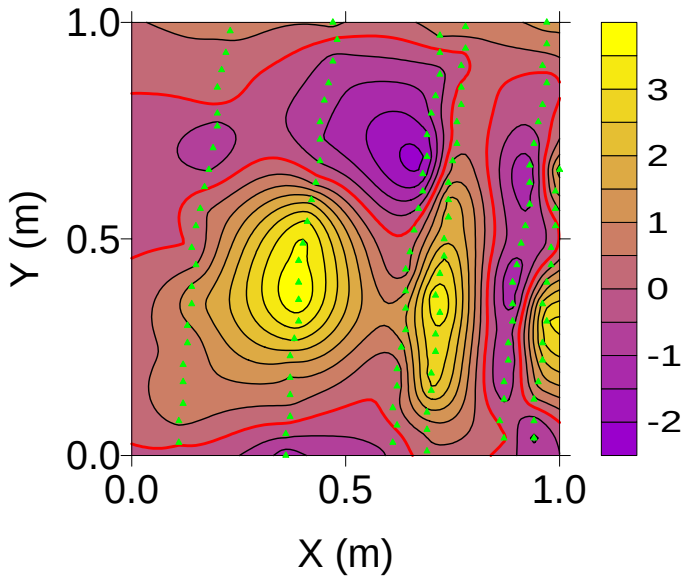

Figure E16. The EAGGN filtered A04 anomaly (L_F = 1 m, L_D = 1 m) as defined by 127 nodes (green triangles) from two swaths. For job 3, using these data, Δ_C is 6 cm, (Z-Z_C) is 16 cm, θ is 37.4 deg, and Ψ is 30.1 deg. By contrast, for single-swath inversion (job 6), Δ_C is 5 cm, (Z-Z_C) is 5 cm, θ is 22.6 deg, and Ψ is 45.2 deg. The zero contour is red and the contour interval is 0.5 nT.

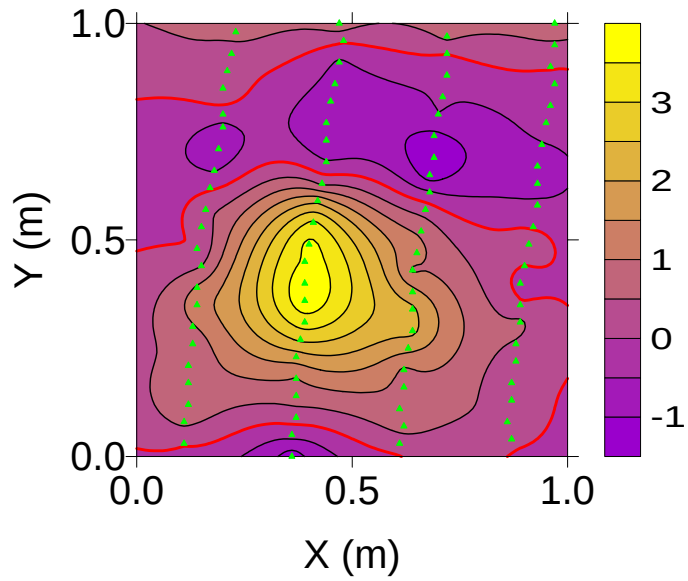

Figure E17. The EAGGN filtered A04 anomaly (L_F = 1 m, L_D = 1 m) and 89 flagged nodes (green triangles) in four tracks of magnetometers in a single MTADS swath. For these data (job 6), Δ_C is 5 cm, (Z-Z_C) is 5 cm, θ is 22.6 deg, and Ψ is 45.2 deg. For single-swath inversion with L_D equal to 1.5 m, the same dipole position was computed. The zero contour is red and the contour interval is 0.5 nT.

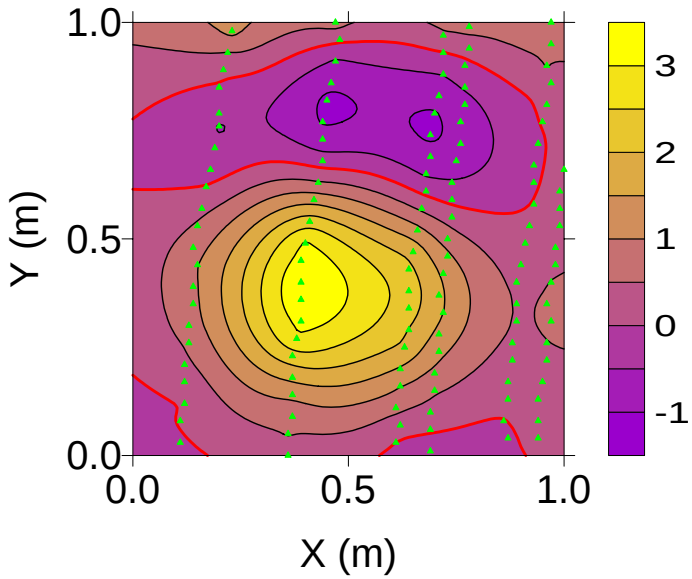

Figure E18. The EAGGN filtered field of the A04 IIF inverse model (L_F = 1 m, L_D = 1 m). Data at 127 nodes (green triangles) for two swaths of the MTADS cart were input to the filter and the inversion of job 3. The zero contour is red and the contour interval is 0.5 nT.

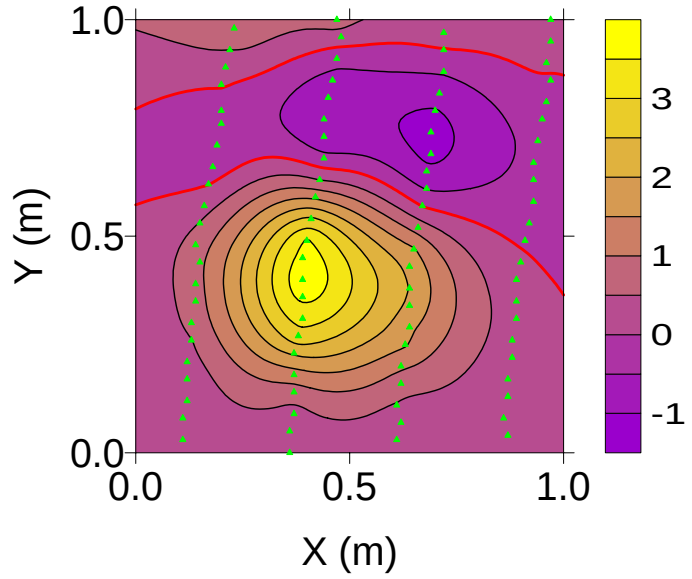

Figure E19. The EAGGN filtered field of the A04 IIF inverse model (L_F = 1 m, L_D = 1 m; job 6). The data at 89 nodes (green triangles) in a single swath were input to the filter and inversion. For this inverse-model Δ_C is 5 cm, (Z-Z_C) is 5 cm, θ is 22.6 deg, δ is –21.2 deg, Ψ is 45.2 deg, and M is 8.1 mA/m^2. The zero contour is red and the contour interval is 0.5 nT.

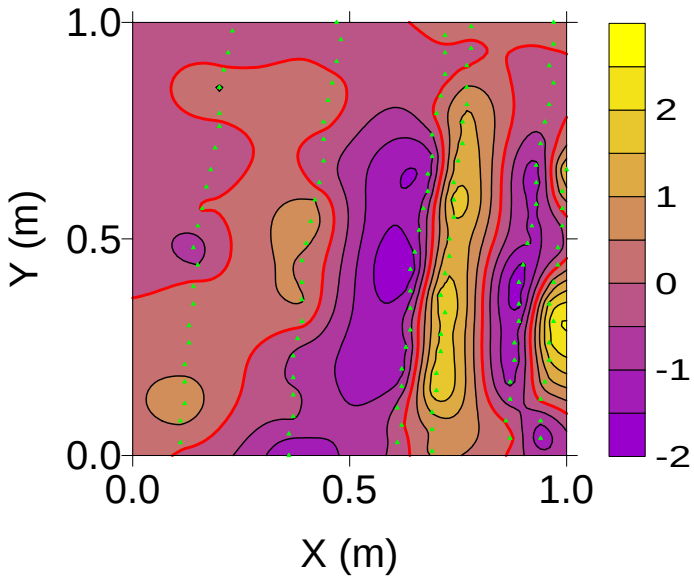

Figure E20. The residual field equal to the EAGGN filtered A04 anomaly (L_F = 1 m, L_D = 1 m) minus the filtered field of the inverse model at 127 nodes (green triangles). For this inversion (job 3), Δ_C is 6 cm, (Z-Z_C) is 16 cm, θ is 37.4 deg, and Ψ is 30.1 deg. The zero contour is red and the contour interval is 0.5 nT.

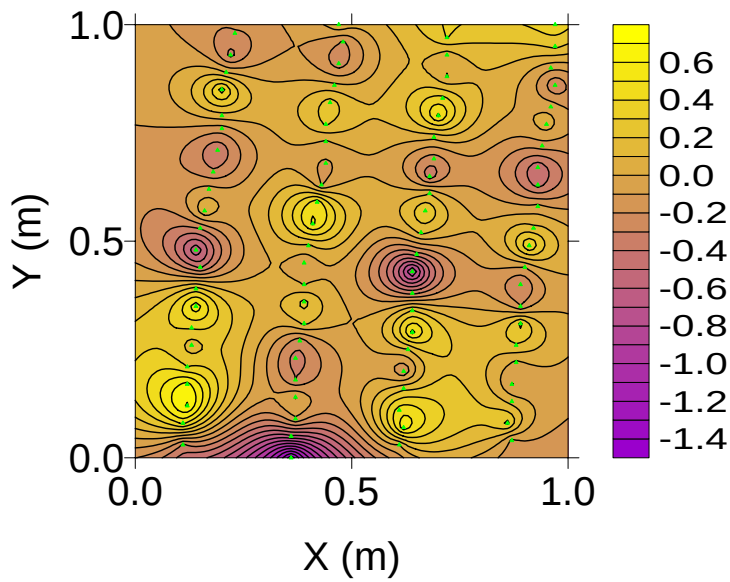

Figure E21. The residual field equal to the EAGGN filtered A04 anomaly (L_F = 1 m, L_D = 1 m) minus the filtered field of the single-swath inverse model (job 6) at nodes (green triangles). For this inversion, Δ_C is 5 cm, (Z-Z_C) is 5 cm, θ is 22.6 deg, and Ψ is 45.2 deg. The zero contour is red and the contour interval is 0.5 nT.

Table E2. A04 dipole (X,Y,Z) and target's center (X_C,Y_C,Z_C) UTM coordinates. X_R = 402000 m. Y_R = 4369000 m. Δ_C and E_Z are absolute horizontal and relative vertical displacements of the dipole from the target's center. [Δx = grid interval; L_D = data window size; L_F = filter size.]

Job	Δx cm	L_D m	L_F m	†	$X-X_R$ m	$Y-Y_R$ m	$X-X_C$ cm	$Y-Y_C$ cm	Δ_C cm	Z cm	$Z-Z_C$ cm	E_Z* %
1	1	1	0.5	E	812.65	584.81	32	-14	35	22	2	4
2	1	1	0.75	E	812.25	584.99	-8	4	9	35	15	33
3	1	1	1	E	812.29	584.98	-5	3	6	36	16	36
4	1	1	0.5	E §	812.27	584.97	-7	3	7	36	16	36
5	1	1	0.75	E §	812.27	584.94	-6	-1	6	27	7	16
6	1	1	1	E §	812.28	584.94	-5	-1	5	25	5	11
7	1	1.5	0.5	E	812.37	584.90	4	-5	6	42	22	49
8	1	1.5	0.75	E	812.29	584.97	-5	2	5	31	11	24
9	1	1.5	1.0	E	812.31	584.96	-2	1	3	34	14	31
10	1	1.5	1.25	E	812.31	584.96	-2	1	3	35	15	33
11	1	1.5	1.5	E	812.31	584.96	-2	1	3	36	16	36
12	1	1.5	0.5	E §	812.26	584.99	-7	5	8	28	8	18
13	1	1.5	0.75	E §	812.28	584.95	-5	0	5	22	2	4
14	1	1.5	1.0	E §	812.28	584.95	-5	0	5	25	5	11
15	1	1.5	1.25	E §	812.28	584.94	-5	-1	5	27	7	16
16	1	1.5	1.5	E §	812.28	584.94	-5	-1	5	29	9	20

† All jobs used the flag-node and IIGE options. **E** = EAGGN filter. § = single swath

* $E_Z = (Z-Z_C)/(Z_C+H_M)$; magnetometer elevation, H_M = 0.25 m; Z_C = 20 cm.

Table E3. A04 dipoles: θ = deviation angle (from earth's field); δ = dipole declination; Ψ = dipole inclination; M = dipole moment. Gx, Gy = gradient components; B = dc bias estimate; R = correlation coefficient. [Δx = grid interval; L_D = data window size; L_F = filter size.]

Job	Δx cm	L_D m	L_F m	†	θ deg	δ deg	Ψ deg	M mA•m^2	Gx nT/m	Gy nT/m	B nT	R
1	1	1	0.5	E	83.6	-105.1	8.4	13.9	-0.06	-0.14	-0.03	0.661
2	1	1	0.75	E	44.7	-30.9	24.2	17.6	0.34	0.03	0.14	0.639
3	1	1	1	E	37.4	-18.3	30.1	18.0	0.22	0.07	0.03	0.752
4	1	1	0.5	E §	41.1	-14.7	26.2	18.9	-0.06	0.13	0.00	0.777
5	1	1	0.75	E §	21.8	-19.9	45.9	9.32	0.03	0.04	-0.04	0.936
6	1	1	1	E §	22.6	-21.2	45.2	8.08	0.00	0.08	-0.05	0.959
7	1	1.5	0.5	E	22.2	10.4	48.1	29.8	-0.17	0.07	-0.01	0.428
8	1	1.5	0.75	E	36.4	-18.2	31.1	12.3	-0.11	-0.06	0.04	0.569
9	1	1.5	1.0	E	33.8	-15.4	33.5	15.0	-0.13	-0.02	0.03	0.722
10	1	1.5	1.25	E	34.0	-16.3	33.3	15.9	-0.06	0.02	0.05	0.798
11	1	1.5	1.5	E	33.6	-16.2	33.7	17.0	0.oo	0.08	0.04	0.845
12	1	1.5	0.5	E §	50.9	-13.2	16.4	10.1	-0.07	-0.02	0.05	0.605
13	1	1.5	0.75	E §	26.5	-17.9	41.0	6.32	-0.10	-0.14	0.07	0.835
14	1	1.5	1.0	E §	28.4	-17.9	39.1	8.12	-0.13	-0.14	0.08	0.889
15	1	1.5	1.25	E §	26.7	-19.1	40.9	9.35	-0.10	-0.07	0.06	0.916
16	1	1.5	1.5	E §	27.4	-19.5	40.2	10.8	-0.09	0.02	0.03	0.929

† All jobs used the flag-node and IIGE options. **E** = EAGGN filter. § = single swath

Table 4. A04 data windows: grid interval, Δx; absolute and relative window size, L_D, R_L; displacement of window's center from target's center, X_W-X_C, Y_W-Y_C; number of nodes along the x-and y-axes, N_X, N_Y; and the number and proportion of nodes flagged for inversion N_F, R_F.

Jobs	Δx (cm)	L_D (m)	R_L†	X_W-X_C (cm)	Y_W-Y_C (cm)	N_X	$N_X \bullet N_Y$	N_F	R_F (%)
1-3	1	1	2.2	0	-2	101	10201	127	1.2
4-6	1	1	2.2	0	-2	101	10201	89	0.9
7-11	1	1.5	3.3	0	-2	151	22801	289	1.3
12-16	1	1.5	3.3	0	-2	151	22801	199	0.9

†R_L= $L_D/(Z_C+H_M)$; depth to target center, Z_C = 20 cm; magnetometer height, H_M = 25 cm.

Appendix F
Target I04 (BDU submunition)

Target I04 is a 0.8 kg BDU submunition , which the AEC emplaced at a depth to center of 11 cm (Figure F1, Table F1). Figures F2-F17 plot the I04 anomaly and results of 27 inversion jobs (Tables F2-F4).

Appendix F Figures

F1. Target I04: BDU submunition 124
F2. Regional setting of I04 anomaly 125
F3. I04 anomaly, as manifest by a closed low engulfed by the much larger J04 anomaly ... 125
F4. I04 anomaly in a 1-m data window 126
F5. Inverse-modeled I04 dipole's field plus IIBE field 126
F6. Residual field: observed anomaly minus sum of I04 dipole's field and IIBE field 127
F7. Inverse-modeled I04 dipole's field plus IIGE field 127
F8. Residual field: observed anomaly minus sum of I04 dipole's field and IIGE field 128
F9. I04 anomaly in a 0.6-m data window 128
F10. Inverse-modeled I04 dipole's field plus IIBE field (job 2) 129
F11. Inverse-modeled I04 dipole's field plus IIGE field (job 3) 129
F12. Residual field: observed anomaly minus sum of dipole's field and IIBE field (job 2) ... 130
F13. Residual field: observed anomaly minus sum of dipole's field and IIGE field (job 3) ... 130
F14. EAGGN filtered I04 anomaly (L_{FX} = 0.75 m, L_{FY} = 0.3 m) 131
F15. EAGGN filtered I04 anomaly (L_{FX} = 0.75 m, L_{FY} = 0.6 m) 131
F16. GGN filtered I04 anomaly (L_{FX} = 0.75 m, L_{FY} = 0.6 m) 132
F17. GGN filtered I04 anomaly (L_{FX} = 0.75 m, L_{FY} = 0.2 m) 132

Appendix F Tables

F1. Ground truth for target I04 124
F2. Dipole positions for anomaly I04 inversions 133
F3. Dipole parameters for anomaly I04 inversions 134
F4. I04 data window parameters 135

Figure F1. Target I04; BDU submunition.

Table F1. Ground truth for target I04.*

Description	BDU submunition
Material	ferrous metallic
Length, L_T	97 mm (3.8 in)
Diameter, D_T	67 mm (2.6 in)
Weight	0.771 kg (1.7 lbs)
Depth, Z_C	11 cm
UTM northing, Yc	4369569.196 m
UTM easting, X_C	402815.212 m
Ratio of depth below magnetometer to target length, R_{DL} †	3.7

† $R_{DL} = (Z_C+H_M)/L_T$; magnetometer elevation, $H_M = 0.25$ m
* source: http://aec.

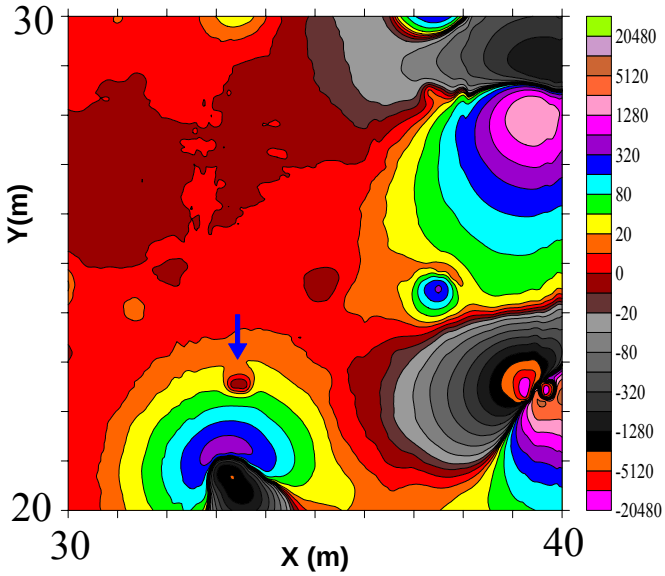

Figure F2. Regional setting of the I04 anomaly (blue arrow). The I04 anomaly is "engulfed" by the J04 anomaly, which results from two pieces or ferrous metallic clutter. The magnetic field contours are at zero and $\pm 2^n \cdot 10$ nT, where n is a non-negative integer.

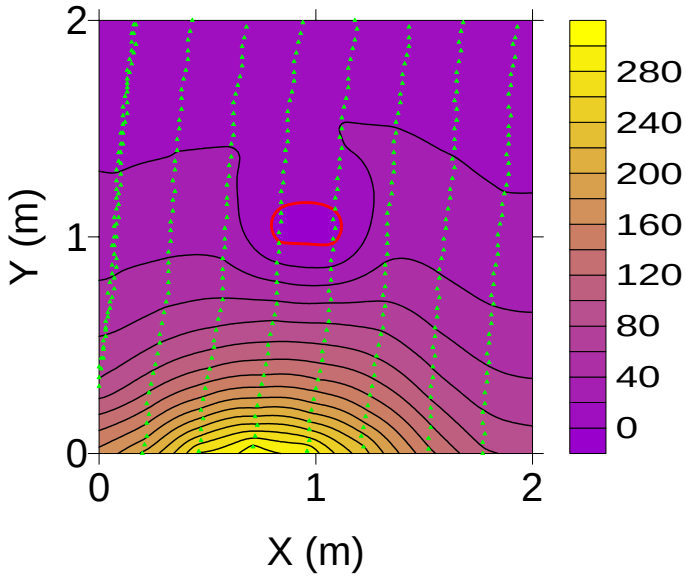

Figure F3. The I04 anomaly as manifest by a closed low engulfed by the peak of the much larger J04 anomaly. The flagged nodes (green triangles) are nearest to measurement stations. The center of this 2-m data window, used in jobs 23-27, is offset from the target by 3 cm. For EEGN IIF inversion job 25 (L_F = 0.75 cm), Δ_C is 5 cm and (Z-Z_C) is 1 cm. For job 24 (L_F = 0.5 cm), Δ_C is 0 cm and (Z-Z_C) is 2 cm. The zero magnetic field contour is red (contour interval = 20 nT).

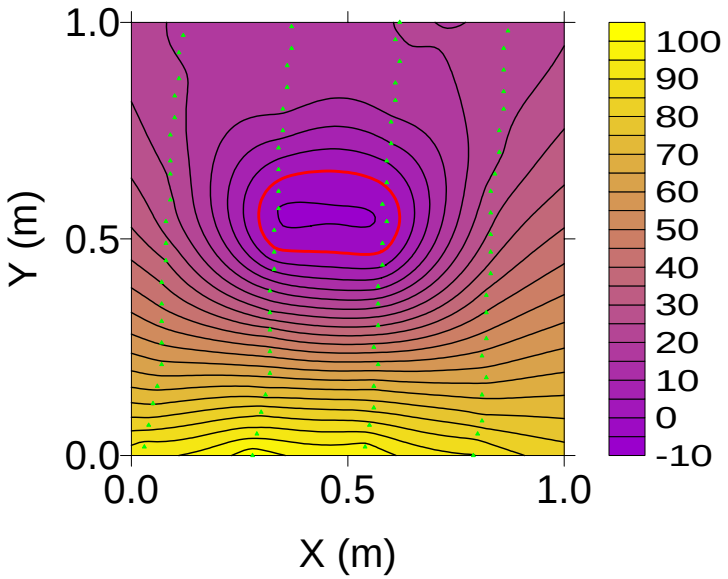

Figure F4. The I04 anomaly as manifest by a closed low near the north edge of the J04 anomaly's peak. The center of this 1-m data window, used in jobs 4-23, is offset from the target by 3 cm. The flagged nodes (green triangles) are nearest to measurement stations in a single swath of the MTADS cart. For non-IIF, IIBE inversion (job 5), Δ_C is 19 cm and $(Z\text{-}Z_C)$ is 53 cm. For IIGE job 7, Δ_C is 16 cm and $(Z\text{-}Z_C)$ is 18 cm. Although IIGE improves the inversion, it is inadequate to the task of overcoming the effects of the J04 anomaly in this data window. The zero contour is red (contour interval = 5 nT).

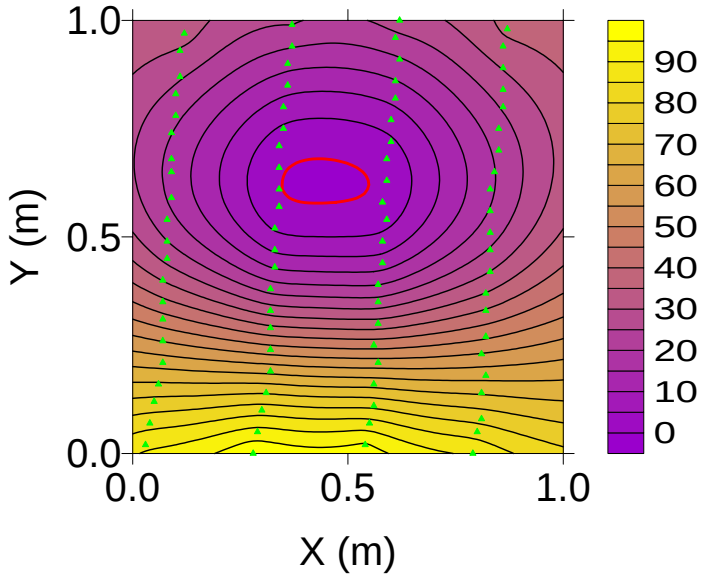

Figure F5. The inverse-modeled I04 dipole's field plus IIBE field derived form job 5. The flagged nodes (green triangles) were used in this inversion. The zero contour is red and the contour interval is 5 nT.

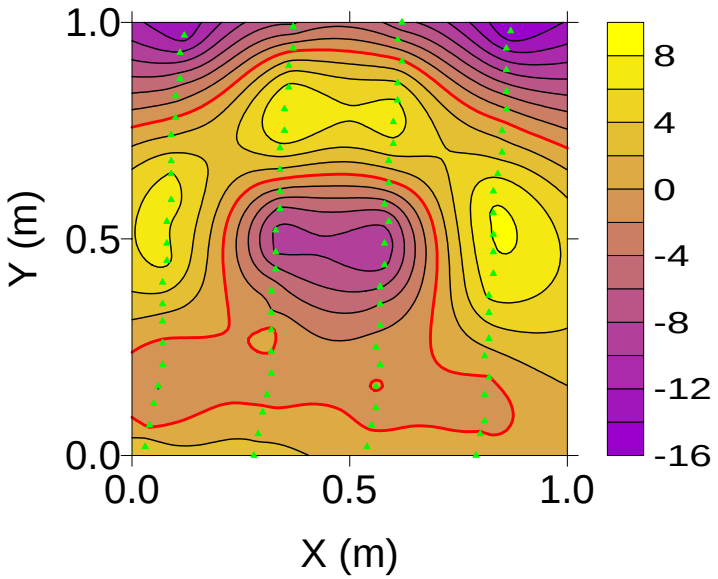

Figure F6. The residual field equal to the observed anomaly minus the sum of the inverse-modeled I04 dipole's field and IIBE field derived form job 5. The flagged nodes (green triangles) were used in this inversion. The zero contour is red and the contour interval is 2 nT.

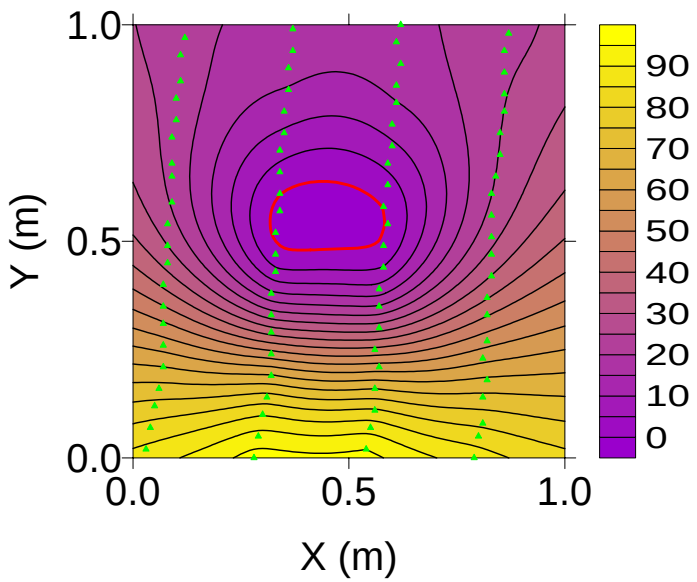

Figure F7. The inverse-modeled I04 dipole's field plus IIGE field derived from job 7. The flagged nodes (green triangles) were used in this inversion. The zero contour is red (contour interval = 5 nT).

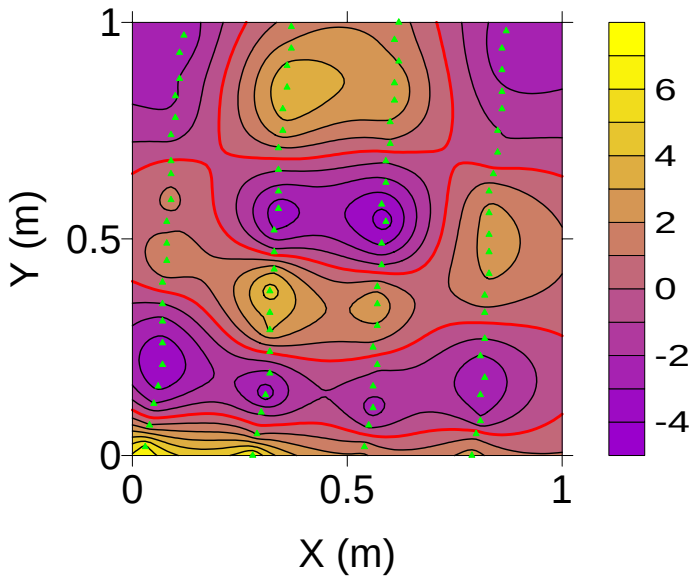

Figure F8. The residual field equal to the observed anomaly minus the sum of the inverse-modeled I04 dipole's field and IIGE field (job 7). The fit to the central peak of the I04 anomaly is improved using IIGE versus IIBE. IIGE, however, is inadequate for this data window. The flagged nodes (green triangles) were used in inversion jobs 5 and 7. The zero contour is red (contour interval = 1 nT).

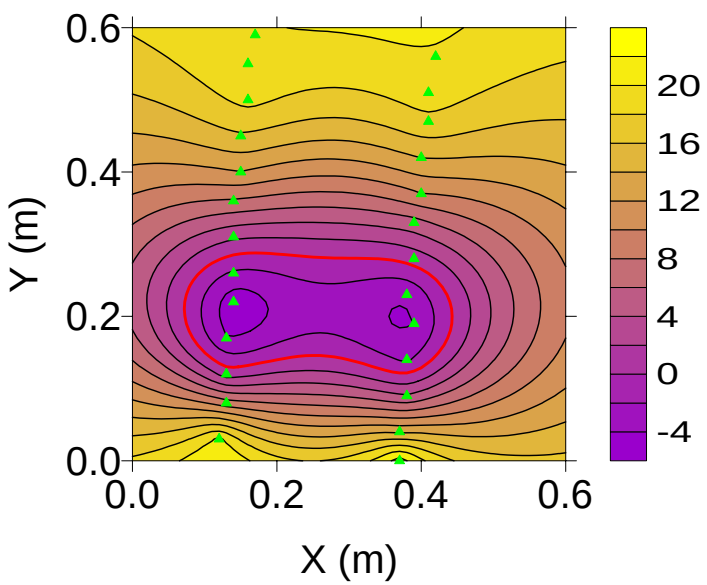

Figure F9. The I04 anomaly contoured from values at flagged nodes (green triangles) nearest to measurement stations in a 0.6-m data windows. For small-window, IIBE job 2, Δ_C is 8 cm, $(Z\text{-}Z_C)$ is –5 cm, θ is 78.2 deg, and Ψ is –10.8 deg. For IIGE job 3, Δ_C is 6 cm, $(Z\text{-}Z_C)$ is 1 cm, θ is 99.7 deg, and Ψ is –31.9 deg. These two inversions yield quite different dipole orientations. Although use of a small window improved the non-IIF inversion, it did not insure an accurate determination of the dipole parameters. The zero contour is red (contour interval = 2 Nt).

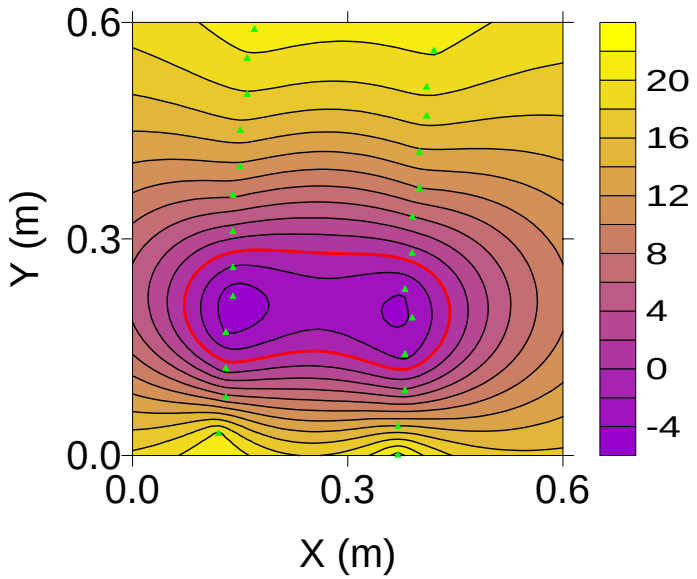

Figure F10. The inverse-modeled I04 dipole's field plus IIBE field from job 2. The flagged nodes (green triangles) were used in this inversion. The zero contour is red (contour interval = 2 nT).

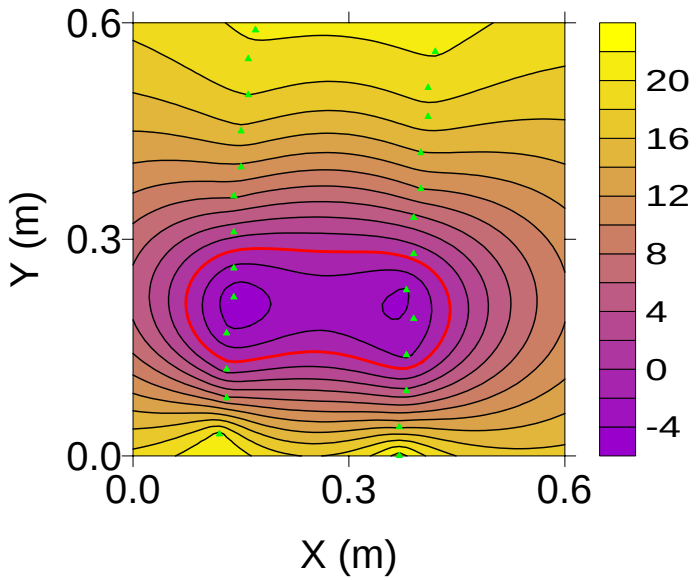

Figure F11. The inverse-modeled I04 dipole's field plus IIGE field from job 3. The flagged nodes (green triangles) were used in this inversion. The zero contour is red (contour interval = 2 nT).

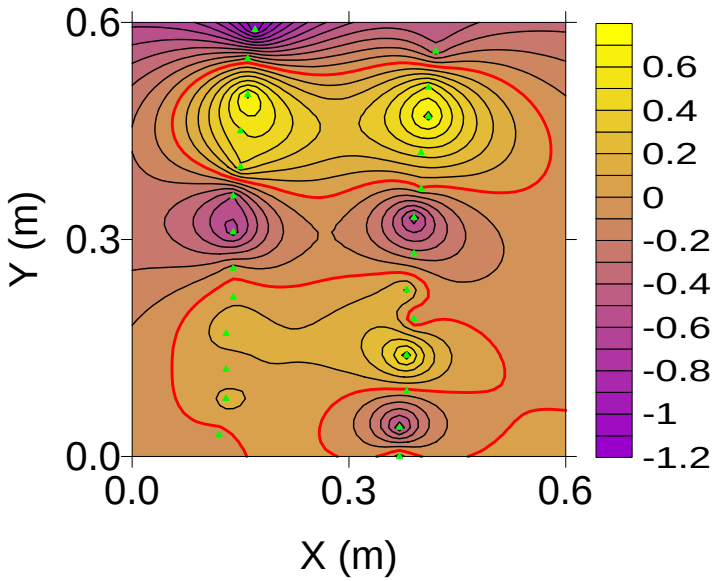

Figure F12. The residual field equal to the observed anomaly minus the sum of the inverse-modeled I04 dipole's field and IIBE field from job 2. The flagged nodes (green triangles) were used in this inversion. The zero contour is red (contour interval = 1 nT).

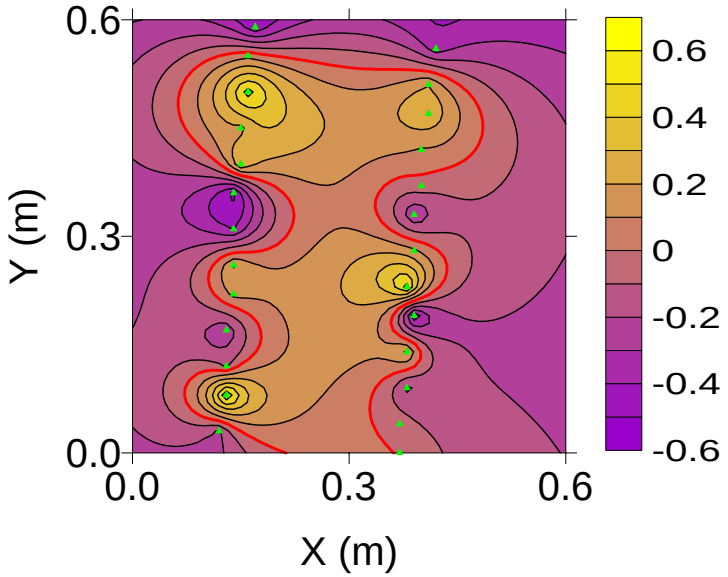

Figure F13. The residual field equal to the observed anomaly minus the sum of the inverse-modeled I04 dipole's field and IIGE field derived from job 3. The flagged nodes (green triangles) were used in this inversion. The zero contour is red (contour interval = 1 nT).

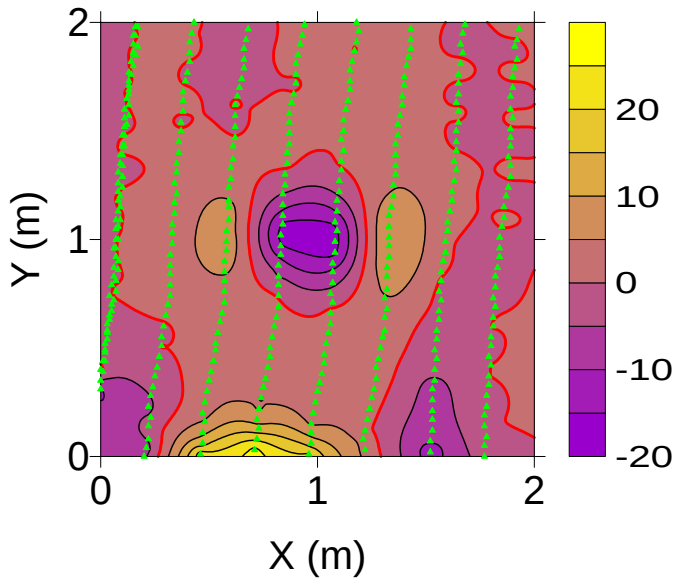

Figure F14. The EAGGN filtered I04 anomaly (L_{FX} = 0.75 m, L_{FY} = 0.3 m) and flagged nodes (green triangles). A co-centered region of these data was used for GGN IIF job 15 (L_D = 1 m). For this inversion, Δ_C is 2 cm, $(Z\text{-}Z_C)$ is 3 cm, θ is 136.5 deg, and Ψ is –68.4 deg. The zero contour is red (contour interval = 5 nT).

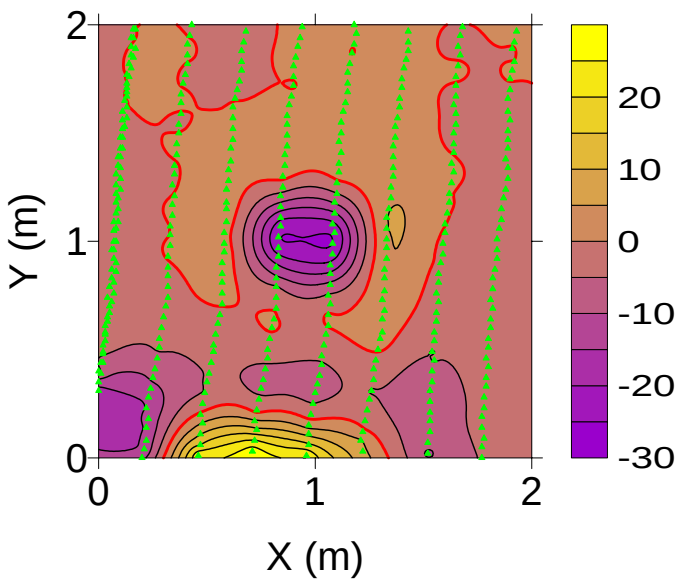

Figure F15. The EAGGN filtered I04 anomaly (L_{FX} = 0.75 m, L_{FY} = 0.6 m) and flagged nodes (green triangles). A co-centered region of these data was used for GGN IIF job 18 (L_D = 1 m). For this inversion, Δ_C is 3 cm, $(Z\text{-}Z_C)$ is 2 cm, θ is 145.7 deg, and Ψ is –76.5 deg. For jobs 14-19 (L_{FX} = 0.75 m, 0.2 m $\leq L_{FY} \leq$ 0.75 m), $2 \leq \Delta_C \leq 4$ cm, $2 \leq (Z\text{-}Z_C) \leq 3$ cm, $131.7 \leq \theta \leq 146.0$ deg, $-63.8 \leq \Psi \leq 76.7$ deg. The zero contour is red (contour interval = 5 nT).

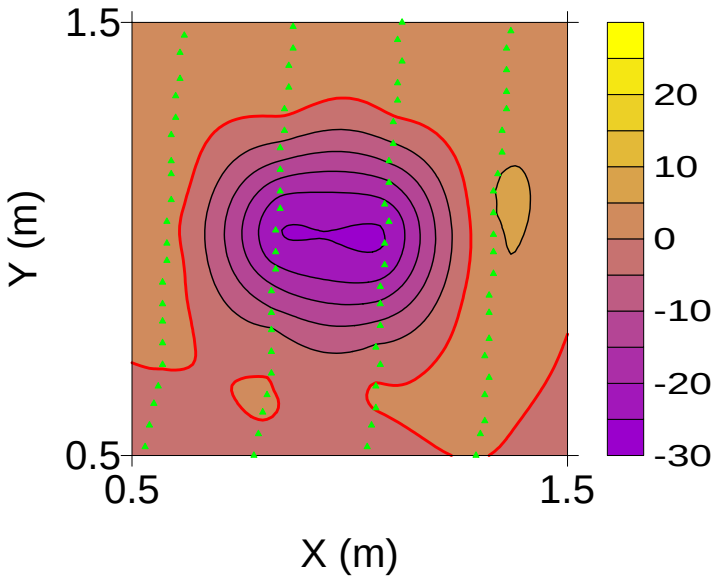

Figure F16. The GGN filtered I04 anomaly (L_{FX} = 0.75 m, L_{FY} = 0.6 m) and flagged nodes (green triangles) used in job 18. This is the central portion of the data shown on the previous figure. The GGN filter has largely removed the effect of the J04 anomaly, which "engulfed" the I04 anomaly at the center of this data window. The I04 anomaly has been distorted by the filter, but IIF compensates for this effect to obtain an accurate inversion. The zero contour is red (contour interval = 5 nT).

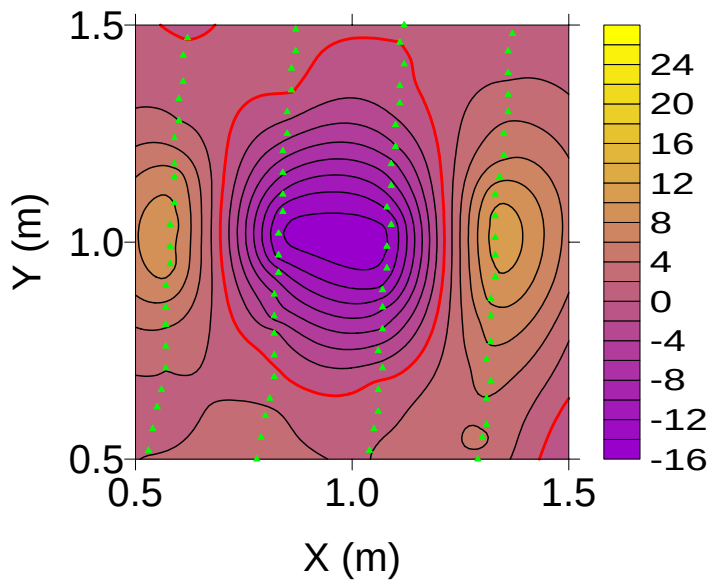

Figure F17. The GGN filtered I04 anomaly (L_{FX} = 0.75 m, L_{FY} = 0.2 m) and flagged nodes (green triangles) used in job 14. The GGN filter has largely removed the effect of the J04 anomaly, which "engulfed" the I04 anomaly at the center of this data window. For this inversion, Δ_C is 2 cm, $(Z\text{-}Z_C)$ is 3 cm, θ is 131.7 deg, and Ψ is –63.8 deg. The zero contour is red (contour interval = 2 nT).

Table F2. I04 dipole (X,Y,Z) and target's center (X_C,Y_C,Z_C) UTM coordinates. X_R = 402000 m; Y_R = 4369000 m. Δ_C and E_Z are absolute horizontal and relative vertical displacements of dipole from target's center. [Δx = grid interval; L_D = data window size; L_F = filter size.]

Job	Δx cm	L_D m	L_F m	†	$X-X_R$ m	$Y-Y_R$ m	$X-X_C$ cm	$Y-Y_C$ cm	Δ_C cm	Z cm	$Z-Z_C$ cm	E_Z* %
1	1	0.6	n/a	AB	815.30	569.15	9	-4	10	14	3	8
2	1	0.6	n/a	B	815.19	569.12	-2	-7	8	6	-5	-14
3	1	0.6	n/a		815.18	569.14	-3	-6	6	12	1	3
4	1	1	n/a	AB	815.20	568.97	-1	-22	22	64	53	147
5	1	1	n/a	B	815.21	569.00	-1	-19	19	64	53	147
6	1	1	n/a	A	815.20	569.02	-1	-17	17	30	19	53
7	1	1	n/a		815.20	569.03	-1	-16	16	29	18	50
8	1	1	0.75	E_2	815.19	569.11	-3	-9	9	17	6	17
9	1	1	0.75	E_3	815.18	569.13	-3	-7	7	16	5	14
10	1	1	0.75	E_4	815.19	569.15	-2	-4	5	14	3	8
11	1	1	0.75	E_5	815.20	569.17	-2	-2	3	14	3	8
12	1	1	0.75	E_6	815.20	569.17	-2	-2	3	15	4	11
13	1	1	0.75	E	815.21	569.15	0	-5	5	20	9	25
14	1	1	0.75	G_2	815.19	569.18	-2	-1	2	14	3	8
15	1	1	0.75	G_3	815.19	569.19	-2	0	2	14	3	8
16	1	1	0.75	G_4	815.19	569.20	-2	1	2	14	3	8
17	1	1	0.75	G_5	815.19	569.21	-2	2	3	14	3	8
18	1	1	0.75	G_6	815.19	569.21	-2	2	3	13	2	6
19	1	1	0.75	G	815.18	569.21	-3	2	4	13	2	6
20	1	1	0.5	G	815.18	569.21	-3	2	4	14	3	8
21	1	1	0.5	E	815.19	569.20	-2	1	2	14	3	8
22	1	1	1	E	815.22	569.07	0	-13	13	26	15	42
23	1	1	1.25	E	815.15	569.33	-7	13	15	35	24	67
24	1	2	0.5	E	815.21	569.20	0	0	0	13	2	6
25	1	2	0.75	E	815.19	569.24	-2	5	5	12	1	3
26	1	2	1	E	815.17	569.29	-4	10	10	17	6	17
27	1	2	1.25	E	815.15	569.33	-7	13	15	35	24	67

† flag-node and IIGE unless noted: **A** = all-node; **B** = IIBE. **E** = EAGGN ($L_{FD} = L_D$).
G = GGN ($L_{FD} > L_D$). $\mathbf{E_n}$= EAGGN (L_{DY} = n • 10 cm). $\mathbf{G_n}$= GGN (L_{DY} = n • 10 cm)
* $E_Z = (Z-Z_C)/(Z_C+H_M)$; magnetometer elevation, H_M = 0.25 m

Table F3. I04 dipole parameters: θ = deviation angle (from earth's field); δ = dipole declination; Ψ =dipole inclination; M = dipole moment. Gx, Gy = gradient components; B = dc bias estimate; R = correlation coefficient. [Δx = grid interval; L_D = data window size; L_F = filter size.]

Job	Δx cm	L_D m	L_F m	†	θ deg	δ deg	Ψ deg	M mA•m^2	Gx nT/m	Gy nT/m	B nT	R
1	1	0.6	n/a	AB	81.5	10.9	-12.6	18.8	n/a	n/a	28.6	0.985
2	1	0.6	n/a	B	78.2	-17.2	-10.8	10.6	n/a	n/a	24.0	0.999
3	1	0.6	n/a		99.7	-25.1	-31.9	18.7	3.44	-28.1	33.2	1.000
4	1	1	n/a	AB	67.4	-14.8	-0.1	508	n/a	n/a	68.26	0.993
5	1	1	n/a	B	72.9	-14.3	-5.6	517	n/a	n/a	73.7	0.993
6	1	1	n/a	A	80.0	-12.9	-12.8	81.1	-5.30	-45.1	52.16	0.998
7	1	1	n/a		84.2	-17.0	-16.8	78.2	1.47	-48.8	54.0	0.999
8	1	1	0.75	E_2	97.6	-24.5	-29.9	29.1	-0.02	1.68	-0.13	0.985
9	1	1	0.75	E_3	105.1	-27.6	-37.1	25.0	0.19	1.74	-0.27	0.983
10	1	1	0.75	E_4	115.4	-26.4	-47.6	19.8	0.20	1.22	-0.58	0.981
11	1	1	0.75	E_5	126.9	-22.8	-59.4	18.9	0.11	0.52	-0.72	0.980
12	1	1	0.75	E_6	128.3	-23.1	-60.8	20.8	0.15	0.23	-0.78	0.979
13	1	1	0.75	E	117.5	-12.5	-50.2	33.2	0.05	-0.18	-0.25	0.980
14	1	1	0.75	G_2	131.7	-29.3	-63.8	19.2	2.88	-2.10	0.89	0.996
15	1	1	0.75	G_3	136.5	-33.4	-68.4	18.8	2.95	-1.57	0.55	0.996
16	1	1	0.75	G_4	141.3	-40.1	-72.8	18.4	3.19	-0.75	0.04	0.997
17	1	1	0.75	G_5	146.0	-50.8	-76.7	18.2	3.52	0.29	-0.64	0.997
18	1	1	0.75	G_6	145.7	-50.4	-76.5	16.7	3.73	1.97	-1.58	0.997
19	1	1	0.75	G	144.0	-64.0	-72.5	16.8	4.86	4.73	-3.04	0.996
20	1	1	0.5	G	143.2	-64.4	-71.6	18.3	5.35	-0.18	-0.71	0.992
21	1	1	0.5	E	141.7	-29.3	-74.0	18.1	0.03	-0.19	-0.58	0.979
22	1	1	1	E	91.5	-15.3	-24.2	60.1	0.48	-0.22	-0.13	0.983
23	1	2	0.5	E	135.1	1.9	-67.5	17.4	0.77	1.12	-0.99	0.728
24	1	2	0.75	E	160.1	-179.3	-87.1	15.0	0.66	2.46	-2.42	0.729
25	1	2	1	E	179.1	169.3	-68.1	21.9	1.36	1.52	-2.98	0.675
26	1	2	1.25	E	164.3	175.7	-51.9	72.5	1.87	-0.14	-2.82	0.632
27	1	2	1.5	E	171.5	163.5	-59.1	31.4	0.65	0.11	-3.99	0.610

† flag-node and IIGE unless noted: **A** = all-node; **B** = IIBE. **E** = EAGGN ($L_{FD} = L_D$).
G = GGN ($L_{FD} > L_D$). **X** = x-then-y high-pass filter; $\blacktriangle_0$ = peak-only (H>0)

Table F4. I04 data windows: grid interval, Δx; absolute and relative window size, L_D, R_L; displacement of window's center from target's center, X_W-X_C, Y_W-Y_C; number of nodes along the x-and y-axes, N_X, N_Y; and the number and proportion of nodes flagged for inversion N_F, R_F.

Jobs	Δx (cm)	L_D (m)	R_L†	X_W-X_C (cm)	Y_W-Y_C (cm)	N_X	$N_X \bullet N_Y$	N_F	R_F (%)
1	1	0.6	1.6	1	15	61	3721	3721	100
2-3	1	0.6	1.6	1	15	61	3721	26	0.7
4, 6	1	1	2.8	3	0	101	10201	10201	100
5, 7-22	1	1	2.8	3	0	101	10201	87	0.9
23-27	1	2	5.6	3	0	201	40401	349	0.9

†$R_L = L_D/(Z_C+H_M)$; depth to target center, Z_C = 11 cm; magnetometer height, H_M = 25 cm.

Appendix G
Target M08 (105 mm projectile)

Figures G1-G6 plot the M08 anomaly and results of inversion jobs. Target M08 is a 105-mm M60 projectile (Figure G7), which the USAEC emplaced sub-horizontally at a depth to center of 57 cm (Table G1). Conclusions are derived from 25 jobs (Tables G2-G4).

Appendix G - Figures

G1. Target M08: 105-mm projectile ……. 137
G2. Regional setting of M08 anomaly ……..…… 138
G3. M08 anomaly in 3-m window ……. 138
G4. EAGGN filtered M08 anomaly (L_F = 0.5 m) …… 139
G5. EAGGN filtered M08 anomaly (L_F = 0.75 m) ……...……. 139
G6. EAGGN filtered M08 anomaly (L_F = 1 m) ……...……. 140
G7. EAGGN filtered M08 anomaly (L_F = 1.5 m) …….……. 140
G8. M08 anomaly (L_D = 2 m) and flagged nodes …….…….…… 141
G9. M08 anomaly and flagged nodes for peak-only inversions ……..….. 141
G10. M08 anomaly and flagged nodes for peak-only, single-swath inversions ……..…….. 142
G11. Anomaly of the inverse-modeled M08 dipole plus IIBE field …….……. 142
G12. Residual field (observed field minus sum of M08 dipole's field and IIBE field) …. 143
G13. Residual field (observed field minus sum of M08 dipole's field and IIGE field) …. 143
G14. EAGGN filtered M08 anomaly (L_F = 0.75 m; L_D = 2 m) …….…… 144
G15. EAGGN filtered M08 anomaly (L_F = 1 m; L_D = 2 m) ……..…… 144

Appendix G - Tables

G1. Ground truth for target M08 ……..…….. 137
G2. Dipole positions for anomaly M08 inversions ……...……. 145
G3. Dipole parameters for anomaly M08 inversions …….…… 146
G4. M08 data window parameters ……...…….. 147

Figure 7. Target M08; 105-mm projectile.

Table 1. M08 ground truth parameters.

Description	Non-standard M60 projectile
Material	Forged Steel
Length, L_T	463 mm
Diameter, D_T	105 mm
Weight	13.608 kg
Grid azimuth, Φ_T	104 deg
Inclination, Ψ_T (nose slightly up)	-2 deg
Depth, Z_C	57 cm
UTM northing, Yc	4369559.840 m
UTM easting, X_C	402808.872 m
Ratio of depth below magnetometer to target length, R_{DL} †	1.8
Vertical projection of target's length, L_V (= $L_T \sin \Psi_T$)	-2 cm
Horizontal projection of target's length, L_H (= $L_T \cos \Psi_T$)	46 cm
Nose-to-center offsets (Xn-Xc, Yn-Yc, Zn-Zc)	(23, -1, -1) cm

† $R_{DL} = (Z_C+H_M)/L_T$; magnetometer elevation, $H_M = 0.25$ m

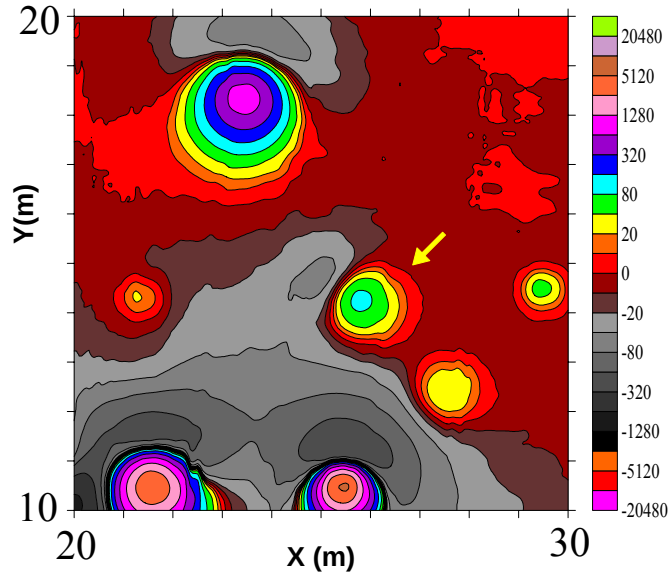

Figure G2. Regional setting of the M08 anomaly (yellow arrow). The M08 anomaly is distorted by larger anomalies to the south. Magnetic field contours are at zero and $\pm 2^n \cdot 10$ nT, where n is a non-negative integer.

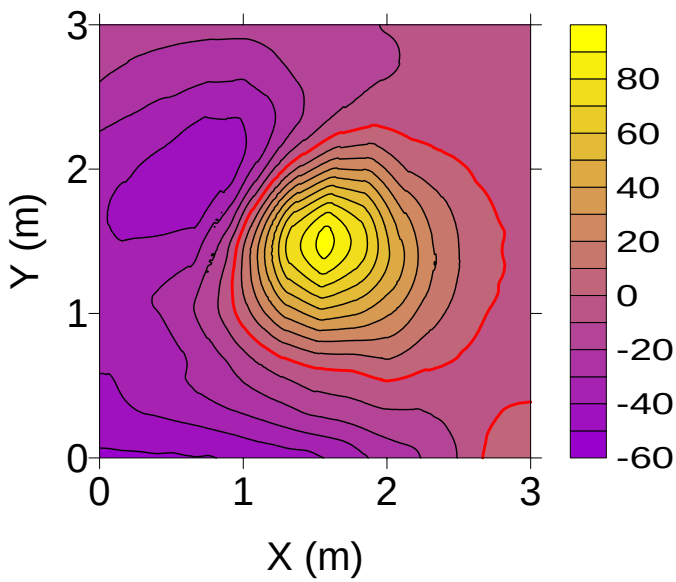

Figure G3. The M08 anomaly (L_D = 3 m; jobs 22-27) including a low west-northwest of the central peak. Negative values in the southwest corner result from larger neighboring anomalies. For IIBE (job 22), Δ_C is 39 cm and θ is 69.1 deg while for IIGE (job 23), Δ_C is 22 cm and θ is 26.1 deg. For IIBE with L_D equal to 2 m (job 6), θ is 51.6 deg and for IIGE (job 8), θ is 39.4 deg. The zero contour is red (contour interval = 10 nT).

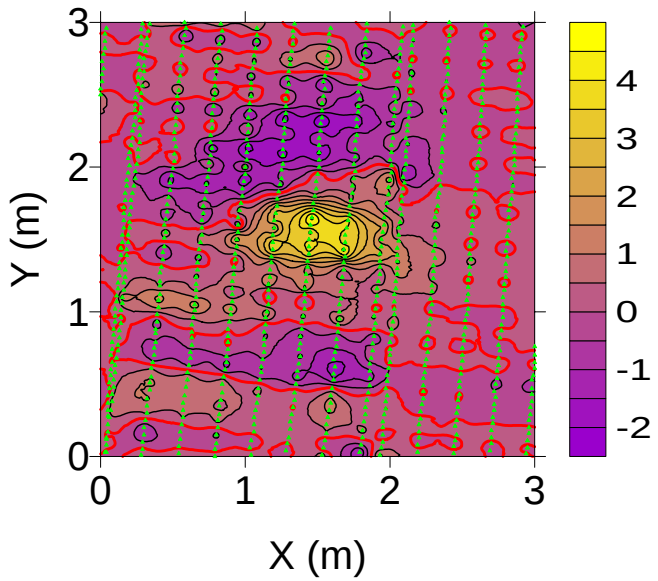

Figure G4. The EAGGN filtered M08 anomaly (L_F = 0.5 m; L_D = 3 m). For job 24 using these data, Δ_C is 11 cm and θ is 37.6 deg. Similarly, for job 9 (L_F = 0.5 m; L_D = 2 m), Δ_C is 12 cm and θ is 32.4 deg. By contrast, for IIBE without IIF (L_D = 3 m, job 22), Δ_C is 39 cm and θ is 69.1 deg. Flagged nodes (green triangles) were used in inversion. The zero contour is red (contour interval = 0.5 nT).

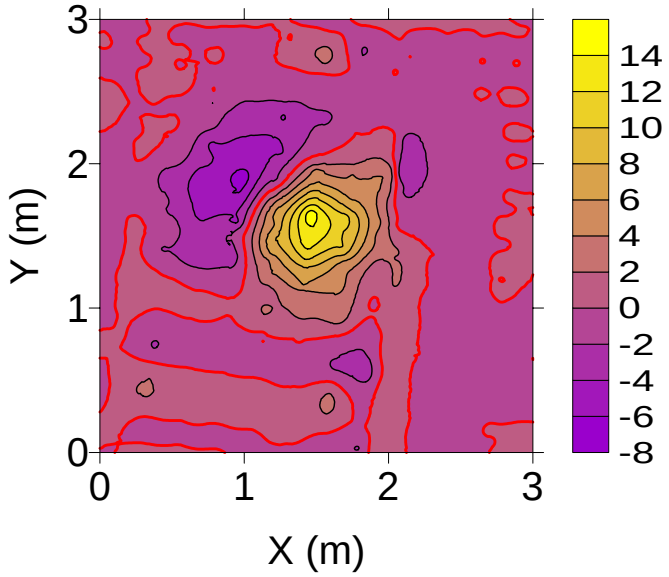

Figure G5. The EAGGN filtered M08 anomaly (L_F = 0.75 m; L_D = 3 m). For job 25 using these data, Δ_C is 11 cm, (Z-Z_C) is 9 cm, and θ is 43.2 deg. Effects of anomalies to the south are virtually nulled. Similarly, for job 26 (L_F = 1 m) and job 27 (L_F = 1.5 m), θ are 43.0 deg and 42.1 deg, respectively. The zero contour is red (contour interval = 2 nT).

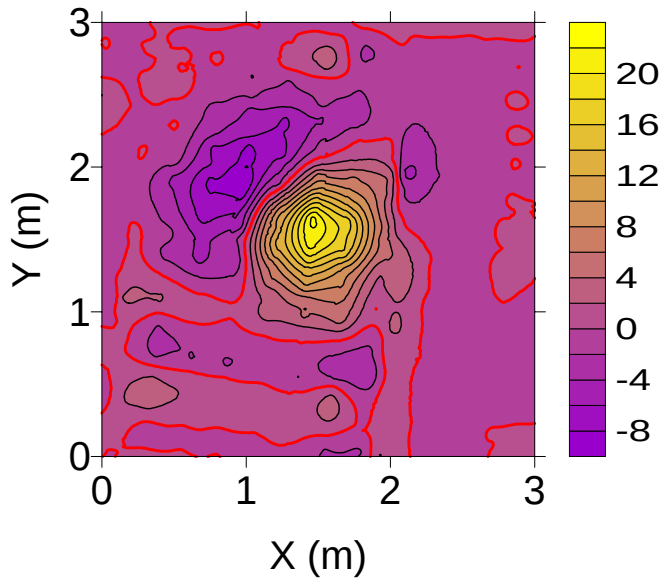

Figure G6. The EAGGN filtered M08 anomaly (L_F = 1 m; L_D = 3 m; job 26) for which θ is 43.0 deg and Ψ, is 42.3 deg. Similarly, for job 11 (L_D = 2 m), θ is 42.6 deg and Ψ is 44.3 deg. The zero contour is red (contour interval = 2 nT).

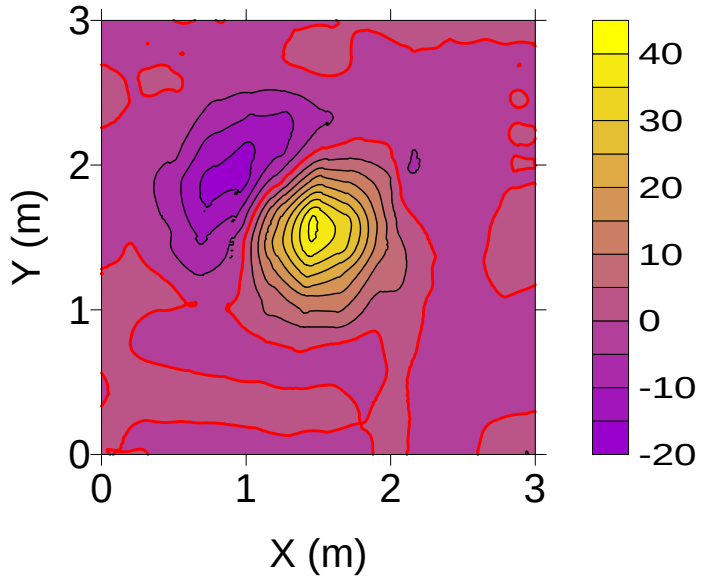

Figure G7. The EAGGN filtered M08 anomaly (L_F = 1.5 m; L_D = 3 m, job 27) for which θ is 42.1 deg. This dipole is 1 cm east, 1 cm south, and 1 cm below that of the 1-m filter (job 26). Consistency of dipole positions and orientations for L_F of 0.75, 1 and 1.5 m, is a favorable indication of accurate results. The zero contour is red (contour interval = 5 nT).

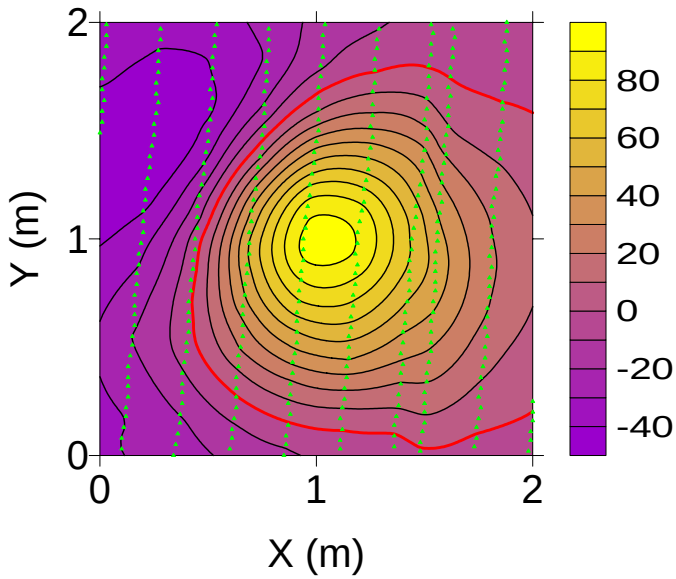

Figure G8. The M08 anomaly (L_D = 2 m) and flagged nodes (green triangles). For IIBE, Δ_C is 22 cm (= 0.48 L_H), (Z-Z_C) is 15 cm (E_Z = 18%), θ is 51.6 deg, and Ψ is 42.9 deg. For IIGE, Δ_C is 20 cm (= 0.43 L_H), (Z-Z_C) is 8 cm (E_Z = 10%), θ is 39.4 deg, and Ψ is 53.6 deg. IIGE yielded better agreement with the sub-horizontal target's depth to center. The zero contour is red (contour interval = 10 nT).

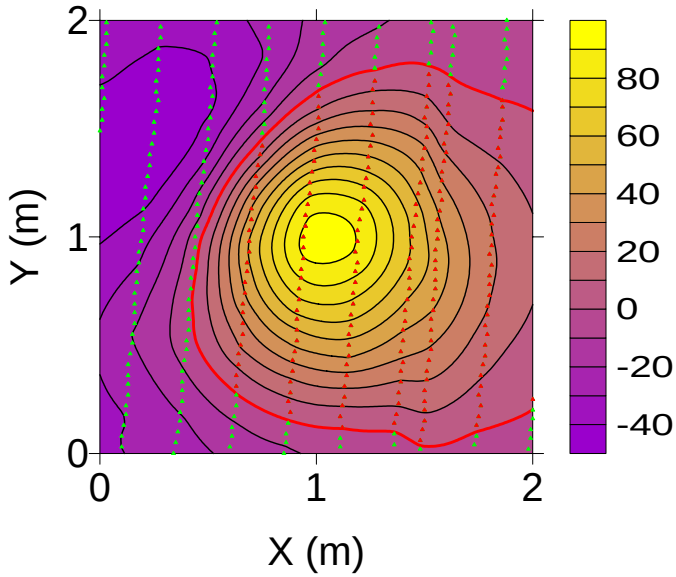

Figure G9. The M08 anomaly and flagged nodes (red triangles) for positive values used in peak-only jobs 17-18. For IIBE job 17, Δ_C is 25 cm, (Z-Z_C) is 7 cm (E_Z = 9%), θ is 34.8 deg, and Ψ is 61.8 deg. For IIGE job 18, Δ_C is 19 cm, (Z-Z_C) is 20 cm (E_Z = 24%), θ is 54.1 deg, and Ψ is 41.8 deg. IIF inversions with larger data windows yield better results than the small-window inversions without IIF. The zero contour is red (contour interval = 10 nT).

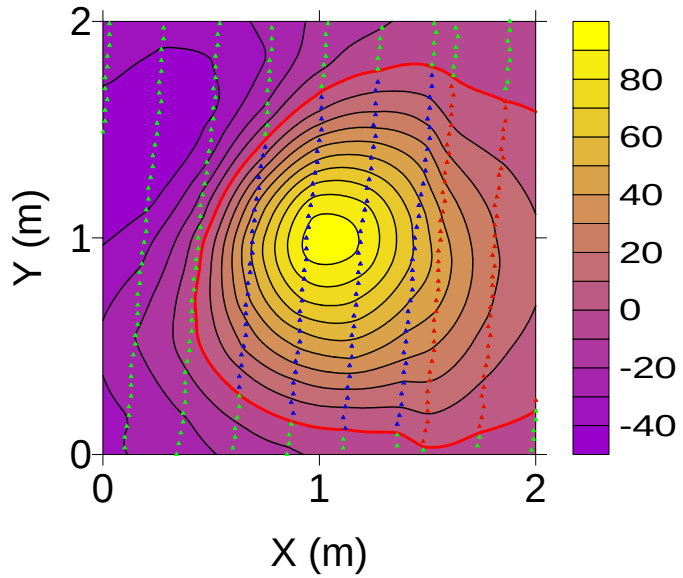

Figure G10. The M08 anomaly and flagged nodes (blue triangles) for peak-only, single-swath inversions. For IIBE (job 19), Δ_C is 20 cm, $(Z\text{-}Z_C)$ is 15 cm, and θ is 44.0 deg. For IIGE (job 20), Δ_C is 15 cm, $(Z\text{-}Z_C)$ is 19 cm, and θ is 44.8 deg. The zero contour is red (contour interval = 10 nT).

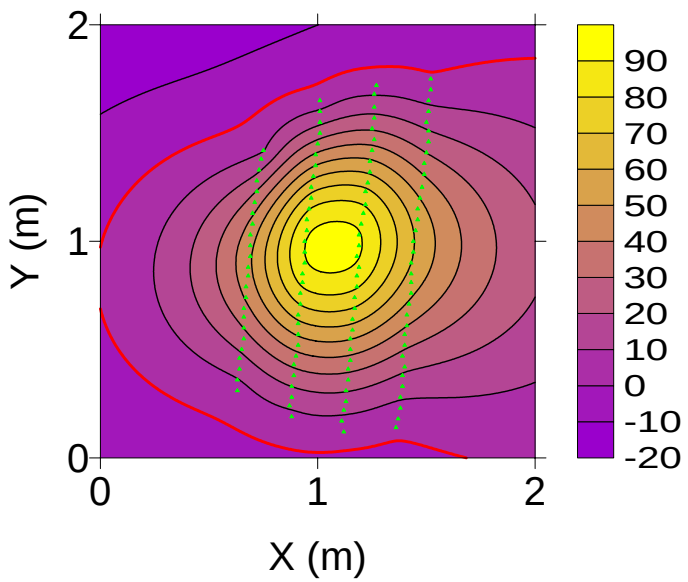

Figure G11. Anomaly of the inverse-modeled M08 dipole plus IIBE field and flagged nodes (green triangles) for the peak-only, single-swath job 19. The contours are based solely on data at the flagged nodes. The zero contour is red (contour interval = 10 nT).

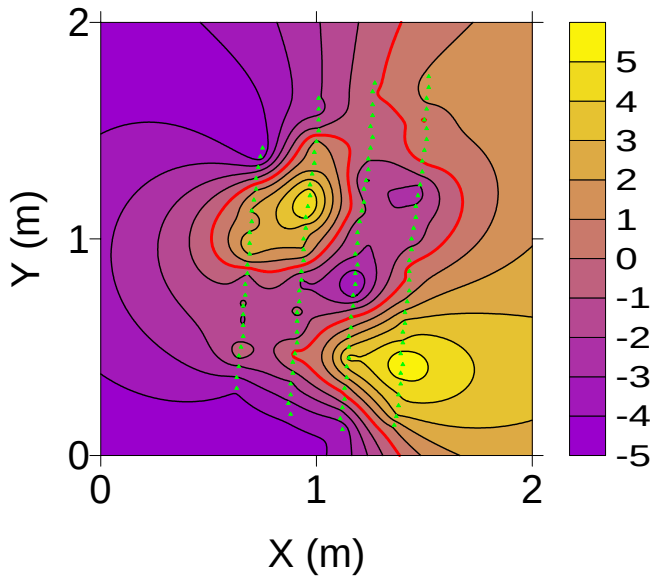

Figure G12. The residual field equal to the observed field minus the sum of the field of the inverse-modeled M08 dipole and IIBE field (job 19). This peak-only, single-swath inversion used data at the flagged nodes (green triangles). The contours are based solely on data at those nodes. The gradients at the southern ends of the magnetometer tracks are apparently the results of anomalies to the south of the M08 target. The zero contour is red (contour interval = 1 nT).

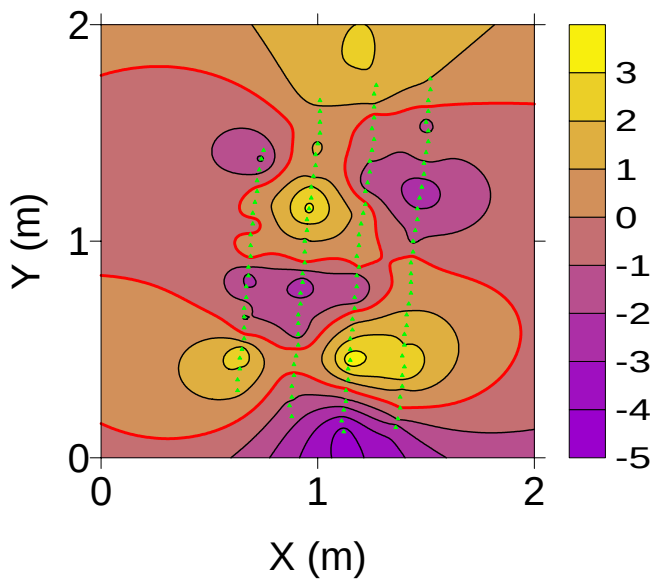

Figure G13. The residual field equal to the observed field minus the sum of the field of the inverse-modeled M08 dipole and IIGE field (job 20). This peak-only, single-swath inversion used data at the flagged nodes (green triangles). Contours are based solely on data at those nodes. Comparison with the residual for the IIBE nodes shows significant differences that are reflected in the different dipole solutions. The zero contour is red (contour interval = 1 nT).

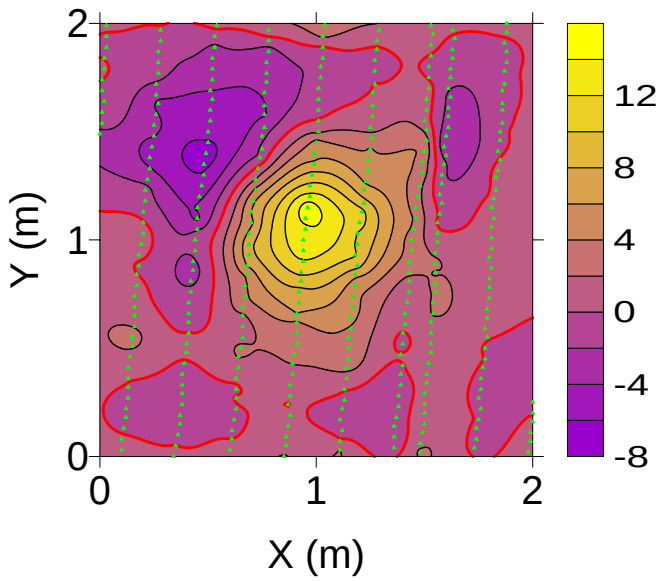

Figure G14. The EAGGN filtered M08 anomaly (L_F = 0.75 m; L_D = 2 m) and flagged nodes (green triangles) used in job 10 for which Δ_C is 11 cm, (Z-Z_C) is 10 cm, and θ is 42.2 deg. The zero contour is red (contour interval = 2 nT).

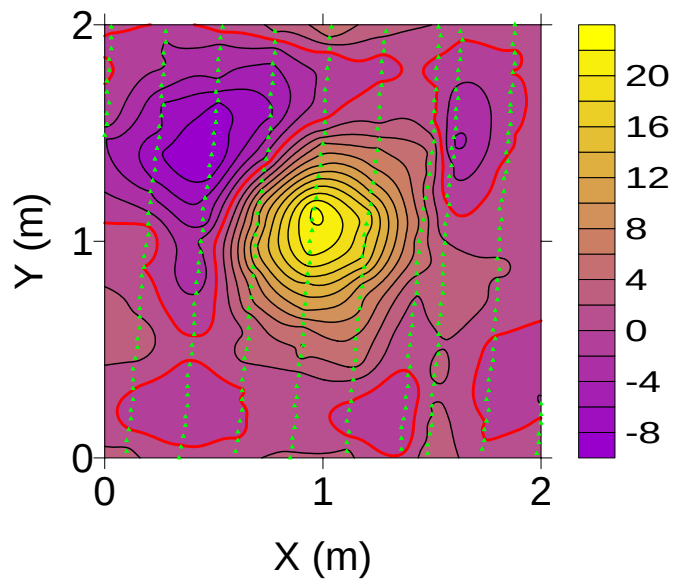

Figure G15. The EAGGN filtered M08 anomaly (L_F = 1 m; L_D = 2 m) and flagged nodes (green triangles) used in job 11 for which Δ_C is 12 cm, (Z-Z_C) is 10 cm, and θ is 42.6 deg. The zero contour is red (contour interval = 2 nT).

Table 2. M08 dipole (X,Y,Z) and target's center (X_C,Y_C,Z_C) UTM coordinates. X_R = 402000 m; Y_R = 4369000 m. Δ_C and E_Z are absolute horizontal and relative vertical displacements of dipolefrom target's center. [Δx = grid interval; L_D = data window size; L_F = filter size.]

Job	Δx cm	L_D m	L_F m	†	$X-X_R$ m	$Y-Y_R$ m	$X-X_C$ cm	$Y-Y_C$ cm	Δ_C cm	Z cm	$Z-Z_C$ cm	E_Z* %
1	5	2	n/a	AB	808.98	559.64	11	-20	23	73	16	20
2	5	2	n/a	B	808.98	559.64	11	-20	23	71	14	17
3	5	2	n/a	A	809.02	559.70	15	-14	20	66	9	11
4	5	2	n/a		809.02	559.70	15	-14	20	65	8	10
5	1	2	n/a	AB	809.00	559.65	12	-19	22	73	16	20
6	1	2	n/a	B	809.00	559.65	12	-19	22	72	15	18
7	1	2	n/a	A	809.02	559.71	14	-13	20	66	9	11
8	1	2	n/a		809.03	559.71	15	-13	20	65	8	10
9	1	2	0.5	E	808.99	559.83	12	-1	12	71	14	17
10	1	2	0.75	E	808.96	559.78	9	-6	11	67	10	12
11	1	2	1	E	808.96	559.77	9	-7	12	67	10	12
12	1	2	n/a	B§	808.99	559.66	12	-18	21	70	13	16
13	1	2	n/a	§	809.01	559.74	14	-10	17	67	10	12
14	1	2	0.5	E§	808.99	559.83	11	-1	11	70	13	16
15	1	2	0.75	E§	808.96	559.78	9	-6	11	67	10	12
16	1	2	1	E§	808.95	559.77	8	-7	11	67	10	12
17	1	2	n/a	B▲$_0$	809.10	559.72	22	-12	25	64	7	9
18	1	2	n/a	▲$_0$	808.92	559.66	5	-18	19	77	20	24
19	1	2	n/a	B▲$_0$§	809.02	559.71	14	-13	20	72	15	18
20	1	2	n/a	▲$_0$§	808.95	559.72	8	-12	15	76	19	23
21	5	2.5	n/a	AB	808.99	559.59	12	-25	27	72	15	18
22	5	2.5	n/a	B	808.99	559.59	12	-25	27	70	13	16
23	5	2.5	n/a	A	809.06	559.76	19	-8	20	65	8	10
24	5	2.5	n/a		809.06	559.76	19	-8	20	64	7	9
25	5	3	n/a	A B	808.96	559.48	8	-36	37	75	18	22
26	5	3	n/a	B	808.96	559.48	8	-36	37	74	17	21
27	5	3	n/a	A	809.06	559.76	19	-8	20	64	7	9
28	5	3	n/a		809.10	559.82	23	-2	23	64	7	9
29	1	3	n/a	B	808.96	559.46	9	-38	39	75	18	22
30	1	3	n/a		809.09	559.77	21	-7	22	64	7	9
31	1	3	0.5	E	808.99	559.83	11	-1	11	67	10	12
32	1	3	0.75	E	808.96	559.78	9	-6	11	66	9	11
33	1	3	1	E	808.96	559.78	9	-6	11	66	9	11
34	1	3	1.5	E	808.97	559.77	10	-7	12	67	10	12

† flag-node and IIGE unless noted: **A**= all-node; **B** = IIBE. **E** = EAGGN ($L_{FD} = L_D$).
▲$_0$ = peak-only (H > 0). **§** = single-swath.
* $E_Z = (Z-Z_C)/(Z_C+H_M)$; magnetometer elevation, H_M = 25 cm; Z_C = 57 cm.

Table 3. M08 dipole parameters: θ = deviation angle (from earth's field); δ = dipole declination; Ψ =dipole inclination; M = dipole moment. Gx, Gy = gradient components; B = dc bias estimate; R = correlation coefficient. [Δx = grid interval; L_D = data window size; L_F = filter size.]

Job	Δx cm	L_D m	L_F m	†	θ deg	δ deg	Ψ deg	M mA•m^2	Gx nT/m	Gy nT/m	B nT	R
1	5	2	n/a	AB	54.2	81.1	40.5	748	n/a	n/a	-21.4	0.992
2	5	2	n/a	B	54.0	80.7	40.5	706	n/a	n/a	-20.3	0.991
3	5	2	n/a	A	42.0	74.6	52.0	543	10.4	0.10	-18.7	0.996
4	5	2	n/a		41.8	73.8	51.9	528	10.3	0.29	-17.8	0.995
5	1	2	n/a	AB	51.9	80.3	42.7	739	n/a	n/a	-21.8	0.992
6	1	2	n/a	B	51.6	79.9	42.9	716	n/a	n/a	-21.3	0.992
7	1	2	n/a	A	40.9	72.1	52.3	542	10.8	0.23	-18.6	0.996
8	1	2	n/a		39.4	70.8	53.6	523	10.8	0.70	-17.8	0.995
9	1	2	0.5	E	32.4	39.7	47.6	660	0.04	-0.07	0.00	0.873
10	1	2	0.75	E	42.2	57.3	43.9	608	0.16	-0.33	-0.03	0.961
11	1	2	1	E	42.6	59.0	44.3	606	0.28	-0.54	-0.01	0.977
12	1	2	n/a	B§	50.5	80.6	44.5	682	n/a	n/a	-23.0	0.996
13	1	2	n/a	§	39.1	60.8	49.4	592	6.78	7.05	-21.2	0.997
14	1	2	0.5	E§	34.9	42.2	45.7	645	0.07	-0.05	0.00	0.882
15	1	2	0.75	E§	41.8	56.3	44.0	609	0.18	-0.20	-0.09	0.980
16	1	2	1	E§	43.9	58.8	42.6	614	0.27	-0.34	-0.10	0.987
17	1	2	n/a	B▲$_0$	34.8	75.8	61.8	427	n/a	n/a	-8.50	0.997
18	1	2	n/a	▲$_0$	54.1	84.2	41.8	905	15.9	-12.2	27.0	0.999
19	1	2	n/a	B▲$_0$§	44.0	75.4	49.9	672	n/a	n/a	-21.3	0.999
20	1	2	n/a	▲$_0$§	44.8	72.6	47.7	830	17.4	-4.72	-28.9	1.000
21	5	2.5	n/a	AB	58.5	88.6	38.6	725	n/a	n/a	-19.8	0.983
22	5	2.5	n/a	B	58.3	88.3	38.7	684	n/a	n/a	-19.0	0.983
23	5	2.5	n/a	A	32.0	56.1	56.2	518	10.0	5.75	-18.0	0.991
24	5	2.5	n/a		31.7	54.3	55.7	506	9.76	6.23	-17.2	0.990
25	5	3	n/a	AB	68.4	98.2	31.3	813	n/a	n/a	-19.7	0.959
26	5	3	n/a	B	68.5	98.6	31.3	794	n/a	n/a	-19.5	0.959
27	5	3	n/a	A	30.9	53.8	56.4	505	9.67	7.35	-17.8	0.980
28	5	3	n/a		22.8	35.5	57.9	502	10.5	8.68	8.68	0.979
29	1	3	n/a	B	69.1	99.8	31.1	812	n/a	n/a	-19.8	0.960
30	1	3	n/a		26.1	46.4	59.3	497	10.2	7.71	-18.1	0.981
31	1	3	0.5	E	37.6	43.5	43.1	578	-0.04	-0.05	0.04	0.794
32	1	3	0.75	E	43.2	56.4	42.3	590	-0.07	-0.10	0.05	0.933
33	1	3	1	E	43.0	55.8	42.3	590	-0.10	-0.16	0.07	0.956
34	1	3	1.5	E	42.1	56.3	43.6	611	-0.15	-0.24	0.02	0.978

† flag-node and IIGE unless noted as follows: **A**= all-node; **B** = IIBE. **E** = EAGGN ($L_{FD} = L_D$).
▲$_0$ = peak-only (H > 0). **§** = single-swath.

Table 4. M08 data windows: grid interval, Δx; absolute and relative window size, L_D, R_L; displacement of window's center from target's center, X_W-X_C, Y_W-Y_C; number of nodes along the x-and y-axes, N_X, N_Y; and the number and proportion of nodes flagged for inversion N_F, R_F.

Jobs	Δx (cm)	L_D (m)	R_L†	X_W-X_C (cm)	Y_W-Y_C (cm)	N_X	$N_X \bullet N_Y$	N_F	R_F (%)
1, 3	5	2	2.4	27	-14	41	1681	1681	100
2, 4	5	2	2.4	27	-14	41	1681	345	20.5
5, 7	1	2	2.4	0	0	201	40401	40401	100
6, 8-11	1	2	2.4	0	0	201	40401	353	0.9
12-16	1	2	2.4	0	0	201	40401	259 §	0.6
17-18	1	2	2.4	0	0	201	40401	195 $▲_0$	0.5
19-20	1	2	2.4	0	0	201	40401	123 $▲_0$§	0.3
21, 23	5	2.5	3.0	27	-14	51	2601	2601	100
22, 24	5	2.5	3.0	27	-14	51	2601	542	20.8
25, 27	5	3	3.7	27	-14	61	3721	3721	100
26, 28	5	3	3.7	27	-14	61	3721	801	21.5
29-34	1	3	3.7	0	0	301	90601	847	0.9

†$R_L = L_D/(Z_C+H_M)$; depth to target center, Z_C = 57 cm; magnetometer height, H_M = 25 cm.
$▲_0$ = peak-only (H > 0). **§** = single-swath.

Appendix H
Target C09 (40 mm projectile)

Target C09 is a 40 mm 0.6-kg projectile, which the AEC emplaced at an inclination of 19 deg and a depth to center of 14 cm (Figure H1, Table H1). Figures H2-H11 plot the C09 anomaly and results of inversion jobs. Conclusions are derived from 35 jobs (Tables H2-H4).

Appendix H Figures

H1. Target C09: 40-mm MKII 230 projectile ……...……. 149
H2. Regional setting of C09 anomaly ……..…….. 150
H3. C09 anomaly in 2-m window ……..…… 150
H4. EAGGN filtered C09 anomaly (L_F = 0.5 m, L_D = 2 m) ……..… 151
H5. EAGGN filtered C09 anomaly (L_F = 1 m, L_D = 2 m) …….…… 151
H6. EAGGN filtered C09 anomaly (L_F = 1.5 m, L_D = 2 m) …….. 152
H7. EAGGN filtered C09 anomaly (L_F = 0.75 m, L_D = 1 m) …… 152
H8. C09 anomaly (L_D = 1 m) and flagged nodes …….…….. 153
H9. C09 anomaly and flagged nodes for peak-only inversions ……. 153
H10. X-then-Y highpass filtered C09 anomaly (L_F = 1.5 m) …… 154
H11. X-then-Y highpass filtered C09 anomaly (L_F = 1 m) …….…….. 154

Appendix H Tables

H1. Ground truth for target C09 ……..…….. 149
H2. Dipole positions for anomaly C09 inversions …….. 155
H3. Dipole parameters for anomaly C09 inversions ……..…… 156
H4. C09 data window parameters …….……. 157

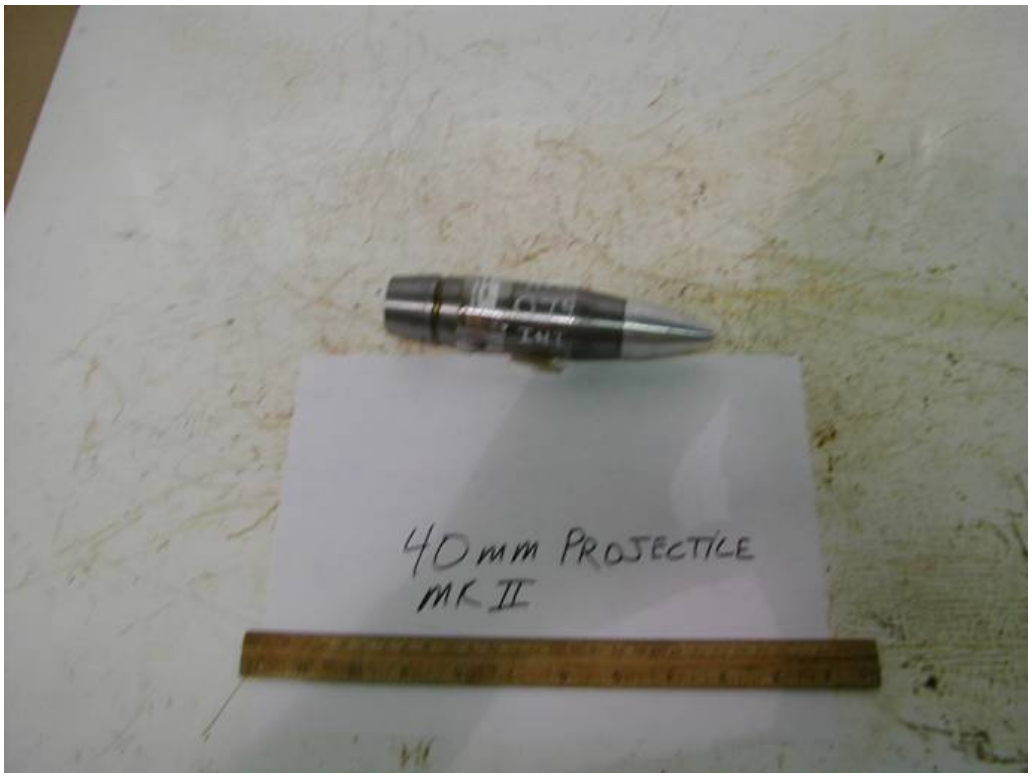

Figure H1. Target C09; 40 mm MKII 230 projectile.

Table H1. Ground truth for Target C09.

Description	MKII Projectile
Material	Steel
Length, L_T	130 mm
Diameter, D_T	40 mm
Weight	0.635 kg
Grid azimuth, Φ_T	78 deg
Inclination, Ψ_T	19 deg
Depth, Z_C	14 cm
UTM northing, Yc	4369579.171
UTM easting, X_C	402803.205
Ratio of depth below magnetometer to target length, R_{DL} †	3.0
Vertical projection of target's length, L_V (= $L_T \sin \Psi_T$)	4 cm
Horizontal projection of target's length, L_H (= $L_T \cos \Psi_T$)	12 cm
Nose-from-center offsets (Xn-Xc, Yn-Yc, Zn-Zc)	(6, 2, 2) cm

† $R_{DL} = (Z_C+H_M)/L_T$; Magnetometer height, $H_M = 0.25$ m

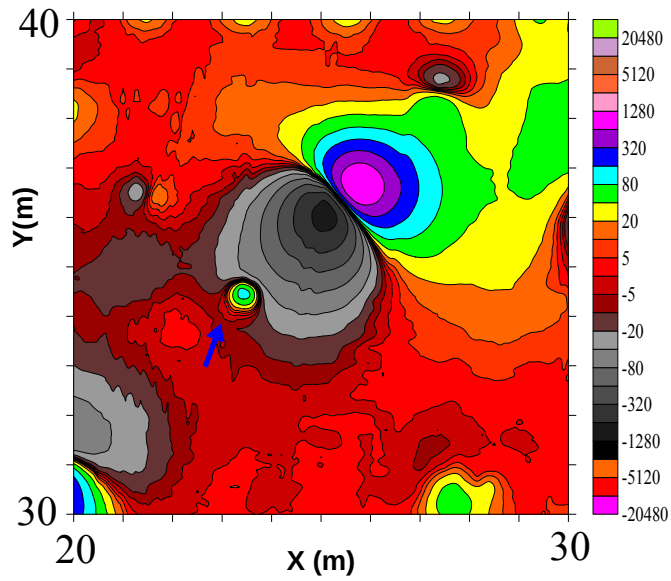

Figure H2. Regional setting of the C09 magnetic anomaly (blue arrow). The C09 anomaly is severely disturbed by the much larger B08 anomaly to the northeast. The magnetic field contours are at zero and $\pm 2^n \cdot 10$ nT, where n is a non-negative integer.

.

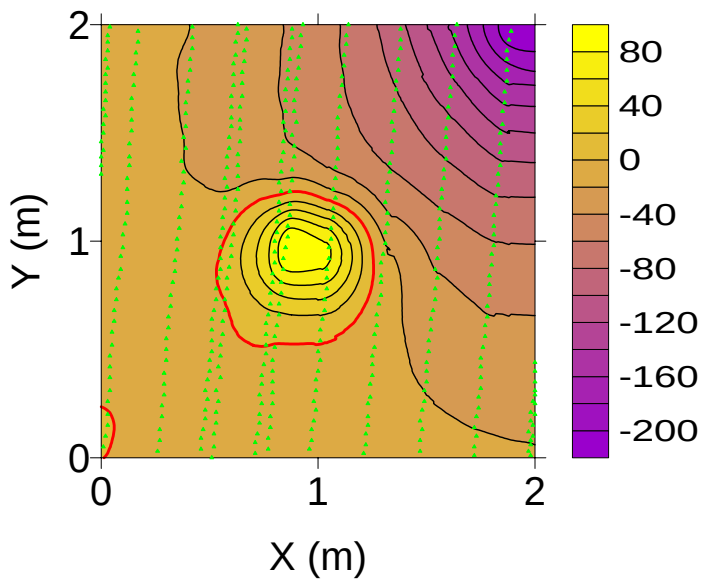

Figure H3. The C09 anomaly in the 2-m data window used in EAGGN IIF inversions (jobs 29-35). These inversions used data at 449 nodes (green triangles). The low in the northeast corner is associated with the B08 anomaly. The gradient of the superimposed B08 anomaly is not constant over the span of the central portion of the C09 anomaly. The zero contour is red and the contour interval is 20 nT.

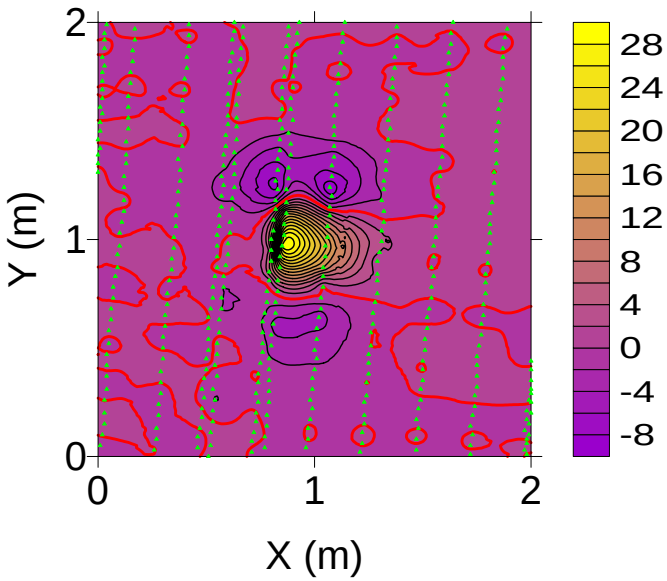

Figure H4. The EAGGN filtered C09 anomaly (L_F = 0.5 m, L_D = 2 m) used in job 29. This inversion used 449 nodes (green triangles). Within this data window the effect of the B08 anomaly is effectively removed by the filter. For job 29, Δ_C is 4 cm, Z is equal to Z_C (= 14 cm), θ is 10.6 deg, and Ψ is 76.0 deg. The zero contour is red and the contour interval is 2 nT.

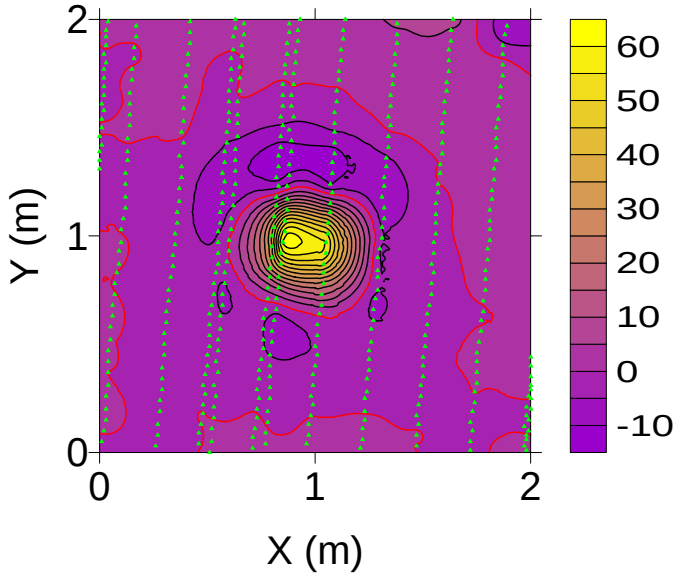

Figure H5. The EAGGN filtered C09 anomaly (L_F = 1 m, L_D = 2 m) and 449 flagged nodes(green triangles) used in job 31 for which θ is 9.7 deg, and Ψ is 75.2 deg. For jobs 29-33 ($0.5 \leq L_F \leq 1.5$ m, L_D = 2 m), Δ_C is 4 cm and Z is equal to Z_C (= 14 cm). The zero contour is red and the contour interval is 5 nT.

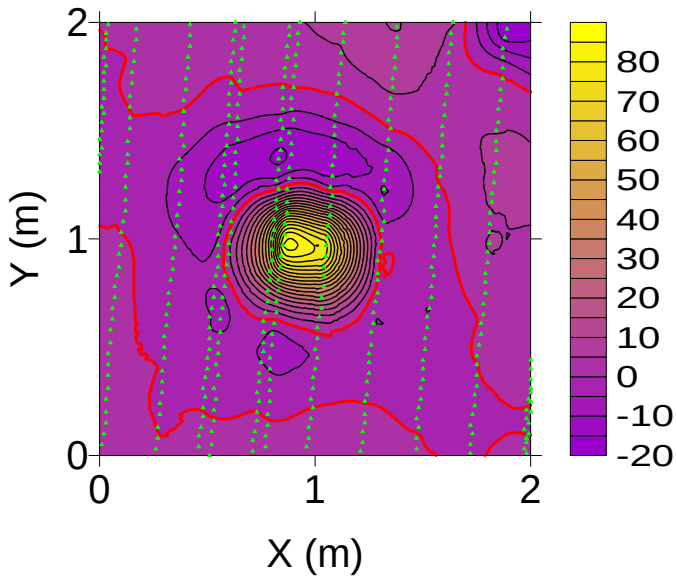

Figure H6. EAGGN filtered C09 anomaly (L_F = 1.5 m, L_D = 2 m) and 449 flagged nodes (green triangles) used in job 33. For this IIF inversion, Δ_C is 4 cm, Z is equal to Z_C (= 14 cm), θ is 13.4 deg, and Ψ is 80.6 deg. For a smaller data window (L_F = 1.5 m, L_D = 1.5 m), Δ_C is 4 cm, $(Z-Z_C)$ is 1 cm, θ is 14.0 deg, and Ψ is 80.1 deg. The zero contour is red (contour interval = 5 nT).

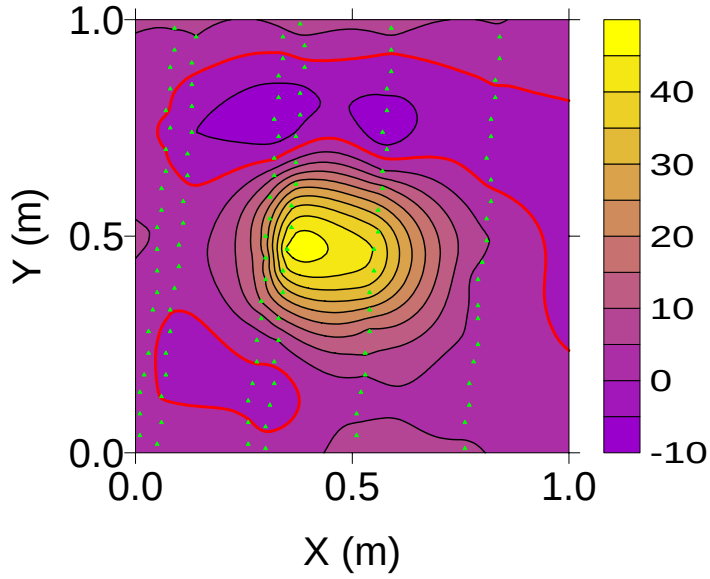

Figure H7. The EAGGN filtered C09 anomaly (L_F = 0.75 m, L_D = 1 m) used in job 6. The 123 flagged nodes (green triangles) are nearest to the magnetometer stations. For IIF inversion of these data, Δ_C is 4 cm, $(Z-Z_C)$ is 1 cm, θ is 10.2 deg, and Ψ is 75.2 deg. IIF inversions using L_F equal to 0.5, 0.75, and 1 m, yielded remarkably consistent dipole parameters. The contour is red and the contour interval is 5 nT.

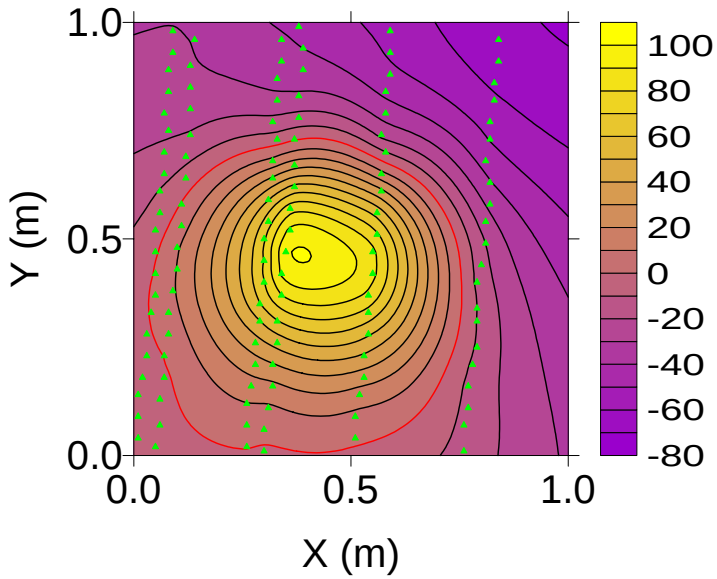

Figure H8. The C09 anomaly and 123 nodes (green triangles) used in jobs 2 and 4-7 (L_D = 1 m). For IIBE (job 2), IIGE (job 4), Δ_C are 6 and 3 cm; (Z-Z_C) are 5 and 2 cm; θ are 21.6 and 15.7 deg, and Ψ are 53.9 and 70.6 deg, respectively. IIGE apparently improves the inversion. Better inversions are obtained, however, with small window inversions (using the peak only) or with IIF. The zero contour is red and the contour interval is 20 nT.

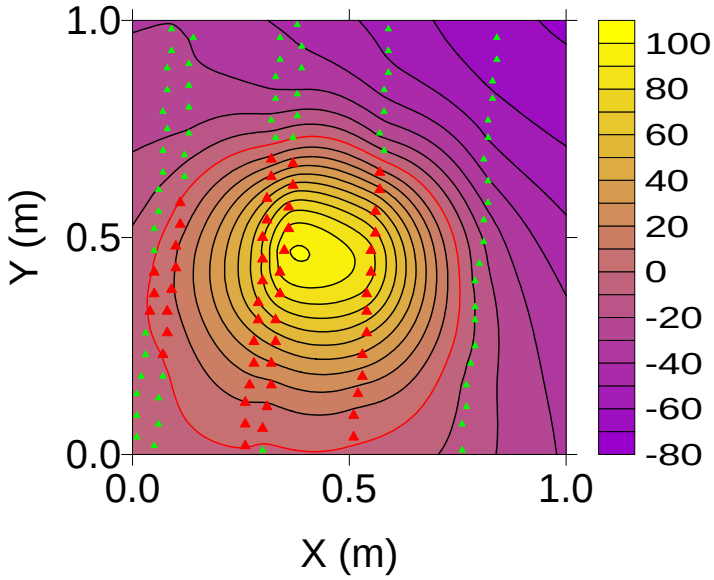

Figure H9. The C09 anomaly and 53 nodes (red triangles) used in peak-only inversion jobs 8-9. The remaining 70 nodes (green triangles) for which the field was negative were excluded. For IIBE (job 8) and IIGE (job 9), (Z-Z_C) are 5 and 2 cm, θ are 12.2 and 8.8 deg, and Ψ are 72.0 and 70.7 deg, respectively. For both of these jobs ΔC is 4 cm. The zero contour is red and the contour interval is 20 nT

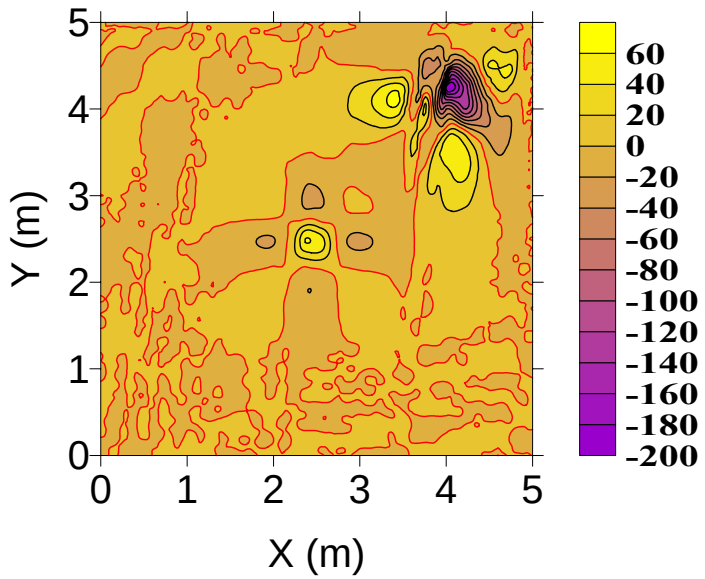

Figure H10. The x-then-y high-pass filtered C09 anomaly (L_F = 1.5 m) located near the center of this window. Filtered data from the central 2-m wide region in this plot was input to job 23. The filter completely separates the C09 anomaly from the B08 anomaly 2 m north and 2 m east. For this inversion, Δ_C is 6 cm; $(Z-Z_C)$ is 1 cm; θ is 3.8 deg, and Ψ is 68.3 deg. The zero contour is red and the contour interval is 20 nT.

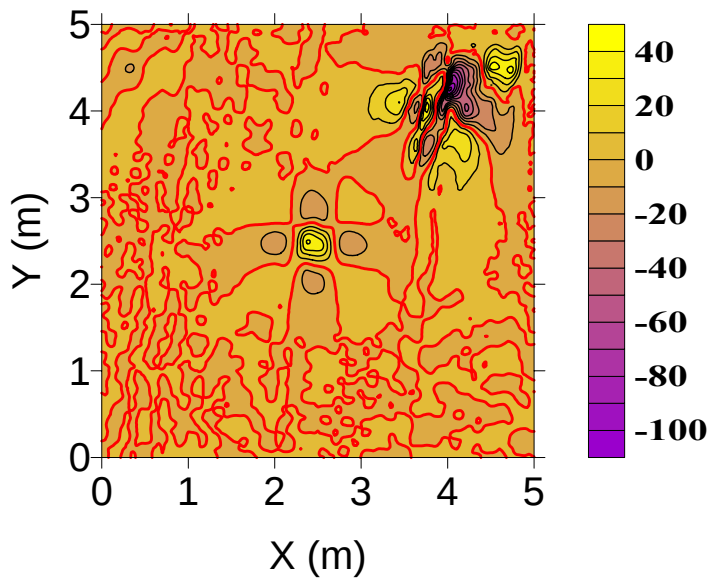

Figure H11. The X-then-Y highpass filtered C09 anomaly (L_F = 1 m) located near the center of this window. Filtered data from the central 2-m wide region in this plot was input to job 22. For this inversion, Δ_C is 6 cm; $(Z-Z_C)$ is 3 cm; θ is 3.6 deg, and Ψ is 66.7 deg. The zero contour is red and the contour interval is 20 nT.

Table H2. C09 dipole (X,Y,Z) and target's center (X_C,Y_C,Z_C) UTM coordinates. X_R = 402000 m; Y_R = 4369000 m. Δ_C and E_Z are absolute horizontal and relative vertical displacements of dipole from target's center. [Δx = grid interval; L_D = data window size; L_F = filter size.]

Job	Δx cm	L_D m	L_F m	†	$X-X_R$ m	$Y-Y_R$ m	$X-X_C$ cm	$Y-Y_C$ cm	Δ_C cm	Z cm	$Z-Z_C$ cm	E_Z* %
1	1	1	n/a	AB	803.19	579.21	-1	4	4	24	10	26
2	1	1	n/a	B	803.18	579.22	-2	5	6	19	5	13
3	1	1	n/a	A	803.20	579.18	0	0	1	18	4	10
4	1	1	n/a		803.19	579.19	-2	2	3	16	2	5
5	1	1	0.5	E	803.17	579.19	-4	2	4	15	1	3
6	1	1	0.75	E	803.17	579.19	-4	2	4	15	1	3
7	1	1	1	E	803.17	579.19	-4	2	4	15	1	3
8	1	1	n/a	B▲$_0$	803.17	579.18	-3	1	4	11	-3	-8
9	1	1	n/a	▲$_0$	803.17	579.19	-4	2	4	15	-1	-3
10	1	1.5	n/a	AB	803.25	579.28	5	11	12	43	29	74
11	1	1.5	n/a	B	803.24	579.26	3	9	10	31	17	44
12	1	1.5	n/a	A	803.06	578.99	-14	-18	23	21	7	18
13	1	1.5	n/a		803.21	579.18	1	1	1	17	3	8
14	1	1.5	0.5	E	803.17	579.19	-4	2	4	14	0	0
15	1	1.5	0.75	E	803.17	579.19	-4	2	4	14	0	0
16	1	1.5	1	E	803.17	579.19	-4	2	4	14	0	0
17	1	1.5	1.25	E	803.17	579.18	-3	1	4	14	0	0
18	1	1.5	1.5	E	803.17	579.18	-3	1	4	15	1	3
19	5	2	n/a	B	803.57	579.74	37	57	68	158	144	369
20	5	2	n/a	A	803.59	579.64	39	47	61	118	104	267
21	5	2	n/a		803.27	579.18	7	1	7	22	8	21
22	5	2	1.0	X	803.17	579.21	-4	4	6	17	3	8
23	5	2	1.5	X	803.17	579.21	-4	4	6	15	1	3
24	5	2	2.0	X	803.22	579.17	2	0	2	16	2	5
25	5	2	1	G	803.17	579.16	-3	-1	3	14	0	0
26	5	2	1	E	803.17	579.21	-4	4	6	15	1	3
27	5	2	1.5	G	803.17	579.21	-4	4	6	14	0	0
28	5	2	1.5	E	803.17	579.16	-3	-1	3	14	0	0
29	1	2	0.5	E	803.17	579.19	-4	2	4	14	0	0
30	1	2	0.75	E	803.17	579.19	-4	2	4	14	0	0
31	1	2	1	E	803.17	579.19	-4	2	4	14	0	0
32	1	2	1.25	E	803.17	579.19	-4	2	4	14	0	0
33	1	2	1.5	E	803.16	579.18	-4	1	4	14	0	0
34	1	2	1.75	E	803.16	579.18	-4	1	4	15	1	3
35	1	2	2	E	803.16	579.18	-4	1	4	15	1	3

† flag-node and IIGE unless noted: **A** = all-node; **B** = IIBE. **E** = EAGGN ($L_{FD} = L_D$).
G = GGN ($L_{FD} > L_D$). **X** = x-then-y high-pass filter; ▲$_0$ = peak-only (H>0)

* $E_Z = (Z-Z_C)/(Z_C+H_M)$; magnetometer elevation, H_M = 0.25 m

Table H3. C09 dipole parameters: θ = deviation angle; δ = dipole declination; Ψ =dipole inclination; M = dipole moment. Gx, Gy = gradient components; B = dc bias estimate; R = correlation coefficient. [Δx = grid interval; L_D = data window size; L_F = filter size.]

Job	Δx cm	L_D m	L_F m	†	θ deg	δ deg	Ψ deg	M mA•m^2	Gx nT/m	Gy nT/m	B nT	R
1	1	1	n/a	AB	22.2	-56.1	57.6	94.0	n/a	n/a	-36.0	0.990
2	1	1	n/a	B	21.6	-47.4	53.9	69.9	n/a	n/a	-28.0	0.992
3	1	1	n/a	A	23.6	-87.0	75.2	57.1	-24.7	-27.0	-31.1	0.997
4	1	1	n/a		15.7	-55.1	70.6	53.0	-22.7	-17.1	-26.0	0.998
5	1	1	0.5	E	10.3	-29.3	76.0	49.3	0.04	0.28	0.02	0.985
6	1	1	0.75	E	10.2	-31.8	75.2	48.2	0.44	0.31	0.07	0.996
7	1	1	1	E	10.1	-30.8	75.3	48.2	0.42	0.37	0.12	0.998
8	1	1	n/a	B▲$_0$	12.2	-44.3	72.0	32.7	n/a	n/a	-10.4	0.999
9	1	1	n/a	▲$_0$	8.8	-34.3	70.7	40.0	-11.5	-2.66	-15.4	0.999
10	1	1.5	n/a	AB	41.7	-62.7	36.9	252	n/a	n/a	-41.3	0.953
11	1	1.5	n/a	B	38.5	-56.6	38.0	151	n/a	n/a	-34.2	0.954
12	1	1.5	n/a	A	79.2	122.8	27.5	84.4	-51.8	-45.8	-33.1	0.977
13	1	1.5	n/a		25.5	-86.9	70.7	56.7	-27.6	-24.5	-28.5	0.983
14	1	1.5	0.5	E	10.5	-30.4	76.0	44.6	0.15	0.08	0.12	0.982
15	1	1.5	0.75	E	9.9	-30.2	75.2	44.1	0.45	0.41	0.35	0.994
16	1	1.5	1	E	9.8	-29.0	75.4	44.1	0.63	0.60	0.53	0.996
17	1	1.5	1.25	E	14.0	-34.7	79.9	44.0	0.68	0.53	0.67	0.997
18	1	1.5	1.5	E	14.0	-32.5	80.1	47.4	0.67	0.66	0.62	0.997
19	5	2	n/a	B	73.1	-61.9	2.8	7080	n/a	n/a	-63.8	0.896
20	5	2	n/a	A	67.8	-56.2	6.5	2704	-18.7	-3.79	-52.3	0.927
21	5	2	n/a		37.0	-104.1	61.1	78.9	-33.8	-29.9	-32.5	0.902
22	5	2	1.0	X	3.6	-20.6	66.7	54.7	-0.73	-0.57	-0.36	0.980
23	5	2	1.5	X	3.8	-21.2	68.3	45.6	-2.70	-2.01	-1.59	0.969
24	5	2	2.0	X	29.1	-96.4	69.2	48.1	-4.71	-3.22	-3.46	0.942
25	5	2	1	G	23.0	-101.3	86.7	43.2	1.13	0.74	0.82	0.991
26	5	2	1	E	3.1	-19.6	67.7	48.2	0.87	1.07	0.68	0.988
27	5	2	1.5	G	3.1	-18.7	68.8	44.6	2.47	2.26	1.94	0.991
28	5	2	1.5	E	21.9	-78.3	87.7	43.4	1.27	1.16	1.24	0.985
29	1	2	0.5	E	10.6	-31.2	76.0	44.6	0.20	0.11	0.09	0.977
30	1	2	0.75	E	9.8	-30.2	75.1	44.1	0.52	0.59	0.38	0.990
31	1	2	1	E	9.7	-29.1	75.2	44.1	0.81	0.85	0.64	0.991
32	1	2	1.25	E	9.6	-27.3	75.5	44.2	1.09	1.23	0.98	0.990
33	1	2	1.5	E	13.4	-8.0	80.6	43.7	1.21	1.41	1.31	0.988
34	1	2	1.75	E	13.6	-6.1	80.8	46.8	1.32	1.67	1.50	0.985
35	1	2	2	E	13.8	-4.7	80.9	46.9	1.30	1.76	1.73	0.981

† flag-node and IIGE unless noted: **A** = all-node; **B** = IIBE. **E** = EAGGN ($L_{FD} = L_D$).
G = GGN ($L_{FD} > L_D$). **X** = x-then-y high-pass filter; ▲$_0$ = peak-only (H>0)

Table H4. C09 data windows: grid interval, Δx; absolute and relative window size, L_D, R_L; displacement of window's center from target's center, X_W-X_C, Y_W-Y_C; number of nodes along the x-and y-axes, N_X, N_Y; and the number and proportion of nodes flagged for inversion N_F, R_F.

Job	Δx (cm)	L_D (m)	R_L†	X_M-X_C (cm)	Y_M-Y_C (cm)	N_X	$N_X \bullet N_Y$	N_F	R_F (%)
1, 3	1	1	2.6	2	0	101	10201	10201	100
2, 4-7	1	1	2.6	2	0	101	10201	123	1.2
8-9	1	1	2.6	2	0	101	10201	53 ▲$_0$	0.5
10, 12	1	1.5	3.8	2	0	151	22801	22801	100
11, 13-18	1	1.5	3.8	2	0	151	22801	255	1.1
19, 21	5	2	5.1	4	3	41	1681	434	25.8
20, 22-24	5	2	5.1	4	3	41	1681	1681	100
25-28	5	2	5.1	4	3	41	1681	434	25.8
29-35	1	2	5.1	2	0	201	40401	449	1.1

†$R_L = L_D/(Z_C+H_M)$; depth to target center, Z_C = 14 cm; magnetometer height, H_M = 25 cm.
▲$_0$ = peak-only (H>0).

Appendix I
Target K09 (155 mm projectile)

Figures I1-I1x plot the K09 anomaly and results of inversion jobs. Target K09 is an 87-cm long, 155 mm howitzer shell (Figure I1), which the USAEC emplaced near vertically (Ψ_T = 81 deg,) at a depth to center of 80 cm (Table I1). Conclusions are derived from 69 jobs (Tables 2-4). In Tables 2-3, entries for jobs with and without IIF are blue and red, respectively, except that green entries indicate constrained inversions, and violet job numbers indicate use of hybrid data. Jobs 1-37 used the real K09 data directly, while jobs 38-70 used hybrid data obtained by adding synthetic neighbors to the K09 anomaly. Discussion in section 5.5.1 is supplemented by the figure captions in this Appendix.

Appendix I - Figures

I1. Target K09: 155 mm howitzer projectile …….. 159
I2. Regional setting of K09 anomaly ……..……. 160
I3. K09 anomaly in 3-m window ……. 160
I4. Inverse-modeled K09 dipole field plus IIGE field (job 18) ……... 161
I5. Residual Field – observed minus K09 dipole and IIGE field ……. 161
I6. EAGGN filtered K09 anomaly (L_F = 0.5 m, job 19) ……..…….. 162
I7. EAGGN filtered K09 anomaly (L_F = 1 m; job 21) ……..…… 162
I8. EAGGN filtered K09 anomaly (L_F = 1.5 m; job 22) ……..……. 163
I9. EAGGN filtered K09 anomaly (L_F = 2 m; job 23) ……..…… 163
I10. Magnetic anomalies in a 6-m data window (used in anomaly stack) ……. 164
I11. Stack of the K09 anomaly with other anomalies moved 14 north ……..…… 164
I12. Stack of the K09 anomaly with other anomalies (2-m window) ……..…….. 165
I13. Stack of the K09 anomaly with other anomalies scaled by a factor of 3 ……..…….. 165
I14. Stack of the K09 anomaly with other anomalies scaled by a factor of 4 ……..……. 166
I15. Stack of the K09 anomaly with other anomalies scaled by a factor of 5 ……..……. 166
I16. The K09 anomaly in a 1.5 m data window used in jobs 37-38 …….. 167
I17. Stack of the K09 anomaly with other anomalies (scale factor = 5; jobs 64-70) ……. 167
I18. EAGGN filtered stack (L_F = 0.5 m, L_D = 1.5 m) ……. 168
I19. EAGGN filtered stack (L_F = 0.75 m, L_D = 1.5 m) …….……. 168
I20. EAGGN filtered stack (L_F = 1 m, L_D = 1.5 m) …… 169
I21. EAGGN filtered stack (L_F = 1.25 m, L_D = 1.5 m) …… 169
I22. EAGGN filtered stack (L_F = 1.5 m, L_D = 1.5 m) …….…….. 170

Appendix I - Tables

I1. Ground truth for target K09 ……...……. 159
I2. Dipole positions for anomaly K09 inversions …… 171
I3. Dipole parameters for anomaly K09 inversions …….. 173
I4. K09 data window parameters ……. 175

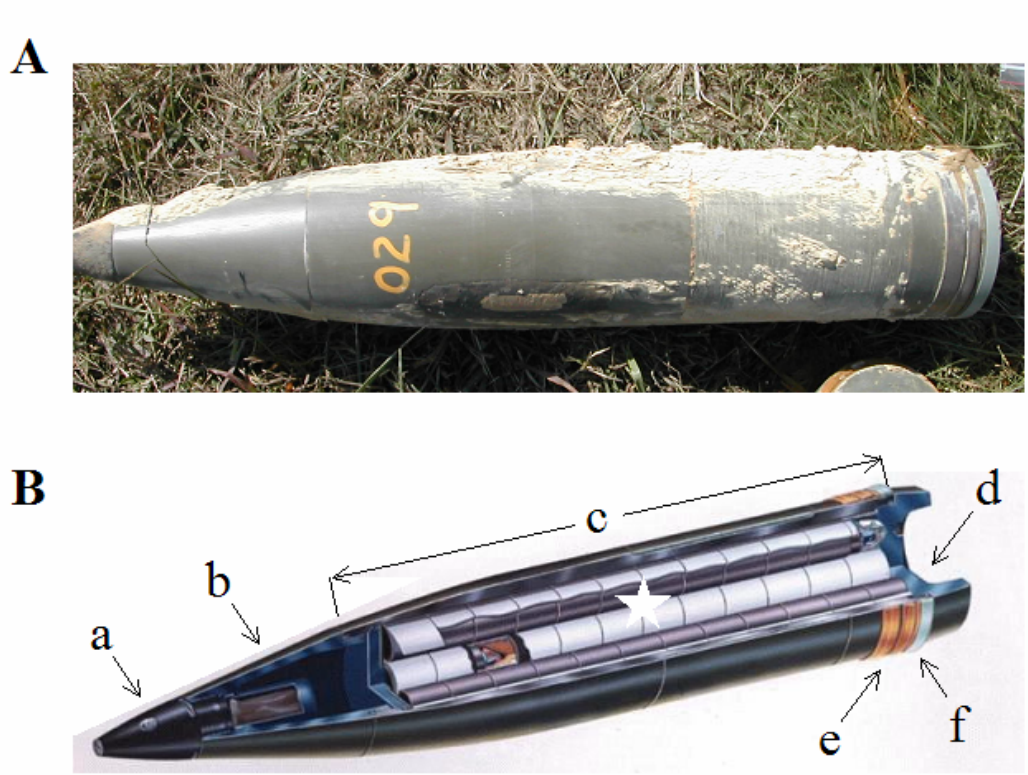

Figure I1. (**A**) Photograph of the inert 155-mm M483A1 howitzer shell emplaced at K09 with an inclination of 81 deg and depth-to-center of 0.80 m. The length of the shell is 0.870 m. (**B**) Diagram showing (a) the nose and fuze assembly made of light weight materials; (b) aluminum ogive; (c) fiberglass covered steel case; (d) aluminum baseplug; (e) copper alloy rotating band; and (f) plastic obturating band of the M483A1 shell. The payload may be high explosives or submunitions as shown. The approximate center of the steel casing (white star) is closer to the base than the nose of the shell. [from René and Kim, 2006]

Table I1. Ground truth for Target K09.

Description	155 mm Howitzer Shell
Material	Forged Steel and Aluminum
Length, L_T	870 mm
Diameter	155 mm
Weight	46.539 kg
Grid azimuth, Φ_T	65 deg
Inclination, Ψ_T	81 deg
Depth, Z_C	80 cm
UTM northing	4369563.445 m
UTM easting	402806.156 m
Ratio of depth below magnetometer to target length, R_{DL} †	1.2
Vertical projection of target's length, L_V (= $L_T \sin \Psi_T$)	86 cm
Horizontal projection of target's length, L_H (= $L_T \cos \Psi_T$)	14 cm
Nose-from-center offsets (Xn-Xc, Yn-Yc, Zn-Zc)	(6, 4, 43) cm

† $R_{DL} = (Z_C+H_M)/L_T$; magnetometer elevation, $H_M = 0.25$ m.

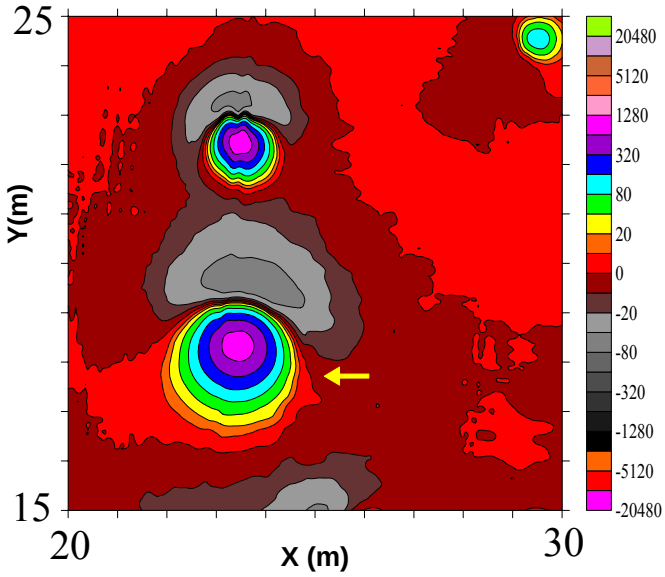

Figure I2. Regional setting of the K09 anomaly (yellow arrow). The anomaly is well isolated from the neighboring anomalies. The magnetic field contours are at zero and $\pm 2^n \cdot 10$ nT, where n is a non-negative integer.

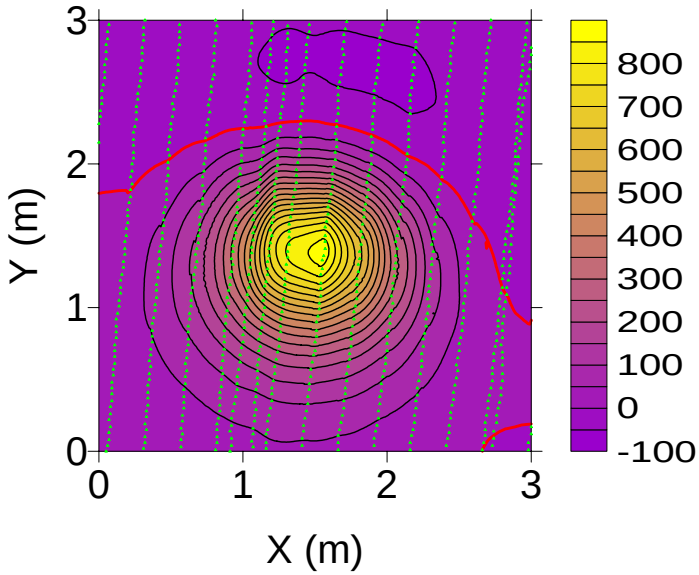

Figure I3. The K09 anomaly in the 3-m data window used in jobs 15-26 and 31-37. The 925 flagged nodes (green triangles) are those that are nearest to measurement stations in three swaths of the MTADS array. The zero contour is red (contour interval = 50 nT).

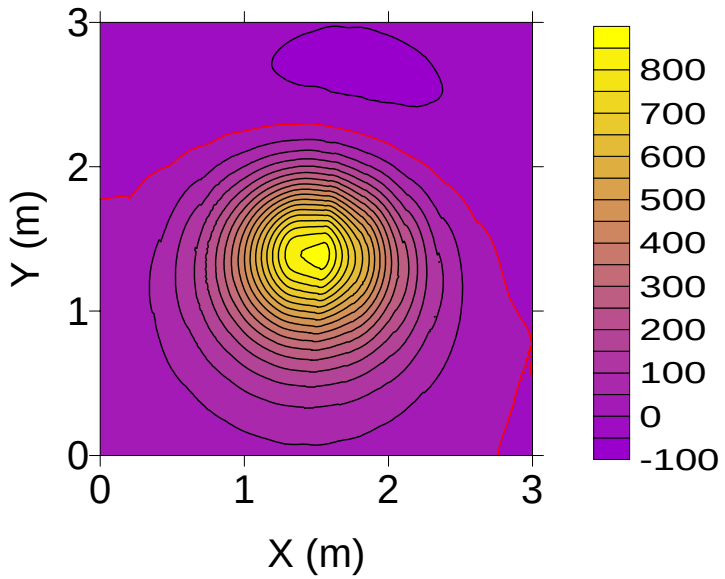

Figure I4. The inverse-modeled K09 dipole field plus IIGE field (job 18). For this flag-node inversion, θ is 16.9 deg and Ψ is 83.5 deg. Similarly for all-node inversion (job 17), θ is 16.9 deg and Ψ is 83.3 deg. For this relatively deep dipole, interpolation in the all-node option has an insignificant effect upon the inversion results. The zero contour is red (contour interval = 50 nT).

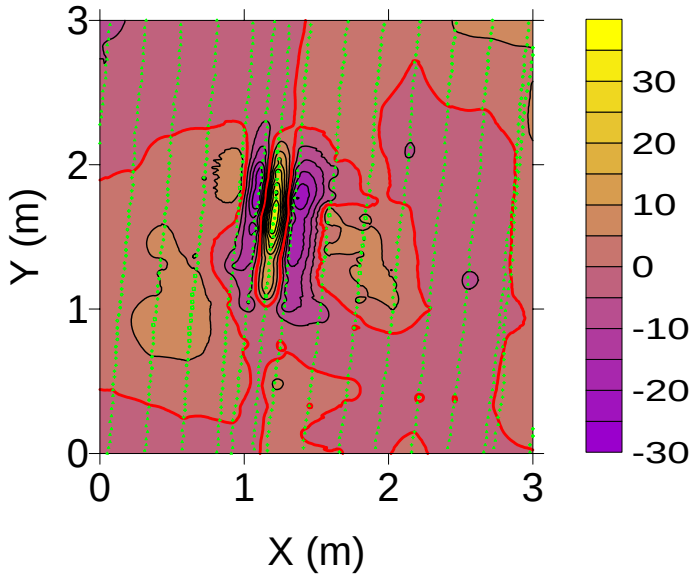

Figure I5. The residual field equal to the observed field minus the inverse-modeled K09 dipole field and the IIGE field (job 18). The 925 flagged nodes (green triangles) are nearest to measurement stations. The residual field is largest in absolute value where swaths of the MTADS array are overlapped. High frequency noise associated with the swath overlap has little effect on the results of inversion without IIF (job 18) or for inversions with IIF using EAGGN filters of size 0.75 m or greater (jobs 20-. The zero contour is red (contour interval = 5 nT).

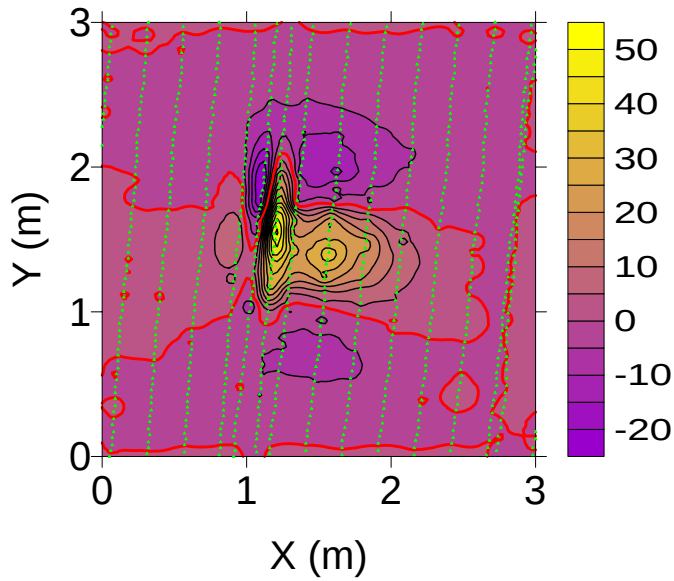

Figure I6. EAGGN filtered K09 anomaly (L_F = 0.5 m, job 19). The flag grid option, with $\Delta x = \Delta y$ = 1 cm, flagged 925 grid nodes (green triangles) nearest to measurement stations in three swaths. The largest absolute values of the filtered anomaly are associated with the overlap of swaths of MTADS arrays. Larger filters yield better inversions for this anomaly. The zero contour is red (contour interval = 5 nT).

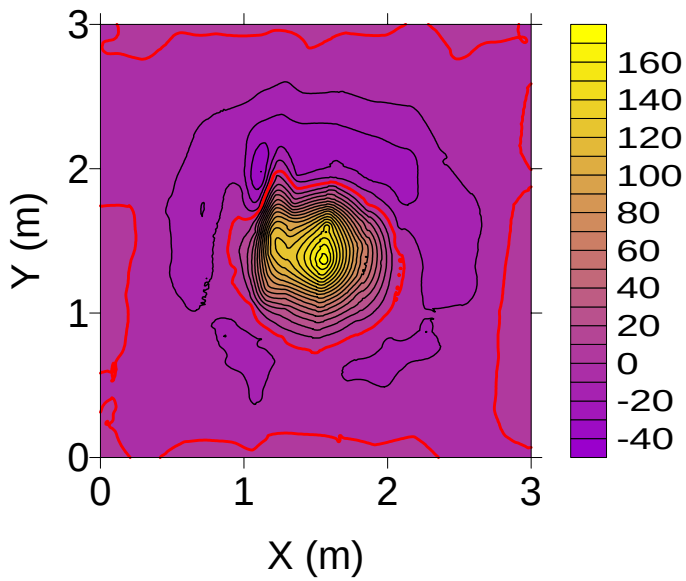

Figure I7. EAGGN filtered K09 anomaly (L_F = 1 m; job 21). The noise associated with swath overlap is less noticeable than for L_F equal to 0.5 m. The filter is constrained in its application to the 3-m inversion window shown here. The zero contour is red (contour interval = 10 nT).

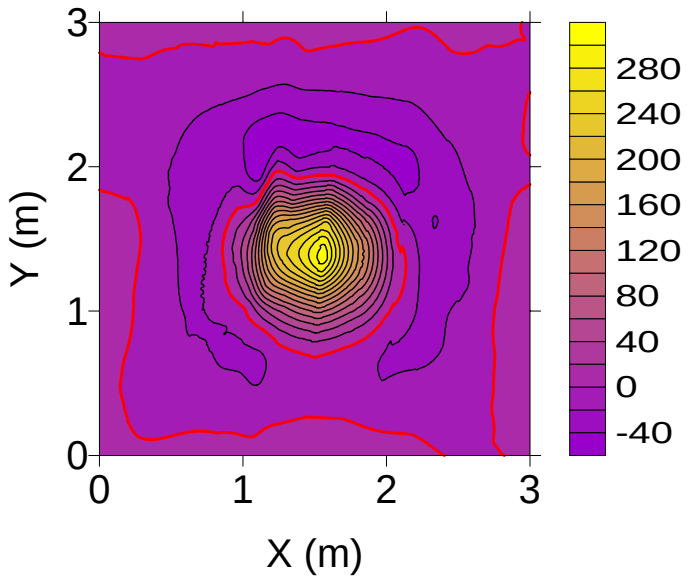

Figure I8. EAGGN filtered K09 anomaly (L_F = 1.5 m; job 22). The noise associated with the swath overlap is less apparent than in the case for L_F equal to 0.5 m. The filter is constrained in its application to the 3-m inversion window shown here (L_{FD} = L_D). The zero contour is red (contour interval = 20 nT).

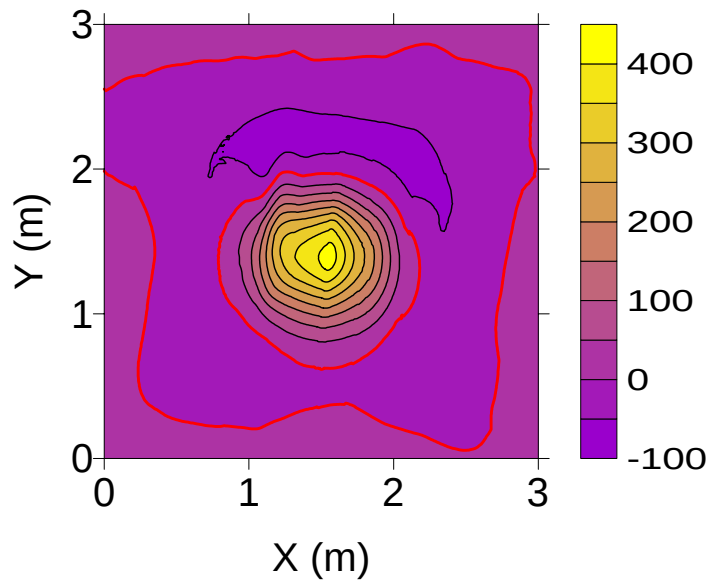

Figure I9. EAGGN filtered K09 anomaly (L_F = 2 m; job 21). The 1-m IIF enhanced the noise associated with the swath overlap by less than in the case of the 0.5-m filter. The filter is constrained in its application to the 3-m inversion window shown here. The zero contour is red (contour interval = 50 nT).

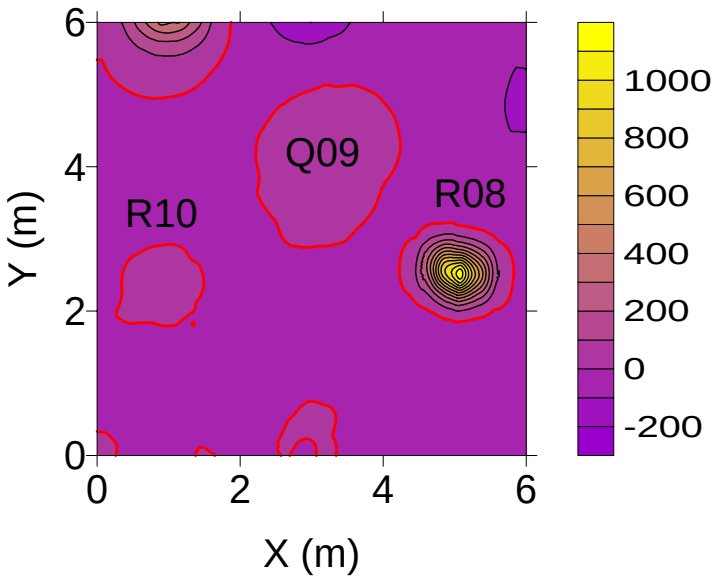

Figure I10. Magnetic anomalies in a 6-m data window. These anomalies were shifted 14 m north, scaled by factors of 1, 2, 3, 4, or 5, and then stacked with the K09 anomaly. The stacked data were input to inversions with and without IIF (jobs 39-70). The zero contour is red (contour interval = 100 nT).

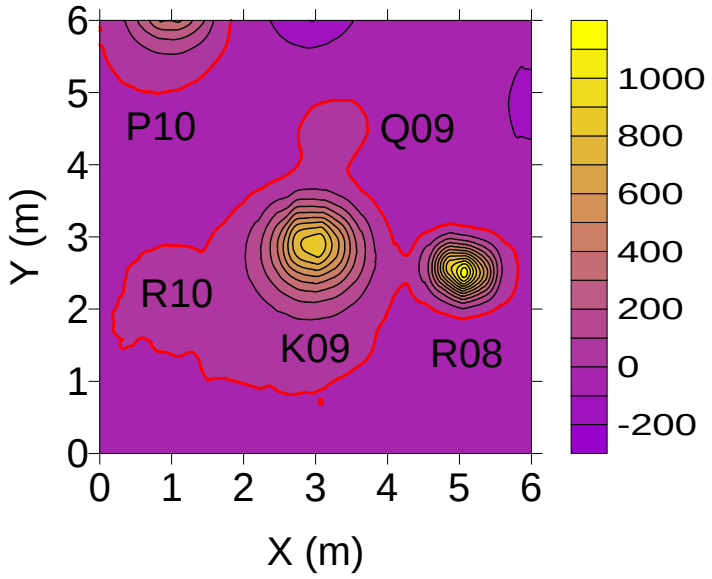

Figure I11. Stack of the K09 anomaly with other anomalies moved 14 north. This effectively moves targets R10, Q09, and R08 to positions 2 m west, north and east of target K09, respectively. The stacked data were input to inversion jobs 39-45. Other jobs scaled the shifted anomalies by factors of 2, 3, 4, or 5 before stacking with the K09 anomaly (jobs 46-70). EAGGN IIF with appropriate parameters improved the accuracy of the K09 dipole parameters derived from the stacked data. With IIF inversion results could closely approximate those obtained from the original data without "synthetic neighbors". The zero contour is red and the contour interval is 100 nT.

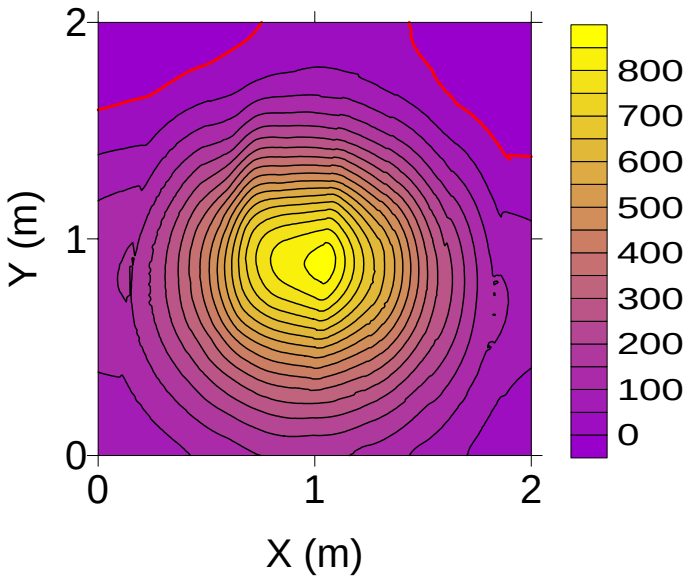

Figure I12. Stack of the K09 anomaly with other anomalies shifted 14 m north (jobs 39-43). For non-IIF IIBE inversion (job 39) Δ_C is 10 cm and θ is 23.9 deg while for non-IIF IIGE inversion (job 40) Δ_C is 10 cm and θ is 21.5 deg. For EAGGN IIF job 42 (L_F = 0.75 m), Δ_C is 8 cm and θ is 16.7 deg. The benefit of IIF is greater when interference from synthetic neighbors is increased by factors of 2, 3, 4, or 5 (jobs 47-70). The zero contour is red and the contour interval is 50 nT.

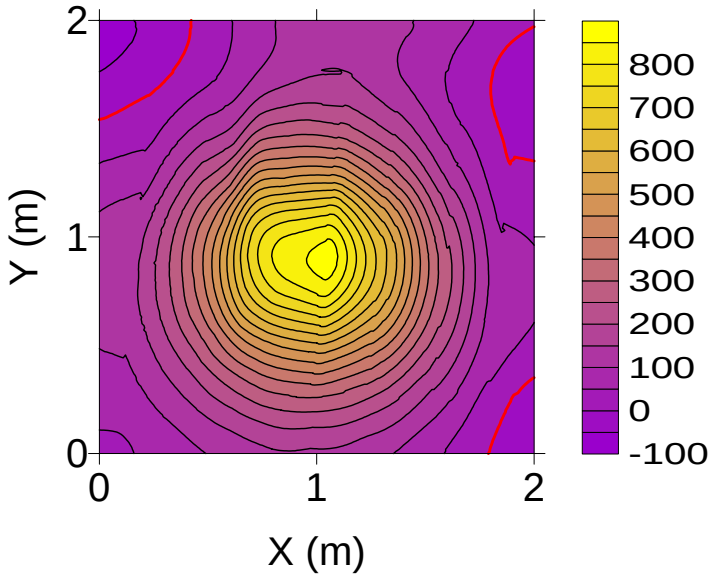

Figure I13. Stack of the K09 anomaly with other anomalies scaled by a factor of 3 and shifted 14 m north (jobs 50-53). For non-IIF IIGE job 50, Δ_C is 16 cm and θ is 29.5 deg. For EAGGN IIF job 51 (L_F = 0.75 m), Δ_C is 9 cm and θ is 21.2 deg. By comparison, for non-IIF IIGE job 18 without interference by synthetic neighbors (L_D = 3 m), Δ_C is 8 cm and θ is 16.9 deg. IIF significantly improved the inversion. The zero contour is red (contour interval = 50 nT).

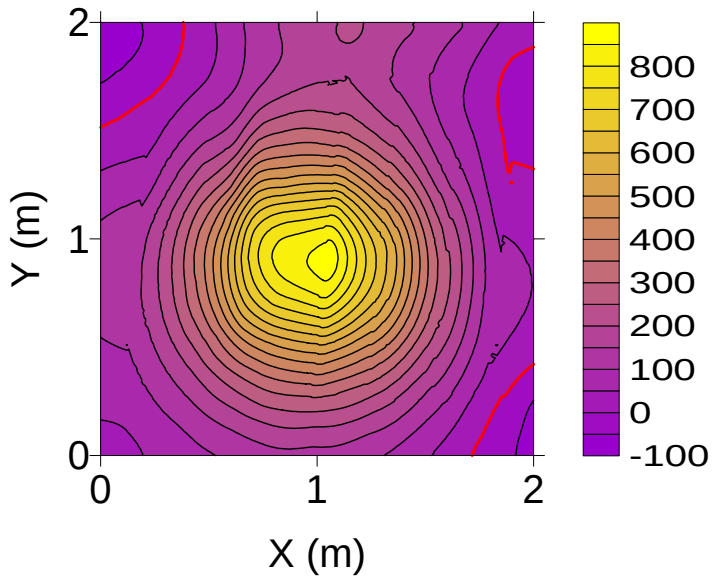

Figure I14. Stack of the K09 anomaly with other anomalies scaled by a factor of 4 and shifted 14 m north (jobs 54-57). For non-IIF IIGE job 54, Δ_C is 35 cm and θ is 59.4 deg. For EAGGN IIF job 55 (L_F = 0.75 m), Δ_C is 11 cm and θ is 23.8 deg. By comparison, for non-IIF IIGE job 18 without interference by synthetic neighbors (L_D = 3 m), Δ_C is 8 cm and θ is 16.9 deg. IIF greatly improved the inversion. The zero contour is red (contour interval = 50 nT).

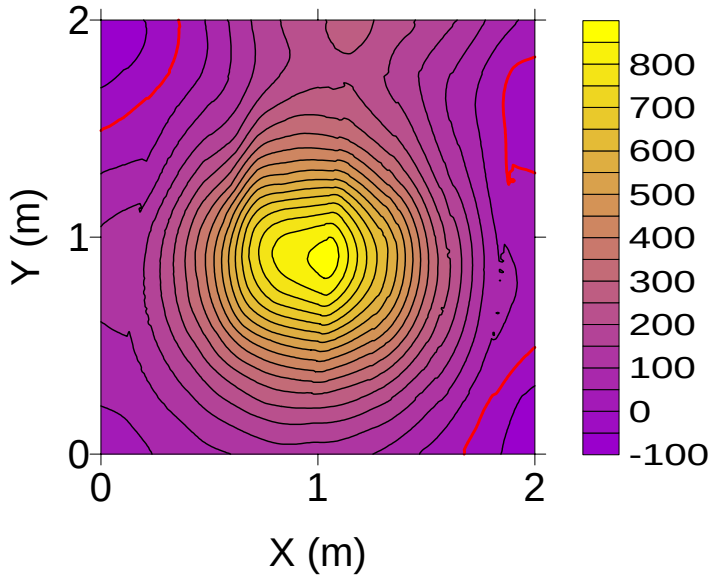

Figure I15. Stack of the K09 anomaly with other anomalies scaled by a factor of 5 and shifted 14 m north (jobs 58-63). For non-IIF IIGE job 58, Δ_C is 37 cm and θ is 60.9 deg. For EAGGN IIF job 59 (L_F = 0.75 m), Δ_C is 12 cm and θ is 26.3 deg. By comparison, for non-IIF IIGE job 18 without interference by synthetic neighbors (L_D = 3 m), Δ_C is 8 cm and θ is 16.9 deg. IIF greatly improved the inversion. The zero contour is red (contour interval = 50 nT).

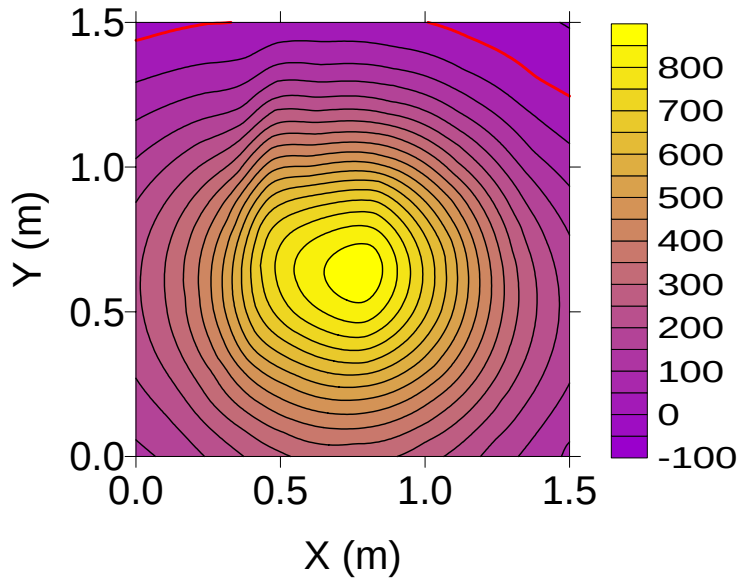

Figure I16. The K09 anomaly in a 1.5 m data window used in jobs 37-38. The zero contour is red (contour interval = 50 nT).

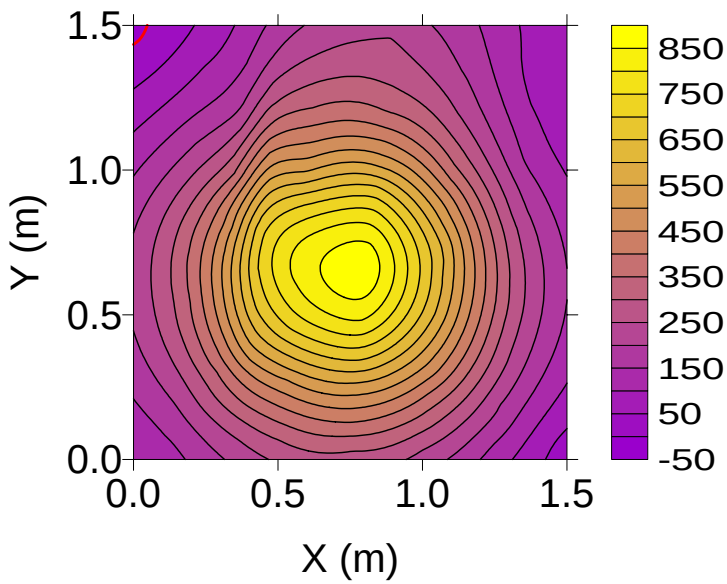

Figure I17. Stack of the K09 anomaly with other anomalies scaled by a factor of 5 and shifted 14 m north (jobs 64-70). For non-IIF, IIBE job 64, Δ_C is 16 cm and θ is 40.5 deg. For non-IIF, IIGE job 65, Δ_C is 37 cm and θ is of 67.6 deg. For EAGGN IIF, with $1 \leq L_F \leq 1.5$ m (jobs 68-70), $10 \leq \Delta_C \leq 12$ cm and $20.2 \leq \theta \leq 23.3$ deg. The zero contour is red (contour interval = 50 nT).

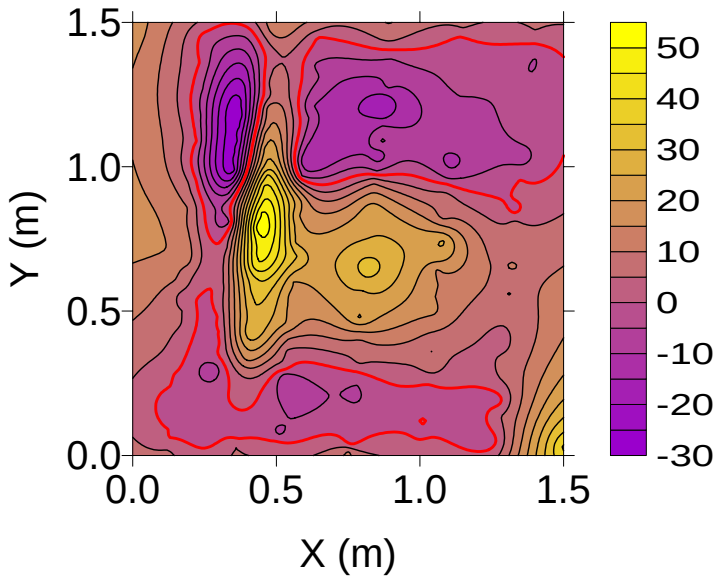

Figure I18. EAGGN filtered stack (L_F = 0.5 m, L_D = 1.5 m) of the K09 anomaly with other anomalies scaled by a factor of 5 and shifted 14 m north (job 66). For this inversion, ΔC is 41 cm and θ is 73.4 deg. A larger filter is required for a satisfactory inversion. High frequency noise associated with the overlap of the MTADS array swaths has been greatly amplified by comparison to the rest of the K09 anomaly. The zero contour is red (contour interval = 5 nT).

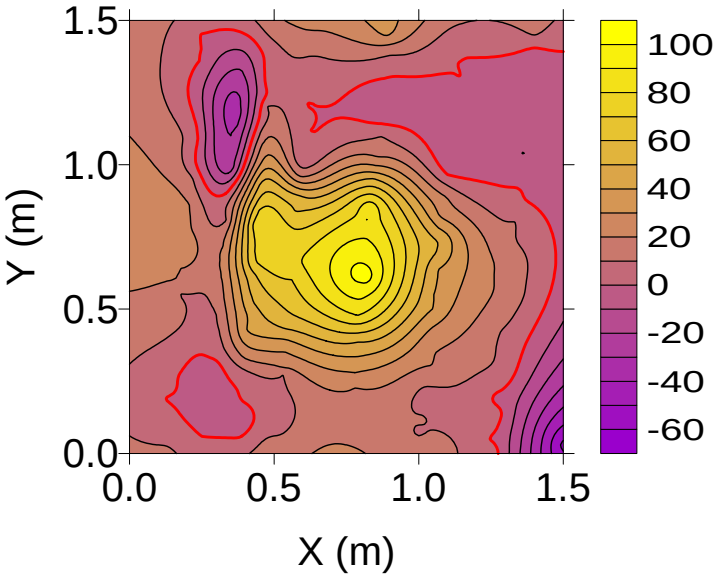

Figure I19. EAGGN filtered stack (L_F = 0.75 m, L_D = 1.5 m) of the K09 anomaly with other anomalies scaled by a factor of 5 and shifted 14 m north (job 67). For this inversion, Δ_C is 5 cm and θ is 6.2 deg. The effect of enhanced noise associated with swath overlap is less than in the case of the 0.5-m filter; however, a larger filter (L_F > 0.75 m) or a larger data window (L_D > 1.5 m) improves inversion for these data. The zero contour is red (contour interval = 10 nT).

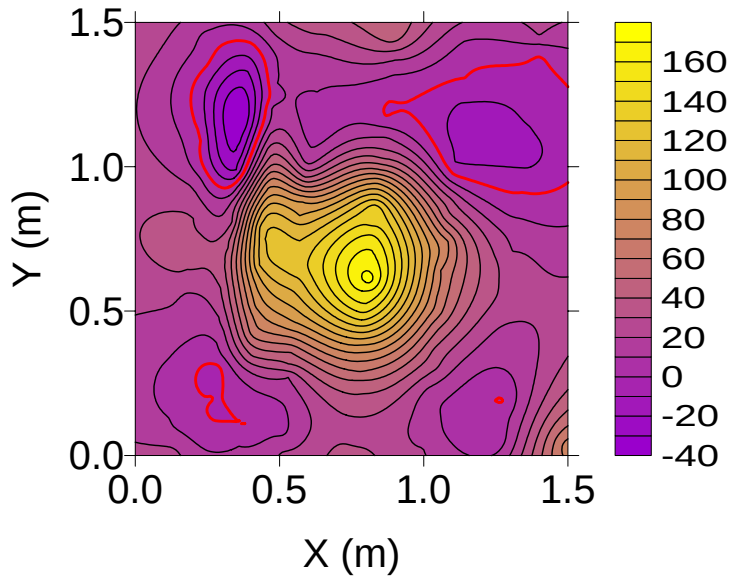

Figure I20. EAGGN filtered stack (L_F = 1 m, L_D = 1.5 m) of the K09 anomaly with other anomalies scaled by a factor of 5 and shifted 14 m north (job 68). For this inversion, Δ_C is 10 cm, (Z-Z_C) is -14 cm, and θ is 20.2 deg. This inversion yielded a dipole just 2 cm south and 1 cm shallower than for non-IIF, IIBE inversion of the K09 anomaly without synthetic neighbors (job 36). The zero contour is red (contour interval = 10 nT).

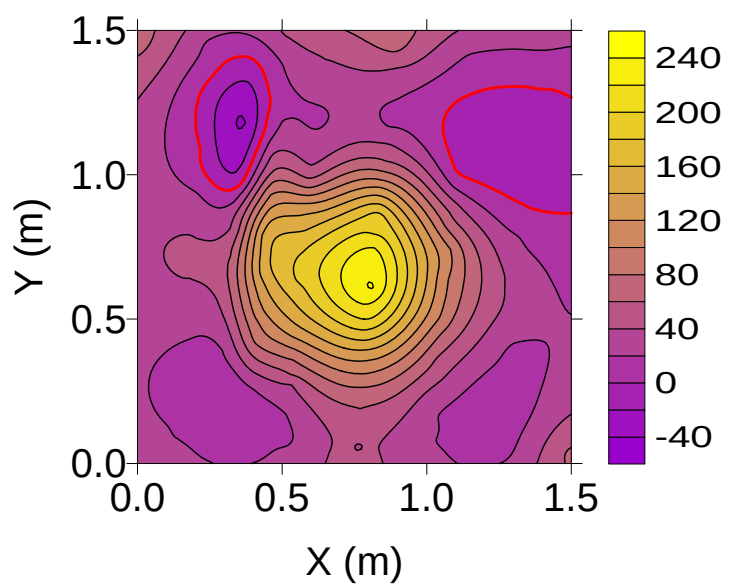

Figure I21. EAGGN filtered stack (L_F = 1.25 m, L_D = 1.5 m) of the K09 anomaly with other anomalies scaled by a factor of 5 and shifted 14 m north (job 69). For this inversion, Δ_C is 10 cm, (Z-Z_C) is -13 cm, and θ is 22.4 deg. This inversion yielded a dipole that is 1 cm directly below the dipole obtained using the 1-m filter (job 68). The zero contour is red (contour interval = 20 nT).

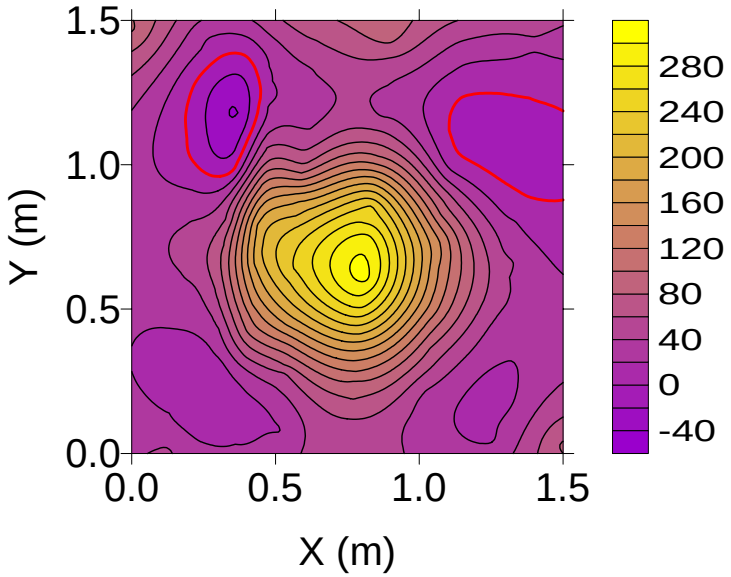

Figure I22. EAGGN filtered stack (L_F = 1.5 m, L_D = 1.5 m) of the K09 anomaly with other anomalies scaled by a factor of 5 and shifted 14 m north (job 70). For this inversion, Δ_C is 12 cm, (Z-Z_C) is -12 cm, and θ is 23.3 deg. The zero contour is red (contour interval = 20 nT).

Table I2. K09 dipole (X,Y,Z) and target's center (X_C,Y_C,Z_C) UTM coordinates. X_R = 402000 m. Y_R = 4369000 m. Δ_C and E_Z are absolute horizontal and relative vertical displacements of the dipole from the target's center. [Δx = grid interval; L_D = data window size; L_F = filter size.]

Job	Δx cm	L_D m	L_F m	†	$X-X_R$ m	$Y-Y_R$ m	$X-X_C$ cm	$Y-Y_C$ cm	Δ_C cm	Z cm	$Z-Z_C$ cm	E_Z* %
1	5	3	n/a	AB	806.10	563.38	-6	-7	9	68	-12	-11
2	5	3	n/a	B	806.10	563.38	-6	-7	9	67	-13	-12
3	5	3	n/a	A	806.10	563.38	-6	-7	9	68	-12	-11
4	5	3	n/a		806.10	563.38	-6	-7	9	67	-13	-12
5	5	3	0.5	E	806.10	563.38	-6	-7	9	68	-12	-11
6	5	3	1.0	E	806.10	563.38	-6	-7	9	67	-13	-12
7	5	3	1.5	E	806.10	563.38	-6	-7	9	67	-13	-12
8	5	3	2.0	E	806.10	563.38	-6	-7	9	67	-13	-12
9	5	3	2.5	E	806.10	563.38	-6	-7	9	67	-13	-12
10	5	3	0.5	EB	806.10	563.38	-6	-7	9	68	-12	-11
11	5	3	1.0	EB	806.10	563.38	-6	-7	9	67	-13	-12
12	5	3	1.5	EB	806.10	563.38	-6	-7	9	67	-13	-12
13	5	3	2.0	EB	806.10	563.38	-6	-7	9	67	-13	-12
14	5	3	2.5	EB	806.10	563.38	-6	-7	9	67	-13	-12
15	1	3	n/a	AB	806.11	563.39	-5	-5	7	68	-12	-11
16	1	3	n/a	B	806.11	563.39	-5	-5	7	67	-13	-12
17	1	3	n/a	A	806.10	563.39	-6	-6	8	68	-12	-11
18	1	3	n/a		806.10	563.39	-6	-6	8	67	-13	-12
19	1	3	0.5	E	805.88	563.28	-27	-17	32	61	-19	-18
20	1	3	0.75	E	806.11	563.39	-5	-5	7	67	-13	-12
21	1	3	1.0	E	806.10	563.40	-6	-5	8	67	-13	-12
22	1	3	1.5	E	806.10	563.39	-6	-6	8	67	-13	-12
23	1	3	2.0	E	806.11	563.39	-5	-5	7	67	-13	-12
24	1	3	1.0	EB	806.10	563.39	-6	-6	8	67	-13	-12
25	1	3	1.5	EB	806.11	563.39	-5	-5	7	67	-13	-12
26	1	3	2.0	EB	806.11	563.39	-5	-5	7	67	-13	-12
27	1	4	n/a	B	806.11	563.39	-5	-5	7	67	-13	-12
28	1	4	n/a		806.10	563.39	-6	-6	8	67	-13	-12
29	1	4	0.75	E	806.11	563.39	-5	-5	7	67	-13	-12
30	1	4	1	E	806.10	563.39	-6	-6	8	67	-13	-12
31	1	3	n/a	T	806.16	563.44	0	0	1	80	0	0
32	1	3	n/a	H	806.16	563.44	0	0	1	68	-12	-11
33	1	3	n/a	D	806.09	563.44	-7	-1	7	80	0	0
34	1	3	0.5	ET	806.16	563.44	0	0	1	80	0	0
35	1	3	0.5	EH	806.16	563.44	0	0	1	67	-13	-12

† flag-node and IIGE unless noted as follows: **A**= all-node; **B** = IIBE. **E** = EAGGN (L_{FD} = L_D).
T, H, D: dipole confined to target center's position, horizontal location, or depth, respectively.
* $E_Z = (Z-Z_C)/(Z_C+H_M)$; magnetometer elevation, H_M = 0.25 m; Z_C = 80 cm.

Table I2 continued. K09 dipole (X,Y,Z) and target's center (X_C,Y_C,Z_C) UTM coordinates. X_R = 402000 m. Y_R = 4369000 m. Δ_C and E_Z are absolute horizontal and relative vertical displacements of the dipole from the target's center.

Job	Δx cm	L_D m	L_F m	†	$X-X_R$ m	$Y-Y_R$ m	$X-X_C$ cm	$Y-Y_C$ cm	Δ_C cm	Z cm	$Z-Z_C$ cm	E_Z* %
36	1	3	0.5	ED	805.92	563.27	-24	-17	30	80	0	0
37	1	1.5	n/a	B	806.10	563.39	-6	-6	8	67	-13	-12
38	1	1.5	n/a		806.10	563.40	-6	-5	8	67	-13	-12
39	1	2	n/a	S_1B	806.10	563.36	-5	-9	10	67	-13	-12
40	1	2	n/a		806.09	563.37	-6	-8	10	67	-13	-12
41	1	2	0.75	S_1E	806.11	563.39	-5	-5	7	67	-13	-12
42	1	2	1	S_1E	806.10	563.39	-6	-6	8	67	-13	-12
43	1	2	1.5	S_1E	806.10	563.39	-6	-6	8	67	-13	-12
44	1	3	n/a	S_1B	806.12	563.34	-4	-10	11	68	-12	-11
45	1	3	n/a	S_1	806.08	563.36	-7	-9	12	68	-12	-11
46	1	2	n/a	S_2	806.07	563.35	-8	-9	12	68	-12	-11
47	1	2	0.75	S_2E	806.10	563.38	-6	-7	9	67	-13	-12
48	1	2	1	S_2E	806.09	563.38	-7	-7	10	66	-14	-13
49	1	2	1.5	S_2E	806.10	563.38	-6	-7	9	66	-14	-13
50	1	2	n/a	S_3	806.04	563.34	-12	-11	16	69	-11	-10
51	1	2	0.75	S_3E	806.10	563.37	-5	-8	9	67	-13	-12
52	1	2	1	S_3E	806.09	563.37	-6	-8	10	66	-14	-13
53	1	2	1.5	S_3E	806.09	563.37	-6	-8	10	66	-14	-13
54	1	2	n/a	S_4	805.90	563.21	-26	-24	35	71	-9	-9
55	1	2	0.75	S_4E	806.09	563.36	-6	-9	11	66	-14	-13
56	1	2	1	S_4E	806.08	563.37	-7	-8	11	66	-14	-13
57	1	2	1.5	S_4E	806.08	563.37	-7	-8	11	66	-14	-13
58	1	2	n/a	S_5	805.87	563.21	-29	-23	37	74	-6	-6
59	1	2	0.75	S_5E	806.09	563.35	-6	-10	12	66	-14	-13
60	1	2	1	S_5E	806.08	563.36	-7	-9	12	65	-15	-14
61	1	2	1.25	S_5E	806.08	563.36	-7	-9	12	66	-14	-13
62	1	2	1.5	S_5E	806.08	563.36	-7	-9	12	66	-14	-13
63	1	2	1.75	S_5E	806.08	563.36	-7	-9	12	66	-14	-13
64	1	1.5	n/a	S_5B	806.07	563.30	-8	-14	16	62	-18	-17
65	1	1.5	n/a	S_5	805.90	563.18	-25	-27	37	67	-13	-12
66	1	1.5	0.5	S_5E	805.80	563.25	-36	-19	41	59	-21	-20
67	1	1.5	0.75	S_5E	806.10	563.46	-5	2	5	77	-3	-3
68	1	1.5	1	S_5E	806.09	563.37	-6	-8	10	66	-14	-13
69	1	1.5	1.25	S_5E	806.09	563.37	-6	-8	10	67	-13	-12
70	1	1.5	1.5	S_5E	806.08	563.36	-7	-9	12	67	-13	-12

† flag-node and IIGE used unless noted: **B** = IIBE. **E** = EAGGN (L_{FD} = L_D).
S_i = anomaly stack (i = scale factor). **D**: dipole confined to target center's depth,
* $E_Z = (Z-Z_C)/(Z_C+H_M)$; magnetometer elevation, H_M = 0.25 m; Z_C = 80 cm.

Table I3. K09 dipole parameters: θ = deviation angle; δ = dipole declination; Ψ =dipole inclination; M = dipole moment. Gx, Gy = gradient components; B = dc bias estimate; R = correlation coefficient. [Δx = grid interval; L_D = data window size; L_F = filter size.]

Job	Δx cm	L_D m	L_F m	†	θ deg	δ deg	Ψ deg	M mA•m^2	Gx nT/m	Gy nT/m	B nT	R
1	5	3	n/a	AB	18.4	-48.6	84.2	3774	n/a	n/a	3.30	1.000
2	5	3	n/a	B	18.4	-47.3	84.2	3695	n/a	n/a	4.21	0.999
3	5	3	n/a	A	18.6	-41.2	85.0	3761	-4.64	-1.59	3.35	1.000
4	5	3	n/a		18.7	-41.1	85.2	3681	-4.72	-2.26	4.39	1.000
5	5	3	0.5	E	20.0	-65.9	84.5	3854	-0.02	-0.05	-0.06	0.902
6	5	3	1.0	E	19.6	-37.5	86.5	3684	-0.23	-0.15	-0.04	0.984
7	5	3	1.5	E	19.5	-36.8	86.3	3685	-0.41	-0.28	-0.09	0.995
8	5	3	2.0	E	19.4	-37.0	86.2	3687	-0.49	-0.39	-0.21	0.997
9	5	3	2.5	E	19.2	-37.5	86.0	3688	-0.48	-0.41	-0.32	0.998
10	5	3	0.5	EB	20.0	-65.6	84.5	3855	n/a	n/a	-0.06	0.902
11	5	3	1.0	EB	19.6	-38.7	86.4	3686	n/a	n/a	-0.04	0.984
12	5	3	1.5	EB	19.4	-38.1	86.2	3687	n/a	n/a	-0.10	0.995
13	5	3	2.0	EB	19.3	-38.0	86.0	3690	n/a	n/a	-0.22	0.997
14	5	3	2.5	EB	19.1	-38.3	85.9	3691	n/a	n/a	-0.32	0.998
15	1	3	n/a	AB	17.3	-49.8	82.2	3777	n/a	n/a	3.89	1.000
16	1	3	n/a	B	17.2	-49.1	82.1	3706	n/a	n/a	4.91	1.000
17	1	3	n/a	A	16.8	-34.5	83.3	3770	-4.88	0.06	3.84	1.000
18	1	3	n/a		16.9	-34.5	83.5	3693	-4.87	-0.48	4.93	1.000
19	1	3	0.5	E	59.9	89.8	37.5	4318	-0.24	-0.30	-0.01	0.869
20	1	3	0.75	E	16.6	-40.3	82.6	3670	-0.10	0.00	0.02	0.952
21	1	3	1.0	E	14.6	-24.2	81.5	3707	-0.21	0.10	0.01	0.980
22	1	3	1.5	E	17.0	-29.7	83.9	3694	-0.38	-0.09	-0.01	0.994
23	1	3	2.0	E	17.3	-44.9	82.9	3703	-0.25	-0.15	-0.04	0.997
24	1	3	1.0	EB	16.9	-29.7	83.8	3698	n/a	n/a	-0.01	0.980
25	1	3	1.5	EB	17.2	45.3	82.8	3703	n/a	n/a	0.00	0.994
26	1	3	2.0	EB	17.2	45.2	82.8	3704	n/a	n/a	-0.04	0.997
27	1	4	n/a	B	17.2	-49.9	82.1	3702	n/a	n/a	5.35	0.999
28	1	4	n/a		16.9	-37.4	83.2	3696	-2.68	0.18	5.39	1.000
29	1	4	0.75	E	16.6	-41.1	82.5	3670	-0.01	0.00	0.01	0.951
30	1	4	1	E	16.9	-29.7	83.8	3697	-0.04	-0.02	-0.01	0.980
31	1	3	n/a	T	14.5	-51.7	71.8	5243	5.20	16.7	-13.0	0.994
32	1	3	n/a	H	15.4	-54.9	72.1	3914	3.04	6.37	6.29	0.997
33	1	3	n/a	D	8.0	-20.9	74.7	5173	-3.01	18.7	-13.5	0.996
34	1	3	0.5	ET	16.2	-55.7	69.1	7035	0.11	0.34	-0.18	0.822
35	1	3	0.5	EH	23.2	-68.2	63.4	4393	0.09	0.07	-0.03	0.835

† flag-node and IIGE unless noted as follows: **A** = all-node; **B** = IIBE. E =EAGGN ($L_{FD} = L_D$)
T, H, D: dipole confined to target center's position, horizontal location, or depth, respectively.

Table I3 continued. K09 dipole parameters: θ = deviation angle (from earth's field); δ = dipole declination; Ψ =dipole inclination; M = dipole moment. Gx, Gy = gradient components; B = dc bias; R = correlation coefficient. [Δx = grid interval; L_D = data window size; L_F = filter size.]

Job	Δx cm	L_D m	L_F m	†	θ deg	δ deg	Ψ deg	M mA•m^2	Gx nT/m	Gy nT/m	B nT	R
36	1	3	0.5	ED	57.6	90.8	40.4	9163	-0.30	-0.13	-0.24	0.842
37	1	1.5	n/a	B	17.0	-35.9	83.4	3704	n/a	n/a	3.71	1.000
38	1	1.5	n/a		14.8	-27.4	81.6	3714	-4.81	5.32	5.57	1.000
39	1	2	n/a	S_1B	23.9	-122.9	87.2	3647	n/a	n/a	6.96	0.999
40	1	2	n/a		21.5	15.1	88.6	3656	-14.4	7.90	8.19	0.999
41	1	2	0.75	S_1E	16.4	-39.0	82.4	3649	0.18	0.22	0.16	0.950
42	1	2	1	S_1E	16.7	-26.8	83.7	3690	0.35	0.44	-0.04	0.979
43	1	2	1.5	S_1E	16.8	-26.1	83.8	3679	0.34	0.94	0.34	0.994
44	1	3	n/a	S_1B	27.0	-141.9	84.1	3768	n/a	n/a	2.31	0.996
45	1	3	n/a	S_1	23.3	93.4	88.0	3759	-11.7	5.23	3.03	0.996
46	1	2	n/a	S_2	24.3	89.3	84.6	3759	-23.7	24.6	8.82	0.998
47	1	2	0.75	S_2E	18.7	-26.7	85.7	3615	0.22	0.17	0.19	0.948
48	1	2	1	S_2E	19.2	0.8	86.3	3502	0.36	0.36	0.36	0.978
49	1	2	1.5	S_2E	19.1	-29.0	86.1	3503	0.58	1.23	1.27	0.993
50	1	2	n/a	S_3	29.5	91.7	75.4	3916	-42.3	39.5	10.3	0.996
51	1	2	0.75	S_3E	21.2	-41.3	88.1	3592	0.38	0.11	0.23	0.946
52	1	2	1	S_3E	21.5	28.4	88.4	3483	0.60	0.40	0.45	0.976
53	1	2	1.5	S_3E	21.5	37.7	88.0	3480	0.57	1.76	1.57	0.991
54	1	2	n/a	S_4	59.4	101.0	42.2	4879	-112	7.23	12.2	0.994
55	1	2	0.75	S_4E	23.8	112.0	88.1	3414	0.38	-0.05	0.47	0.942
56	1	2	1	S_4E	21.7	58.4	86.2	3466	0.64	0.81	0.60	0.972
57	1	2	1.5	S_4E	21.8	60.4	85.5	3465	0.55	2.66	2.03	0.988
58	1	2	n/a	S_5	60.9	95.7	38.7	5527	-124	30.8	6.96	0.992
59	1	2	0.75	S_5E	26.3	141.7	86.1	3400	0.53	-0.09	0.52	0.937
60	1	2	1	S_5E	24.1	94.3	86.1	3300	0.86	0.71	1.02	0.968
61	1	2	1.25	S_5E	24.1	90.9	85.5	3445	0.79	2.01	1.54	0.980
62	1	2	1.5	S_5E	24.0	88.9	85.2	3449	0.77	3.18	2.36	0.985
63	1	2	1.75	S_5E	24.0	86.8	84.9	3447	0.34	4.40	3.19	0.987
64	1	1.5	n/a	S_5B	40.5	148.6	71.6	2957	n/a	n/a	62.4	0.997
65	1	1.5	n/a	S_5	67.6	105.5	34.7	4536	-172	-26.9	43.0	0.998
66	1	1.5	0.5	S_5E	73.4	80.6	19.0	5408	-0.72	2.71	-1.28	0.878
67	1	1.5	0.75	S_5E	6.2	-22.1	62.9	5831	0.30	5.44	-0.70	0.938
68	1	1.5	1	S_5E	20.2	-37.0	87.2	3429	2.22	2.45	1.08	0.974
69	1	1.5	1.25	S_5E	20.4	-15.7	87.6	3613	1.39	4.18	0.74	0.985
70	1	1.5	1.5	S_5E	23.3	87.4	87.2	3618	1.56	4.62	0.53	0.989

† flag-node and IIGE unless noted: **B** = IIBE. **E** = EAGGN ($L_{FD} = L_D$).
S_i = anomaly stack (i = scale factor). **D** = dipole confined to target center's depth.

Table I4. K09 data windows: grid interval, Δx; absolute and relative window size, L_D, R_L; displacement of window's center from target's center, X_W-X_C, Y_W-Y_C; number of nodes along the x-and y-axes, N_X, N_Y; and the number and proportion of nodes flagged for inversion N_F, R_F.

Jobs	Δx (cm)	L_D (m)	R_L†	X_W-X_C (cm)	Y_W-Y_C (cm)	N_X	$N_X \bullet N_Y$	N_F	R_F (%)
1, 3	5	3	2.9	0	2	61	3721	3721	100
2, 4-14	5	3	2.9	0	2	61	3721	878	23.6
15, 17	1	3	2.9	-3	-6	301	90601	90601	100
16, 18-26	1	3	2.9	-3	-6	301	90601	925	1.0
27-30	1	4	3.8	-3	-6	401	160801	1691	1.1
31-36, 44-45	1	3	2.9	-3	-6	301	90601	925	1.0
37-38, 64-70	1	1.5	1.4	-3	-6	151	22801	229	1.0
39-43, 46-63	1	2	1.9	-3	-6	201	40401	402	1.0

†$R_L = L_D/(Z_C+H_M)$; depth to target center, Z_C = 80 cm; magnetometer height, H_M = 0.25 m.

Appendix J
Target B01 (Rocket Warhead)

Target B01 is a 2.75-in XM230 rocket warhead, which the AEC emplaced at a depth to center of 23 cm (Figure J1, Table J1). Figures J2-J11 plot the B01 anomaly and inversion results. Conclusions are derived from 19 jobs applied to the real data and 20 jobs using the real data plus a synthetic background field (Tables J2-J4). Discussion in section 5.5.1 is supplemented by the figure captions in this Appendix.

Appendix J - Figures

J1. Target B01: 2.75-in rocket warhead ……. 177
J2. Regional setting of B01 anomaly …… 178
J3. B01 anomaly in 2-m window …… 178
J4. B01 anomaly in 1-m window …… 179
J5. EAGGN filtered B01 anomaly (L_F = 0.5 m) …… 179
J6. EAGGN filtered B01 anomaly (L_F = 0.75 m) …… 180
J7. EAGGN filtered B01 anomaly (L_F = 1 m) …… 180
J8. Synthetic background field used in B01 hybrid data …… 181
J9. Hybrid data equal to B01 anomaly plus synthetic background …… 181
J10. EAGGN filtered synthetic background field …… 182
J11. EAGGN filtered hybrid data (L_F = 0.75 m) …… 182

Appendix J - Tables

J1. Ground truth for target B01 …… 177
J2. Dipole positions for anomaly B01 inversions …… 183
J3. Dipole parameters for anomaly B01 inversions …… 185
J4. B01 data window parameters …… 187

Appendix J

Results for Target B01 (Rocket Warhead)

Target B01 is a 2.75-in XM230 rocket warhead, which the USAEC emplaced at a depth to center of 23 cm (Figure J1, Table J1). Figures J2-J11 plot the B01 anomaly and inversion results. Conclusions are derived from 19 jobs applied to the real data and 20 jobs using the real data plus a synthetic background field (Tables J2-J4).

Figure J1. Target B01; 2.75-in (72 mm) XM230 rocket warhead.

Table J1. Ground truth for target B01.

Description	XM230 rocket warhead
Material	Cast Iron (base)
Length, L_T	403 mm
Diameter, D_T	72 mm (2.75 in)
Weight	4.060 kg
Grid azimuth, Φ_T	210 deg
Inclination, Ψ_T	39 deg
Depth, Z_C	23 cm
UTM northing, Yc	4369584.021 m
UTM easting, X_C	402818.574 m
Ratio of depth below magnetometer to target length, R_{DL} †	1.2
Vertical projection of target's length, L_V (= $L_T \sin \Psi_T$)	25 cm
Horizontal projection of target's length, L_H (= $L_T \cos \Psi_T$)	31 cm
Nose-from-center offsets (Xn-Xc, Yn-Yc, Zn-Zc)	(-5, -15, 13) cm

† $R_{DL} = (Z_C+H_M)/L_T$; Magnetometer height, $H_M = 0.25$ m

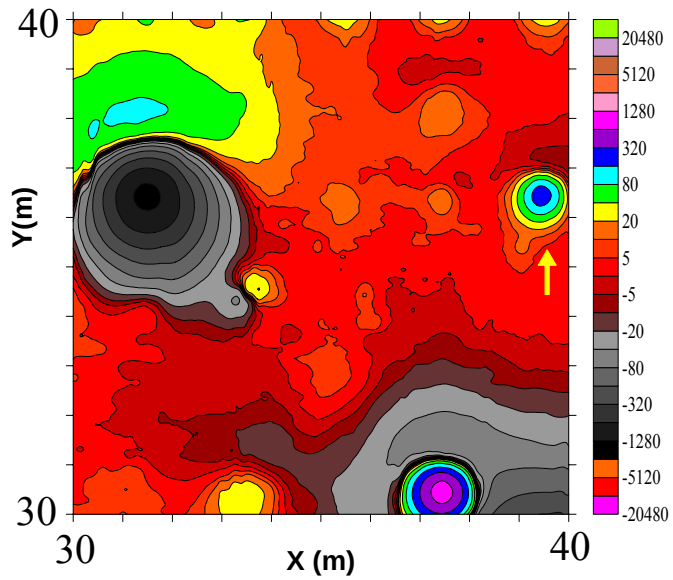

Figure J2. Regional setting of the B01 anomaly (yellow arrow). The anomaly is truncated by the eastern edge of the 40-m x 40-m data set that was used. The magnetic field contours are at zero and $\pm 2^n \cdot 10$ nT, where n is a non-negative integer.

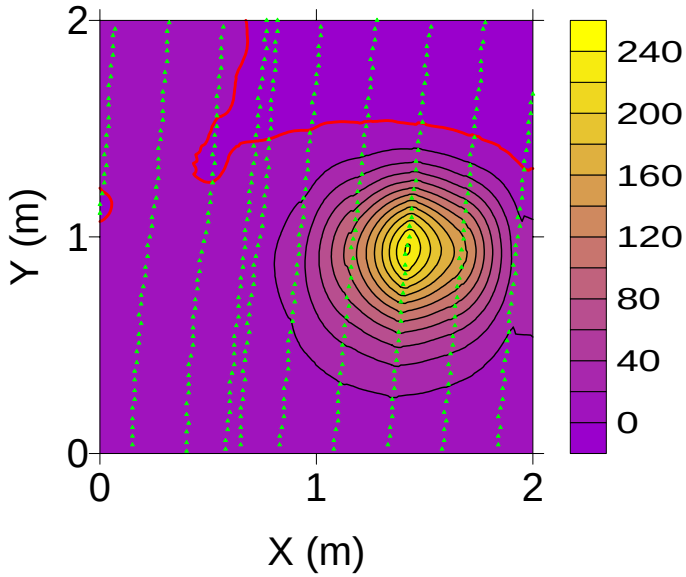

Figure J3. The B01 anomaly in the 2-m data window used in jobs 14-17. The data window is located along an artificial survey edge. The flagged nodes (421 green triangles) were used in flag-node inversions. The data in this window are from two swaths of the MTADS cart. The zero contour is red (contour interval = 20 nT).

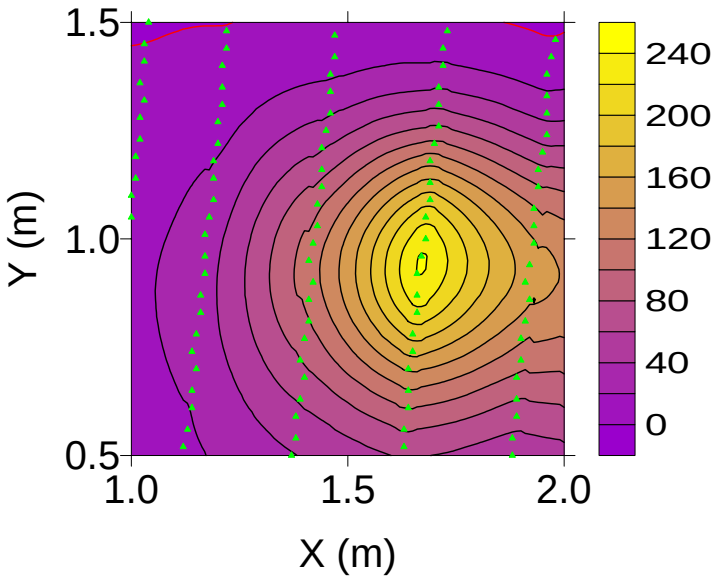

Figure J4. The B01 anomaly in the 1-m data window used in jobs 1-4. The data window is located along an artificial survey edge. The 103 flagged nodes (green triangles) were used in flag-node inversions. For IIBE job 2, Δ_C is 4 cm, $(Z\text{-}Z_C)$ is 4 cm, θ is 21.3 deg, and Ψ is 86.9 deg. For IIGE job 4, Δ_C is 4 cm, $(Z\text{-}Z_C)$ is 4 cm, θ is 25.3 deg, and Ψ is 85.5 deg. Peak-only inversions using values greater than 20 nT (jobs 8-9) yielded θ equal to 21.3 and 20.8 deg for IIBE and IIGE, respectively. The zero contour is red (contour interval = 20 nT).

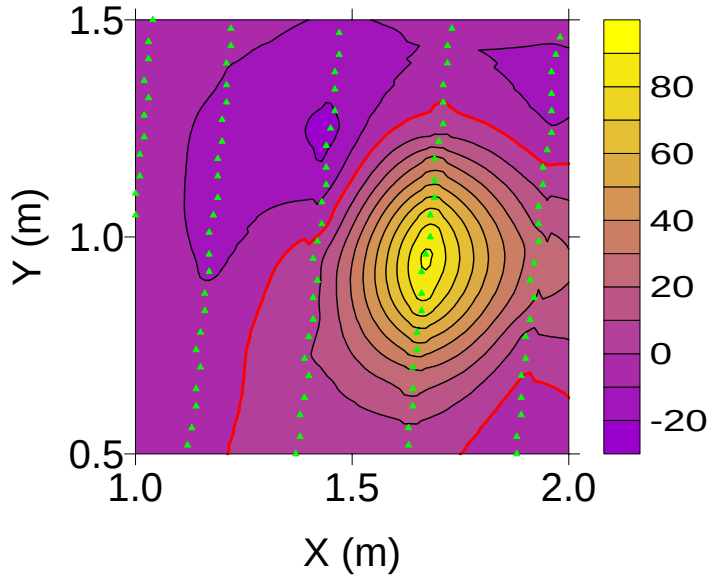

Figure J5. The EAGGN filtered B01 anomaly (L_F = 0.5 m, L_D = 1 m) used in job 5. The filter was applied to the data in a 2-m window (Figure 2). Filtered data at 103 nodes (green triangles) were used in inversion. In this 1-m window, the filter was edge-adaptive only along the right (eastern) artificial survey edge. For job 5, θ is 29.8 deg, versus 26.5 and 26.1 deg for L_F equal to 0.75 and 1 m, respectively. The zero contour is red and the contour interval is 10 nT.

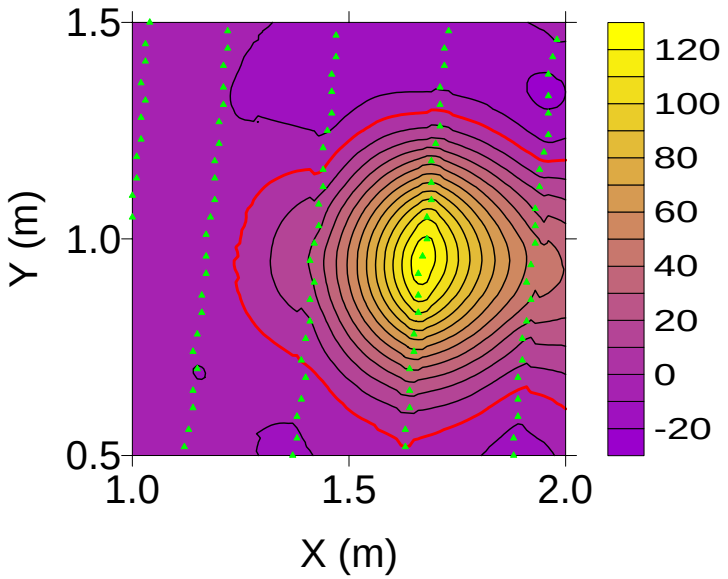

Figure J6. The EAGGN filtered B01 anomaly (L_F = 0.75 m, L_{FD} = 2 m, L_D = 1 m) used in job 6. The filter was edge-adaptive only along the right (eastern) artificial survey edge. Filtered data at 103 flagged nodes (green triangles) were used in inversion. For job 6, Δ_C is 4 cm, (Z-Z_C) is 4 cm, θ is 26.5 deg, and Ψ is 81.6 deg. The zero contour is red (contour interval = 10 nT).

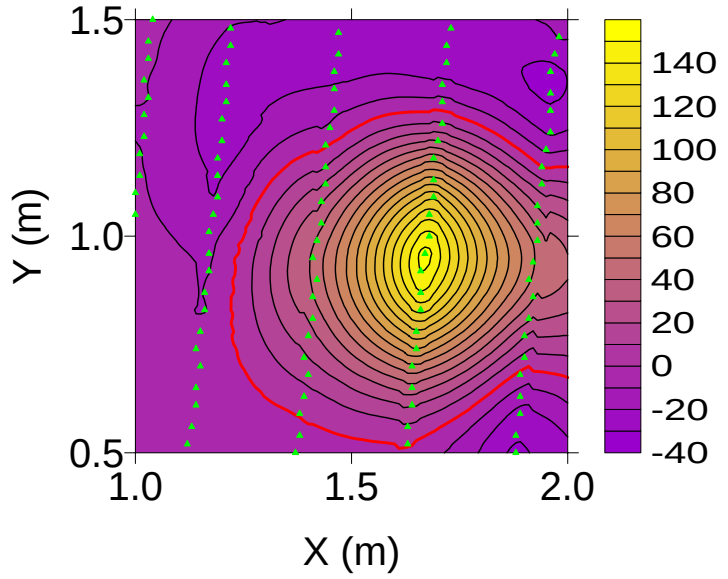

Figure J7. The EAGGN filtered B01 anomaly (L_F = 1 m, L_{FD} = 2 m, L_D = 1 m) used in job 7. The filter was applied to data in the 2-m window (Figure 2). Within the 1-m inversion window, the filter was edge-adaptive only along the right (eastern) artificial survey edge. The filtered data at 103 flagged nodes (green triangles) were used inversion. For job 7, θ is 26.1 deg. The zero contour is red (Contour interval = 10 nT).

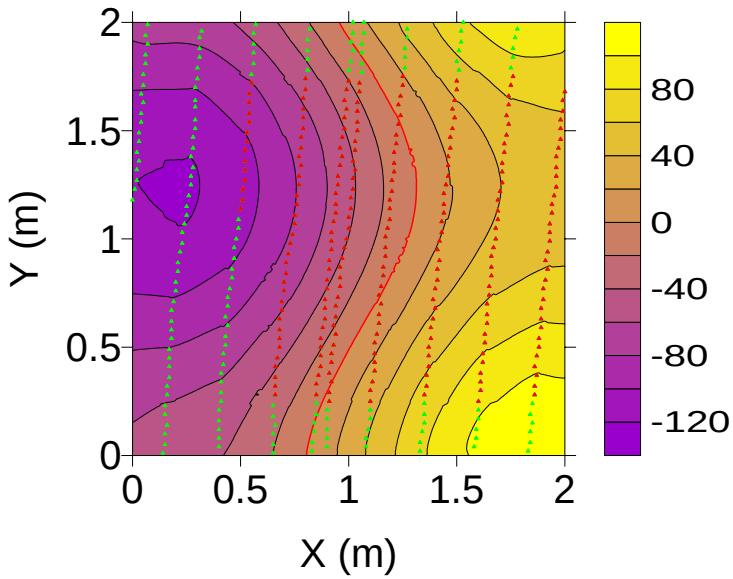

Figure J8. The synthetic background field that is added to the B01 anomaly to create hybrid data for jobs 20-39. The 451 flagged nodes (red and green triangles) were used in filtering. Filtered or unfiltered data at 253 nodes (red triangles) were input to inversion (L_D = 1.5 m). The zero contour is red (contour interval = 20 nT).

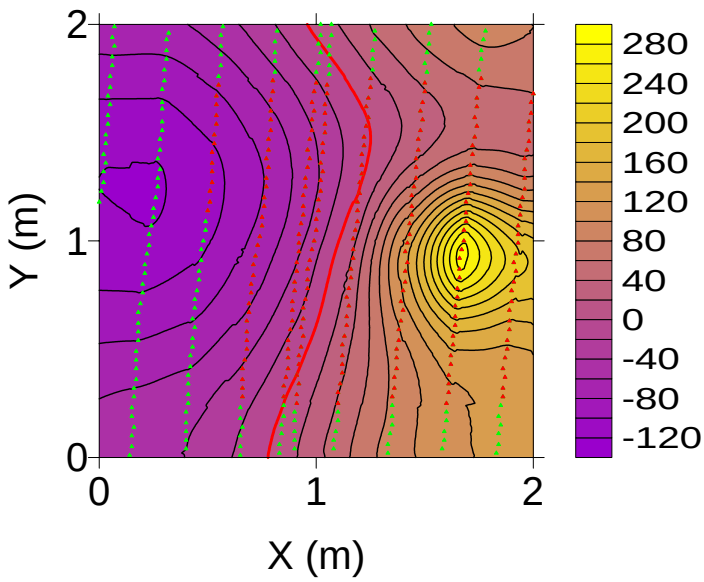

Figure J9. Hybrid data equal to the B01 anomaly plus synthetic background field (jobs 20-39). For IIBE job 21 using 253 nodes (red triangles, L_D = 1.5 m), ΔC is 33 cm, (Z-ZC) is 49 cm, θ is 63.5 deg, and Ψ is 31.5 deg. For peak-only (values > 20 nT), IIBE job 24, the results are better; Δ_C is 7 cm, ($Z-Z_C$) is 2 cm, θ is 27.1 deg, and Ψ is 62.5 deg. By contrast, for peak-only inversion of the B01 anomaly without synthetic background (job 8), Δ_C is 5 cm, ($Z-Z_C$) is 3 cm, θ is 21.3 deg, and Ψ is 84.2 deg. IIGE improves the hybrid data inversion, as does IIF. The 451 nodes (red and green triangles) were used in filtering (L_{FD} = 2 m). Filtered or unfiltered data at 253 nodes (red triangles) were input to inversion (L_D = 1.5 m). The zero contour is red (contour interval = 20 nT).

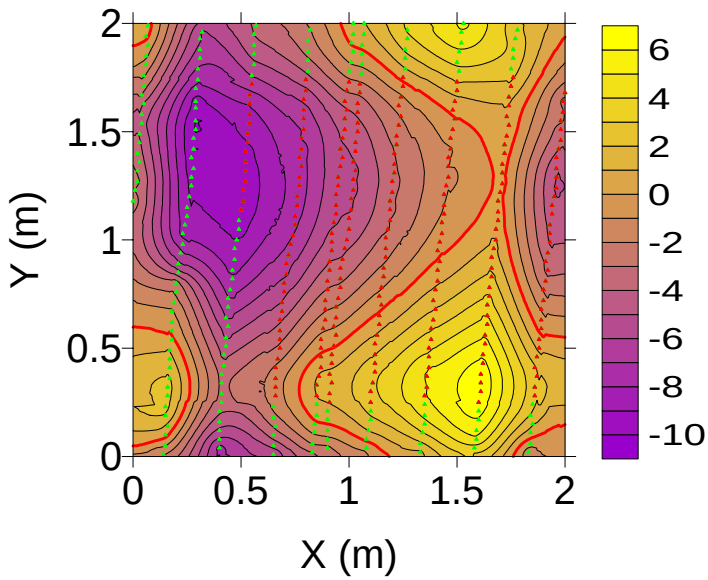

Figure J10. The EAGGN filtered synthetic background field (L_F = 0.75 m). The unfiltered background at 451 nodes (green and red triangles) was summed with the real data of the B01 anomaly then filtered before inversion. Although EAGGN filter coefficients vary with output location, each filtered value is a linear combination of the input data. Thus, the filtered hybrid data equal the sum of the filtered synthetic background field (shown here) and the filtered real data. Filtered data at 253 nodes (red triangles) were input to inversion job 35 (L_D = 1.5 m). The zero contour is red (contour interval = 1 nT).

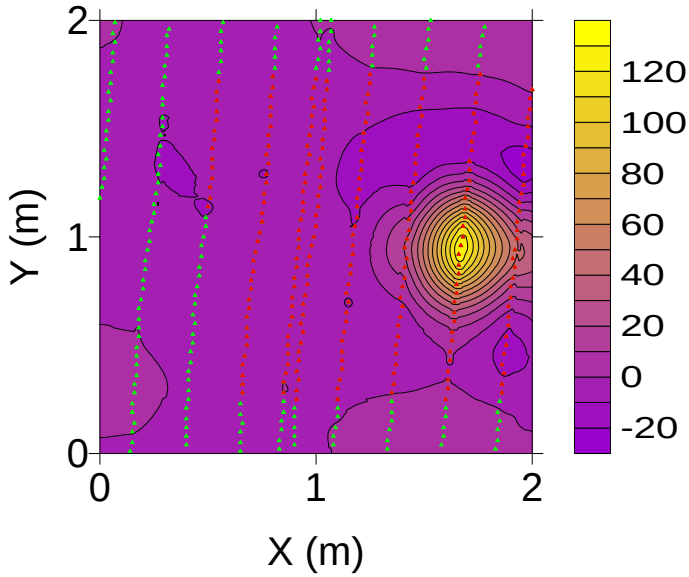

Figure J11. The EAGGN filtered hybrid data (L_F = 0.75 m) used in job 35. The 451 nodes (green and red triangles) were used in filtering and the output data at 253 nodes (red triangles) were input to inversion (L_D = 1.5 m). For this job, Δ_C is 5 cm, (Z-Z_C) is 3 cm, θ is 16.0 deg, and Ψ is 83.2 deg. The zero contour is red and the contour interval is 1 nT.

Table J2. B01 dipole (X,Y,Z) and target's center (X_C,Y_C,Z_C) UTM coordinates. X_R = 402000 m; Y_R = 4369000 m. Δ_C and E_Z are absolute horizontal and relative vertical displacements of dipole from target's center. [Δx = grid interval; L_D = data window size; L_F = filter size.] ‡

Job	Δx cm	L_D m	L_F m	†	$X-X_R$ m	$Y-Y_R$ m	$X-X_C$ cm	$Y-Y_C$ cm	Δ_C cm	Z cm	$Z-Z_C$ cm	E_Z* %
1	1	1	n/a	AB	818.53	584.04	-4	2	5	28	5	10
2	1	1	n/a	B	818.54	584.04	-3	2	4	27	4	8
3	1	1	n/a	A	818.53	584.04	-4	2	5	29	6	12
4	1	1	n/a		818.53	584.03	-4	1	4	27	4	8
5	1	1	0.5	^{2}E	818.55	584.02	-3	0	3	27	4	8
6	1	1	0.75	^{2}E	818.53	584.03	-4	1	4	27	4	8
7	1	1	1	^{2}E	818.53	584.03	-4	1	4	28	5	10
8	1	1	n/a	B▲$_2$	818.53	584.04	-4	2	5	26	3	6
9	1	1	n/a	▲$_2$	818.53	584.04	-4	2	5	27	4	8
10	5	2	n/a	AB	818.54	584.04	-3	2	4	29	6	12
11	5	2	n/a	B	818.54	584.04	-3	2	4	27	4	8
12	5	2	n/a	A	818.54	584.04	-3	2	4	29	6	12
13	5	2	n/a		818.54	584.04	-3	2	4	28	5	10
14	1	2	n/a	AB	818.54	584.03	-3	1	3	29	6	12
15	1	2	n/a	B	818.55	584.03	-2	1	2	27	4	8
16	1	2	n/a	A	818.54	584.03	-3	1	3	29	6	12
17	1	2	n/a		818.54	584.03	-3	1	3	28	5	10
18	1	1.5	n/a	B	818.54	584.04	-3	2	4	27	4	8
19	1	1.5	n/a		818.54	584.04	-3	2	4	28	5	10
20^H	1	1.5	n/a	AB	818.31	583.84	-27	-19	33	73	50	104
21^H	1	1.5	n/a	B	818.31	583.84	-27	-19	33	72	49	102
22^H	1	1.5	n/a	A	818.52	584.06	-6	4	7	22	-1	-2
23^H	1	1.5	n/a		818.53	584.08	-4	6	7	21	-2	-4
24^H	1	0.75	n/a	B	818.53	584.02	-5	0	5	27	4	8
25^H	1	0.75	n/a		818.42	583.92	-15	-10	18	27	4	-4
26^H	1	1	0.5	^{2}E	818.55	584.02	-3	0	3	28	5	10
27^H	1	1	0.75	^{2}E	818.53	584.03	-4	1	4	28	5	10
28^H	1	1	1	^{2}E	818.52	584.03	-5	1	5	29	6	12
29^H	1	1.5	0.75	^{2}E$_2$	818.59	584.04	2	2	3	29	6	12
30^H	1	1.5	0.75	^{2}E$_3$	818.58	584.04	1	2	2	29	6	12
31^H	1	1.5	0.75	^{2}E$_4$	818.57	584.05	0	3	3	28	5	10
32^H	1	1.5	0.75	^{2}E$_5$	818.56	584.05	-1	3	3	28	5	10
33^H	1	1.5	0.75	^{2}E$_6$	818.55	584.04	-2	2	3	27	4	8

‡ table continued next page (jobs 34-39)

^{H} hybrid data: synthetic background field (Figure J8) added to B01 anomaly.

† flag-node and IIGE unless noted: **A** = all-node; **B** = IIBE. ▲$_2$ = peak-only (H > 20).
^{2}**E$_n$** = EAGGN (L_{FD} = 2 m; L_D = 1.5 m; if postfix subscripted: L_{FY} = n •10 cm).

* $E_Z = (Z-Z_C)/(Z_C+H_M)$; magnetometer elevation, H_M = 0.25 m

Table J2 continued. B01 dipole (X,Y,Z) and target's center (X_C,Y_C,Z_C) UTM coordinates. X_R = 402000 m; Y_R = 4369000 m. Δ_C and E_Z are absolute horizontal and relative vertical displacements of dipole from target's center. [Δx = grid interval; L_D = data window size; L_F = filter size.]

Job	Δx cm	L_D m	L_F m	†	$X-X_R$ m	$Y-Y_R$ m	$X-X_C$ cm	$Y-Y_C$ cm	Δ_C cm	Z cm	$Z-Z_C$ cm	E_Z* %
34[H]	1	1.5	0.5	[2]E	818.55	584.04	-2	2	3	27	4	8
35[H]	1	1.5	0.75	[2]E	818.54	584.05	-3	3	5	26	3	6
36[H]	1	1.5	1	[2]E	818.54	584.05	-3	3	5	27	4	8
37[H]	1	1.5	1.25	[2]E	818.54	584.05	-3	3	5	27	4	8
38[H]	1	1.5	1.5	[2]E	818.54	584.06	-4	4	5	26	3	6
39[H]	1	1.5	1.75	[2]E	818.54	584.06	-4	4	5	26	3	6

[H] hybrid data: synthetic background field (Figure J8) added to B01 anomaly.

† [2]**E** = EAGGN (L_{FD} = 2 m; L_D = 1.5 m).

* $E_Z = (Z-Z_C)/(Z_C+H_M)$; magnetometer elevation, H_M = 0.25 m

Table 3. B01 dipole parameters: θ = deviation angle (from earth's field); δ = dipole declination; Ψ =dipole inclination; M = dipole moment. Gx, Gy = gradient components; B = dc bias estimate; R = correlation coefficient. [Δx = grid interval; L_D = data window size; L_F = filter size.] ‡

Job	Δx cm	L_D m	L_F m	†	θ deg	δ deg	Ψ deg	M mA•m^2	Gx nT/m	Gy nT/m	B nT	R
1	1	1	n/a	AB	21.4	31.0	88.1	178	n/a	n/a	9.10	1.000
2	1	1	n/a	B	21.3	-34.7	88.4	174	n/a	n/a	8.88	1.000
3	1	1	n/a	A	21.1	43.6	86.9	190	-5.95	3.11	7.00	1.000
4	1	1	n/a		25.3	108.7	85.5	176	-8.38	-2.99	8.59	1.000
5	1	1	0.5	^{2}E	29.8	125.2	81.1	179	-1.08	-1.35	0.90	0.998
6	1	1	0.75	^{2}E	26.5	96.0	81.6	176	-2.05	-1.79	1.38	0.999
7	1	1	1	^{2}E	26.1	99.2	82.8	187	-4.40	-0.73	1.41	0.999
8	1	1	n/a	B▲$_2$	21.3	47.8	86.9	163	n/a	n/a	12.2	1.000
9	1	1	n/a	▲$_2$	20.8	51.6	84.2	176	-12.9	6.86	8.95	1.000
10	5	2	n/a	AB	22.8	-101.8	88.0	190	n/a	n/a	5.45	0.999
11	5	2	n/a	B	22.7	-97.7	88.0	177	n/a	n/a	6.11	0.999
12	5	2	n/a	A	22.5	-90.5	88.6	191	-1.58	0.68	5.39	0.999
13	5	2	n/a		22.5	-90.3	88.5	186	-1.50	0.62	5.62	0.999
14	1	2	n/a	AB	24.5	-133.0	86.9	190	n/a	n/a	5.35	0.999
15	1	2	n/a	B	24.7	-119.1	85.1	178	n/a	n/a	5.80	0.999
16	1	2	n/a	A	24.4	-139.8	87.4	191	-1.50	0.17	5.29	0.999
17	1	2	n/a		24.4	-141.1	87.5	186	-1.68	0.09	5.49	0.999
18	1	1.5	n/a	B	21.6	-56.3	88.4	176	n/a	n/a	7.31	0.999
19	1	1.5	n/a		21.4	-46.3	88.4	185	-0.90	0.98	6.60	0.999
20^H	1	1.5	n/a	AB	64.5	84.4	30.2	1635	n/a	n/a	-7.13	0.982
21^H	1	1.5	n/a	B	63.5	84.6	31.5	1555	n/a	n/a	-6.79	0.978
22^H	1	1.5	n/a	A	11.2	-40.6	72.6	118	139	-30.2	18.6	0.993
23^H	1	1.5	n/a		13.7	-44.9	64.6	120	139.3	-30.3	13.1	0.991
24^H	1	0.75	n/a	B	25.5	69.5	73.8	188	n/a	n/a	49.5	0.999
25^H	1	0.75	n/a		73.5	104.9	28.1	238	-55.8	-116	55.8	1.000
26^H	1	1	0.5	^{2}E	28.5	136.3	83.5	197	-1.52	-2.75	0.53	0.996
27^H	1	1	0.75	^{2}E	25.8	97.0	82.9	191	-2.03	-6.41	-0.41	0.996
28^H	1	1	1	^{2}E	25.5	97.8	83.7	202	-6.77	-8.09	-2.35	0.995
29^H	1	1.5	0.75	^{2}E$_2$	25.1	-90.1	73.5	230	3.53	-1.11	0.25	0.991
30^H	1	1.5	0.75	^{2}E$_3$	24.3	-93.8	77.4	223	3.81	-1.41	0.09	0.991
31^H	1	1.5	0.75	^{2}E$_4$	20.6	-77.0	79.0	202	4.39	-1.88	-0.19	0.991
32^H	1	1.5	0.75	^{2}E$_5$	19.9	-70.1	82.8	196	4.71	-2.46	-0.49	0.991
33^H	1	1.5	0.75	^{2}E$_6$	19.6	-53.9	85.4	177	5.11	-3.21	-0.89	0.991

‡ table continued next page (jobs 34-39)

^{H} hybrid data: synthetic background field (Figure J8) added to B01 anomaly.

† flag-node and IIGE unless noted: **A** = all-node; **B** = IIBE. ▲$_2$ = peak-only (H > 20).

^{2}**E$_n$** = EAGGN (L_{FD} = 2 m; L_D = 1.5 m; if subscripted: L_{FY} = n •10 cm).

Table 3 continued. B01 dipole parameters: θ = deviation angle; δ = dipole declination; Ψ =dipole inclination; M = dipole moment. Gx, Gy = gradient components; B = dc bias estimate; R = correlation coefficient. [Δx = grid interval; L_D = data window size; L_F = filter size.]

Job	Δx cm	L_D m	L_F m	†	θ deg	δ deg	Ψ deg	M mA•m^2	Gx nT/m	Gy nT/m	B nT	R
34^H	1	1.5	0.5	^{2}E	18.9	-52.0	84.5	182	3.87	-2.17	-0.57	0.991
35^H	1	1.5	0.75	^{2}E	16.0	-9.8	83.2	162	5.72	-4.03	-1.51	0.992
36^H	1	1.5	1	^{2}E	16.7	-50.8	80.9	173	7.84	-6.17	-4.15	0.985
37^H	1	1.5	1.25	^{2}E	16.5	-51.9	80.1	172	8.74	-7.80	-6.29	0.982
38^H	1	1.5	1.5	^{2}E	14.6	-51.3	74.7	164	10.4	-8.02	-9.42	0.978
39^H	1	1.5	1.75	^{2}E	14.2	-50.5	73.9	164	10.9	-7.64	-11.2	0.975

^{H} hybrid data: synthetic background field (Figure J8) added to B01 anomaly.
† ^{2}**E** = EAGGN (L_{FD} = 2 m; L_D = 1.5 m).

Table 4. B01 data windows: grid interval, Δx; absolute and relative window size, L_D, R_L; displacement of window's center from target's center, X_W-X_C, Y_W-Y_C; number of nodes along the x-and y-axes, N_X, N_Y; and the number and proportion of nodes flagged for inversion N_F, R_F.

Jobs	Δx (cm)	L_D (m)	R_L†	X_W-X_C (cm)	Y_W-Y_C (cm)	N_X	$N_X \bullet N_Y$	N_F	R_F (%)
1, 3	1	1	2.1	-23	-1	101	10201	10201	100
2, 4-7	1	1	2.1	-23	-1	101	10201	103	1.0
8-9	1	1	2.1	-23	-1	101	10201	74▲$_2$	0.7
10, 12	5	2	4.2	-45	-3	41	1681	1681	100
11, 13	5	2	4.2	-45	-3	41	1681	388	23.1
14, 16	1	2	4.2	-47	-5	201	40401	40401	1.0
15, 17	1	2	4.2	-47	-5	201	40401	421	1.0
18-19	1	1.5	3.1	-35	-3	151	22801	253	1.1
20, 22	1	1.5	3.1	-35	-3	151	22801	40401	100
21, 23	1	1.5	3.1	-35	-3	151	22801	253	1.1
24-25	1	0.75	1.6	-10	0	76	5776	51	0.9
26-28	1	1	2.1	-23	-1	101	10201	103	1.0
29-39	1	1.5	3.1	-35	-3	151	22801	253	1.1

† R_L= $L_D/(Z_C+H_M)$; depth to target center, Z_C = 23 cm; magnetometer height, H_M = 25 cm.
▲$_2$ = peak-only (H > 20).

Appendix K
Target H12 (60 mm mortar round)

Figures K1-K11 plot the H12 anomaly and results of inversion jobs. Target H12 is a 60-mm, 1.3-kg M49 mortar round, which the AEC emplaced vertically (nose-down) at a depth to center of 22 cm (Figure K1, Table K1). Conclusions are derived from 34 jobs (Tables K2-K4)

Appendix K Figures

K1. Target H12: 60 mm M49 mortar round …… 188
K2. Regional setting of H12 anomaly …… 189
K3. H12 anomaly in 2-m data window with flagged nodes …… 189
K4. H12 anomaly (L_D = 1.5 m) and 328 flagged nodes …… 190
K5. H12 anomaly and flagged nodes for peak-only inversions …… 190
K6. EAGGN filtered H12 anomaly (L_F = 0.75 m, L_D = 2 m) …… 191
K7. EAGGN filtered H12 anomaly (L_F = 1 m, L_D = 2 m) …… 191
K8. EAGGN filtered H12 anomaly (L_F = 1.5 m, L_D = 2 m) …… 192
K9. EAGGN filtered H12 anomaly (L_F = 2 m, L_D = 2 m) …… 192
K10. Single-swath EAGGN filtered H12 anomaly (L_F = 0.5 m, L_D = 1.5 m) …… 193
K11. Single-swath EAGGN filtered H12 anomaly (L_F = 1.25 m, L_D = 1.5 m) …… 193

Appendix K Tables

K1. Ground truth for target H12 …… 188
K2. Dipole positions for anomaly H12 inversions …… 194
K3. Dipole parameters for anomaly H12 inversions …… 195
K4. H12 data window parameters …… 196

Figure K1. Target H12; 60 mm M49 mortar round.

Table K1. Ground truth for Target H12.

Description	M49 Mortar Round
Material	Cast Polymethacrylimide and Forged Steel
Length, L_T	240 mm
Diameter, D_T	60 mm
Weight	1.315 kg
Grid azimuth, Φ_T	38 deg
Inclination, Ψ_T	90 deg
Depth, Z_C	22 cm
UTM northing, Yc	4369568.232
UTM easting, X_C	402799.077
Ratio of depth below magnetometer to target length, R_{DL} †	2.0
Vertical projection of target's length, L_V (= $L_T \sin \Psi_T$)	24 cm
Horizontal projection of target's length, L_H (= $L_T \cos \Psi_T$)	0 cm
Nose-from-center offsets (Xn-Xc, Yn-Yc, Zn-Zc)	(0, 0, 12) cm

† $R_{DL} = (Z_C+H_M)/L_T$; magnetometer height, $H_M = 0.25$ m

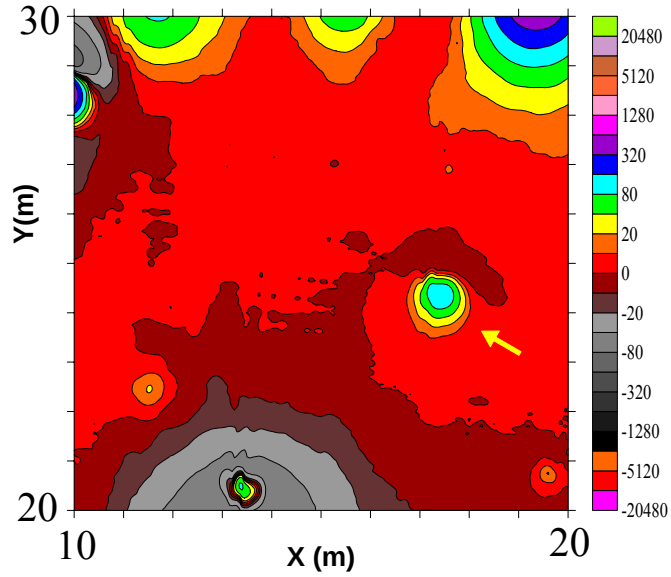

Figure K2. Regional setting of the H12 anomaly (yellow arrow). The magnetic field contours are at zero and $\pm 2^n \cdot 10$ nT, where n is a non-negative integer.

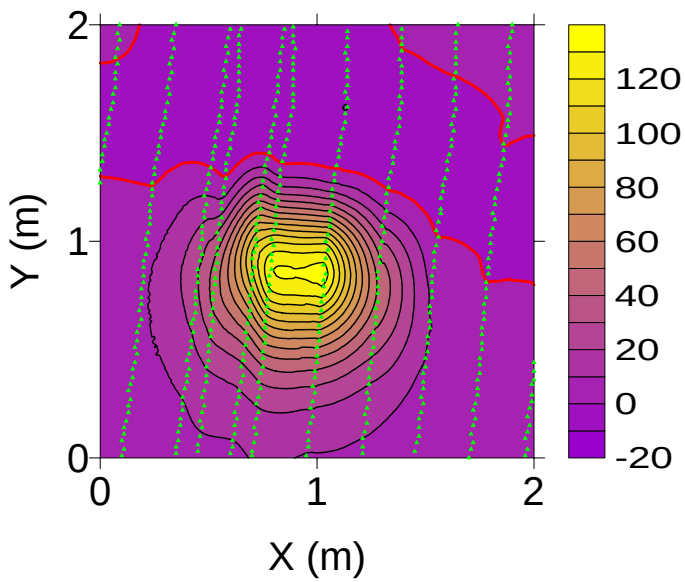

Figure K3. The H12 anomaly in the 2-m data window used in jobs 16-26. Flag-node inversions used 556 nodes (green triangles) nearest to the magnetometer stations. For IIBE inversion without IIF (job 16), Δ_C is 4 cm, $(Z-Z_C)$ is 6 cm (= 0.25 L_V), θ is 10.8 deg, and Ψ is 74.7 deg. For IIGE inversion without IIF (job 18), Δ_C is 2 cm, $(Z-Z_C)$ is 7 cm (= 0.29 L_V), θ is 7.2 deg, and Ψ is 69.4 deg. The zero contour is red and the contour interval is 10 nT.

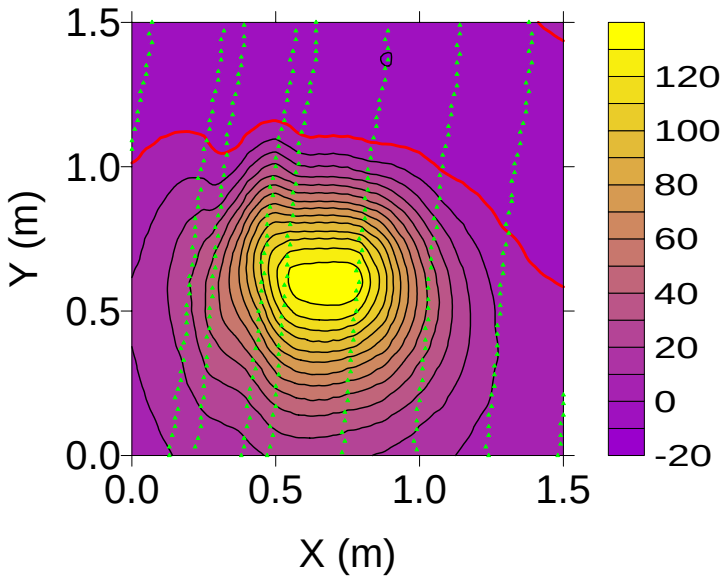

Figure K4. The H12 anomaly (L_D = 1.5 m) and 328 flagged nodes (green triangles). For flag-node non-IIF, IIBE job 2, Δ_C is 4 cm, (Z-Z_C) is 7 cm (= 0.29 L_V), θ is 11.0 deg, and Ψ is 75.0 deg. Similarly, for IIGE job 4, Δ_C is 3 cm, (Z-Z_C) is 7 cm (= 0.29 L_V), θ is 9.1 deg, and Ψ is 71.9 deg. The corresponding all-node inversions yield slightly deeper dipoles: for IIBE, (Z-Z_C) is 9 cm; for IIGE, (Z-Z_C) is 10 cm. The zero contour is red and the contour interval is 10 nT.

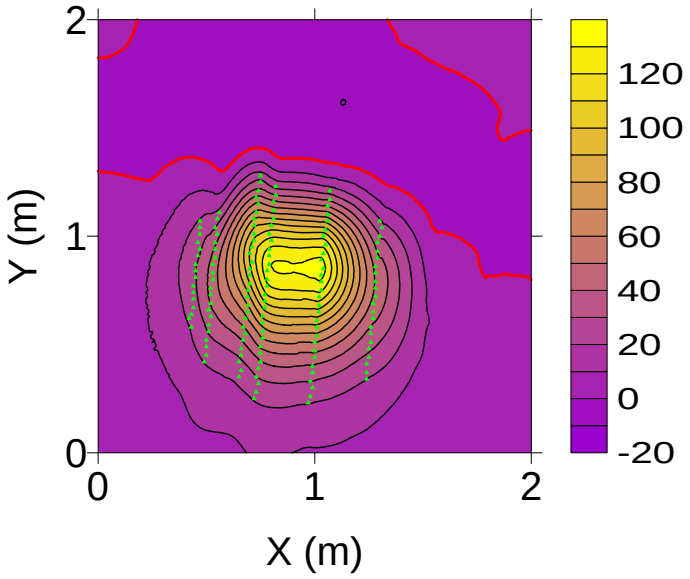

Figure K5. The H12 anomaly (L_D = 2 m) and 146 flagged nodes (green triangles) for values greater than 20 nT used for peak-only inversions. For non-IIF, peak-only, IIBE job 31, Δ_C is 3 cm, (Z-Z_C) is 8 cm, θ is 15.4 deg, and Ψ is 71.5 deg. Similarly, for IIGE job 32, Δ_C is 3 cm, (Z-Z_C) is 8 cm, θ is 22.5 deg, and Ψ is 74.7 deg. The zero contour is red and the contour interval is 10 nT.

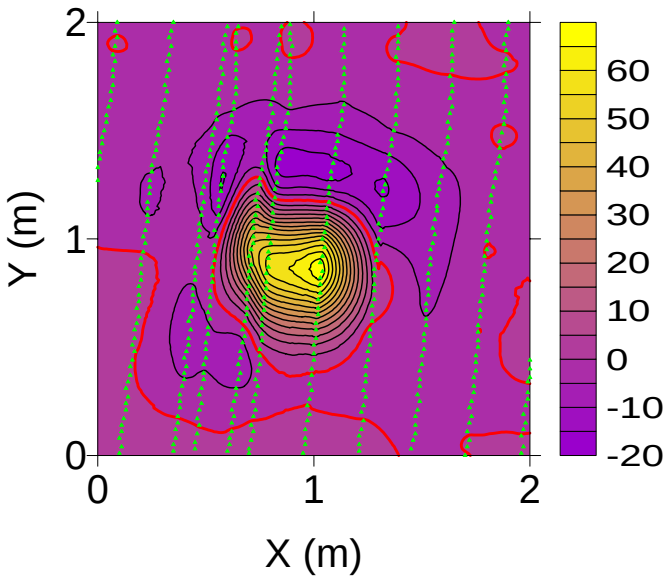

Figure K6. The EAGGN filtered H12 anomaly (L_F = 0.75 m, L_D = 2 m) For inversion of these data (job 25), Δ_C is 3 cm, (Z-Z_C) is 7 cm, θ is 10.6 deg, and Ψ is 71.9 deg. The zero contour is red and the contour interval is 5 nT.

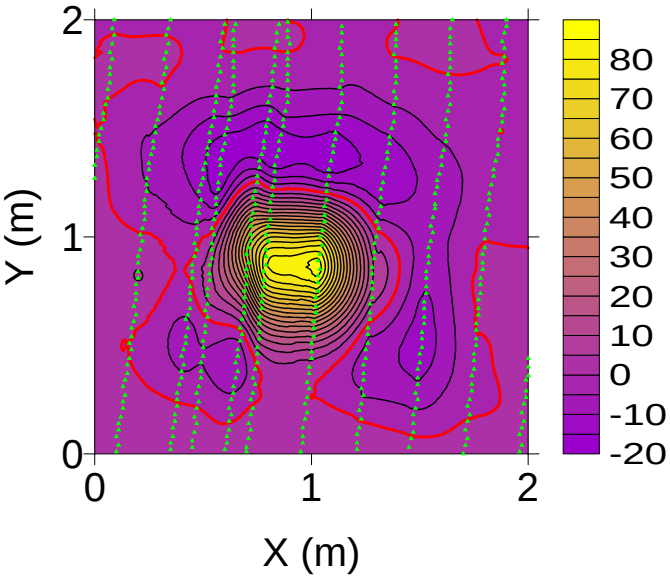

Figure K7. The EAGGN filtered H12 anomaly (L_F = 1 m, L_D = 2 m) For inversion of these data (job 26), Δ_C is 3 cm, (Z-Z_C) is 8 cm, θ is 9.6 deg, and Ψ is 72.4 deg. The zero contour is red and the contour interval is 5 nT.

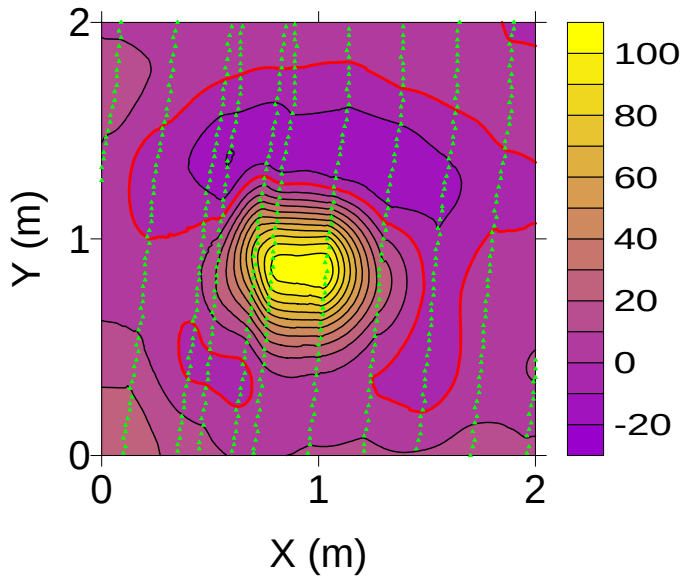

Figure K8. The EAGGN filtered H12 anomaly (L_F = 1.5 m, L_D = 2 m) For inversion of these data (job 28), Δ_C is 3 cm, (Z-Z_C) is 7 cm, θ is 9.4 deg, and Ψ is 72.4 deg. The zero contour is red and the contour interval is 10 nT.

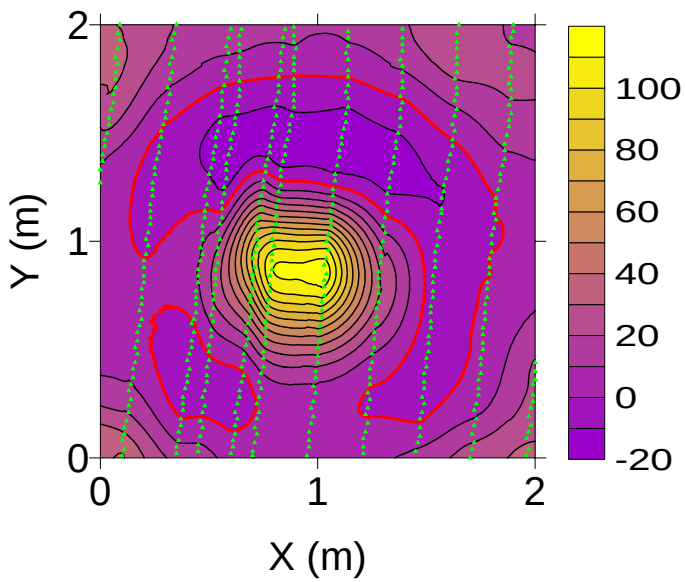

Figure K9. The EAGGN filtered H12 anomaly (L_F = 2 m, L_D = 2 m) For inversion of these data (job 30), Δ_C is 3 cm, (Z-Z_C) is 7 cm, θ is 9.2 deg, and Ψ is 72.3 deg. The zero contour is red and the contour interval is 10 nT.

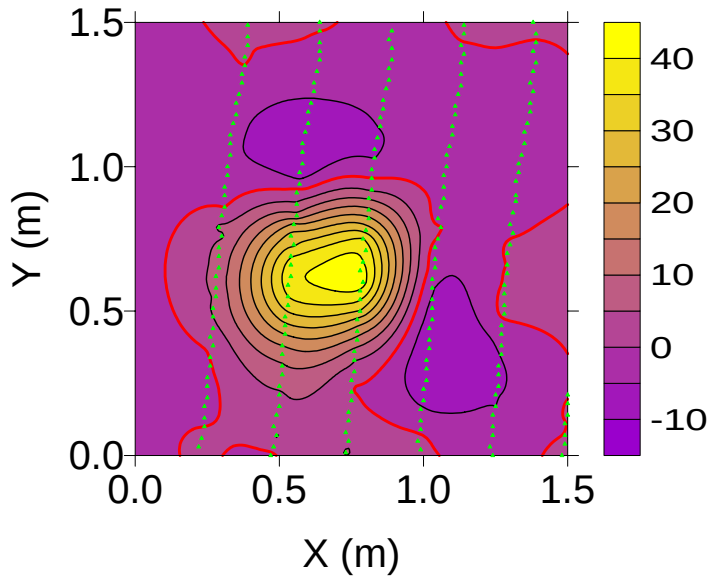

Figure K10. The EAGGN filtered H12 anomaly (L_F = 0.5 m, L_D = 1.5 m) and flagged nodes (green triangles) used in single-swath inversion. For inversion of these data (job 12), Δ_C is 4 cm, (Z-Z_C) is 7 cm, θ is 6.7 deg, and Ψ is 73.6 deg. The zero contour is red and the contour interval is 10 nT.

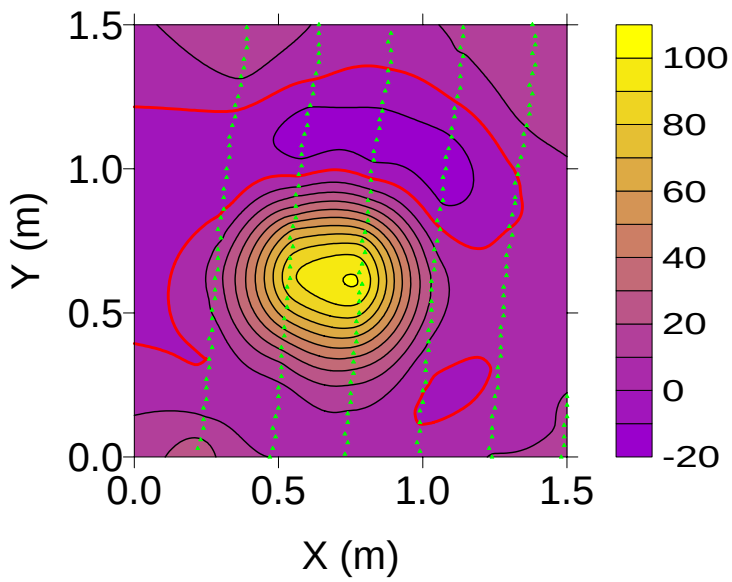

Figure K11. The EAGGN filtered H12 anomaly (L_F = 1.25 m, L_D = 1.5 m) and flagged nodes (green triangles) used in single-swath inversion. For inversion of these data (job 15), Δ_C is 4 cm, (Z-Z_C) is 7 cm, θ is 6.5 deg, and Ψ is 73.4 deg. The zero contour is red and the contour interval is 10 nT.

Table K2. H12 dipole (X,Y,Z) and target's center (X_C,Y_C,Z_C) UTM coordinates. X_R = 402000 m; Y_R = 4369000 m. Δ_C and E_Z are absolute horizontal and relative vertical displacements of the dipole from the target's center. [Δx = grid interval; L_D = data window size; L_F = filter size.]

Job	Δx cm	L_D m	L_F m	†	$X-X_R$ m	$Y-Y_R$ m	$X-X_C$ cm	$Y-Y_C$ cm	Δ_C cm	Z cm	$Z-Z_C$ cm	E_Z* %
1	1	1.5	n/a	AB	799.09	568.18	1	-5	5	31	9	19
2	1	1.5	n/a	B	799.08	568.19	1	-4	4	29	7	15
3	1	1.5	n/a	A	799.08	568.19	1	-4	4	32	10	21
4	1	1.5	n/a		799.08	568.20	1	-3	3	29	7	15
5	1	1.5	0.5	E	799.09	568.20	2	-3	3	31	9	19
6	1	1.5	0.75	E	799.09	568.19	2	-4	4	30	8	17
7	1	1.5	1	E	799.08	568.20	1	-3	3	30	8	17
8	1	1.5	1.25	E	799.08	568.20	1	-3	3	29	7	15
9	1	1.5	1.5	E	799.08	568.20	1	-3	3	29	7	15
10	1	1.5	n/a	B§	799.08	568.18	0	-5	5	29	7	15
11	1	1.5	n/a	§	799.07	568.19	0	-4	4	29	7	15
12	1	1.5	0.5	E§	799.07	568.19	0	-4	4	29	7	15
13	1	1.5	0.75	E§	799.07	568.20	0	-3	3	29	7	15
14	1	1.5	1	E§	799.07	568.19	0	-4	4	29	7	15
15	1	1.5	1.25	E§	799.07	568.19	0	-4	4	29	7	15
16	5	2	n/a	A B	799.11	568.19	3	-5	6	30	8	17
17	5	2	n/a	B	799.11	568.19	3	-5	6	28	6	13
18	5	2	n/a	A	799.11	568.19	3	-5	6	30	8	17
19	5	2	n/a		799.11	568.19	3	-5	6	29	7	15
20	5	2	1	G	799.11	568.19	3	-5	6	29	7	15
21	5	2	1.5	G	799.11	568.19	3	-5	6	29	7	15
22	1	2	n/a	B	799.08	568.19	1	-4	4	28	6	13
23	1	2	n/a		799.08	568.21	1	-2	2	29	7	15
24	1	2	0.5	E	799.09	568.20	2	-3	3	30	8	17
25	1	2	0.75	E	799.08	568.20	1	-3	3	29	7	15
26	1	2	1	E	799.08	568.20	1	-3	3	30	8	17
27	1	2	1.25	E	799.08	568.20	1	-3	3	29	7	15
28	1	2	1.5	E	799.08	568.20	1	-3	3	29	7	15
29	1	2	1.75	E	799.08	568.20	1	-3	3	29	7	15
30	1	2	2	E	799.08	568.20	1	-3	3	29	7	15
31	1	2	n/a	B▲$_2$	799.10	568.19	3	-4	5	30	8	17
32	1	2	n/a	▲$_2$	799.11	568.18	3	-6	6	30	8	17
33	1	2	n/a	B§	799.08	568.18	0	-5	5	28	6	13
34	1	2	n/a	§	799.07	568.20	0	-3	3	28	6	13

† flag-node and IIGE unless noted: **A** = all-node; **B** = IIBE. **E** = EAGGN ($L_{FD} = L_D$).
▲$_2$ = peak-only (H > 20). **§** = single-swath. **G** = GGN ($L_{FD} > L_D$).
* $E_Z = (Z-Z_C)/(Z_C+H_M)$; magnetometer elevation, H_M = 0.25 m

Table K3. H12 dipole parameters: θ = deviation angle; δ = dipole declination; Ψ =dipole inclination; M = dipole moment. Gx, Gy = gradient components; B = dc bias estimate; R = correlation coefficient. [Δx = grid interval; L_D = data window size; L_F = filter size.] ‡

Job	Δx cm	L_D m	L_F m	†	θ deg	δ deg	Ψ deg	M mA•m^2	Gx nT/m	Gy nT/m	B nT	R
1	1	1.5	n/a	AB	11.9	-37.7	76.0	135	n/a	n/a	2.47	0.998
2	1	1.5	n/a	B	11.0	-36.3	75.0	128	n/a	n/a	2.98	0.998
3	1	1.5	n/a	A	9.0	-33.3	72.3	145	0.81	3.61	2.10	0.998
4	1	1.5	n/a		9.1	-34.0	71.9	130	1.10	1.48	3.20	0.998
5	1	1.5	0.5	E	11.0	-40.8	70.9	150	0.44	0.37	-0.14	0.962
6	1	1.5	0.75	E	15.6	-55.3	71.8	138	1.09	-0.11	-0.35	0.986
7	1	1.5	1	E	9.9	-36.8	72.0	137	0.10	0.37	-0.11	0.992
8	1	1.5	1.25	E	10.1	-37.2	72.1	130	0.19	-0.15	-0.06	0.994
9	1	1.5	1.5	E	9.7	-36.0	72.2	130	-0.02	0.03	-0.14	0.995
10	1	1.5	n/a	B§	9.3	-21.5	76.0	128	n/a	n/a	2.60	1.000
11	1	1.5	n/a	§	5.9	-17.8	72.8	129	-1.20	1.96	2.89	1.000
12	1	1.5	0.5	E§	6.7	-17.4	73.6	129	-0.19	0.13	0.04	0.998
13	1	1.5	0.75	E§	3.3	-16.6	69.9	130	-0.32	0.34	0.07	0.999
14	1	1.5	1	E§	6.6	-17.3	73.6	129	-0.03	-0.02	-0.15	0.999
15	1	1.5	1.25	E§	6.5	-17.4	73.4	129	-0.06	0.06	-0.16	1.000
16	5	2	n/a	AB	14.3	-50.6	74.3	129	n/a	n/a	3.59	0.996
17	5	2	n/a	B	15.3	-54.2	74.5	123	n/a	n/a	3.80	0.996
18	5	2	n/a	A	14.3	-51.1	73.1	130	1.03	1.13	3.58	0.997
19	5	2	n/a		15.5	-55.2	73.8	129	1.21	0.42	3.41	0.996
20*	5	2	1	G	20.0	-70.7	73.0	130	0.19	-0.14	-0.02	0.978
21*	5	2	1.5	G	18.5	-66.1	73.9	113	0.29	-0.26	-0.03	0.989
22	1	2	n/a	B	10.8	-36.1	74.7	122	n/a	n/a	3.96	0.997
23	1	2	n/a		7.2	-30.1	69.4	130	0.53	2.10	3.89	0.997
24	1	2	0.5	E	10.5	-39.3	71.2	140	0.11	0.04	-0.06	0.962
25	1	2	0.75	E	10.6	-39.3	71.9	130	0.17	-0.08	-0.17	0.985
26	1	2	1	E	9.6	-35.2	72.4	137	0.23	0.07	-0.26	0.992
27	1	2	1.25	E	9.6	-35.4	72.3	130	0.26	-0.05	-0.25	0.994
28	1	2	1.5	E	9.4	-34.4	72.5	130	0.01	-0.02	-0.21	0.996
29	1	2	1.75	E	9.4	-34.5	72.4	130	0.03	-0.10	-0.26	0.996
30	1	2	2	E	9.2	-34.1	72.3	130	-0.01	-0.06	-0.27	0.996
31	1	2	n/a	B▲$_2$	15.4	-54.6	71.5	137	n/a	n/a	1.68	0.998
32	1	2	n/a	▲$_2$	22.5	-81.8	74.7	135	5.27	-8.63	1.64	0.998
33	1	2	n/a	B§	9.0	-21.9	75.6	121	n/a	n/a	3.70	0.999
34	1	2	n/a	§	3.4	-17.7	69.8	124	-0.88	2.35	4.01	0.999

† flag-node and IIGE unless noted: **A** = all-node; **B** = IIBE. **E** = EAGGN ($L_{FD} = L_D$).
▲$_2$ = peak-only (H > 20). **§** = single-swath. **G** = GGN ($L_{FD} > L_D$).
* GGN filter derived from $F_{CP\text{-}PYRAMID}$

Table 4. H12 data windows: grid interval, Δx; absolute and relative window size, L_D, R_L; displacement of window's center from target's center, X_W-X_C, Y_W-Y_C; number of nodes along the x-and y-axes, N_X, N_Y; and the number and proportion of nodes flagged for inversion N_F, R_F.

Jobs	Δx (cm)	L_D (m)	R_L†	X_W-X_C (cm)	Y_W-Y_C (cm)	N_X	$N_X \bullet N_Y$	N_F	R_F (%)
1, 3	1	1.5	3.2	7	2	151	22801	22801	100
2, 4-9	1	1.5	3.2	7	2	151	22801	328	1.4
10-15	1	1.5	3.2	7	2	151	22801	**224 §**	1.0
16, 18	5	2	4.3	9	4	41	1681	1681	100
17, 19-21	5	2	4.3	9	4	41	1681	420	25.0
22-30	1	2	4.3	7	2	201	40401	556	1.4
31-32	1	2	4.3	7	2	201	40401	146 $▲_2$	0.4
33-34	1	2	4.3	7	2	201	40401	**357 §**	0.9

†$R_L = L_D/(Z_C+H_M)$; depth to target center, Z_C = 22 cm; magnetometer height, H_M = 25 cm.
$▲_2$ = peak-only (H > 20). § = single-swath.

Appendix L
Target H03 (40 mm projectile)

Target H03 is a 40 mm, 1-kg projectile, which the AEC emplaced sub-horizontally at a depth to center of 40 cm (Figure L1, Table L1). Figures L2-L5 plot the H03 anomaly and results of inversion jobs. Conclusions are derived from 35 jobs (Tables L2-L4)

Appendix L - Figures

L1. Target H03: 40-mm projectile ……..……...…… 198
L2. Regional setting of the H03 anomaly ……...….…….. 199
L3. H03 anomaly in 2-m window …….…… 199
L4. Inverse-modeled H03 dipole plus IIGE field …….…… 200
L5. Inverse-modeled H03 dipole plus IIBE field …….…….…… 200
L6. IIBE inverse-modeled H03 dipole field …….…… 201
L7. Difference field: job 26's dipole plus IIGE field, minus job 24's dipole plus IIBE field ... 201
L8. Residual field: observed field minus sum of H03 dipole and IIGE field ……... 202
L9. Residual field: observed field minus sum of H03 dipole and IIBE field ……..... 202
L10. Sum of the H03 inverse-modeled dipole and IIGE fields (trough-only inversion) …..… 203
L11. Sum of the H03 inverse-modeled dipole and IIBE fields (trough-only inversion) …..… 203
L12. The H03 anomaly (L_D = 1 m) and flagged nodes ……. 204
L13. Residual field (observed field minus sum of M08 dipole's field and IIGE field) …….. 204
L14. EAGGN filtered H03 anomaly (L_F = 0.5 m; L_D = 1 m) …… 205
L15. EAGGN filtered H03 anomaly (L_F = 0.5 m; L_D = 1.5 m) ……..... 205
L16. EAGGN filtered H03 anomaly (L_F = 0.75 m; L_D = 1 m) ……..… 206
L17. EAGGN filtered H03 anomaly (L_F = 0.75 m; L_D = 1.5 m) …….….. 206
L18. EAGGN filtered H03 anomaly (L_F = 1 m; L_D = 1 m) ……... 207
L19. EAGGN filtered H03 anomaly (L_F = 1 m; L_D = 1.5 m) …… 207
L20. EAGGN filtered field of inverse modeled H03 dipole plus IIGE field (L_F = 0.75 m) …. 208
L21. Residual field: filtered anomaly minus filtered dipole and IIGE fields (L_F = 0.75 m) …. 208
L22. EAGGN filtered field of inverse modeled H03 dipole plus IIGE field (L_F = 1 m) …..… 209
L23. Residual field: filtered anomaly minus filtered dipole and IIGE fields (L_F = 1 m) …….. 209
L24. The H03 anomaly (L_D = 1.1 m) and flagged nodes in a single-swath window ……. 210
L25. EAGGN filtered H03 anomaly (L_F = 1 m, job 35) …….. 210

Appendix L - Tables

L1. Ground truth for target H03 …….…… 197
L2. Dipole positions for anomaly H03 inversions ……...…….. 211
L3. Dipole parameters for anomaly H03 inversions …….…… 212
L4. H03 data window parameters ……..…… 213

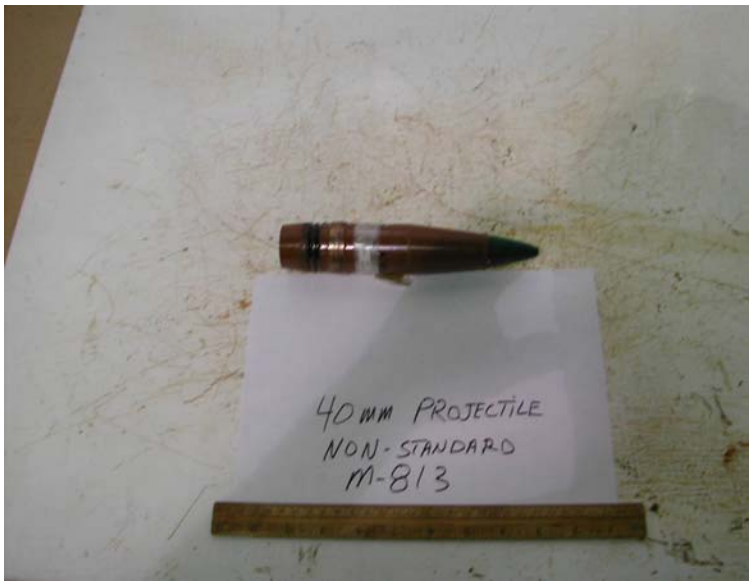

Figure L1. Target H03; 40 mm M813 non-standard projectile.

Table L1. Ground Truth Parameters for Target C09.

Description	M813 Non-standard Projectile
Material	Alloy Steel
Length, L_T	207 mm
Diameter, D_T	40 mm
Weight	0.975 kg
Grid azimuth, Φ_T	304 deg
Inclination, Ψ_T	8 deg
Depth, Z_C	40 cm
UTM northing, Yc	4369571.533 m
UTM easting, X_C	402816.8434 m
Ratio of depth below magnetometer to target length, R_{DL} †	3.1
Vertical projection of target's length, L_V (= $L_T \sin \Psi_T$)	3 cm
Horizontal projection of target's length, L_H (= $L_T \cos \Psi_T$)	20 cm
Nose-from-center offsets (Xn-Xc, Yn-Yc, Zn-Zc)	(-9, 4, 1) cm

† $R_{DL} = (Z_C+H_M)/L_T$; Magnetometer height, $H_M = 0.25$ m

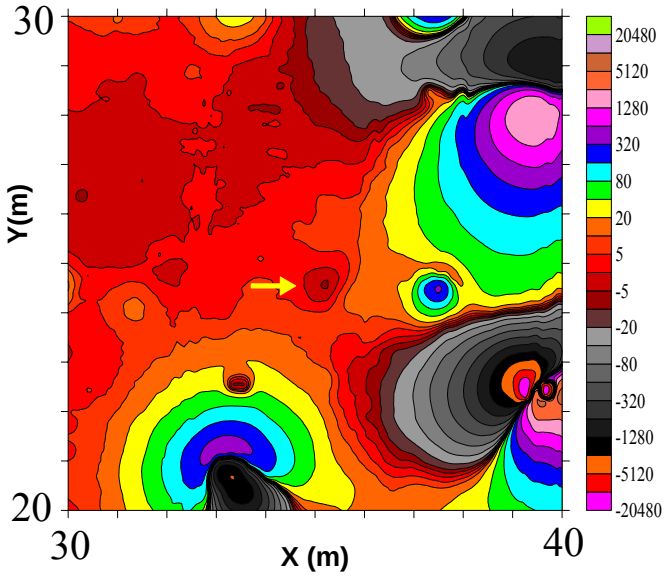

Figure L2. Regional setting of the H03 anomaly (yellow arrow), which is strongly disturbed by several nearby anomalies. The magnetic field contours are at zero and $\pm 2^n \cdot 5$ nT, where n is a non-negative integer.

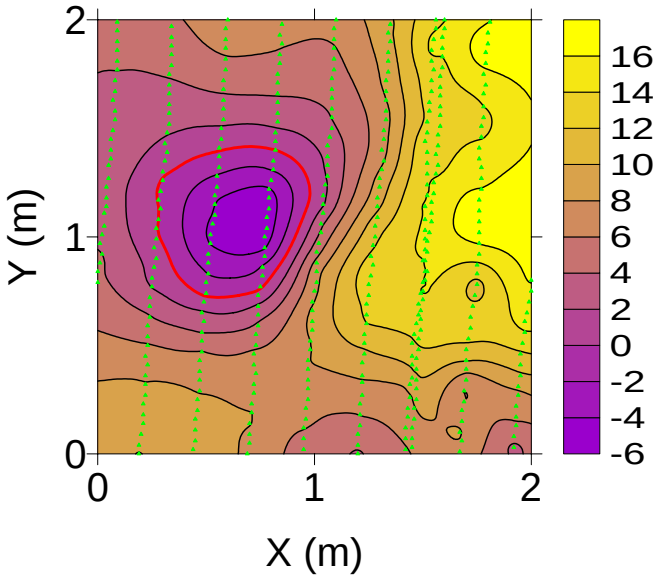

Figure L3. The H03 anomaly in the 2-m data window used in jobs 23-26. The anomaly low, with a minimum of –5.0 nT, is distinct but disturbed by neighboring anomalies. Any significant associated peak may be merged with the neighboring anomalies. Flagged nodes (399 green triangles) were used in flag-node inversions (jobs 24 and 26). The zero contour is red and the contour interval is 2 nT.

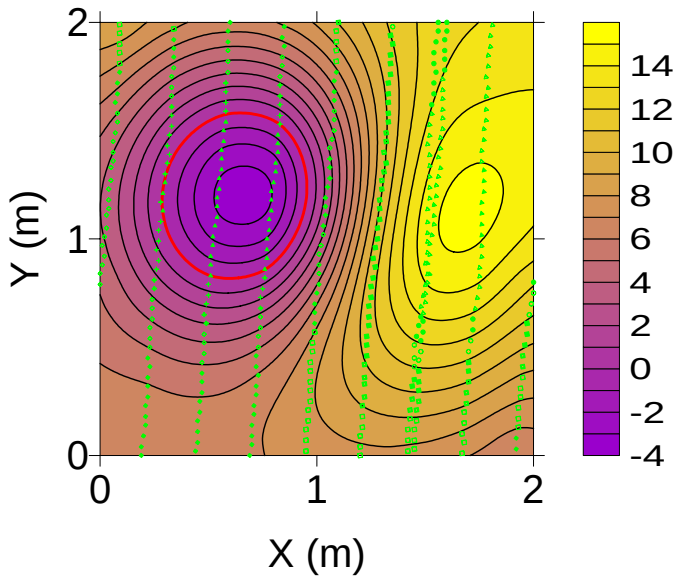

Figure L4. Inverse-modeled H03 dipole plus IIGE field (L_D = 2 m) at 399 flagged nodes (green triangles). For this inversion (job 26), Δ_C is 11 cm, (Z-Z_C) is 44 cm, θ is 86.5 deg, and Ψ is –4.5 deg. For IIGE (L_D = 1.5 m) job 14, (Z-Z_C) is 2 cm and Ψ is –1.4 deg. For IIGE (L_D = 1 m) job 4, (Z-Z_C) is 26 cm and Ψ is 7.0 deg. All of these dipoles are too deep. The zero contour is red and the contour interval is 1 nT.

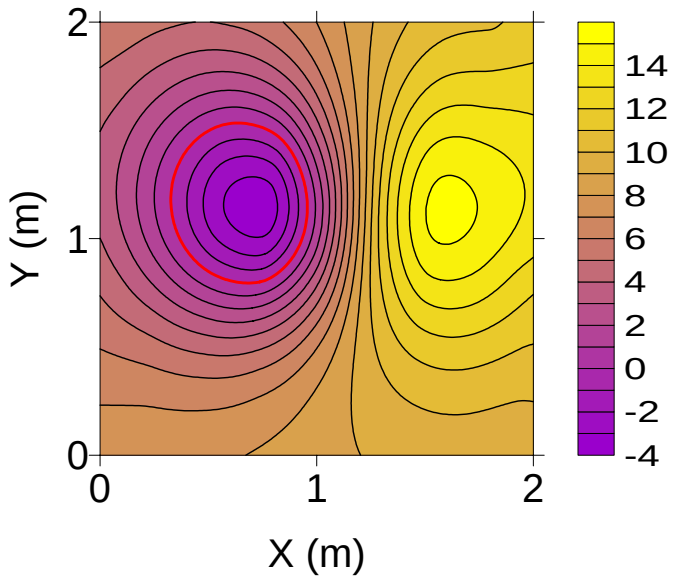

Figure L5. Inverse-modeled H03 dipole plus IIBE field (L_D = 2 m) from job 24. For this inversion, Δ_C is 9 cm, (Z-Z_C) is 24 cm, θ is 94.4 deg, and Ψ is –9.1 deg, and the dc-bias is 8.25 nT. For IIBE job 12 (L_D = 1.5 m), (Z-Z_C) is 12 cm, Ψ is –5.9 deg, and the dc-bias is 7.43 nT. For IIBE job 2 (L_D = 1 m), (Z-Z_C) is 7 cm, Ψ is 2.4 deg, and the dc-bias is 7.43 nT.. IIF and non-IIF, IIBE inversions gave shallower dipoles than those of the IIGE inversions, which were too deep. The non-constant gradient background field is unsuitable for success of non-IIF, IIGE inversions. The zero contour is red and the contour interval is 1 nT.

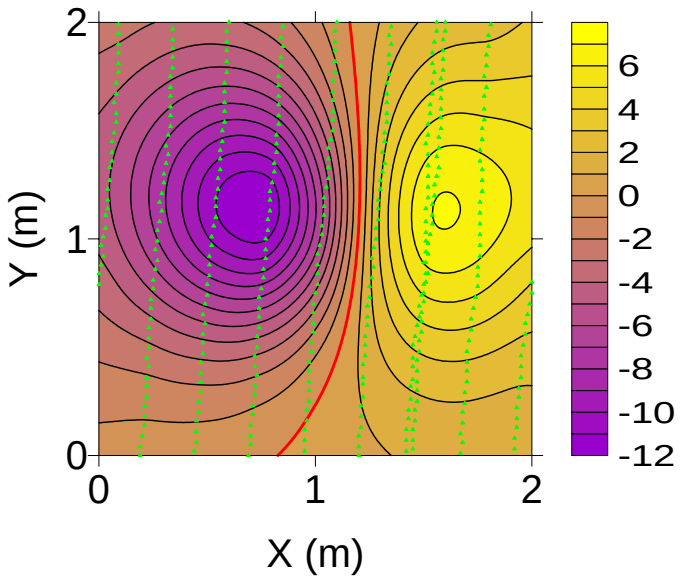

Figure L6. IIBE inverse-modeled H03 dipole's field (job 24). The IIBE field has been removed from the field shown in the previous figure. The contours were generated only from the data at the 399 flagged nodes used in inversion. The zero contour is red and the contour interval is 1 nT.

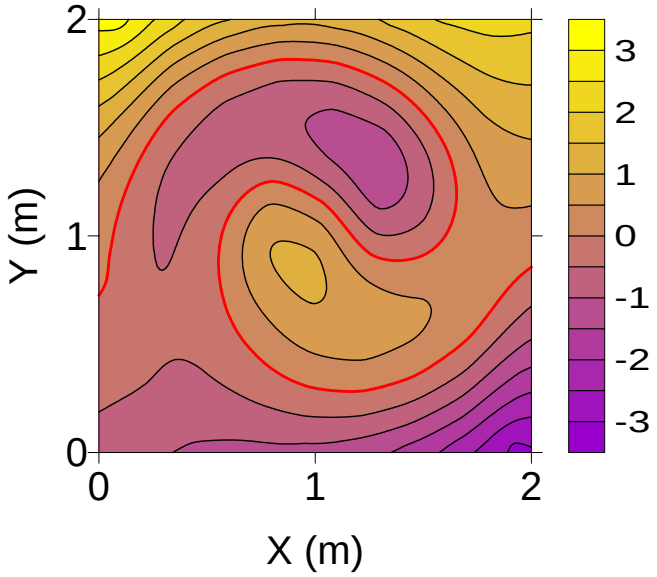

Figure L7. The difference field equal to the sum of the inverse-modeled H03 dipole and IIGE field for job 26 minus the sum of the inverse-modeled H03 dipole and IIBE field for job 24. The "yin-yang" feature in the center of the window reflects the difference in orientation of the job 26 and job 24 dipoles. Closely spaced contours in the southeast and northwest corners reflect the northwest gradient of the job 26 IIGE field. The differences in the results of IIBE and IIGE inversions and apparent deviation of the background field from a constant gradient indicate that IIF inversions may be more successful. Without IIF, one can also try small-window inversions. The zero contour is red and the contour interval is 0.5 nT.

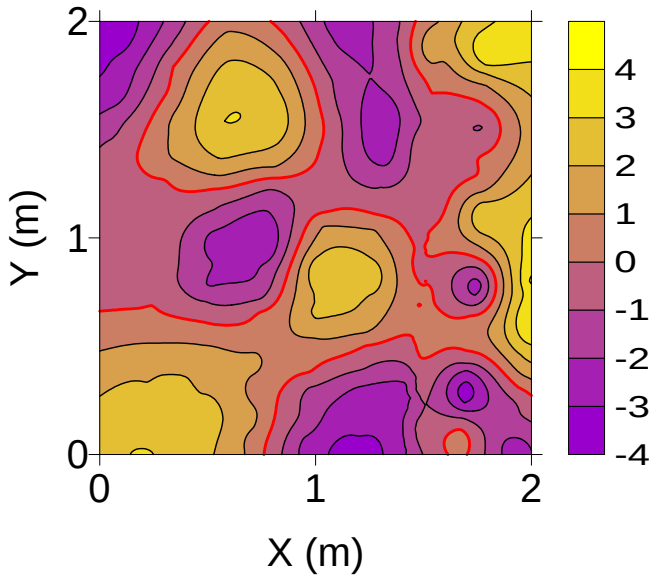

Figure L8. The residual field equal to the observed field minus the sum of the inverse-modeled H03 dipole and IIGE field (job 26). For this inversion, Δ_C is 11 cm, $(Z\text{-}Z_C)$ is 44 cm, θ is 86.5 deg, and Ψ is -4.5 deg. The zero contour is red and the contour interval is 1 nT.

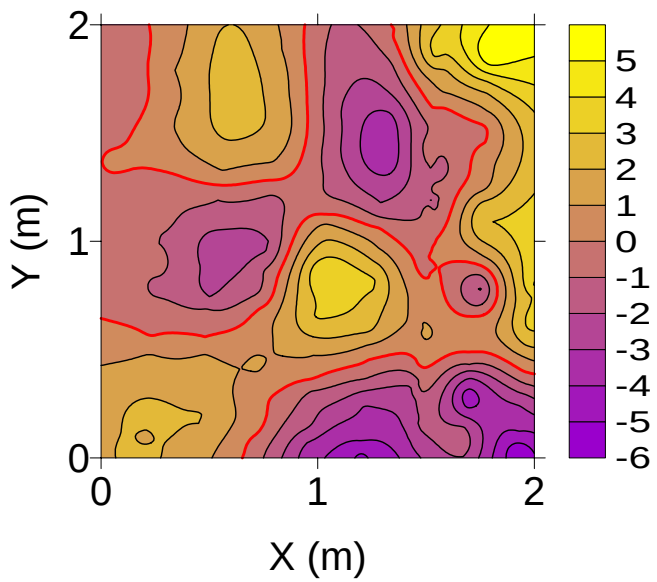

Figure L9. The residual field equal to the observed field minus the sum of the inverse-modeled H03 dipole and IIBE field (job 24). For this inversion, Δ_C is 9 cm, $(Z\text{-}Z_C)$ is 24 cm, θ is 94.4 deg, and Ψ is –9.1 deg. The zero contour is red and the contour interval is 1 nT.

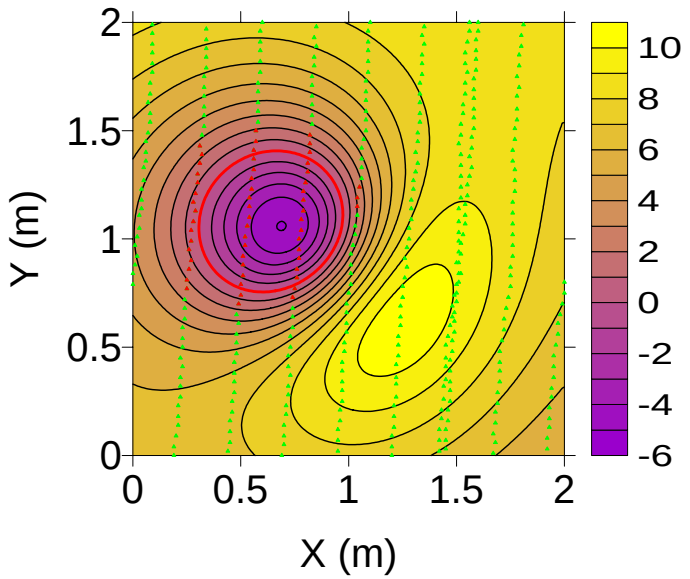

Figure L10. The sum of the H03 inverse modeled dipole and IIGE fields derived from trough-only job 28 using 56 flagged nodes (red triangles) for which the input field was less than 2 nT. The 343 nodes for which the field exceeded 2 nT (green triangles) were not used. For job 28, Δ_C is 12 cm (= 0.59 L_H), (Z-Z_C) is 9 cm, θ is 84.7 deg, and Ψ is -9.5 deg. The zero contour is red and the contour interval is 1 nT.

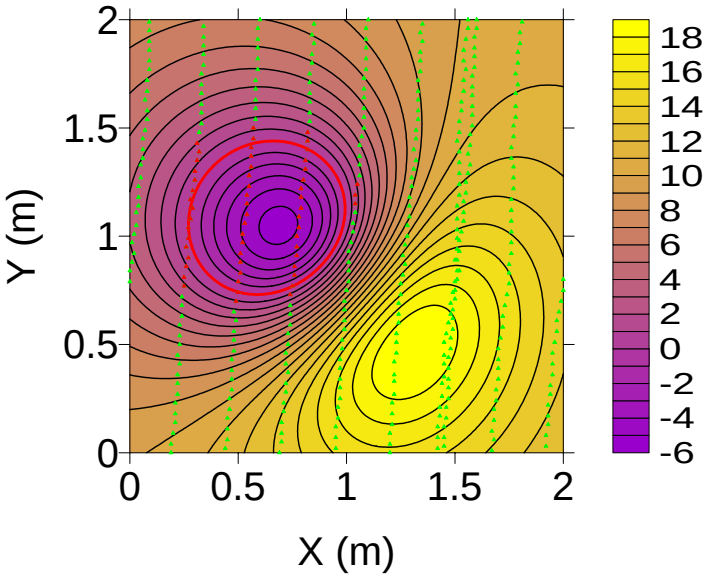

Figure L11. The sum of the H03 inverse model and IIBE field derived from job 27, which used 56 flagged nodes (red triangles) where the input field is less than 2 nT. For job 27, Δ_C is 19 cm (= 0.93 L_H), (Z-Z_C) is 19 cm, θ is 75.9 deg, and Ψ is –0.2 deg. The trough-only IIGE dipole (job 28) is nearer than the IIBE dipole to the target center. The zero contour is red and the contour interval is 1 nT.

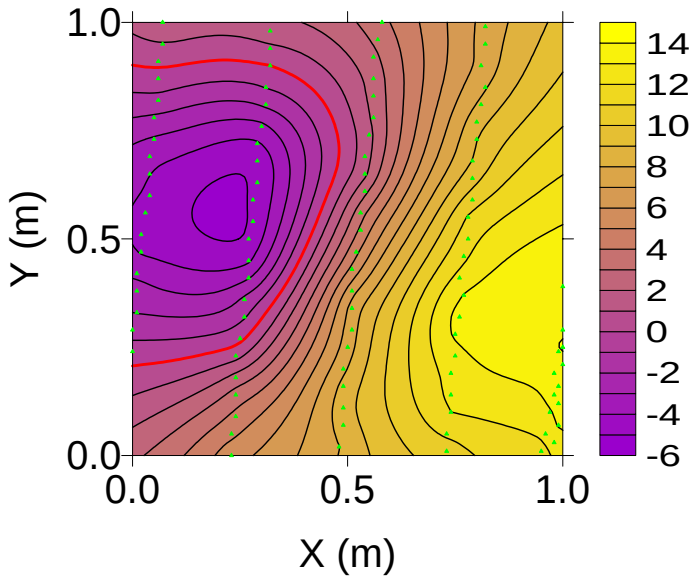

Figure L12. The H03 anomaly (L_D = 1 m). Flag-node inversions (jobs 2, 4-10) use 101 nodes (green triangles). For all-node and flag-node non-IIF, IIBE jobs 1 and 2, (Z-Z_C) are 8 and 7 cm, and θ are 81.6 and 78.5 deg, respectively. For all-node and flag-node non-IIF, IIGE jobs 3 and 4, (Z-Z_C) are 30 and 26 cm, and θ are 74.1 and 73.4 deg, respectively. The differences between all-node and flag-node inversions are significant. The zero contour is red and the contour interval is 1 nT.

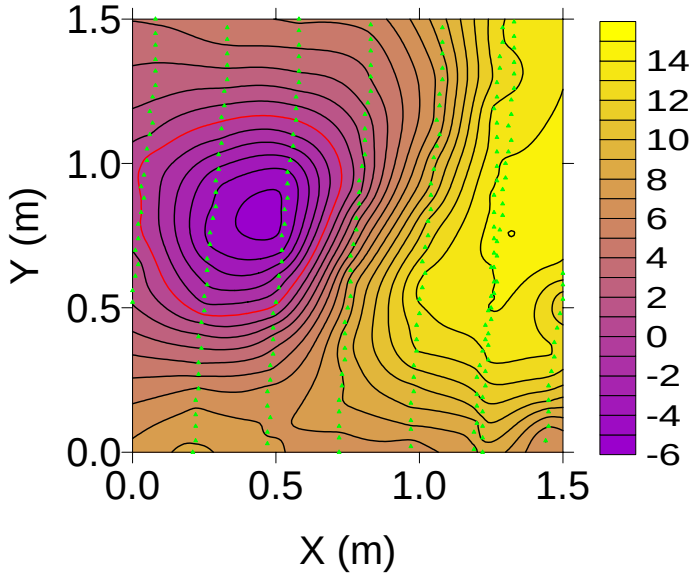

Figure L13. The H03 anomaly (L_D = 1.5 m). Flag-node inversions (jobs 12, 14-22) used 236 nodes (green triangles). For all-node and flag-node non-IIF, IIBE jobs 11 and 12, (Z-Z_C) are 16 and 12 cm, and θ are 88.8 and 88.7 deg, respectively. For all-node and flag-node non-IIF, IIGE jobs 13 and 14, (Z-Z_C) are 40 and 25 cm, and θ are 81.6 and 81.3 deg, respectively. The differences between all-node and flag-node inversions are significant. The zero contour is red and the contour interval is 1 nT.

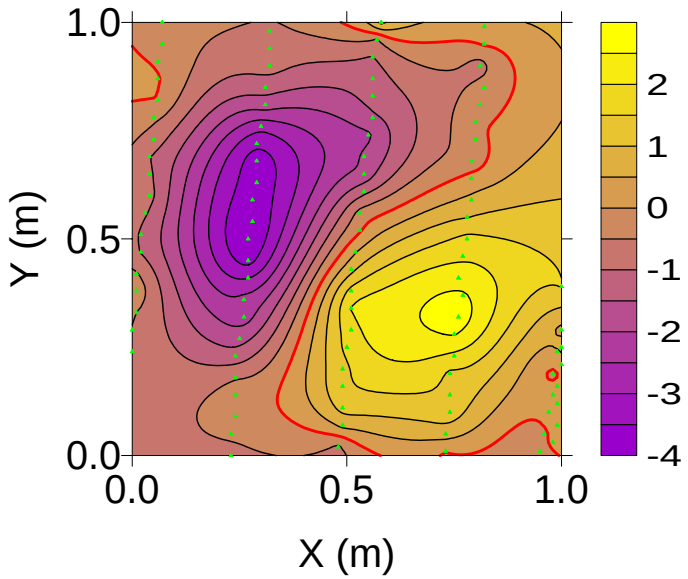

Figure L14. The EAGGN filtered H03 anomaly (L_F = 0.5 m, L_D = 1 m). For IIF with IIGE job 5, using 101 nodes (green triangles), Δ_C is 5 cm, (Z-Z_C) is -10 cm, θ is 70.4 deg, and Ψ is 7.3 deg. The dipole is too shallow; however, for this data window, larger filters (L_F > 0.5 m) improved the results. The zero contour is red and the contour interval is 0.5 nT.

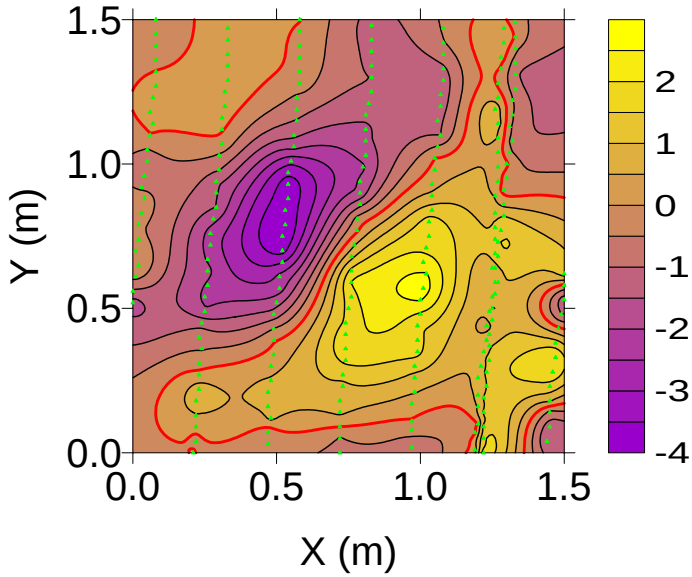

Figure L15. The EAGGN filtered H03 anomaly (L_F = 0.5 m, L_D = 1.5 m). For IIF with IIGE job 15 using 236 nodes (green triangles), Δ_C = 7 cm, Z is equal to Z_C (= 40 cm), θ is 76.4 deg, and Ψ is –1.5 deg. Given the difficult environment of the background field the dipole position is good; however θ is greater than 60 deg and one might therefore interpret that the target has significant remenance. The zero contour is red and the contour interval is 0.5 nT.

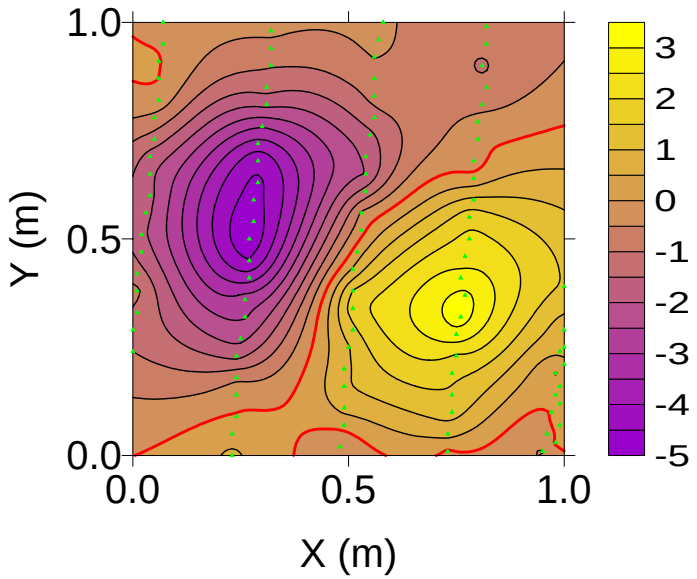

Figure L16. The EAGGN filtered H03 anomaly (L_F = 0.75 m, L_D = 1 m). For IIF with IIGE job 6, using 101 nodes (green triangles), Δ_C is 7 cm, (Z-Z_C) is –5 cm, θ is 74.0 deg, and Ψ is 4.8 deg. The dipole depth is closer to the target's center than for the job 5 (L_F = 0.75 m). The zero contour is red and the contour interval is 0.5 nT.

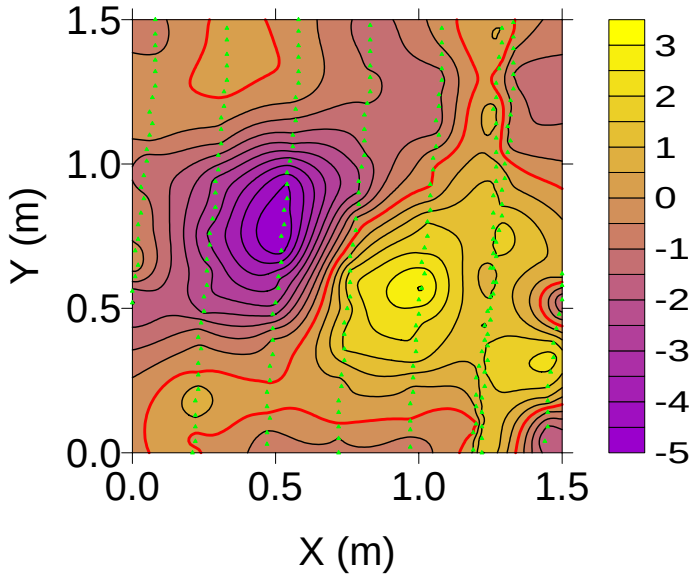

Figure L17. The EAGGN filtered H03 anomaly (L_F = 0.75 m, L_D = 1.5 m). For IIF with IIGE inversion (job 16) using 236 nodes (green triangles), Δ_C = 11 cm, (Z-Z_C) is 5 cm, θ is 74.5 deg, and Ψ is 4.1 deg. As in all 35 jobs (Table L3), θ is greater than 60 deg, which would suggest that the target has significant remanence. The zero contour is red and the contour interval is 0.5 nT.

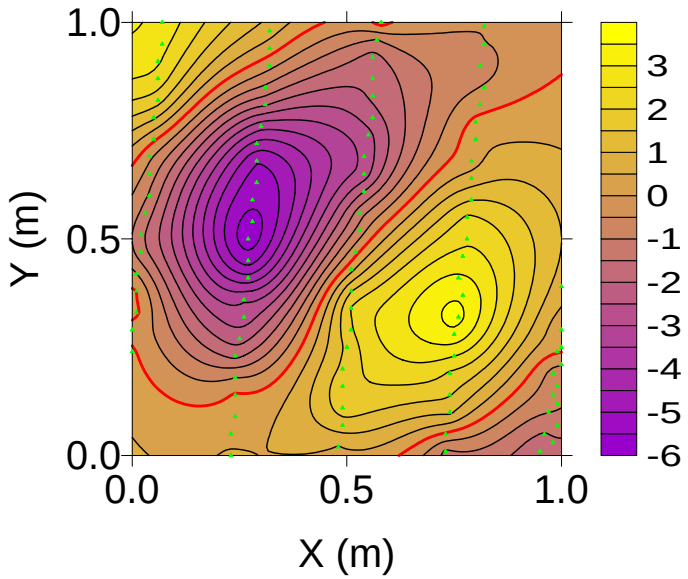

Figure L18. The EAGGN filtered H03 anomaly (L_F = 1 m, L_D = 1 m). For IIF with IIGE job 7, using 101 nodes (green triangles), Δ_C = 5 cm, Z is equal to Z_C (= 40 cm), θ is 79.0 deg, and Ψ is –1.4 deg. The zero contour is red and the contour interval is 0.5 nT.

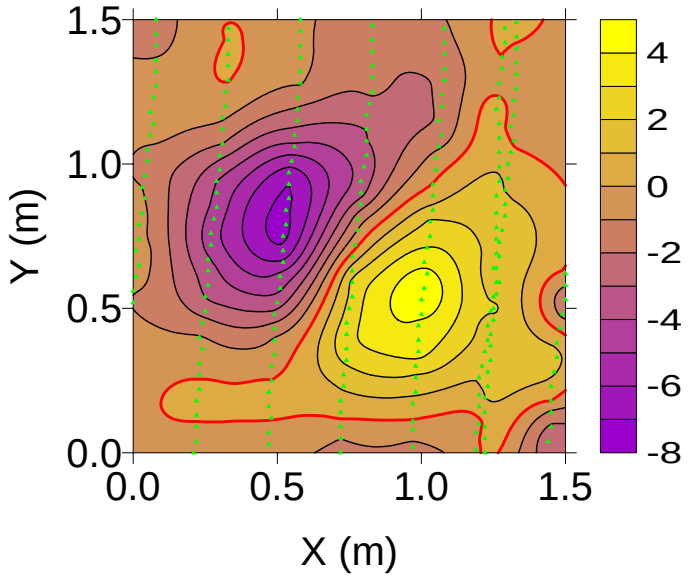

Figure L19. The EAGGN filtered H03 anomaly (L_F = 1 m, L_D = 1.5 m). For IIF with IIGE job 17, using 236 nodes (green triangles), Δ_C = 9 cm, (Z-Z_C) is 9 cm, θ is 71.3 deg, and Ψ is 7.0 deg. The zero contour is red and the contour interval is 1 nT.

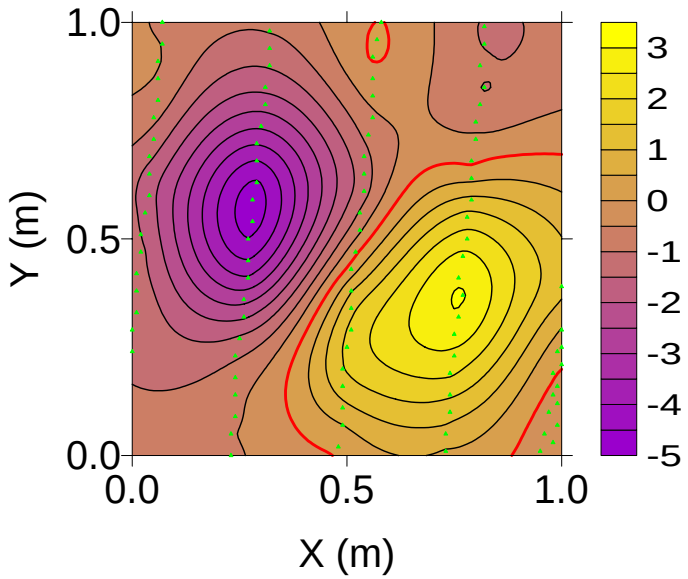

Figure L20. The EAGGN filtered field of the inverse modeled H03 dipole plus the IIGE field (L_F = 0.75 m, L_D = 1 m, job 6). For job 6, using 101 nodes (green triangles), Δ_C is 7 cm, (Z-Z_C) is -5 cm, θ is 74.0 deg, and Ψ is 4.8 deg. The results for IIF job 9 using IIBE vary little from those of job 6. The zero contour is red and the contour interval is 0.5 nT.

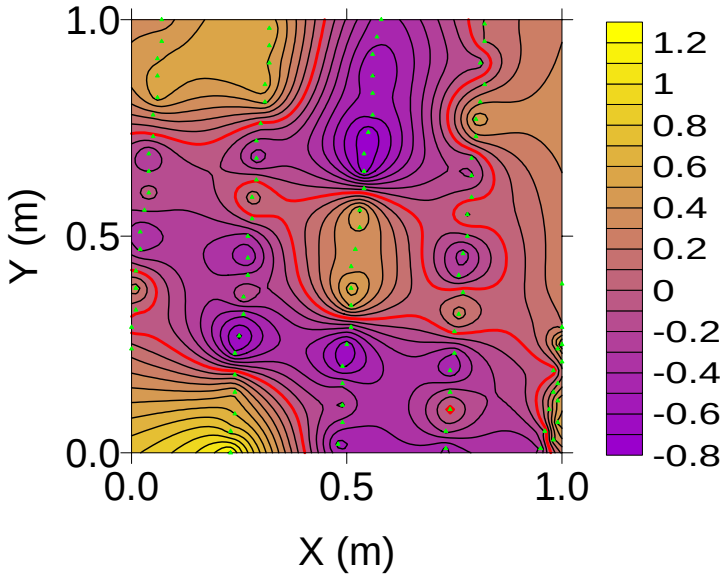

Figure L21. The residual field equal to the EAGGN filtered anomaly minus the sum of the filtered field of the inverse modeled H03 dipole plus the IIGE field (L_F = 0.75 m, L_D = 1 m) derived by job 6. The inversion used 101 flagged nodes (green triangles) nearest to the magnetometer stations. The zero contour is red and the contour interval is 0.1 nT.

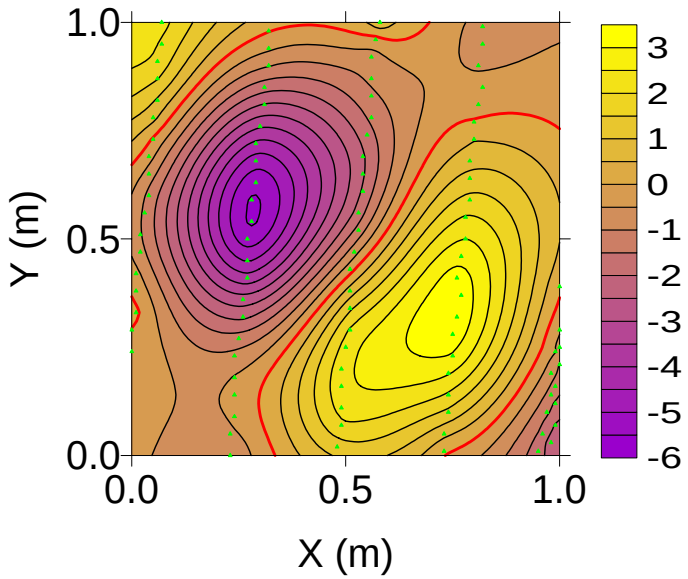

Figure L22. The EAGGN filtered field of the inverse modeled H03 dipole plus the IIGE field (L_F = 1 m, L_D = 1 m). For IIF, IIGE and IIBE jobs 7 and 10, using 101 nodes (green triangles), Δ_C is 5 cm and Z is equal to Z_C (= 40 cm). For jobs 7 and 10, θ are 79.0 and 79.2 deg and Ψ are –1.4 and –1.6 deg, respectively. The zero contour is red and the contour interval is 0.5 nT.

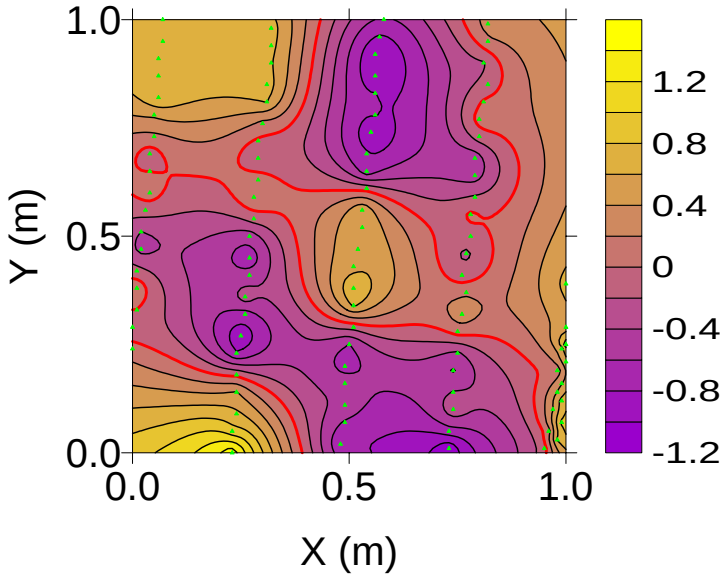

Figure L23. The residual field equal to the EAGGN filtered anomaly minus the sum of the filtered field of the inverse modeled H03 dipole plus the IIGE field (L_F = 1 m, L_D = 1 m) derived by job 7. The inversion used 101 flagged nodes (green triangles) nearest to the magnetometer stations. The zero contour is red and the contour interval is 0.2 nT.

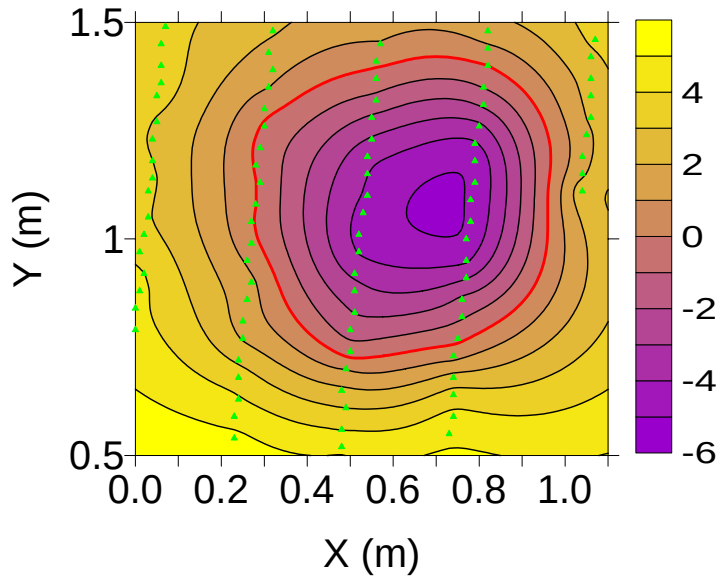

Figure L24. The H03 anomaly defined by 92 flagged nodes in a polygonal window. The contours are based only on the data at flagged nodes. Jobs 31- 35 used these data. The zero contour is red and the contour interval is 0.2 nT.

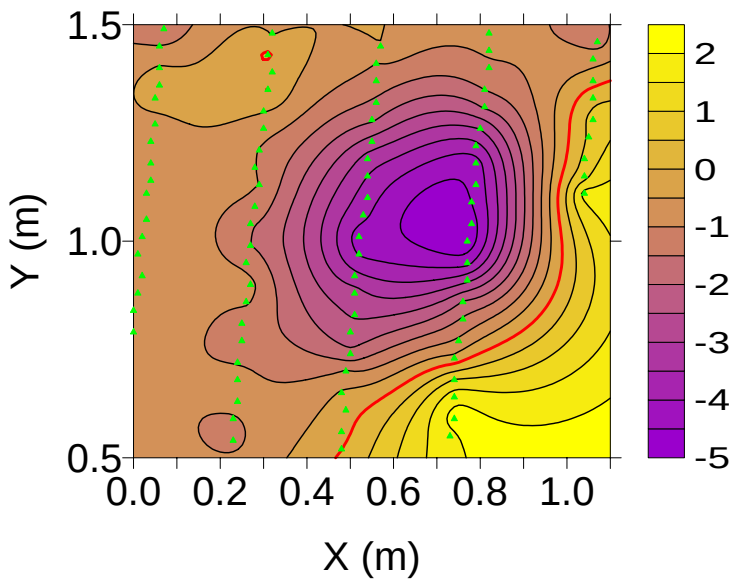

Figure L25. The EAGGN filtered H03 anomaly (L_F = 1 m, job 35). The filter was confined to input and output at the 92 flagged nodes shown here. For job 35, Δ_C is 13 cm, Z is equal to Z_C (= 40 cm), θ is 80.1 deg, and Ψ is –2.0 deg. The contours are based only on the data at flagged nodes. The zero contour is red and the contour interval is 0.2 nT.

Table 2. H03 dipole (X,Y,Z) and target's center (X_C,Y_C,Z_C) UTM coordinates. X_R = 402000 m; Y_R = 4369000 m. Δ_C and E_Z are absolute horizontal and relative vertical displacements of dipolefrom target's center. [Δx = grid interval; L_D = data window size; L_F = filter size.]

Job	Δx cm	L_D M	L_F m	†	$X-X_R$ m	$Y-Y_R$ m	$X-X_C$ cm	$Y-Y_C$ cm	Δ_C cm	Z cm	$Z-Z_C$ cm	E_Z* %
1	1	1	n/a	AB	816.88	571.46	3	-7	8	48	8	12
2	1	1	n/a	B	816.88	571.43	4	-10	11	47	7	11
3	1	1	n/a	A	816.90	571.47	6	-6	9	70	30	46
4	1	1	n/a		816.91	571.43	7	-10	12	66	26	40
5	1	1	0.50	E	816.86	571.49	2	-5	5	30	-10	-15
6	1	1	0.75	E	816.85	571.46	0	-7	7	35	-5	-8
7	1	1	1	E	816.84	571.48	0	-5	5	40	0	0
8	1	1	0.50	EB	816.85	571.48	1	-5	5	31	-9	-14
9	1	1	0.75	EB	816.85	571.46	0	-7	7	35	-5	-8
10	1	1	1	EB	816.84	571.48	0	-5	5	40	0	0
11	1	1.5	n/a	AB	816.91	571.52	6	-1	6	56	16	25
12	1	1.5	n/a	B	816.89	571.51	4	-2	5	51	12	18
13	1	1.5	n/a	A	816.93	571.53	8	0	8	80	40	62
14	1	1.5	n/a		816.91	571.52	6	-1	6	65	25	38
15	1	1.5	0.5	E	816.84	571.46	-1	-7	7	40	0	0
16	1	1.5	0.75	E	816.85	571.42	1	-11	11	45	5	8
17	1	1.5	1	E	816.91	571.46	6	-7	9	49	9	14
18	1	1.5	1.25	E	816.91	571.46	6	-7	9	52	12	19
19	1	1.5	0.50	EB	816.85	571.46	0	-7	7	44	4	6
20	1	1.5	0.75	EB	816.86	571.43	2	-11	11	49	9	14
21	1	1.5	1.00	EB	816.91	571.46	6	-7	9	49	9	14
22	1	1.5	1.25	EB	816.91	571.46	6	-7	9	52	12	18
23	1	2	n/a	AB	816.95	571.61	11	8	13	71	31	48
24	1	2	n/a	B	816.91	571.59	7	5	9	64	24	37
25	1	2	n/a	A	816.97	571.64	12	10	16	108	68	105
26	1	2	n/a		816.93	571.60	9	7	11	84	44	68
27	1	2	n/a	B▼$_2$	816.89	571.35	4	-18	19	59	19	29
28	1	2	n/a	▼$_2$	816.79	571.42	-5	-11	12	49	9	14
29	1	2	n/a	B▼$_0$	816.90	571.35	5	-18	19	48	8	12
30	1	2	n/a	▼$_0$	816.70	571.45	-15	-9	17	40	0	0
31	1	1.1	n/a	B§	816.83	571.41	-2	-12	13	53	13	20
32	1	1.1	n/a	§	816.76	571.41	-8	-13	15	43	3	5
33	1	1.1	0.5	E§	816.86	571.39	2	-14	14	31	-9	-14
34	1	1.1	0.75	E§	816.84	571.41	-1	-12	12	42	2	3
35	1	1.1	1	E§	816.79	571.41	-5	-12	13	40	0	0

† flag-node and IIGE unless noted: **A** = all-node; **B** = IIBE. **E** = EAGGN (L_{FD} = L_D).
▼$_0$ = trough-only (H < 0). ▼$_2$ = trough only (H < 2). **§** = single-swath.
* $E_Z = (Z-Z_C)/(Z_C+H_M)$; magnetometer elevation, H_M = 0.25 m; Z_C = 40 cm.

Table L3. H03 dipole parameters: θ = deviation angle; δ = dipole declination; Ψ = dipole inclination; M = dipole moment. Gx, Gy = gradient components; B = dc bias estimate; R = correlation coefficient. [Δx = grid interval; L_D = data window size; L_F = filter size.]

Job	Δx cm	L_D m	L_F m	†	θ deg	δ deg	Ψ deg	M mA•m^2	Gx nT/m	Gy nT/m	B nT	R
1	1	1	n/a	AB	81.6	54.8	-0.6	45.5	n/a	n/a	6.32	0.994
2	1	1	n/a	B	78.5	54.0	2.4	44.4	n/a	n/a	5.96	0.996
3	1	1	n/a	A	74.1	48.7	5.1	151	-8.10	8.92	6.81	0.995
4	1	1	n/a		73.4	51.7	7.0	122	-6.49	5.65	6.04	0.996
5	1	1	0.50	E	70.4	43.8	7.3	15.0	0.32	0.30	-0.24	0.975
6	1	1	0.75	E	74.0	47.5	4.8	20.9	0.08	-0.04	-0.24	0.973
7	1	1	1	E	79.0	44.9	-1.4	29.2	0.09	0.17	-0.04	0.966
8	1	1	0.50	EB	74.7	46.1	3.6	16.5	n/a	n/a	-0.20	0.973
9	1	1	0.75	EB	74.0	47.5	4.8	21.1	n/a	n/a	-0.24	0.973
10	1	1	1	EB	79.2	45.2	-1.6	29.2	n/a	n/a	-0.04	0.965
11	1	1.5	n/a	AB	88.8	61.5	-5.7	63.8	n/a	n/a	7.65	0.986
12	1	1.5	n/a	B	88.7	60.6	-5.9	55.9	n/a	n/a	7.43	0.989
13	1	1.5	n/a	A	81.6	54.7	-0.6	187	-5.34	4.87	8.34	0.990
14	1	1.5	n/a		81.3	51.7	-1.4	102	-2.03	4.10	7.60	0.992
15	1	1.5	0.50	E	76.4	36.7	-1.5	28.6	0.17	-0.18	-0.08	0.869
16	1	1.5	0.75	E	74.5	47.2	4.1	36.6	0.17	-0.16	-0.15	0.879
17	1	1.5	1	E	71.3	45.6	7.0	45.4	0.23	0.12	-0.31	0.920
18	1	1.5	1.25	E	74.8	48.5	4.3	53.6	0.13	-0.04	-0.20	0.917
19	1	1.5	0.50	EB	75.1	36.1	-0.2	37.3	n/a	n/a	-0.08	0.867
20	1	1.5	0.75	EB	73.8	47.1	4.9	46.8	n/a	n/a	-0.15	0.878
21	1	1.5	1	EB	72.2	47.0	6.5	46.2	n/a	n/a	-0.30	0.919
22	1	1.5	1.25	EB	74.8	48.7	4.4	54.0	n/a	n/a	-0.20	0.916
23	1	2	n/a	AB	94.5	70.9	-8.0	105	n/a	n/a	8.60	0.975
24	1	2	n/a	B	94.4	68.3	-9.1	83.9	n/a	n/a	8.25	0.979
25	1	2	n/a	A	85.9	60.1	-3.1	386	-5.00	4.32	9.64	0.982
26	1	2	n/a		86.5	58.3	-4.5	181	-2.38	3.22	8.64	0.984
27	1	2	n/a	B▼$_2$	75.9	38.8	-0.2	90.7	n/a	n/a	9.82	0.990
28	1	2	n/a	▼$_2$	84.7	38.7	-9.5	44.2	-0.85	1.82	6.89	0.991
29	1	2	n/a	B▼$_0$	68.6	44.0	9.3	59.7	n/a	n/a	7.60	0.995
30	1	2	n/a	▼$_0$	82.1	18.5	-11.9	21.2	-0.91	6.27	3.49	0.998
31	1	1.1	n/a	B§	85.9	40.4	-10.2	54.0	n/a	n/a	7.55	0.991
32	1	1.1	n/a	§	86.3	41.3	-10.4	31.0	-1.66	-0.47	5.87	0.993
33	1	1.1	0.5	E§	66.3	62.2	18.9	23.4	0.10	0.05	-0.09	0.966
34	1	1.1	0.75	E§	74.4	51.6	5.9	36.5	-0.02	0.04	-0.04	0.982
35	1	1.1	1	E§	80.1	46.4	-2.0	28.5	0.07	0.10	-0.06	0.985

† flag-node and IIGE unless noted: **A** = all-node; **B** = IIBE. **E** = EAGGN ($L_{FD} = L_D$).
▼$_0$ = trough-only (H < 0). ▼$_2$ = trough only (H < 2). **§** = single-swath.

Table L4. C13 data windows: grid interval, Δx; absolute and relative window size, L_D, R_L; displacement of window's center from target's center, X_W-X_C, Y_W-Y_C; number of nodes along the x-and y-axes, N_X, N_Y; and the number and proportion of nodes flagged for inversion N_F, R_F.

Jobs	Δx (cm)	L_D (m)	R_L†	X_M-X_C (cm)	Y_M-Y_C (cm)	N_X	$N_X \bullet N_Y$	N_F*	R_F (%)
1, 3	1	1	1.5	1	0	101	10201	10201	100
2, 4-10	1	1	1.5	1	0	101	10201	101	1.0
11, 13	1	1.5	2.3	1	0	151	22801	22801	100
12, 14-22	1	1.5	2.3	1	0	151	22801	236	1.0
23,25	1	2	3.1	1	0	201	40401	40401	100
24, 26	1	2	3.1	1	0	201	40401	399	1.0
28-29	1	2	3.1	1	0	201	40401	56$\blacktriangledown_2$	0.1
29-30	1	2	3.1	1	0	201	40401	34$\blacktriangledown_0$	0.1
31-35	1	1.1	3.1	1	0	111	11211	92§	0.8

† $R_L = L_D/(Z_C+H_M)$; depth to target center, Z_C = 40 cm; magnetometer height, H_M = 0.25 m.

* $\blacktriangledown_0$ = trough-only (H < 0). $\blacktriangledown_2$ = trough only (H < 2). **§** = single-swath.

Appendix M
Target A07 (57 mm Projectile)

Figures M1-M13 plot the A07 anomaly and results of inversion jobs. Target A07 is an M86 57 mm projectile, which the AEC emplaced at a depth to center, Z_C, of 26 cm (Figure M1, Table M1). Conclusions are derived from 23 jobs (Tables M2-M4):

Appendix M Figures

M1. Target A07: 57mm M86 projectile ……. 215
M2. Regional setting of A07 anomaly …….…….. 216
M3. A07 anomaly in 1.5-m window with flagged nodes …… 216
M4. A07 anomaly in 1-m window with flagged nodes …….. 217
M5. A07 anomaly and flagged nodes for trough-only inversion ……. 217
M6. A07 anomaly in 1-m window with 350 flagged nodes ……..……. 218
M7. EAGGN filtered A07 anomaly (L_F = 0.75 m, L_D = 2 m) …….. 218
M8. EAGGN filtered A07 anomaly (L_F = 1.5 m, L_D = 2 m) …….. 219
M9. EAGGN filtered A07 anomaly (L_F = 2 m, L_D = 2 m) …….. 219
M10. EAGGN filtered A07 anomaly (L_F = 0.5 m, L_D = 1.5 m) …… 220
M11. EAGGN filtered A07 anomaly (L_F = 1 m, L_D = 1.5 m) …… 220
M12. EAGGN filtered A07 anomaly (L_F = 0.5 m, L_D = 1 m) ……...…… 221
M13. EAGGN filtered A07 anomaly (L_F = 1 m, L_D = 1 m) …….……. 221

Appendix M Tables

M1. Ground truth for target A07 ……...……. 215
M2. Dipole positions for anomaly A07 inversions ……...……. 222
M3. Dipole parameters for anomaly A07 inversions ……. 223
M4. A07 data window parameters …….…… 224

Figure M1. Target A07: 57 mm M86 projectile.

Table M1. A07 ground truth parameters.

Description	M86 Projectile
Material	Steel
Length, L_T	170 mm
Diameter, D_T	57 mm
Weight	2.722 kg
Grid azimuth, Φ_T	195 deg
Inclination, Ψ_T	3 deg
Depth, Z_C	26 cm
UTM northing, Yc	4369583.78 m
UTM easting, X_C	402806.34 m
Ratio of depth below magnetometer to target length, R_{DL} †	3.0
Vertical projection of target's length, L_V (= $L_T \sin \Psi_T$)	1 cm
Horizontal projection of target's length, L_H (= $L_T \cos \Psi_T$)	17 cm
Nose-from-center offsets (Xn-Xc, Yn-Yc, Zn-Zc)	(-1, -8, 0) cm

† $R_{DL} = (Z_C+H_M)/L_T$; Magnetometer height, $H_M = 0.25$ m

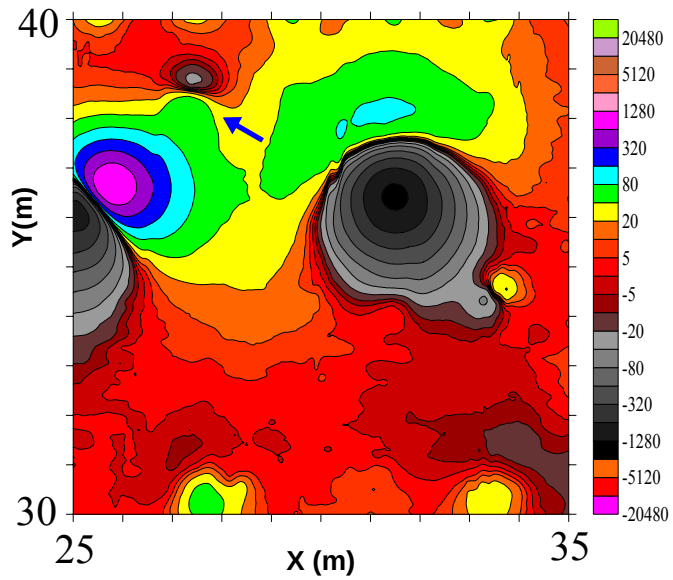

Figure M2. Regional setting of the A07 magnetic anomaly (blue arrow). The positive portion of the A07 anomaly is merged with that of the B08 anomaly. Truncated anomalies along the northern edge are caused by buried steel spheres that define the northern boundary of the Blind Test Area. The magnetic field contours are at zero and $\pm 2^n \cdot 10$ nT, where n is a non-negative integer.

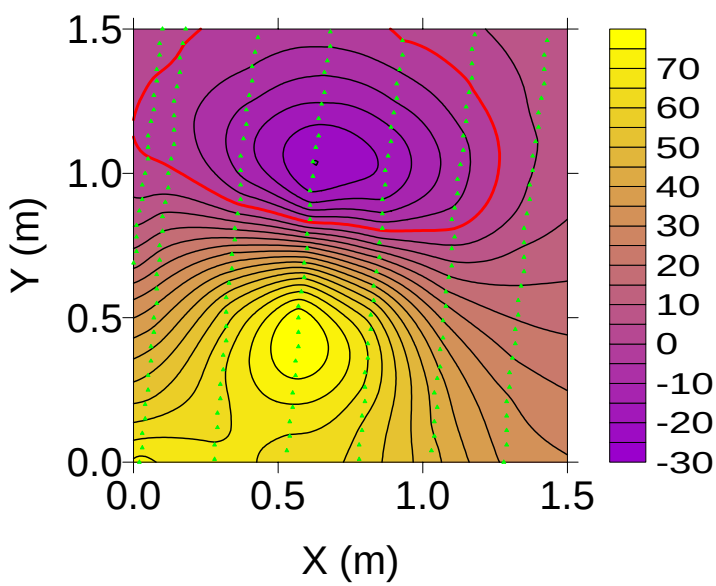

Figure M3. The A07 anomaly (L_D = 1.5 m) and 200 nodes (green triangles) flagged for use in inversions. For flag-node IIBE inversion (job 9), Δ_C is 9 cm, $(Z\text{-}Z_C)$ is 25 cm, θ is 51.0 deg, and Ψ is 16.5 deg. For IIGE inversion (job 11), Δ_C is 9 cm, $(Z\text{-}Z_C)$ is 13 cm, θ is 52.1 deg, and Ψ is 15.2 deg. IIGE inversion improves the depth estimate relative to IIBE inversion. The corresponding all-node inversions (jobs 8 and 10) yield approximately the same dipole positions and orientations. IIF improves the inversion results and yields significantly shallower dipoles. The zero contour is red and the contour interval is 5 nT.

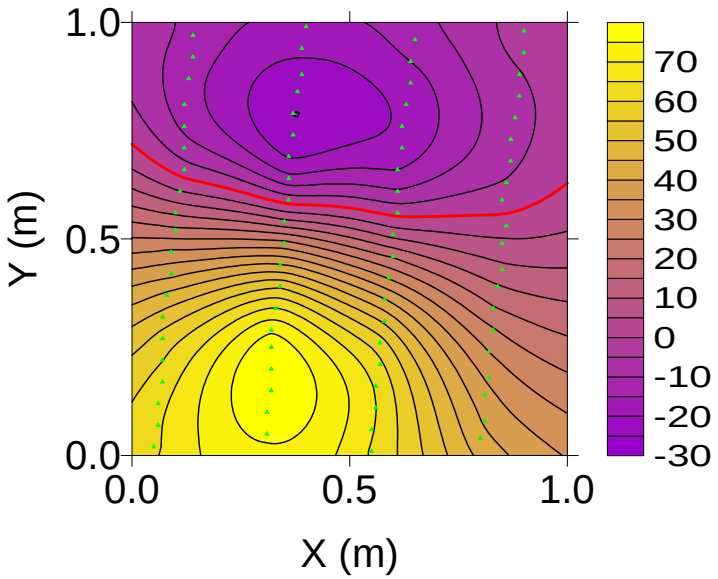

Figure M4. The A07 anomaly (L_D = 1 m) and 80 nodes (green triangles) flagged for use in inversions. For flag-node, single-swath IIBE job 2, Δ_C is 5 cm, (Z-Z_C) is 15 cm, θ is 49.8 deg, and Ψ is 17.8 deg. For IIGE job 4, Δ_C is 6 cm, (Z-Z_C) is 12 cm, θ is 51.7 deg, and Ψ is 15.8 deg. The corresponding all-node inversions (jobs 1 and 3) yield approximately the same dipole positions and orientations. The smaller window (L_D = 1 m) improves the results. IIF further improves the results. The zero contour is red and the contour interval is 5 nT.

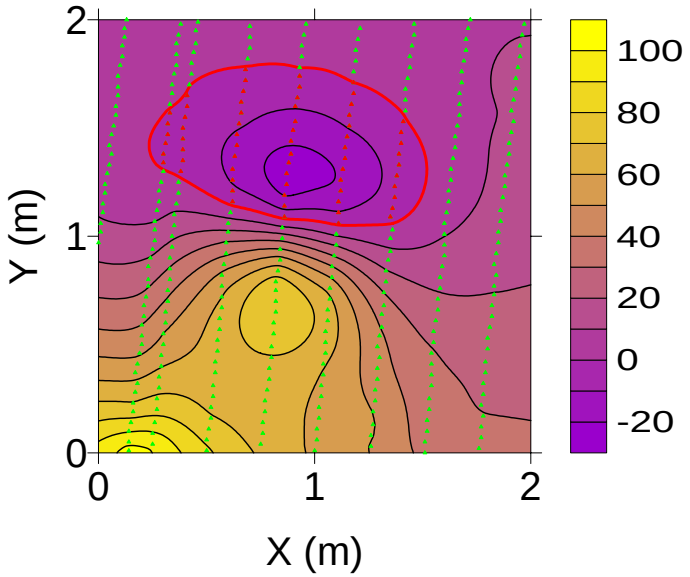

Figure M5. The A07 anomaly and 65 nodes (red triangles) with negative values used in jobs 24-25. For IIBE, Δ_C is 10 cm (= 0.59 L_H), (Z-Z_C) is -1 cm, θ is 49.8 deg, and Ψ is 17.8 deg. For IIGE, Δ_C is 8 cm, (Z-Z_C) is 2 cm, θ is 51.7 deg, and Ψ is 15.8 deg. These trough-only inversions improve the dipole depth for the sub-horizontal projectile (Ψ_T = 3 deg); however, Δ_C is less for each of the 14 IIF inversions that were run. The zero contour is red and the contour interval is 10 nT.

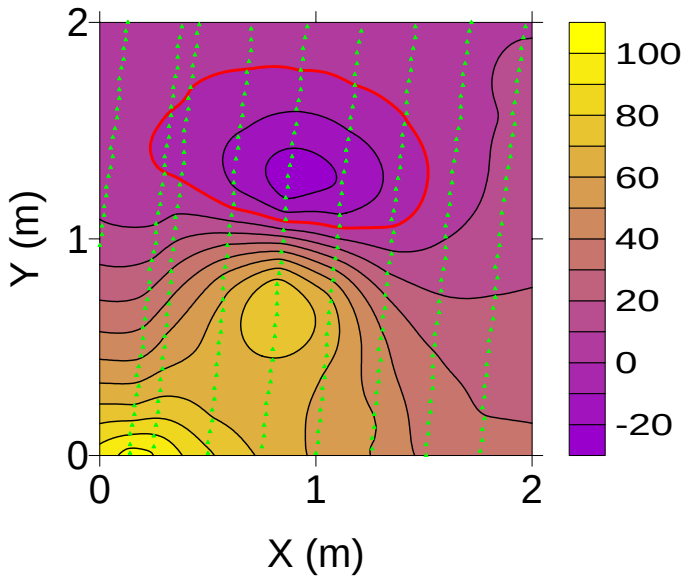

Figure M6. The unfiltered A07 anomaly in a 2-m data window and 350 flagged nodes (green triangles) used in EAGGN IIF inversion jobs (17-23). This data window is too large for inversion without IIF; nevertheless, EAGGN IIF inversions yield consistent results for $L_F \geq 0.75$ m and L_D equal to 1, 1.5 and 2 m (jobs 6-7, 13-16, and 18-23). For those jobs, $4 \leq (\Delta_C) \leq 6$ cm, $4 \leq (Z\text{-}Z_C) \leq 6$ cm, $51.7 \leq \theta \leq 55.1$ deg, and $12.4 \leq \Psi \leq 16.1$ deg. The zero contour is red and the contour interval is 10 nT.

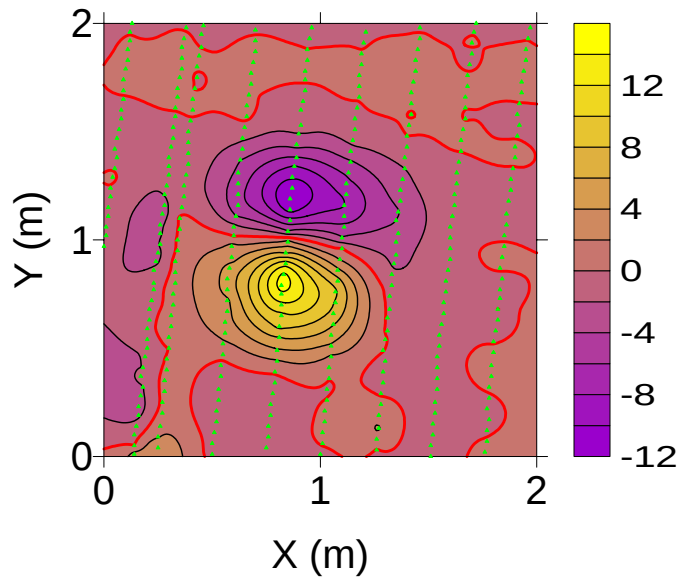

Figure M7. The EAGGN filtered A07 anomaly ($L_F = 0.75$ m; $L_D = 2$ m) and 350 flagged nodes (green triangles) used in job 16. For this inversion, Δ_C is 4 cm (= 0.24 L_H), $(Z\text{-}Z_C)$ is 6 cm, E_Z is 12 %, θ is 52.0 deg, and Ψ is 15.7 deg. For IIF with $0.5 \leq L_F \leq 2$ m and L_D equal to 2 m (jobs 17-23), 4 cm $\leq \Delta_C \leq$ 5 cm, 4 cm $\leq (Z\text{-}Z_C) \leq$ 7 cm, $51.7 \leq \theta \leq 52.6$ deg, and $15.6 \leq \Psi \leq 16.1$ deg. Among these inversions, the one with L_F equal to 0.5 m determines the greatest value for Δ_C, $(Z\text{-}Z_C)$, and θ, and the least value for Ψ. The zero contour is red and the contour interval is 2 nT.

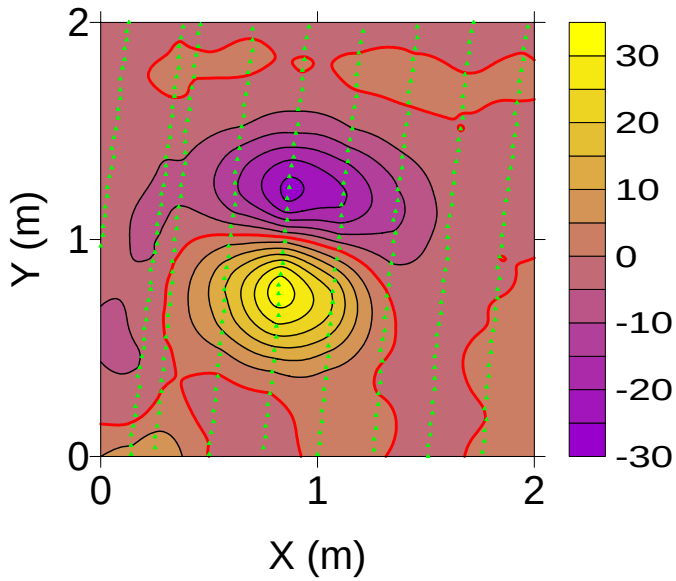

Figure M8. The EAGGN filtered A07 anomaly (L_F = 1.5 m; L_D = 2 m) and 350 flagged nodes (green triangles) used in job 21. For L_F equal to 0.75, 1, and 1.25 m (jobs 20-22), the dipole positions are identical, Δ_C is 4 cm (= 0.24 L_H), (Z-Z_C) is 6 cm, E_Z is 12 %, 51.7 $\leq\theta \leq$ 52.0 deg, and 15.7 $\leq \Psi \leq$ 16.1 deg. The zero contours are red and the contour interval is 5 nT.

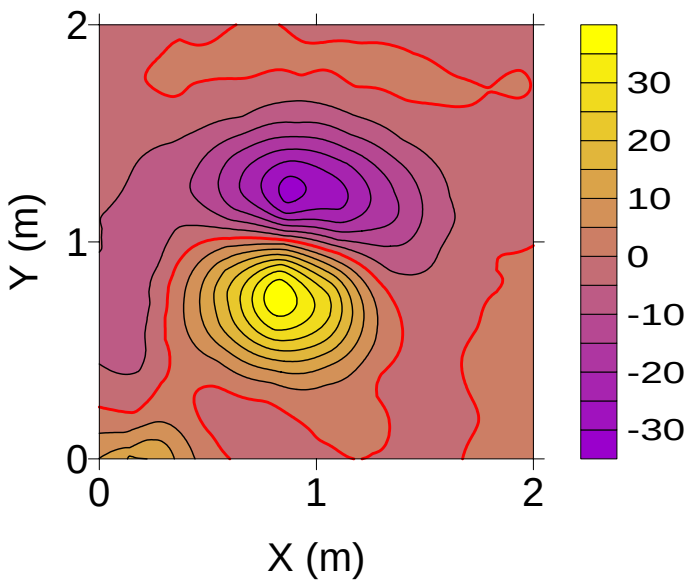

Figure M9. The EAGGN filtered A07 anomaly (L_F = 2 m; L_D = 2 m) and 350 flagged nodes (green triangles) used in job 23. Although the dipole solution varies little from those with L_F equal to 0.75, 1, or 1.25 m, the smaller filters may be preferred since a residual effect of the B08 anomaly is more apparent in the southwest corner of the data window for the larger filter. For L_F equal to 2 m, Δ_C is 4 cm (= 0.24 L_H), (Z-Z_C) is 4 cm (E_Z = 8 %), θ is 51.9 deg, and Ψ is 15.8 deg. The zero contours are red and the contour interval is 5 nT.

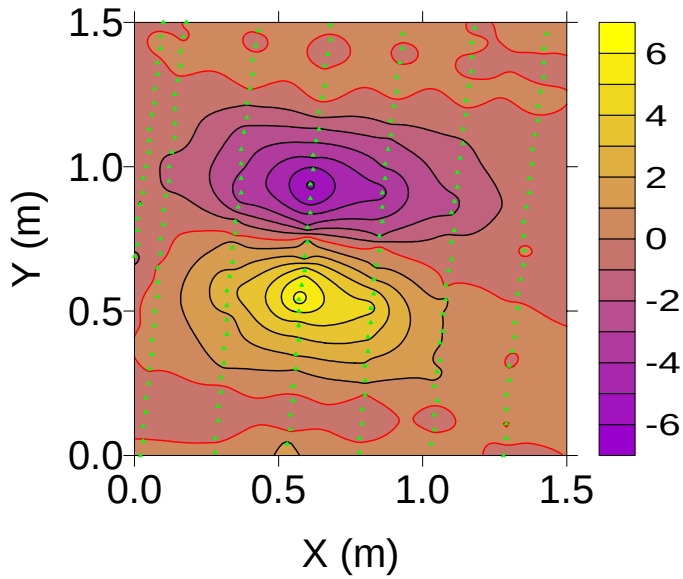

Figure M10. The EAGGN filtered A07 anomaly (L_F = 0.5 m; L_D = 1.5 m) and 200 flagged nodes (green triangles) used in job 12. All tracks except for the westernmost belong to a single swath. Although a larger filter is generally desirable for cross-line magnetometer spacing of 0.25 m, the dipole solution in this case differs little from the solutions for larger filters. The dipole positions are identical for $0.75 \leq LF \leq 1.5$ m. For LF equal to 0.5 m the position is offset from those solutions by only 1 cm. The zero contours are red and the contour interval is 0.5 nT.

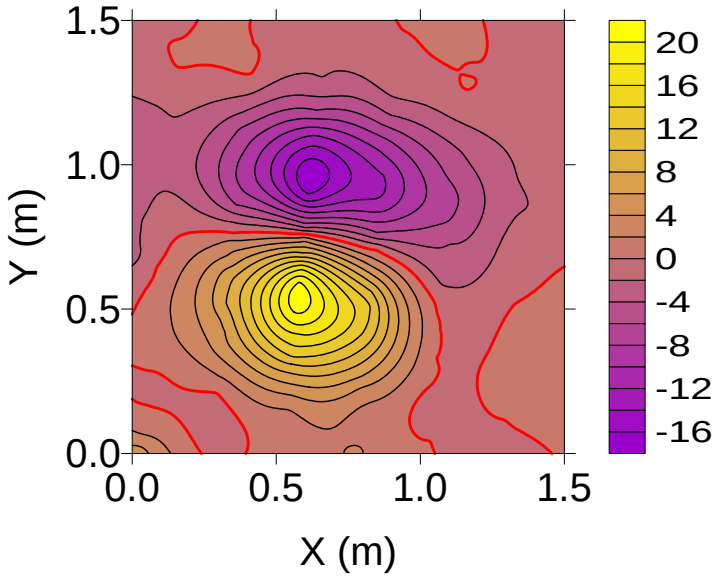

Figure M11. The EAGGN filtered A07 anomaly (L_F = 1 m; L_D = 1.5 m) used in job 12. For $0.75 \leq L_F \leq 1.5$ m, the dipole positions are identical, Δ_C is 4 cm, $(Z\text{-}Z_C)$ is 6 cm (E_Z = 12 %), $52.2 \leq \theta \leq 52.3$ deg, and $15.4 \leq \Psi \leq 15.5$ deg. The zero contours are red and the contour interval is 2 nT.

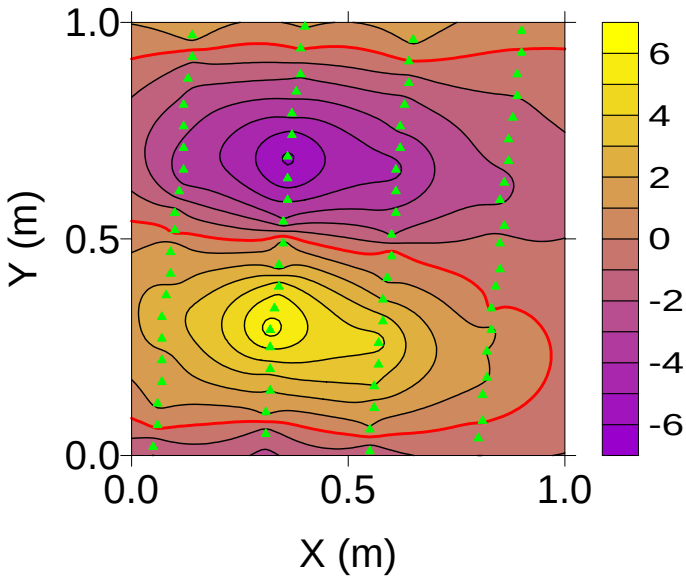

Figure M12. The EAGGN filtered A07 anomaly (L_F = 0.5 m; L_D = 1 m) and 80 flagged nodes (green triangles) used in job 5. For this inversion, Δ_C is 6 cm, (Z-Z_C) is 7 cm (E_Z = 14 %), θ is 59.1 deg, and Ψ is 8.7 deg. The zero contours are red and the contour interval is 1 nT.

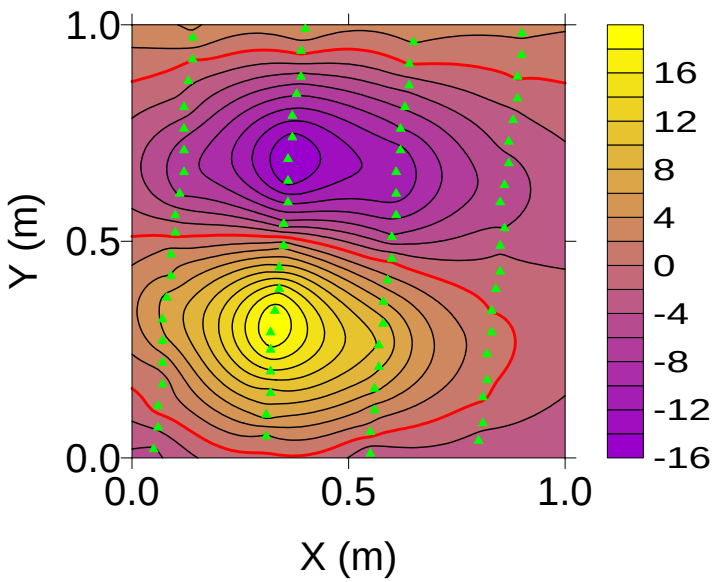

Figure M13. The EAGGN filtered A07 anomaly (L_F = 1 m; L_D = 1 m) and 80 flagged nodes (green triangles) used in job 7. For this inversion, Δ_C is 5 cm, (Z-Z_C) is 5 cm (E_Z = 10 %), θ is 55.1 deg, and Ψ is 12.4 deg. The zero contours are red and the contour interval is 2 nT.

Table M2. A07 dipole (X,Y,Z) and target's center (X_C,Y_C,Z_C) UTM coordinates. X_R = 402000 m; Y_R = 4369000 m. Δ_C and E_Z are absolute horizontal and relative vertical displacements of dipole from target's center. [Δx = grid interval; L_D = data window size; L_F = filter size.]

Job	Δx cm	L_D m	L_F m	†	$X-X_R$ m	$Y-Y_R$ m	$X-X_C$ cm	$Y-Y_C$ cm	Δ_C cm	Z cm	$Z-Z_C$ cm	E_Z* %
1	1	1	n/a	AB§	806.29	583.77	-5	-1	5	41	15	29
2	1	1	n/a	B§	806.29	583.77	-5	-1	5	40	14	27
3	1	1	n/a	A§	806.28	583.78	-6	0	6	40	14	27
4	1	1	n/a	§	806.28	583.78	-6	0	6	38	12	24
5	1	1	0.5	E§	806.29	583.82	-5	4	6	33	7	14
6	1	1	0.75	E§	806.29	583.81	-5	3	6	32	6	12
7	1	1	1	E§	806.30	583.81	-4	3	5	31	5	10
8	1	1.5	n/a	AB	806.26	583.77	-8	-1	8	50	24	47
9	1	1.5	n/a	B	806.25	583.76	-9	-2	9	51	25	49
10	1	1.5	n/a	A	806.26	583.77	-8	-1	8	41	15	29
11	1	1.5	n/a		806.25	583.77	-9	-1	9	39	13	25
12	1	1.5	0.5	E	806.29	583.80	-5	2	5	32	6	12
13	1	1.5	0.75	E	806.30	583.80	-4	2	4	32	6	12
14	1	1.5	1	E	806.30	583.80	-4	2	4	32	6	12
15	1	1.5	1.25	E	806.30	583.80	-4	2	4	32	6	12
16	1	1.5	1.5	E	806.30	583.80	-4	2	4	32	6	12
17	1	2	0.5	E	806.29	583.80	-5	2	5	33	7	14
18	1	2	0.75	E	806.30	583.80	-4	2	4	32	6	12
19	1	2	1	E	806.30	583.80	-4	2	4	32	6	12
20	1	2	1.25	E	806.30	583.80	-4	2	4	32	6	12
21	1	2	1.5	E	806.30	583.80	-4	2	4	31	5	10
22	1	2	1.75	E	806.30	583.80	-4	2	4	31	5	10
23	1	2	2	E	806.30	583.80	-4	2	4	30	4	8
24	1	2	n/a	B▼$_0$	806.26	583.84	-8	6	10	25	-1	-2
25	1	2	n/a	▼$_0$	806.27	583.83	-7	5	8	28	2	4

† flag-node and IIGE unless noted: **A** = all-node; **B** = IIBE. **E** = EAGGN (L_{FD} = L_D).
▼$_0$ = trough-only (H < 0)
* $E_Z = (Z-Z_C)/(Z_C+H_M)$; magnetometer elevation, H_M = 0.25 m

Table M3. A07 dipole parameters: θ = deviation angle; δ = dipole declination; Ψ = dipole inclination; M = dipole moment. Gx, Gy = gradient components; B = dc bias estimate; R = correlation coefficient. [Δx = grid interval; L_D = data window size; L_F = filter size.]

Job	Δx cm	L_D m	L_F m	†	θ deg	δ deg	Ψ deg	M mA•m^2	Gx nT/m	Gy nT/m	B nT	R
1	1	1	n/a	AB	49.9	-20.8	17.7	175.6	n/a	n/a	18.2	1.000
2	1	1	n/a	B	49.8	-20.9	17.8	170.9	n/a	n/a	18.1	0.999
3	1	1	n/a	A	51.7	-19.8	15.8	166.5	-2.63	-1.55	18.9	1.000
4	1	1	n/a		51.7	-19.0	15.8	153.6	-4.78	-2.56	19.0	1.000
5	1	1	0.5	E	59.1	-23.0	8.7	110.1	0.01	0.06	-0.04	0.988
6	1	1	0.75	E	54.6	-19.3	12.9	101.4	-0.14	-0.02	-0.06	0.996
7	1	1	1	E	55.1	-19.4	12.4	94.6	-0.29	0.10	-0.06	0.997
8	1	1.5	n/a	AB	52.2	-20.2	15.4	256	n/a	n/a	20.7	0.995
9	1	1.5	n/a	B	51.0	-19.3	16.5	268	n/a	n/a	20.3	0.992
10	1	1.5	n/a	A	52.3	-17.9	15.1	164	-4.18	-10.1	20.8	0.996
11	1	1.5	n/a		52.1	-16.0	15.2	149	-5.07	-12.9	20.6	0.993
12	1	1.5	0.5	E	52.3	-25.5	15.7	102	0.13	0.07	-0.11	0.976
13	1	1.5	0.75	E	52.3	-22.2	15.5	101	0.07	0.19	-0.22	0.988
14	1	1.5	1	E	52.3	-22.1	15.4	102	0.14	0.21	-0.38	0.991
15	1	1.5	1.25	E	52.2	-22.2	15.5	102	0.25	0.27	-0.49	0.993
16	1	1.5	1.5	E	52.3	-22.2	15.4	102	0.33	0.32	-0.58	0.992
17	1	2	0.5	E	52.6	-26.4	15.6	111	0.19	0.19	-0.14	0.948
18	1	2	0.75	E	52.0	-22.4	15.7	102	0.15	0.25	-0.27	0.961
19	1	2	1	E	51.9	-22.8	15.9	102	0.36	0.46	-0.51	0.970
20	1	2	1.25	E	51.7	-22.9	16.1	102	0.52	0.59	-0.72	0.976
21	1	2	1.5	E	51.7	-22.8	16.1	96.0	0.64	0.61	-0.96	0.978
22	1	2	1.75	E	51.8	-22.7	16.0	95.9	0.71	0.65	-1.14	0.977
23	1	2	2	E	51.9	-22.5	15.8	90.8	0.74	0.59	-1.31	0.974
24	1	2	n/a	B▼$_0$	52.1	-21.9	15.6	55.9	n/a	n/a	6.49	0.997
25	1	2	n/a	▼$_0$	52.5	-23.3	15.3	69.0	3.02	0.35	7.95	0.998

† flag-node and IIGE unless noted: **A** = all-node; **B** = IIBE. **E** = EAGGN ($L_{FD} = L_D$).
▼$_0$ = trough-only (H < 0)

Table M4. A07 data windows: grid interval, Δx; absolute and relative window size, L_D, R_L; displacement of window's center from target's center, X_W-X_C, Y_W-Y_C; number of nodes along the x-and y-axes, N_X, N_Y; and the number and proportion of nodes flagged for inversion N_F, R_F.

Jobs	Δx (cm)	L_D (m)	R_L†	X_W-X_C (cm)	Y_W-Y_C (cm)	N_X	$N_X \bullet N_Y$	N_F	R_F (%)
1, 3	1	1	2.0	9	6	101	10201	10201	100
2, 4-7	1	1	2.0	9	6	101	10201	80	0.8
8, 10	1	1.5	2.9	9	6	151	22801	22801	100
9, 11-16	1	1.5	2.9	9	6	151	22801	200	0.9
17-23	1	2	3.9	9	6	201	40401	350	0.9
24-25	1	2	3.9	9	6	201	40401	65▼$_0$	0.2

†$R_L = L_D/(Z_C+H_M)$; depth to target center, Z_C = 26 cm; magnetometer height, H_M = 25 cm.
▼$_0$ = trough-only ($H < 0$)

Appendix N
Target B10 (BDU submunition)

Target B10 is a 0.8-kg BDU submunition, which the AEC emplaced at a depth to center of 13 cm (Figure N1, Table N1). Figures N2-N9 plot the anomaly and results of inversion jobs. The results and descriptions of 17 jobs are also presented in Tables N2-N4.

Appendix N Figures

N1. Target B10: BDU submunition ……..…… 226
N2. Regional setting of B10 anomaly ……...…… 227
N3. B10 anomaly of a BDU submunition (LD = 1.5 m) and flagged nodes …….. 227
N4. B10 anomaly of a BDU submunition (LD = 1.0 m) …….…….. 228
N5. EAGGN filtered B10 anomaly (L_F = 0.5 m, L_D = 1.5 m) …… 228
N6. EAGGN filtered B10 anomaly (L_F = 0.5 m, L_D = 1 m) …… 229
N7. EAGGN filtered B10 anomaly (L_F = 0.75 m, L_D = 1 m) ……. 229
N8. EAGGN filtered B10 anomaly (L_F = 1 m, L_D = 1 m) …….. 230
N9. EAGGN filtered B10 anomaly (L_F = 1.5 m, L_D = 1.5 m) …… 230

Appendix N Tables

N1. Ground truth for target B10 ……...……. 226
N2. Dipole positions for anomaly B10 inversions ……...…….. 231
N3. Dipole parameters for anomaly B10 inversions ……..…… 232
N4. B10 data window parameters …….. 232

Figure N1. Target B10; BDU submunition.

Table N2. Ground truth for target B10.

Description	BDU submunition
Material	ferrous metallic
Length, L_T	97 mm (3.8 in)
Diameter, D_T	67 mm (2.6 in)
Weight	0.771 kg (1.7 lbs)
Grid azimuth, Φ_T	212 deg
Inclination, Ψ_T	22 deg
Depth, Z_C	13 cm
UTM northing, Yc	4369580.717 m
UTM easting, X_C	402800.837 m
Ratio of depth below magnetometer to target length, R_{DL} †	3.9
Vertical projection of target's length, L_V (= $L_T \sin \Psi_T$)	4 cm
Horizontal projection of target's length, L_H (= $L_T \cos \Psi_T$)	9 cm
Nose-from-center offsets (Xn-Xc, Yn-Yc, Zn-Zc)	(-2, -4, 2) cm

† $R_{DL} = (Z_C+H_M)/L_T$; magnetometer elevation, $H_M = 0.25$ m

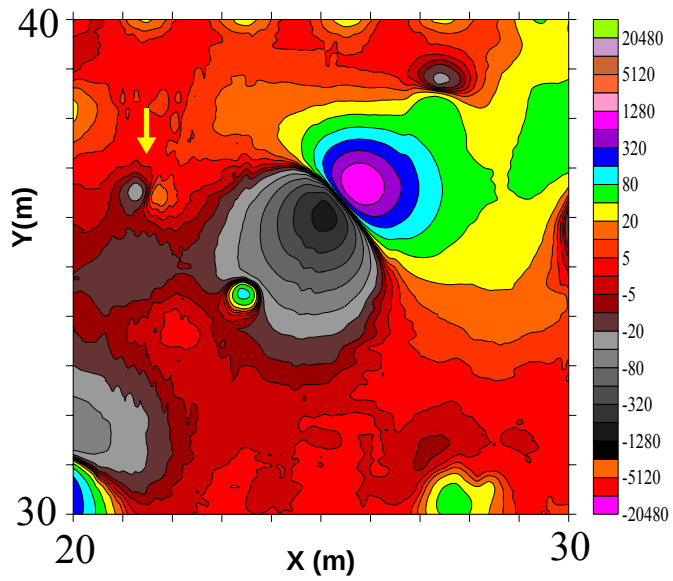

Figure N2. Regional setting of the B10 anomaly (yellow arrow). The magnetic field contours are at zero and $\pm 2^n \cdot 5$ nT, where n is a non-negative integer.

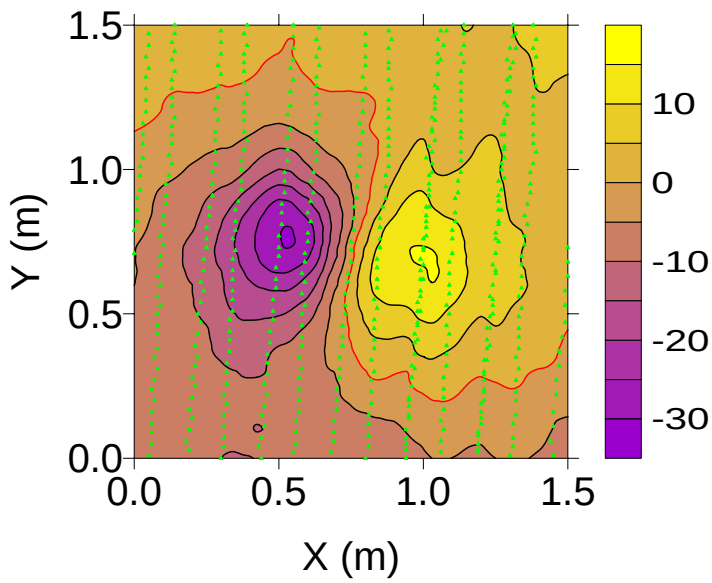

Figure N3. The B10 anomaly of a BDU submunition (L_D = 1.5 m) and 550 flagged nodes (green triangles) nearest to magnetometer stations.

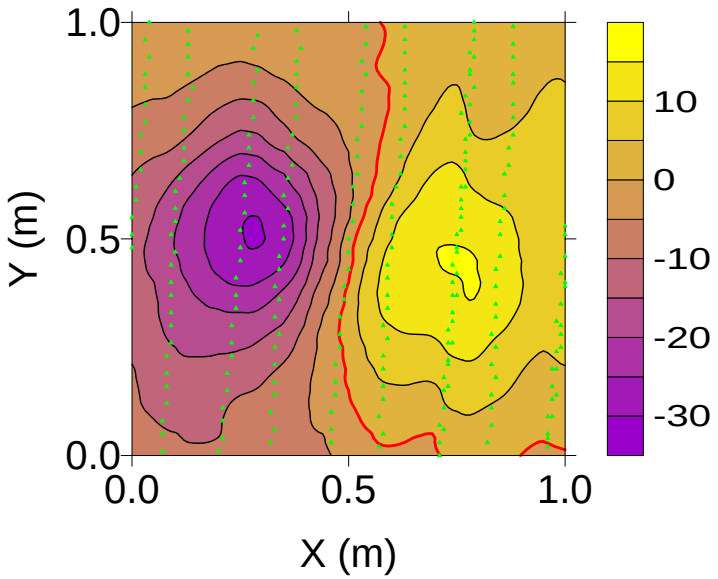

Figure N4. The B10 anomaly of a BDU submunition (L_D = 1.0 m) and 251 flagged nodes (green triangles) nearest to magnetometer stations.

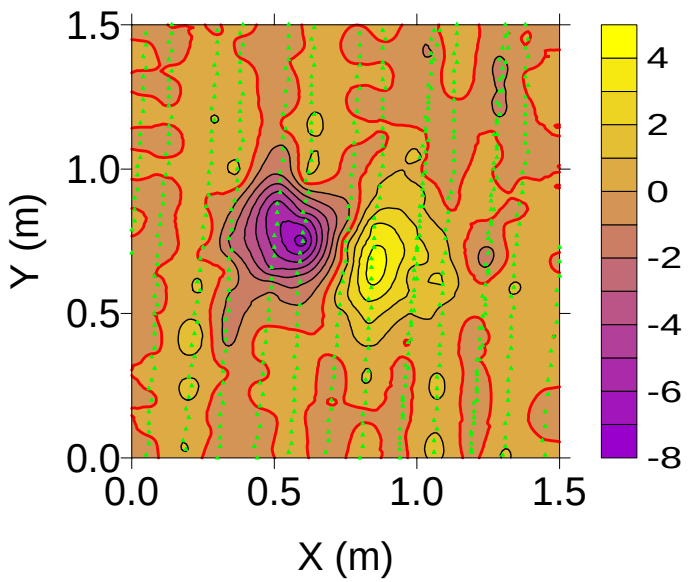

Figure N5. The EAGGN filtered B10 anomaly of a BDU submunition (L_F = 0.5 m, L_D = 1.5 m) and 550 flagged nodes (green triangles) nearest to magnetometer stations. The central 1-m x 1-m co-centered portion of this data window was used for GGN IIF inversion.

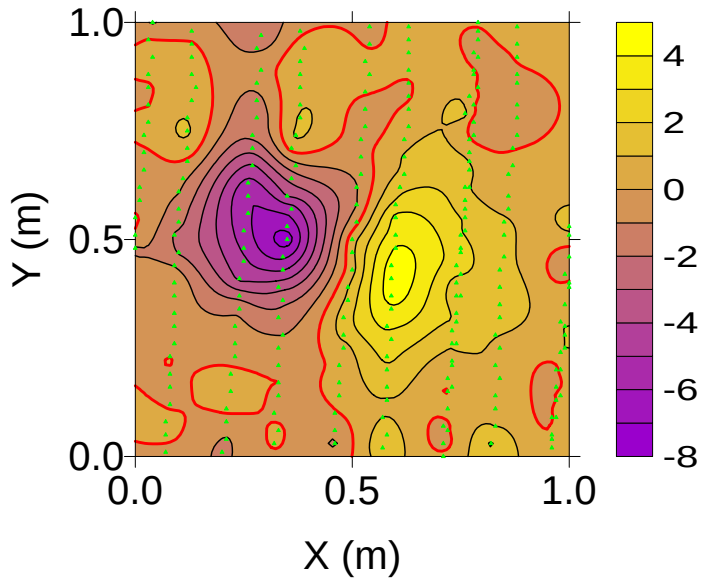

Figure N6. The EAGGN filtered B10 anomaly (L_F = 0.5 m, L_D = 1 m) and 251 flagged nodes (green triangles) nearest to magnetometer stations.

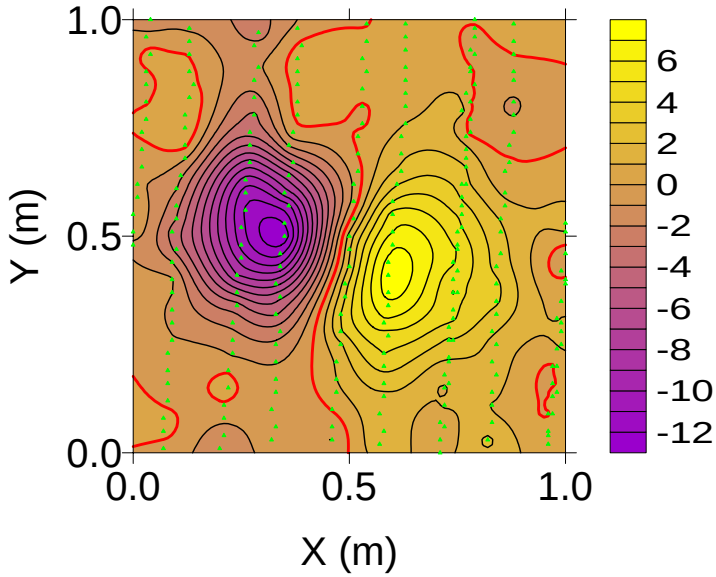

Figure N7. The EAGGN filtered B10 anomaly (L_F = 0.75 m, L_D = 1 m) and 251 flagged nodes (green triangles) nearest to magnetometer stations.

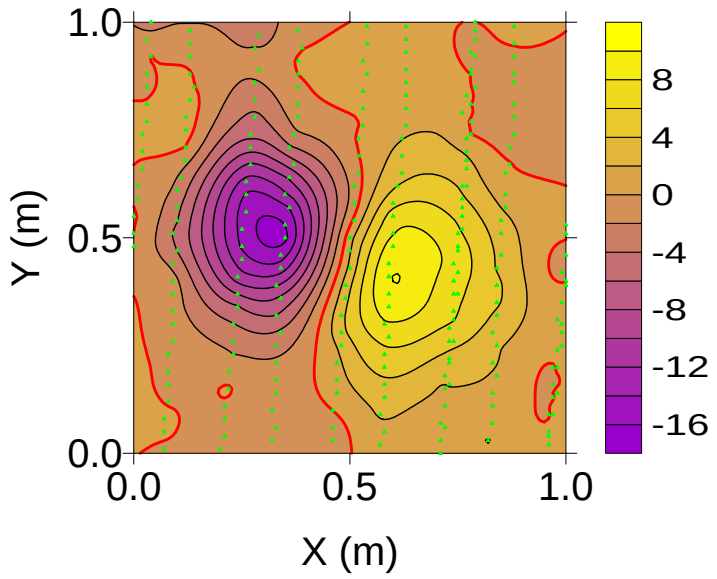

Figure N8. The EAGGN filtered B10 anomaly (L_F = 1 m, L_D = 1 m) and 251 flagged nodes (green triangles) nearest to magnetometer stations.

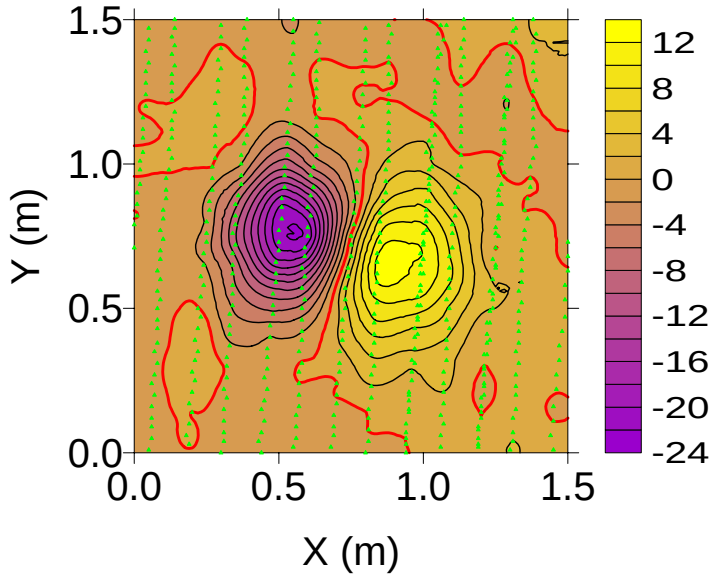

Figure 9. The EAGGN filtered B10 anomaly (L_F = 1.5 m, L_D = 1.5 m) and 550 flagged nodes (green triangles) nearest to magnetometer stations.

Table 4. B10 dipole (X,Y,Z) and target's center (X_C,Y_C,Z_C) UTM coordinates. X_R = 402000 m; Y_R = 4369000 m. Δ_C and E_Z are absolute horizontal and relative vertical displacements of dipole from target's center. [Δx = grid interval; L_D = data window size; L_F = filter size.]

Job	Δx cm	L_D m	L_F m	†	$X-X_R$ m	$Y-Y_R$ m	$X-X_C$ cm	$Y-Y_C$ cm	Δ_C cm	Z cm	$Z-Z_C$ cm	E_Z* %
1	1	1	n/a	AB	800.88	580.68	4	-4	6	16	3	8
2	1	1	n/a	B	800.88	580.68	4	-4	6	15	2	5
3	1	1	n/a	A	800.89	580.68	5	-4	6	18	5	13
4	1	1	n/a		800.90	580.67	6	-5	8	17	4	11
5	1	1	0.5	G	800.86	580.71	3	-1	3	17	4	11
6	1	1	0.5	E	800.85	580.70	2	-1	2	17	4	11
7	1	1	0.75	E	800.86	580.71	3	-1	3	17	4	11
8	1	1	1	E	800.87	580.71	4	-1	4	16	3	8
9	1	1.5	n/a	AB	800.88	580.67	4	-5	7	18	5	13
10	1	1.5	n/a	B	800.87	580.66	4	-5	7	16	3	8
11	1	1.5	n/a	A	800.90	580.67	6	-5	8	16	3	8
12	1	1.5	n/a		800.90	580.67	6	-5	8	15	2	5
13	1	1.5	0.5	E	800.86	580.71	3	-1	3	16	3	8
14	1	1.5	0.75	E	800.86	580.71	3	-1	3	16	3	8
15	1	1.5	1	E	800.88	580.70	4	-2	4	15	2	5
16	1	1.5	1.25	E	800.88	580.70	4	-2	4	15	2	5
17	1	1.5	1.5	E	800.89	580.69	5	-3	6	15	2	5

† flag-node and IIGE unless noted: **A** = all-node; **B** = IIBE. **E** = EAGGN ($L_{FD} = L_D$).
G = GGN ($L_{FD} > L_D$).

* $E_Z = (Z-Z_C)/(Z_C+H_M)$; magnetometer elevation, H_M = 0.25 m

Table 5. B10 dipole parameters: θ = deviation angle (from earth's field); δ = dipole declination; Ψ =dipole inclination; M = dipole moment. Gx, Gy = gradient components; B = dc bias estimate; R = correlation coefficient. [Δx = grid interval; L_D = data window size; L_F = filter size.]

Job	Δx cm	L_D m	L_F m	†	θ deg	δ deg	Ψ deg	M mA•m^2	Gx nT/m	Gy nT/m	B nT	R
1	1	1	n/a	AB	90.7	68.5	-4.6	19.0	n/a	n/a	-2.13	0.981
2	1	1	n/a	B	90.6	68.5	-4.8	17.9	n/a	n/a	-2.01	0.982
3	1	1	n/a	A	83.9	63.6	0.4	22.4	-1.63	7.71	-2.43	0.989
4	1	1	n/a		82.8	64.3	1.9	21.1	-1.45	7.11	-2.58	0.988
5	1	1	0.5	G	84.8	60.5	-1.8	21.7	-0.23	0.08	-0.02	0.920
6	1	1	0.5	E	86.8	59.4	-4.4	21.3	0.09	-0.08	0.05	0.928
7	1	1	0.75	E	85.5	59.9	-2.8	21.6	0.09	-0.14	0.00	0.972
8	1	1	1	E	84.3	60.9	-1.1	19.9	0.05	-0.08	-0.07	0.982
9	1	1.5	n/a	AB	94.9	75.7	-6.6	20.8	n/a	n/a	-1.92	0.926
10	1	1.5	n/a	B	94.5	74.7	-6.4	18.7	n/a	n/a	-1.90	0.926
11	1	1.5	n/a	A	83.5	64.7	1.3	18.9	0.68	7.50	-2.21	0.979
12	1	1.5	n/a		83.3	64.2	1.3	18.0	0.55	7.37	-2.15	0.979
13	1	1.5	0.5	E	85.3	61.1	-2.1	19.6	-0.05	-0.14	0.00	0.872
14	1	1.5	0.75	E	86.1	60.6	-3.1	19.7	-0.10	-0.12	0.01	0.942
15	1	1.5	1	E	84.5	61.6	-1.0	18.2	-0.06	-0.12	-0.02	0.965
16	1	1.5	1.25	E	84.8	61.6	-1.3	18.3	-0.06	-0.13	-0.05	0.973
17	1	1.5	1.5	E	83.1	62.5	0.8	18.3	-0.06	-0.07	-0.13	0.977

† flag-node and IIGE unless noted: **A** = all-node; **B** = IIBE. **E** = EAGGN ($L_{FD} = L_D$).
G = GGN ($L_{FD} > L_D$).

Table 7. B10 data windows: grid interval, Δx; absolute and relative window size, L_D, R_L; displacement of window's center from target's center, X_W-X_C, Y_W-Y_C; number of nodes along the x-and y-axes, N_X, N_Y; and the number and proportion of nodes flagged for inversion N_F, R_F.

Jobs	Δx (cm)	L_D (m)	R_L†	X_W-X_C (cm)	Y_W-Y_C (cm)	N_X	$N_X \cdot N_Y$	N_F	R_F (%)
1, 3	1	1	2.6	1	1	101	10201	10201	100
2, 4-8	1	1	2.6	1	1	101	10201	251	2.5
9, 11	1	1.5	3.9	1	1	151	22801	22801	100
10, 12-17	1	1.5	3.9	1	1	151	22801	550	2.4

†$R_L = L_D/(Z_C+H_M)$; depth to target center, Z_C = 13 cm; magnetometer height, H_M = 25 cm.

Appendix O
Target A02 (60 mm M49 mortar round)

Target A02 is a 60-mm, 1.3-kg M49 mortar round, which the AEC emplaced nose-up at a slight inclination of –9 deg and depth to center of 61 cm (Figure O1, Table O1). Figures O2-O11 plot the A02 anomaly and results of inversion jobs. Conclusions are derived from 35 jobs (Tables O2-O4):

Appendix O Figures

O1. Target A02: 60-mm M49 mortar round …….……. 234
O2. Regional setting of A02 anomaly ……..…… 235
O3. A02 anomaly and 612 flagged nodes in 2.5-m window ……. 235
O4. A02 inverse-model dipole's field plus IIBE field (job 19) ……...…….. 236
O5. Residual field: observed field minus sum of the A02 dipole's field plus IIBE field ….. 236
O6. A02 anomaly in a 2.5 x 2-m data window and 481 nodes ……..…… 237
O7. A02 anomaly and 309 nodes used on single-swath inversions ……..…. 237
O8. EAGGN filtered single-swath A02 anomaly (LF = 0.75 m) …….……. 238
O9. EAGGN filtered single-swath A02 anomaly (LF = 1.25 m) …….……. 238
O10. EAGGN filtered single-swath A02 anomaly (LF = 1.75 m) ……. 239
O11. A02 anomaly and nodes used in single- and multi-swath inversions peak-only jobs …... 239

Appendix O Tables

O1. Ground truth for target A02 ……...……. 134
O2. Dipole positions for anomaly A02 inversions ……...…..…… 240
O3. Dipole parameters for anomaly A02 inversions …….…… 241
O4. A02 data window parameters …….. 242

Figure O1. Target A02; 60 mm M49 mortar round.

Table O1. Ground truth parameters for Target A02.

Description	M49 Mortar Round
Material	Cast Polymethacrylimide and Forged Steel
Length, L_T	240 mm
Diameter, D_T	60 mm
Weight	1.315 kg
Grid azimuth, Φ_T	146 deg
Inclination, Ψ_T	-9 deg (nose up, subhorizontal)
Depth, Z_C	61 cm
UTM northing, Yc	4369585.621 m
UTM easting, X_C	402816.207 m
Ratio of depth below magnetometer to target length, R_{DL} †	3.6
Vertical projection of target's length, L_V (= $L_T \sin \Psi_T$)	-4 cm
Horizontal projection of target's length, L_H (= $L_T \cos \Psi_T$)	24 cm
Nose-from-center offsets (Xn-Xc, Yn-Yc, Zn-Zc)	(8, -8, -2) cm

† $R_{DL} = (Z_C+H_M)/L_T$; magnetometer height, $H_M = 0.25$ m

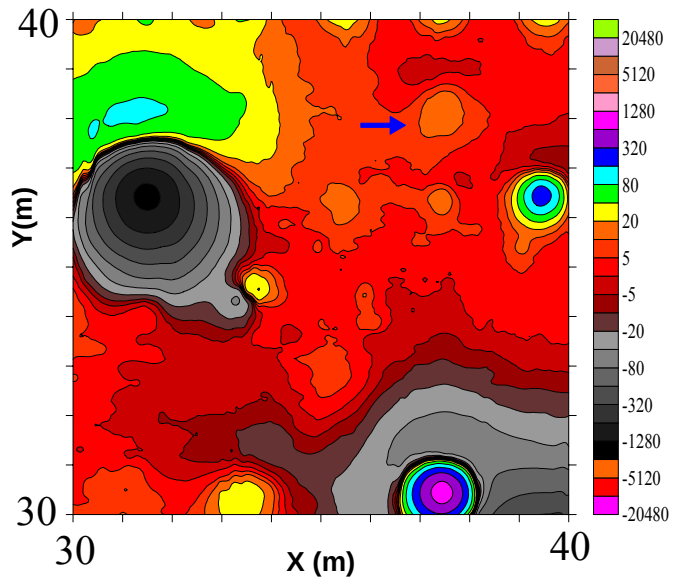

Figure O2. Regional setting of the A02 anomaly (blue arrow). The magnetic field contours are at zero and $\pm 2^n \cdot 5$ nT, where n is a non-negative integer.

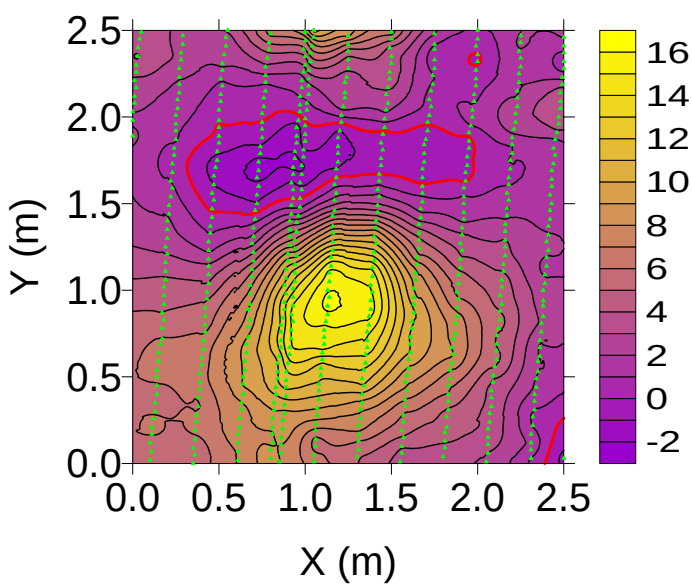

Figure O3. The A02 anomaly and 612 flagged nodes (green triangles) nearest to magnetometer stations ($\Delta x = \Delta y = 1$ cm). The zero contour (red) encloses a magnetic low north of the target. The edge of an anomaly to the north is of a metallic sphere at the edge of the APG BTA. For IIBE inversion of the flagged data (job 19), Δ_C is 6 cm, $(Z\text{-}Z_C)$ is –7 cm, θ is 31.0 deg, and Ψ is 36.8 deg. Similarly, for all-node IIBE inversion (job 18), Δ_C is 5 cm, $(Z\text{-}Z_C)$ is –7 cm, θ is 31.0 deg, and Ψ is 36.7 deg. The sub-horizontal mortar shell is sufficiently deep (Z_C = 61 cm) and interpolation to all nodes may preserve the anomaly shape. The contour interval is 1 nT.

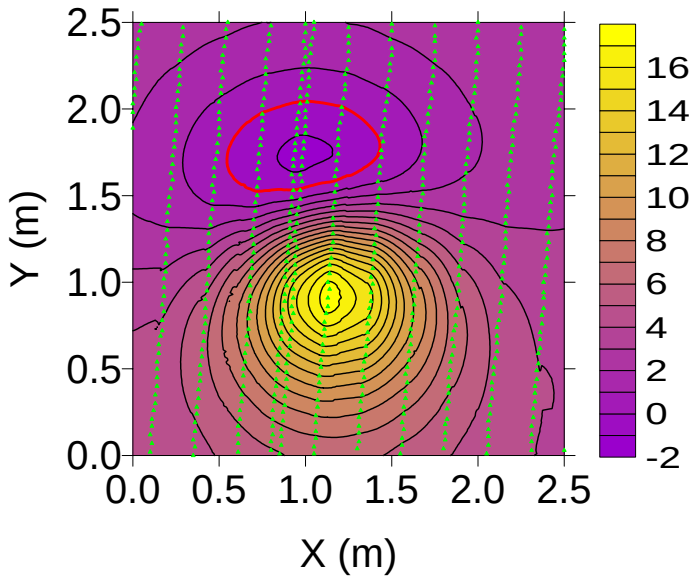

Figure O4. The A02 inverse-model dipole's field plus IIBE field (job 19). This inversion used 612 flagged nodes (green triangles). For this inversion, Δ_C is 6 cm, $(Z-Z_C)$ is -7 cm, θ is 31.0 deg, and Ψ is 36.8 deg. Excluding the anomaly of the metallic sphere north of target A02 improves the inversion. The zero contour is red and the contour interval is 1 nT.

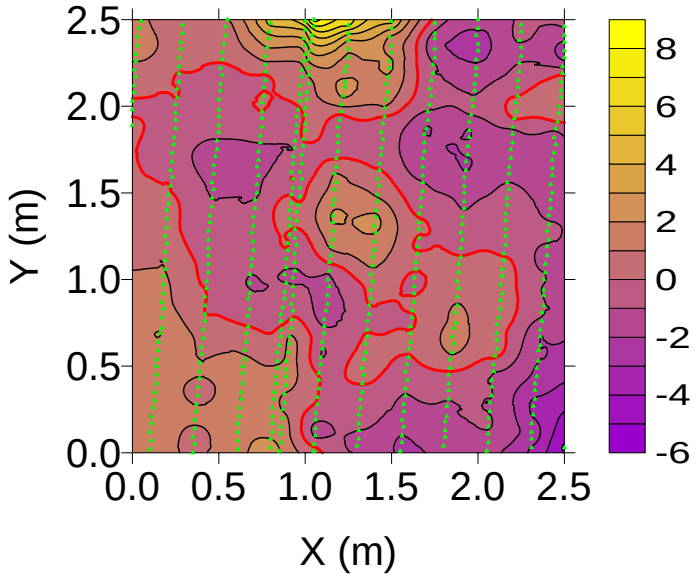

Figure O5. The residual field equal to the observed field minus the sum of the A02 inverse-model dipole's field plus IIBE field (job 19). This inversion used 612 flagged nodes (green triangles). The large positive residual on the north edge of the window is the result of the field of a metallic sphere on the edge of the APG BTA. Jobs 22-35 eliminated the nodes for Y > 2. The zero contour is red and the contour interval is 1 nT.

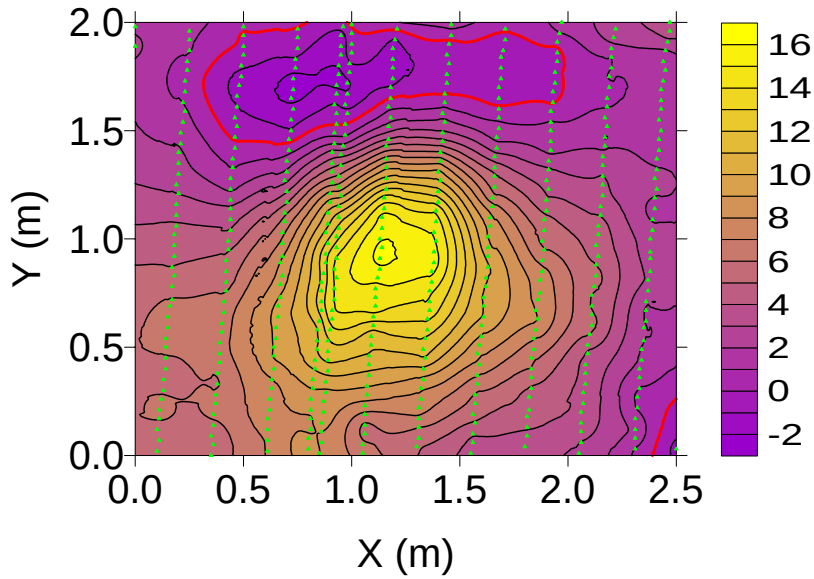

Figure O6. The A02 anomaly in a 2.5 x 2-m data window and 481 nodes (green triangles) used in jobs 22-35. For IIBE inversion (job 22), Δ_C is 6 cm, $(Z-Z_C)$ is 2 cm, θ is 31.5 deg, and Ψ is 36.3 deg. For IIGE inversion (job 23), Δ_C is 6 cm, $(Z-Z_C)$ is 2 cm, θ is 37.7 deg, and Ψ is 31.6 deg. The zero contour is red and the contour interval is 1 nT.

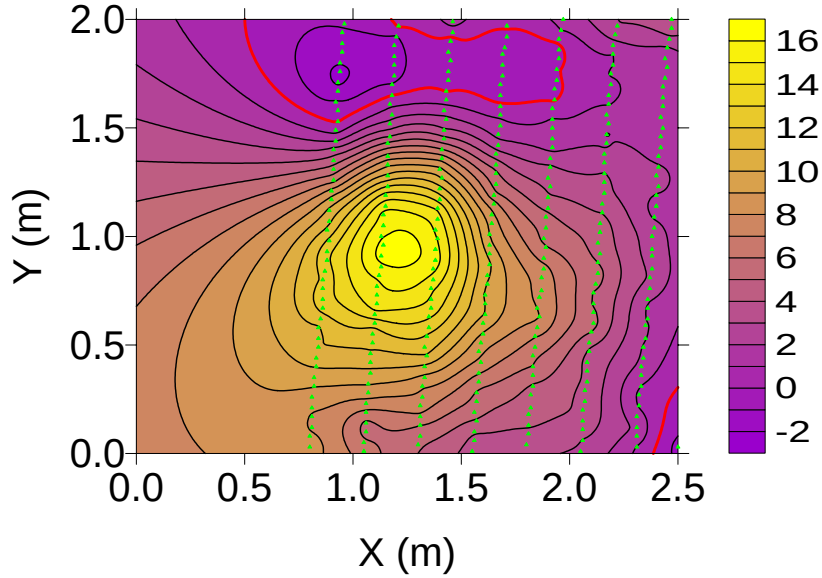

Figure O7. The A02 anomaly in the data window used in inversion jobs 26-27. These inversions used 309 flagged nodes (green triangles) from a single swath of the MTADS cart. For IIBE inversion (job 26), Δ_C is 6 cm, $(Z-Z_C)$ is 5 cm, θ is 25.4 deg, and Ψ is 43.2 deg. For IIGE inversion (job 27), Δ_C is 7 cm, $(Z-Z_C)$ is 4 cm, θ is 42.0 deg, and Ψ is 25.5 deg. The results for IIGE inversion differ significantly from those of IIBE inversion. The zero contour is red and the contour interval is 1 nT.

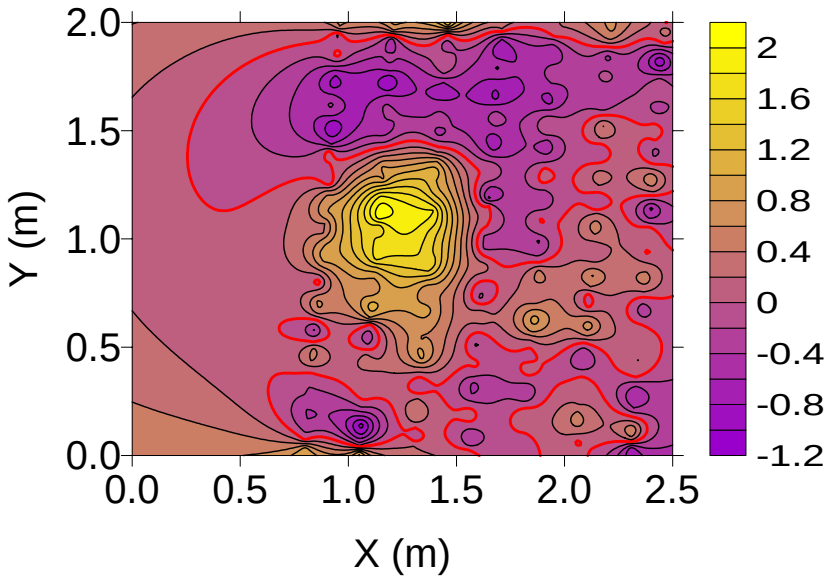

Figure O8. The EAGGN filtered single-swath A02 anomaly (L_F = 0.75 m) used in job 30. For this inversion, Δ_C is 5 cm, (Z-Z_C) is 3 cm, θ is 23.2 deg, and Ψ is 44.2 deg. For a larger filter (L_F = 1 m; job 31), Δ_C is 7 cm, (Z-Z_C) is 4 cm, θ is 25.2 deg, and Ψ is 42.2 deg. IIF inversion jobs 30-35, with $0.75 \leq LF \leq 2$ m, yield the following: $3 \leq \Delta_C \leq 5$ cm, $2 \leq (Z\text{-}Z_C) \leq 3$ cm, $23.2 \leq \theta \leq 28.8$ deg, and $38.5 \leq \Psi \leq 44.2$ deg. The zero contour is red and the contour interval is 0.2 nT.

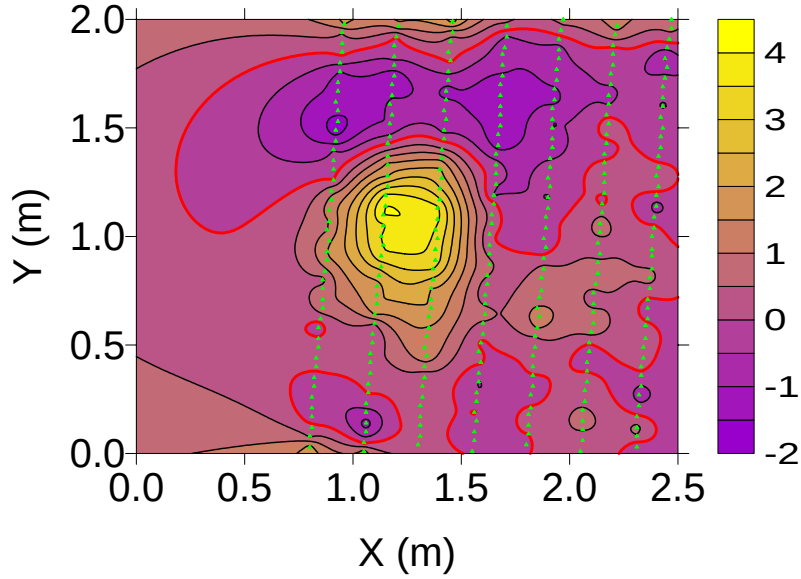

Figure O9. The EAGGN filtered single-swath A02 anomaly (L_F = 1.25 m) and 308 nodes (green triangles) used in job 32. For this inversion, Δ_C is 4 cm, (Z-Z_C) is 3 cm, θ is 26.3 deg, and Ψ is 41.0 deg. For a larger filter (L_F = 1.5 m; job 33), the dipole position is unchanged, θ is 27.6 deg, and Ψ is 39.6 deg. The zero contour is red and the contour interval is 0.5 nT.

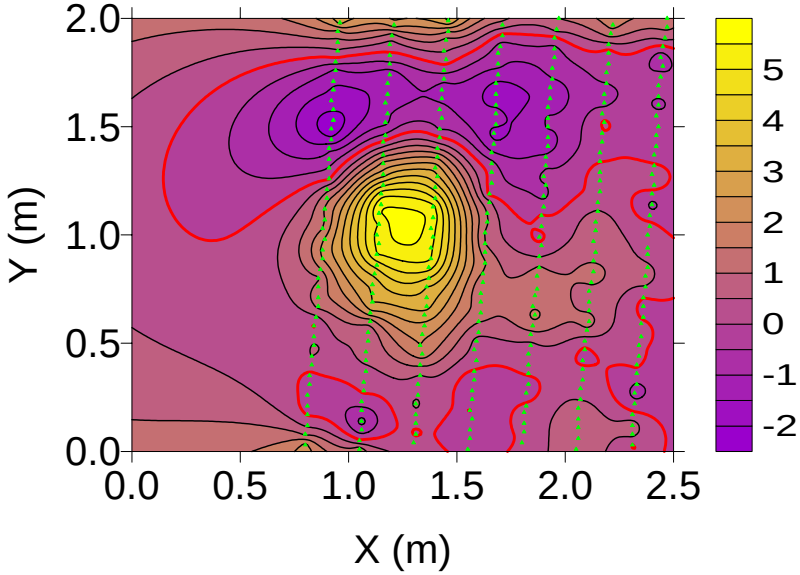

Figure O10. The EAGGN filtered single-swath A02 anomaly (L_F = 1.75 m) and 308 nodes (green triangles) used in job 34 for which Δ_C is 3 cm, (Z-Z_C) is 2 cm, θ is 27.4 deg, and Ψ is 39.9 deg. For L_F equal to 2 m (job 35), the dipole position is unchanged, θ is 28.8 deg, and Ψ is 38.5 deg. The zero contour is red and the contour interval is 0.5 nT.

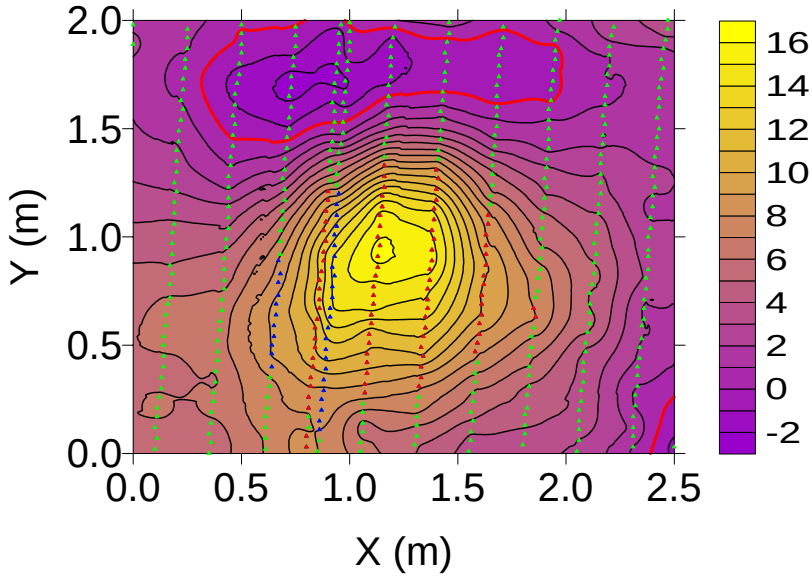

Figure O11. The A02 anomaly. Jobs 24-25 used 124 nodes (red and blue triangles) with values exceeding 8 nT. For IIBE (job 24) and IIGE (job 25), (Z-Z_C) are –11 and –4 cm, and θ are 40.2 and 32.1 deg, respectively. Single-swath jobs 28-29 used 89 nodes (red triangles). For IIBE and IIGE, (Z-Z_C) are –14 and –10 cm, and θ are 35.6 and 25.0 deg, respectively. These results differ significantly from those of IIF inversions (jobs 30-35). The zero contour is red and the contour interval is 1 nT.

Table O2. A02 dipole (X,Y,Z) and target's center (X_C,Y_C,Z_C) UTM coordinates. X_R = 402000 m; Y_R = 4369000 m. Δ_C and E_Z are absolute horizontal and relative vertical displacements of dipole from target's center. [Δx = grid interval; L_D = data window size; L_F = filter size.]

Job	Δx cm	L_D m	L_F m	†	$X-X_R$ m	$Y-Y_R$ m	$X-X_C$ cm	$Y-Y_C$ cm	Δ_C cm	Z cm	$Z-Z_C$ cm	E_Z* %
1	1	2	n/a	AB	816.16	585.59	-5	-3	5	59	-2	-2
2	1	2	n/a	B	816.16	585.58	-5	-4	6	59	-2	-2
3	1	2	n/a	A	816.15	585.59	-6	-3	6	58	-3	-3
4	1	2	n/a		816.16	585.59	-5	-3	5	58	-3	-3
5	1	2	0.75	E	816.17	585.66	-4	4	5	56	-5	-6
6	1	2	1	E	816.17	585.65	-4	3	5	58	-3	-3
7	1	2	1.25	E	816.17	585.64	-4	2	4	59	-2	-2
8	1	2	1.5	E	816.17	585.64	-4	2	4	60	-1	-1
9	1	2	1.75	E	816.17	585.64	-4	2	4	60	-1	-1
10	1	2	2	E	816.16	585.63	-4	0	4	61	0	0
11	5	2.5	n/a	AB	816.17	585.59	-4	-3	5	54	-7	-8
12	5	2.5	n/a	B	816.17	585.59	-4	-3	5	54	-7	-8
13	5	2.5	n/a	A	816.16	585.64	-5	1	5	62	1	1
14	5	2.5	n/a		816.12	585.58	-9	-4	10	63	2	3
15	5	2.5	1.0	E	816.16	585.64	-5	1	5	61	0	0
16	5	2.5	1.5	E	816.16	585.64	-5	1	5	61	0	0
17	5	2.5	2.0	E	816.16	585.64	-5	1	5	62	1	1
18	1	2.5	n/a	AB	816.16	585.59	-5	-3	5	54	-7	-8
19	1	2.5	n/a	B	816.16	585.58	-5	-4	6	54	-7	-8
20	1	2.5	n/a	A	816.14	585.61	-7	-1	7	61	0	0
21	1	2.5	n/a		816.14	585.60	-7	-2	7	61	0	0
22	1	2.5#	n/a	B	816.15	585.60	-6	-2	6	63	2	2
23	1	2.5#	n/a		816.14	585.62	-6	0	6	63	2	2
24	1	2.5#	n/a	B▲$_8$	816.08	585.52	-13	-10	16	50	-11	-13
25	1	2.5#	n/a	▲$_8$	816.12	585.56	-9	-7	11	57	-4	-5
26	1	2.5#	n/a	B§	816.16	585.58	-5	-4	6	66	5	6
27	1	2.5#	n/a	§	816.19	585.69	-2	7	7	65	4	5
28	1	2.5#	n/a	B▲$_8$§	816.14	585.55	-7	-7	10	47	-14	-16
29	1	2.5#	n/a	▲$_8$ §	816.19	585.56	-2	-6	7	51	-10	-12
30	1	2.5#	0.75	E §	816.22	585.67	1	4	5	64	3	3
31	1	2.5#	1.0	E §	816.22	585.67	1	4	5	64	3	3
32	1	2.5#	1.25	E §	816.21	585.66	0	4	4	64	3	3
33	1	2.5#	1.50	E §	816.21	585.66	0	4	4	64	3	3
34	1	2.5#	1.75	E §	816.21	585.65	0	3	3	63	2	2
35	1	2.5#	2.00	E §	816.21	585.65	0	3	3	63	2	2

† flag-node and IIGE unless noted: **A** = all-node; **B** = IIBE. **E** = EAGGN (L_{FD} = L_D).
▲$_8$ = peak-only (H>8 nT) § = single-swath
* $E_Z = (Z-Z_C)/(Z_C+H_M)$; magnetometer elevation, H_M = 0.25 m
# data excluded from the northern 0.5 m portion of the 2.5 x 2.5 m window used in jobs 18-21.

Table O3. M08 dipole parameters: θ = deviation angle (from earth's field); δ = dipole declination; Ψ =dipole inclination; M = dipole moment. Gx, Gy = gradient components; B = dc bias estimate; R = correlation coefficient. [Δx = grid interval; L_D = data window size; L_F = filter size.]

Job	Δx cm	L_D m	L_F m	†	θ deg	δ deg	Ψ deg	M mA•m^2	Gx nT/m	Gy nT/m	B nT	R
1	1	2	n/a	AB	30.7	0.3	37.2	60.7	n/a	n/a	3.12	0.991
2	1	2	n/a	B	30.3	0.8	37.7	60.7	n/a	n/a	3.15	0.992
3	1	2	n/a	A	33.9	8.9	35.4	59.4	-0.99	-0.17	3.18	0.993
4	1	2	n/a		33.5	7.1	35.5	59.7	-0.92	-0.09	3.26	0.993
5	1	2	0.75	E	34.2	10.7	35.5	52.6	-0.03	-0.10	0.00	0.813
6	1	2	1	E	33.0	9.8	36.5	58.8	-0.04	-0.04	-0.03	0.884
7	1	2	1.25	E	31.3	8.3	38.0	61.8	-0.07	-0.14	-0.07	0.922
8	1	2	1.5	E	31.6	6.5	37.4	65.3	-0.09	-0.11	-0.12	0.941
9	1	2	1.75	E	32.1	4.9	36.6	65.6	-0.07	-0.06	-0.13	0.951
10	1	2	2	E	32.0	5.5	36.7	68.5	-0.05	-0.01	-0.16	0.956
11	5	2.5	n/a	AB	29.4	-3.0	38.3	50.8	n/a	n/a	3.40	0.971
12	5	2.5	n/a	B	30.4	-2.7	37.2	51.2	n/a	n/a	3.45	0.937
13	5	2.5	n/a	A	40.2	7.8	28.8	73.8	-1.53	0.86	3.41	0.982
14	5	2.5	n/a		38.3	12.6	31.7	74.9	-1.53	0.87	3.33	0.959
15	5	2.5	1.0	E	32.6	9.1	36.8	67.7	0.07	-0.06	-0.02	0.799
16	5	2.5	1.5	E	33.4	7.4	35.6	68.1	0.07	-0.11	-0.05	0.888
17	5	2.5	2.0	E	34.6	5.4	34.1	71.6	0.05	-0.10	-0.09	0.919
18	1	2.5	n/a	AB	31.0	-2.4	36.7	51.3	n/a	n/a	3.41	0.974
19	1	2.5	n/a	B	31.0	-1.9	36.8	51.3	n/a	n/a	3.48	0.975
20	1	2.5	n/a	A	39.5	10.0	29.8	70.8	-1.51	0.71	3.37	0.984
21	1	2.5	n/a		38.6	9.7	30.8	70.3	-1.44	0.76	3.45	0.983
22	1	2.5 #	n/a	B	31.5	-1.1	36.3	70.1	n/a	n/a	2.86	0.988
23	1	2.5 #	n/a		37.7	8.9	31.6	73.7	-1.39	0.23	3.00	0.993
24	1	2.5 #	n/a	B ▲$_8$	40.2	28.5	34.2	36.2	n/a	n/a	5.68	0.999
25	1	2.5 #	n/a	▲$_8$	35.6	28.4	39.3	51.1	-1.35	-1.52	4.43	0.999
26	1	2.5 #	n/a	B §	25.4	3.6	43.2	77.0	n/a	n/a	1.99	0.992
27	1	2.5 #	n/a	§	42.0	-4.2	25.5	81.6	-1.51	1.35	2.83	0.994
28	1	2.5 #	n/a	B▲$_8$§	32.1	14.4	38.9	29.3	n/a	n/a	5.99	0.999
29	1	2.5 #	n/a	▲$_8$§	25.0	15.1	46.4	34.2	-1.78	-1.05	5.30	0.999
30	1	2.5 #	0.75	E §	23.2	-16.5	44.2	72.1	0.07	-0.06	-0.01	0.812
31	1	2.5 #	1	E §	25.2	-16.4	42.2	72.3	0.10	-0.08	0.01	0.876
32	1	2.5 #	1.25	E §	26.3	-14.1	41.0	72.3	0.09	-0.09	0.02	0.908
33	1	2.5 #	1.5	E §	27.6	-13.4	39.6	72.4	0.08	-0.08	0.03	0.928
34	1	2.5 #	1.75	E §	27.4	-11.3	39.9	68.8	0.07	-0.08	0.02	0.938
35	1	2.5 #	2	E §	28.8	-9.7	38.5	69.2	0.06	-0.06	0.00	0.946

† flag-node and IIGE unless noted: **A** = all-node; **B** = IIBE. **E** = EAGGN (L_{FD} = L_D).
▲$_8$ = peak-only (H>8 nT) § = single-swath
data excluded from the northern 0.5 m portion of the 2.5 x 2.5 m window used in jobs 18-21.

Table O4. M08 data windows: grid interval, Δx; absolute and relative window size, L_D, R_L; displacement of window's center from target's center, X_W-X_C, Y_W-Y_C; number of nodes along the x-and y-axes, N_X, N_Y; and the number and proportion of nodes flagged for inversion N_F, R_F.

Jobs	Δx (cm)	L_D (m)	R_L†	X_W-X_C (cm)	Y_W-Y_C (cm)	N_X	$N_X \bullet N_Y$	N_F	R_F (%)
1, 3	1	2	2.3	6	4	201	40401	40401	100
2, 4-10	1	2	2.3	6	4	201	40401	401	1.0
11, 13	5	2.5	2.9	7	6	51	2601	2601	100
12, 14-17	5	2.5	2.9	7	6	51	2601	579	22.3
18, 20	1	2.5	2.9	6	4	251	63001	63001	100
19, 21	1	2.5	2.9	6	4	251	63001	612	1.0
22-23	1	2.5#	2.9	#	#	251	50451	481	1.0
24-25	1	2.5#	2.9	# ▲	# ▲	251	50451	124	0.2
26-27	1	2.5#	2.9	# §	# §	251	50451	309	0.6
28-29	1	2.5#	2.9	# ▲§	# ▲§	251	50451	89	0.2
30-35	1	2.5#	2.9	# §	# §	251	50451	308	0.6

†$R_L = L_D/(Z_C+H_M)$; depth to target center, Z_C = 61 cm; magnetometer height, H_M = 0.25 m.
data excluded from the northern 0.5 m portion of the 2.5 x 2.5 m window used in jobs 18-21.
▲ data with values less than 8 nT were excluded
§ data from a single swath were input to inversion

APPENDIX P

The 40 x 40-m APG BTA MTADS Magnetic Field Data

Figure P1 shows the APG BTA magnetic field intensity in a 40 x 40-m window. A de-median filter was applied by others so the lowest-frequency components of the background field were already removed. These data were kriged with a 5-cm grid interval. Then the flag-node option was applied before input to the EAGGN filter (L_F = 2 m). The filtered data (Figure P2) can be compared to the to analytic signal, which is the amplitude of the 3D gradient of the magnetic field intensity (Figure P3).

The EAGGN is a high-pass filter that helps to separate anomalies in much the same way as the analytic signal; however, it preserves information about the orientation of the magnetic dipole sources and is therefore suitable for input to IIF full point-dipole inversion. In actual applications to inversion of UXO data such as in the APG BTA survey, a 1-cm grid interval was generally used 1 cm and the filter size was generally less than 2 m. In the four corners of the map area the actual size of the filter is reduced to 1 m x 1 m. Away from the corners and along the sides, the filter is reduced to a 2 x 1 m size automatically according to the zero-dc and gradient-nulling criteria. Along the north and west edges, parts of anomalies due to buried metallic spheres are apparent. These anomalies are preserved by the EAGGN filter without an obvious edge-effect artifact. It took 30 s to apply the EAGGN filter to the APG BTA data using a laptop computer with a processor speed of 1.6 GHz.

By appropriately transforming an un-gapped, zero-dc, symmetric filter, the edge-adaptive gapped gradient-nulling (EAGGN) filter used in Figure P1 was derived automatically. It adjusts to the locations of data points not filling a regular grid, to data for which the filter extends across a gap, and to data for which a fixed-dimension filter would extend beyond the bounds of the survey. In this particular application, the filter varied from point to point throughout the survey area because it was applied only to data at nodes nearest to measurement stations. The 5-cm grid interval is much smaller that the 25-cm separation of magnetometers on the MTADS cart. Thus about one fourth of the nodes were flagged for filter input and filtered values were only output at flagged nodes. The distortion of target signals is intentional and would be compensated for by IIF. Effects of measurement noise are more clearly indicated in EAGGN-filtered data (Figure P2) than in unfiltered data (Figure P1). The EAGGN filter will automatically reach across any gap that is less than half the filter's dimension in the direction transverse to the gap. GGN filters attenuate low spatial frequency geologic noise as well as overlapping fields of nearby UXO and clutter.

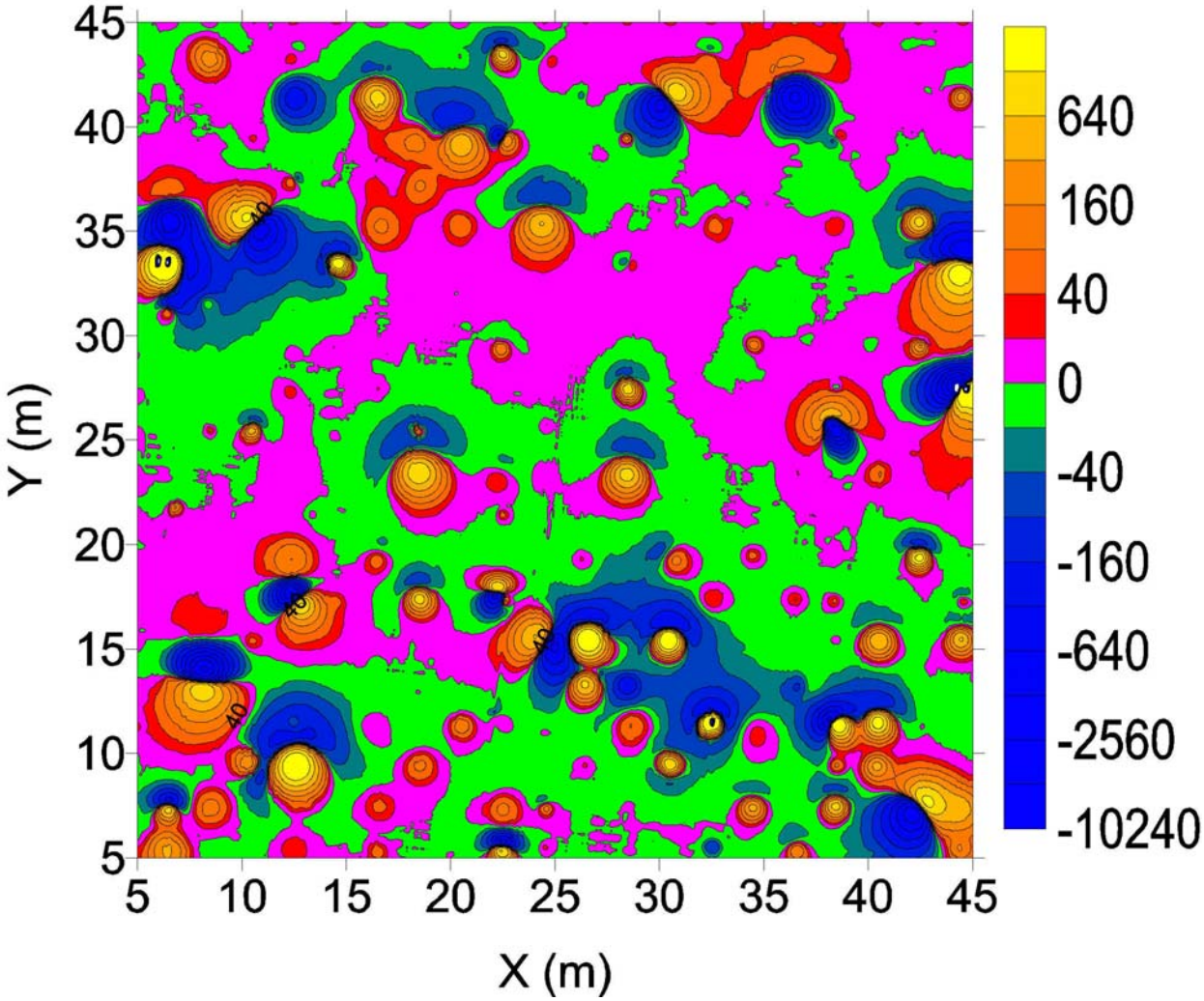

Figure P1. The APG BTA magnetic field intensity map in a 40 x 40-m data window. The anomalies occur where targets of UXO or metallic clutter were buried at nodes of a grid with 2-m intervals. Only some of the grid nodes have targets emplaced. Along the north edge of this data window, the partial anomalies of buried metallic spheres are visible. To the south of that lies the targets in row A and at the southern edge of the data window are the truncated anomalies of row T. The intermediate rows of targets are labeled alphabetically. Along the east edge of the data window the targets are also truncated. These lie in column 1 and the remaining north-south columns of emplaced targets are labeled numerically from east to west. The left and right edges are approximately along the magnetic north direction. The contours are at zero and $\pm 2^n \bullet 20$ nT, where n is a non-negative integer.

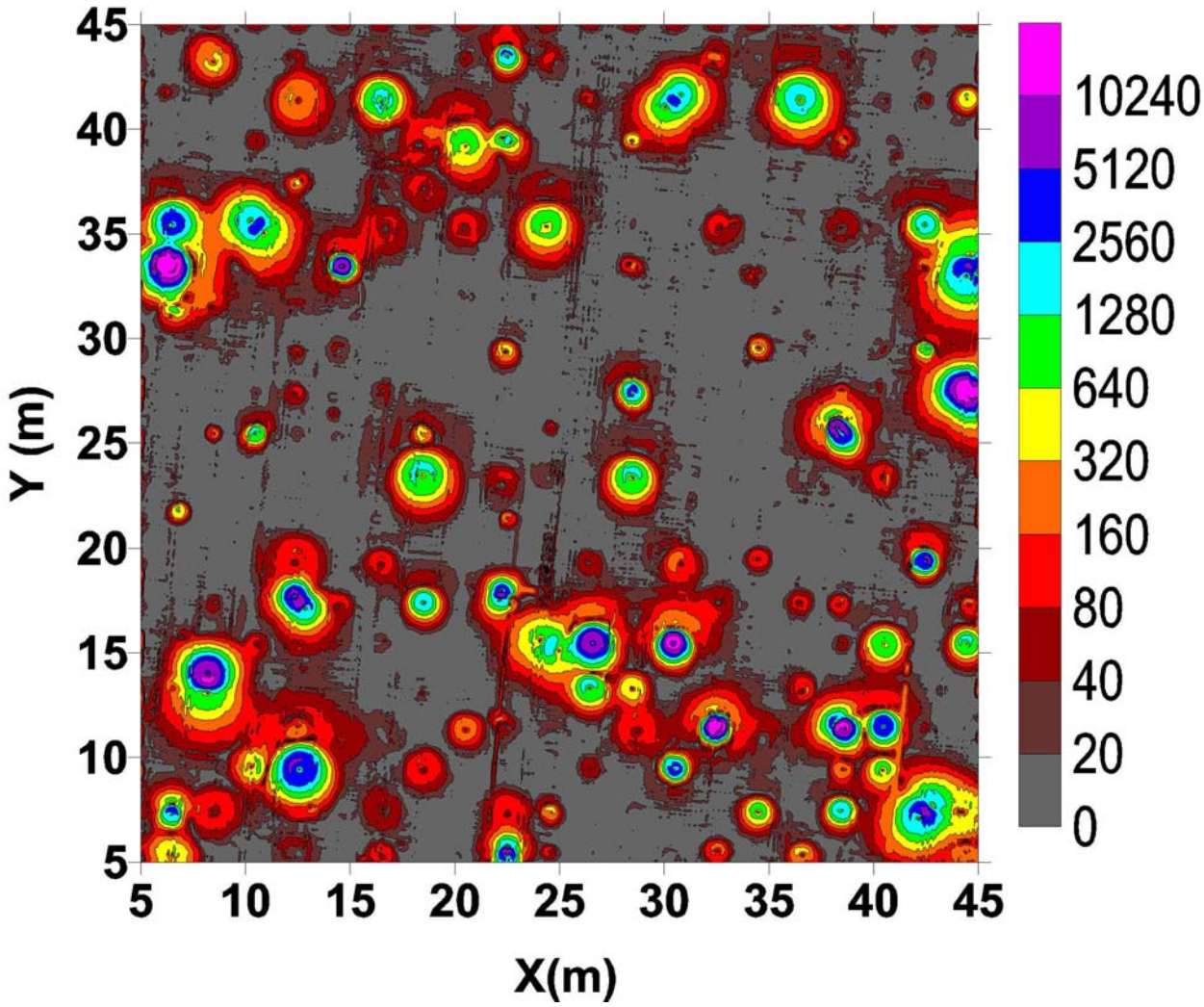

Figure P2. The APG BTA total gradient (analytic signal) map. The peaks lie above the buried targets. The analytic signal can be used to locate the target and to estimate the total dipole moment and depth of the magnetic dipole for that target. These estimated x-, y-, z- coordinates are then input as initial estimates to full dipole inversion of the original data. That inversion yields the orientation of the magnetic dipole as well as the location, depth and strength of the dipole. The linear patterns of noise trending slightly east of north define the direction of profiling. This swath overlap noise may result from positional or other errors or may even be artifacts of de-median filtering in places. The contours are at zero and $2^n \bullet 20$ nT/m, where n is a non-negative integer.

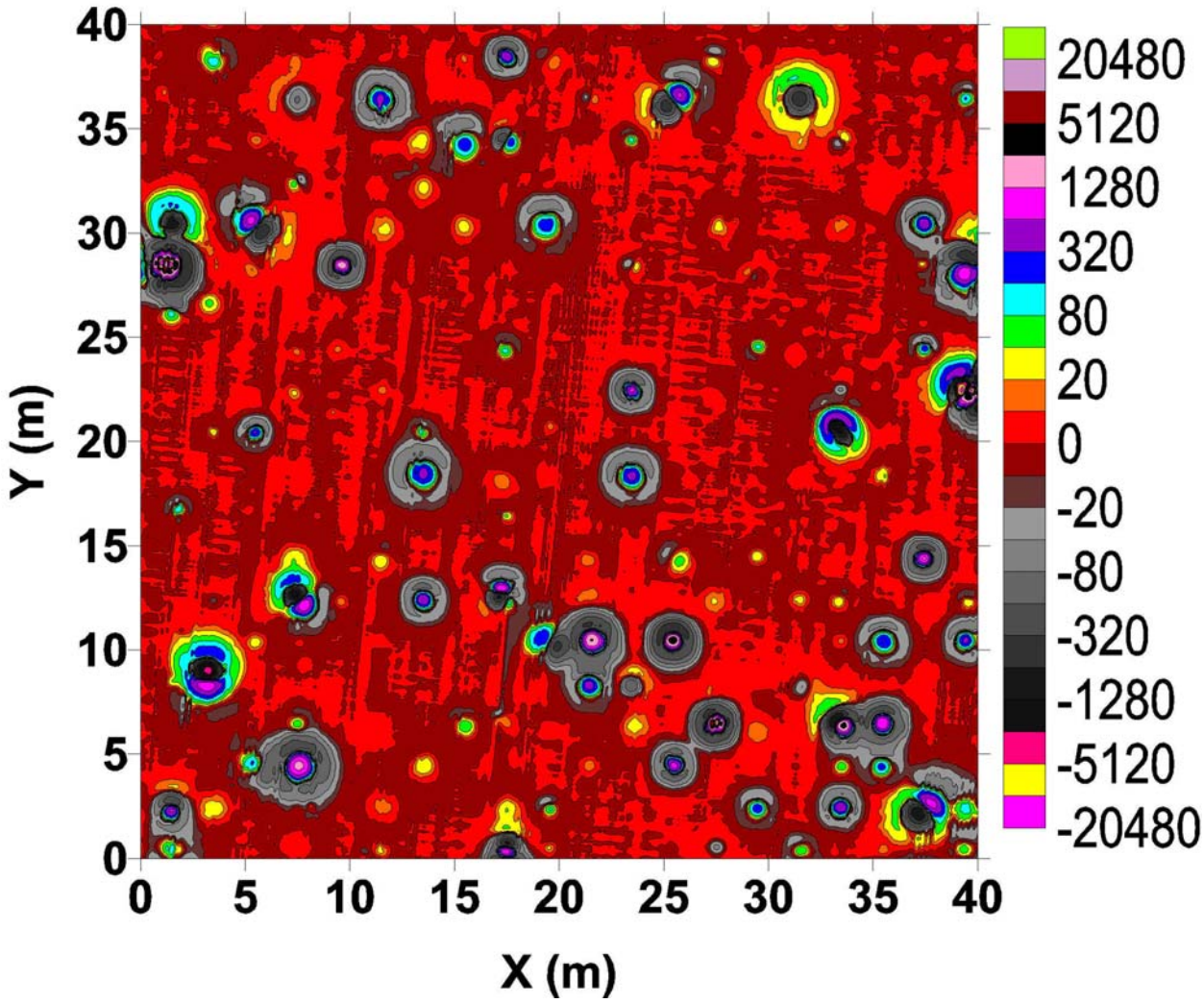

Figure P3. The EAGGN filtered APG BTA magnetic field intensity (LF = 2 m). The overall appearance is somewhat like the analytic signal and the partial anomalies along the north edge are clearly preserved. The anomalies are better separated than in the unfiltered data because the low-frequency tails of the anomalies are attenuated. A shorter filter was generally more useful in intra-inversion filtering (IIF). The swath overlap noise trending east of north is apparent as in the case of the analytic signal. The anomalies appear to be more compact and significantly distorted by the filter; however, the information about magnetic orientation is preserved and the filtered data can be input to full dipole inversion. The contours are at zero and ± 2n • 10 nT., where n is a non-negative integer.

Appendix Q

Anomaly Stack of Yuma Proving Ground Magnetic Anomalies

Figure Q1 shows the analytic signal of the MTADS magnetic field at the Yuma Proving Ground Calibration Area, UXO Standardized Test Site (STS), near Yuma, Arizona. The targets are buried in a regular grid. To enhance the value of such data for testing purposes the anomaly stack can take advantage of the principle of superposition for anomalies that are small relative to the total field of the earth. Figure Q2 shows the result of stacking data from two different parts of the calibration area. These stacked data can be used for testing inversions in a richer environment of seeded targets with greater overlap of anomalies thereby enhancing the value of the STS data.

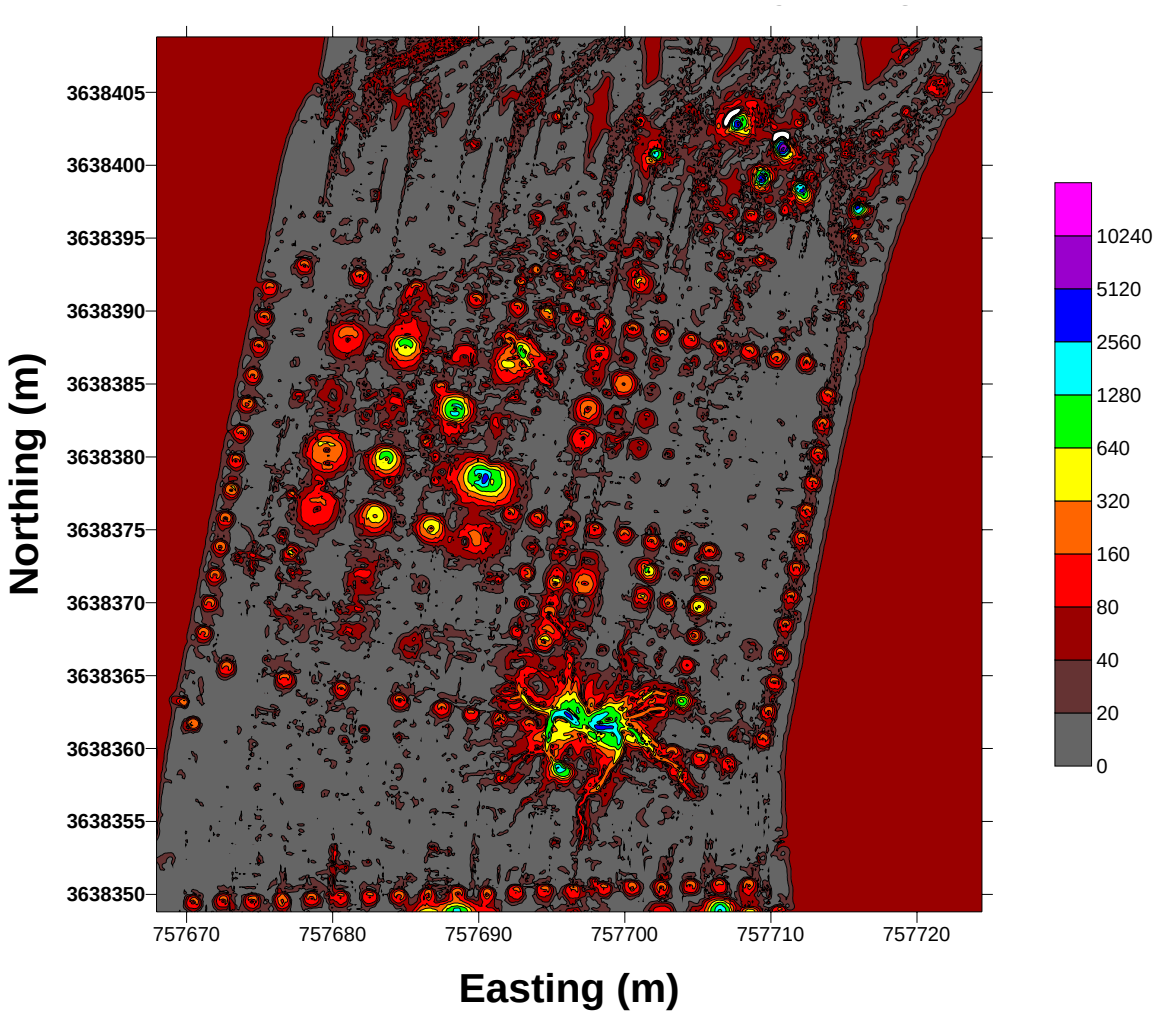

Figure Q1. The analytic signal of the magnetic field at the Yuma Proving Ground Calibration Area. The contour interval is 20 nT/m.

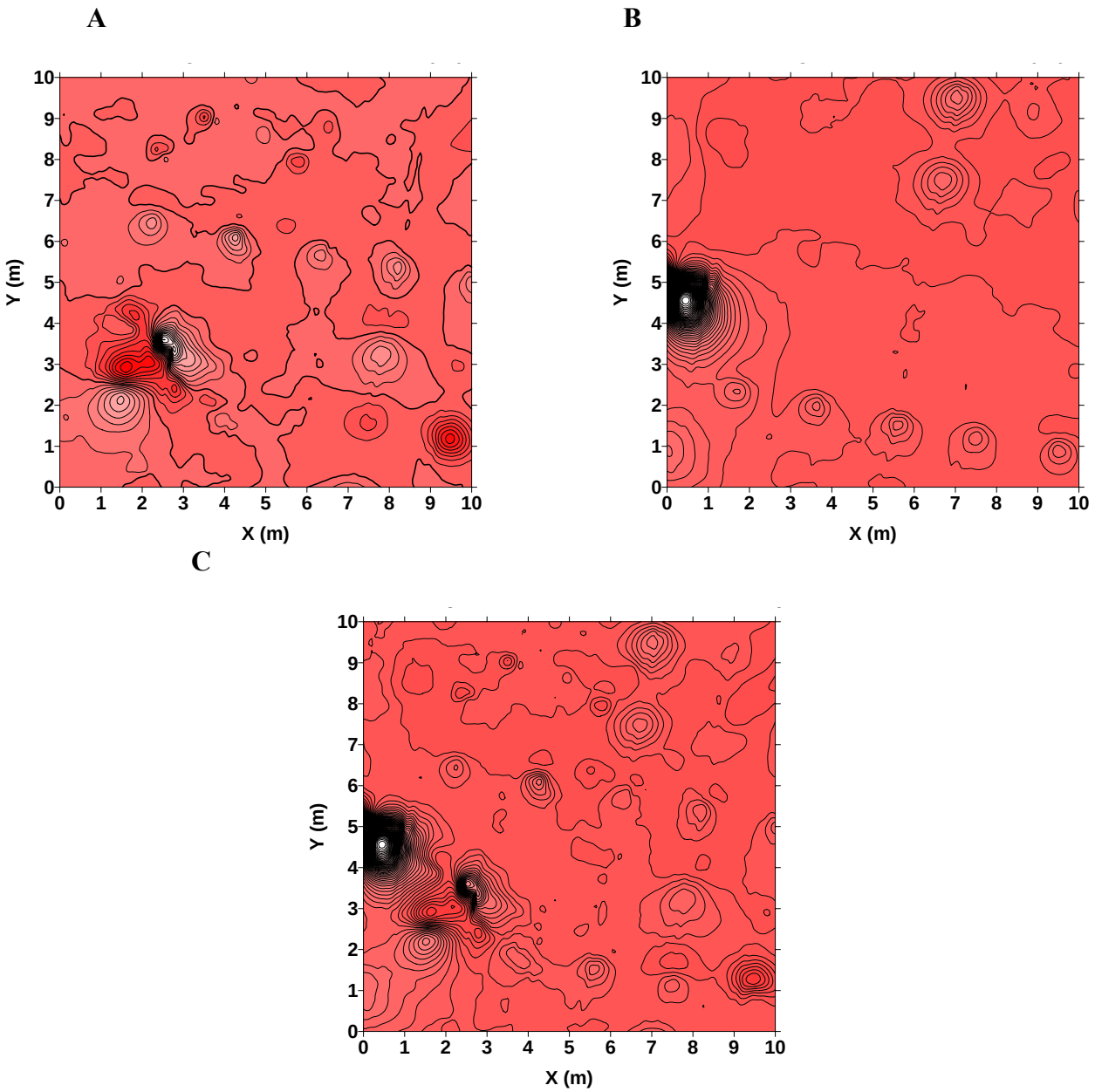

Figure Q2. A. anomalies in a 10 x 10-m area of the YPG Calibrations area. **B.** anomalies in another 10 x 10-m area. **C.** Stack of these two data sets. By the principal of superposition of anomalies, the stacked data are the same as if the sources of the background field and the seeded targets were combined. The stacked data thus provide a richer environment of targets for tests of inversions at essentially no cost. The contour interval is 20 nT.

Appendix R

List of Publications

Technical Report:

1. René, R. M., and Kim, K. Y., 2006, Intra-inversion filtering for improved inversion in unexploded ordnance (UXO) magnetic field surveys: Earth Resources Research and Development, Journal of the Research Institute for Development of Earth Resources, Kangwon National University, Chunchon, Kangwon-do, Korea, vol. 20, p. 17-33.

Scientific Papers published as Conference/Symposium Proceedings:

1. René, R. M., and Kim, K. Y., 2006, Magnetic field surveys for unexploded ordnance (UXO), magnetic field inversion, and intra-inversion filtering; Proceedings of 2006 RIDER International Symposium on 'Geophysical Methods for Shallow Targets', held on June 13, 2006 in Chunchon, Korea, Research Institute for Development of Earth Resources, Kangwon National University, Korea.; cd 10 pp

2. René, R. M., Kim, K. Y. and Park, C. H., 2006, Magnetic field inversion and intra-inversion filtering using edge-adaptive, gapped gradient-nulling filters: applications to surveys for unexploded ordnance (UXO); Proceedings of Joint Conference of Korean Geological Survey and Korean Society of Exploration Geophysicists, 6 pages (includes abstract in Korean).

3. René, R. M., and Kim, K. Y., 2006, Edge-adaptive and gapped gradient-nulling intra-inversion filters for application to UXO magnetic field surveys: Proceedings of the Symposium on the Application of Geophysics to Engineering and Environmental Problems (SAGEEP 2006), 1710-1724.

4. René, R. M., Park, C. H., and Kim, K. Y., 2006, Edge-adaptive gapped gradient-nulling filters and inversion of magnetic fields in a lake survey of possible dredging hazards and UXO: Proceedings of the Symposium on the Application of Geophysics to Engineering and Environmental Problems (SAGEEP 2006), 1697-1709.

5. René, R. M., and Kim, K. Y., (accepted), Effects of intra-inversion filtering on the accuracy of UXO magnetic dipole inversions using standardized test site data: Proceedings of the Symposium on the Application of Geophysics to Engineering and Environmental Problems (SAGEEP 2007), 12 pages.

Published Technical Abstracts:

1. René, R. M., and Kim, K. Y., 2005, Intra-inversion filtering for use of magnetic fields to locate and characterize magnetic dipoles for unexploded ordnance (UXO) cleanup: abstract and Munitions Management Poster Number 143, Partners in Environmental Technology Technical Symposium and Workshop, SERDP and ESTCP, Washington, D. C., Nov. 29-Dec. 1, 2005.

2. René, R. M., and Kim, K. Y., 2006, Edge-adaptive gapped gradient-nulling (EAGGN) and other intra-inversion filtering for improved magnetic field inversion in UXO surveys: abstract and Munitions Management Poster, Partners in Environmental Technology Technical Symposium and Workshop, SERDP and ESTCP, Washington, D. C., Nov. 28-30, 2006.